

# **The Seismic Behavior of Steel Structures with Semi-Rigid Diaphragms**

Chia-hung Fang

Dissertation submitted to the Faculty of the Virginia Polytechnic Institute and State University  
in partial fulfillment of the requirements for the degree of

Doctor of Philosophy  
in  
Civil Engineering

Roberto T. Leon, Chair  
Finley A. Charney  
W. Samuel Easterling  
Ioannis Koutromanos  
Cristopher D. Moen

August 07, 2015  
Blacksburg, Virginia, USA

Keywords: Semi-rigid diaphragms, Rigid diaphragms, Pushover analysis, Nonlinear dynamic analysis

© Copyright 2015, Chia-hung Fang

# **The Seismic Behavior of Steel Structures with Semi-Rigid Diaphragms**

Chia-hung Fang

## **Abstract**

This thesis investigates the torsional performance of steel structures with and without rigid diaphragm constraints through numerical simulations and evaluates the appropriateness of relevant design provisions in current seismic design codes. In the first part of the work, six theme structures with different (1) in-plane stiffness of diaphragm, and (2) horizontal configurations of vertical braced frames were designed and their performance evaluated through both nonlinear static and dynamic analyses.

Comparisons of the analytical results between the structures with and without rigid diaphragm constraints indicate that the in-plane rigidity of the diaphragms affects the efficiency of in-plane force transfer mechanisms, resulting in different global ductility and strength demands. Rigid diaphragm structures exhibit higher global strengths as well as higher torsional rotation capacity because of the infinite in-plane stiffness of the diaphragm. Semi-rigid diaphragm structures have higher ductility demands due to the finite in-plane diaphragm stiffness. The inclusion of bi-axial forces in the analyses reduces the structural strength and increases the ductility demands on the peripheral frames.

The axial forces in the collectors and chords that make up the diaphragm depend on (1) the sequence of brace buckling and (2) vertical configuration of the braced frames. The results show higher axial forces in collectors in the roof diaphragms, and higher chord axial forces in the third floor diaphragms. The shear connections in the beams that make up both the collectors and

chords are susceptible to failure due to the significant increment of axial forces in those members. The conventional beam analogy used in design can severely underestimate the axial forces in chords and collectors when the structures step into the inelastic stage.

## **Acknowledgement**

The author would like to express his special thanks to his advisor, Dr. Roberto T. Leon, who has mentored him during the last three years. His encouragement and continuous guidance made possible the completion of this study. He has helped to develop and organize the author's background to explore an interesting area: Earthquake Engineering. It has been a real pleasure and privilege to work with him.

Appreciation and thanks are also extended to the dissertation advisory committee made up by Dr. Finley Charney, Dr. Samuel Easterling, Dr. Cristopher Moen and Dr. Ioannis Koutromanos. Their technical expertise, recommendations, and continuous support throughout this research were invaluable. The author looks forward to continuing these relationships in the future.

In addition, the author wants to express his appreciation to Dr. Walter Yang at Georgia Tech. His technical suggestions and support were important to the author in overcoming some difficulties in the study. The author would also like to acknowledge his friends, both at Virginia Tech and Georgia Tech, for their help during the author's stay in the U.S: Yu Gao, YouYou Cao, Daniel Kim, Johnn Judd and Jeena Jayamon at VT; Dapeng Zhu, Chuhee Cho, Xiaohua Yi and Pablo Vega-Behar at GT.

Finally, the author would like to thank his parents and parents-in-laws for their loving support and encouragement. In particular, my wife, Selena Chen, thank her for her patience, love, and encouragement. This is such an honor for the author to have her company in his life.

## Table of Contents

Abstract.....	ii
Acknowledgement .....	iv
Table of Contents.....	v
List of Figures.....	x
List of Tables .....	xix
Chapter 1 Introduction.....	1
1.1 Background and Motivation .....	1
1.2 Methodology .....	5
1.3 Objectives and Research Tasks.....	6
1.4 Organization of the Thesis.....	9
Chapter 2 Literature review.....	11
2.1 Introduction.....	11
2.2 Functions of diaphragms.....	11
2.3 Other relevant topics .....	13
2.4 Review of design procedures .....	28
2.5 Concepts and assumptions for diaphragms in seismic design .....	31
Chapter 3 Structural modeling and design .....	35
3.1 Introduction.....	35
3.2 Analysis platforms .....	36
3.3 Description of theme structures .....	37
3.4 Design of the theme structures.....	40
3.4.1 <i>Material properties and gravity loads</i> .....	40
3.4.2 <i>Site conditions</i> .....	41
3.4.3 <i>Seismic design parameters</i> .....	43
3.4.4 <i>Load combinations</i> .....	44
3.4.5 <i>Story drift and P-Delta effects</i> .....	44
3.4.6 <i>Member sizes</i> .....	45
3.4.7 <i>Demand and Capacity (D/C) ratio check for members</i> .....	47
3.4.8 <i>Discussion of horizontal irregularities in the diaphragms</i> .....	48

3.5	Simulation details for structural components in OpenSEES .....	49
3.5.1	<i>Columns in LFRS</i> .....	49
3.5.2	<i>Braces</i> .....	51
3.5.3	<i>Beams in SCBFs</i> .....	55
3.5.4	<i>Beams in SMRFs</i> .....	59
3.5.5	<i>Panel zones</i> .....	60
3.5.6	<i>Composite action of the beam in internal gravity beams</i> .....	61
3.5.7	<i>Composite action of the beam in external gravity beams</i> .....	65
3.6	Simulation details for semi-rigid and rigid diaphragms in OpenSEES .....	70
3.6.1	<i>Rigid diaphragms</i> .....	70
3.6.2	<i>Semi-rigid diaphragms</i> .....	72
3.7	Application of vertical loads and mass .....	73
3.8	Consideration of effect of nonlinear geometry .....	74
3.9	Period comparison between SAP2000 and OpenSEES .....	74
3.10	Nonlinear static (Pushover) analyses .....	75
3.10.1	<i>Lateral load pattern in rigid diaphragm structures</i> .....	76
3.10.2	<i>Lateral load pattern in semi-rigid diaphragm structures</i> .....	76
3.11	Nonlinear dynamic analyses .....	77
3.11.1	<i>Direct integration analysis</i> .....	77
3.11.2	<i>Damping ratios</i> .....	78
3.11.3	<i>Selection and scaling of Ground Motions</i> .....	79
3.12	Initial designs .....	80
Chapter 4 The behavior of the steel structures considering the effects of semi-rigid diaphragms.....		82
4.1	Introduction.....	82
4.2	Classifications .....	82
4.3	X-braced frame .....	83
4.3.1	<i>Related simulation details</i> .....	83
4.3.2	<i>Capacity curves</i> .....	84
4.3.3	<i>P-Delta effect</i> .....	86
4.4	Chevron-braced frame .....	87
4.4.1	<i>Capacity curves</i> .....	88

4.5	Moment frame.....	89
4.5.1	Capacity curves.....	90
4.6	Single-story 3D structure .....	92
4.6.1	Description of the structure .....	92
4.6.2	Shell element simulation .....	93
4.6.3	Capacity curves.....	95
4.6.4	Rotational deformation of the 3D structure.....	97
4.7	Conclusions.....	99
Chapter 5 The behavior of 3D steel structures with semi-rigid and rigid diaphragms with accidental torsions.....		101
5.1	Introduction.....	101
5.2	Classification and notation of the theme structures in nonlinear analyses .....	102
5.3	Nonlinear analyses for the structures with $M_{ta}$ .....	103
5.3.1	Modification of diaphragm mass distribution for theme structures .....	108
5.4	Nonlinear static (Pushover) analyses (NSA) .....	110
5.4.1	Pushover load patterns for the structures with $M_{ta_1}$ and $M_{ta_2}$ .....	110
5.4.2	Capacity curves for each configuration.....	113
5.4.3	Rotation behavior of diaphragms .....	123
5.4.4	Inter-story drift ratios .....	128
5.4.5	Contribution of individual systems .....	129
5.5	Nonlinear dynamic analyses (NDA).....	132
5.5.1	Variation of torsion coefficients.....	133
5.5.2	Absolute and relative maximum rotational angles for diaphragms .....	134
5.5.3	Maximum inter-story drift ratios .....	143
5.5.4	Maximum roof drift ratios and base shears.....	147
5.6	Conclusions.....	151
Chapter 6 Behavior evaluation of peripheral frames in the 3D models .....		154
6.1	Introduction.....	154
6.2	Behavior of peripheral moment frames in asymmetric structures .....	154
6.2.1	Discussion of the reaction curves for SMRFs.....	155
6.3	P-M-M interaction of the columns in moment and braced frames .....	158
6.4	Dynamic response for peripheral frames .....	165

6.5	Conclusions.....	167
Chapter 7	Seismic Behavior of Collectors and Chords.....	169
7.1	Introduction.....	169
7.2	Diaphragm design based on ASCE 7.....	170
7.2.1	<i>Collectors and chords</i> .....	170
7.2.2	<i>Diaphragm design forces based on ASCE 7-10</i> .....	172
7.2.3	<i>Beam analogy for the design of chords and collectors in diaphragms</i> .....	174
7.3	Behavior of collectors in the NSA.....	178
7.4	Behavior of chords in the NSA.....	180
7.5	Behavior of collectors in NDA.....	182
7.6	Behavior of chords in the NDA.....	184
7.7	Comparison between analytical results and conventional design provisions.....	186
7.7.1	<i>Evaluation of axial forces in chords and collectors based on AISC seismic provision</i> .....	186
7.7.2	<i>Verifications of the behavior of edge collectors and chords</i> .....	190
7.8	Conclusions.....	191
Chapter 8	Conclusions and Recommendations.....	194
References	.....	201
Appendix A	.....	206
Appendix B	.....	217
Appendix C	.....	237
C.1	Introduction.....	238
C.2	Orthotropic stiffness modification for composite slab.....	239
C.3	The simulation of flexible diaphragm-base line structures.....	241
C.4	The simulation of flexible diaphragm-simplified structure.....	244
C.4.1	<i>Concepts of beam-truss model</i> .....	244
C.4.2	<i>Parameters study of the beam-truss model</i> .....	247
C.4.3	<i>Simplified structures simulation</i> .....	250
C.5	Analysis results and comparison.....	252
C.5.1	<i>Comparison of flexible and rigid diaphragm structures</i> .....	252
C.5.2	<i>Comparison between baseline and simplified structures -TYPE A</i> .....	254

C.5.3 Comparison of baseline and simplified structures -TYPE A1, B1 and C1.....	255
C.6 Conclusion.....	258
Appendix D.....	262
D.1 Introduction.....	262
D.2 Description of theme structures .....	264
D.3 Modification of diaphragm mass distribution.....	267
D.4 Nonlinear static analyses (NSA).....	271
D.4.1 Lateral load distributions in NSA for the structures with $M_{ta}$ .....	271
D.4.2 Capacity curves.....	271
D.4.3 Rotation behavior of the diaphragms.....	273
D.4.4 Bi-axial NSA for the structures with $M_{ta}$ .....	275
D.5 Nonlinear Dynamic Analyses (NDA) for the C2 structures with $M_{ta}$ .....	279
D.5.1 The selection of $G.M_s$ .....	279
D.5.2 Rotation angles of diaphragms .....	279
D.5.3 Maximum inter-story drift ratio .....	282
D.6 Conclusions.....	283

## List of Figures

Figure 1-1 Rigid diaphragm model.....	1
Figure 1-2 Diaphragms and vertical frames in a structure (Sabelli R. et al., 2011) .....	2
Figure 1-3 Collectors and chords in a diaphragm (Sabelli R. et al., 2011).....	2
Figure 2-1 Shear flow in collector beams (American Institute of Steel Construction, 2010b) ....	12
Figure 2-2 Experimental versus analytical strength (Easterling W. S. and Porter M. L., 1994a)	14
Figure 2-3 Configurations of 3D RC frames (Ju S. H. and Lin M. C., 1999) .....	15
Figure 2-4 Comparison of column shears (Ju S. H. and Lin M. C., 1999).....	16
Figure 2-5 Summary of shear error with suggested error bounds (Saffarini H.S. and Qudaimat M.M., 1992) .....	17
Figure 2-6 Nonlinear truss models for diaphragm simulation in OpenSEES (Tremblay R. and Stiemer S. F., 1996) .....	18
Figure 2-7 Displacement modal static response of UBC design structures as a function of diaphragm flexibility (Fleischman R. B. and Farrow K. T., 2001).....	20
Figure 2-8 Original two-story structure and analytical lumped mass model (Sadashiva V. K. et al., 2012) .....	21
Figure 2-9 Variation of torsional amplification with roof drift ratio from pushover analysis (Erduran E. and Ryan K. L., 2011).....	23
Figure 2-10 In-plane force distribution in a diaphragm (Sabelli R. et al., 2011).....	25
Figure 2-11 Simulation of typical braced frame (Sabelli R. et al., 2013).....	28
Figure 2-12 Definition of flexible diaphragm by ASCE 7 (American Society of Civil Engineers, 2010) .....	30
Figure 2-13 Deep beam model for diaphragm design (Sabelli R. et al., 2011) .....	33
Figure 3-1 Plan layout of theme structures (a) C1 (b) C2.....	38
Figure 3-2 Elevation of typical (a) braced frame, (b) moment frame, and (c) gravity frame.....	40
Figure 3-3 Design spectrum.....	42
Figure 3-4 Risk-target maximum considered spectrum.....	43
Figure 3-5 Dimensions of RBS (NEHRP, 2010).....	45
Figure 3-6 Typical layout of (a) slab system and (b) composite deck.....	47
Figure 3-7 Fiber beam and column sections in 3D OpenSEES models .....	51
Figure 3-8 Fiber brace section in 3D models.....	52
Figure 3-9 Individual brace model with imperfection .....	53
Figure 3-10 Hysteretic loops for brace simulated by different element types and numbers .....	53

Figure 3-11 Hysteretic loops of brace with (a) fracture and (b) fatigue effects .....	54
Figure 3-12 Simulation of brace including imperfection.....	55
Figure 3-13 Fiber sections for beam sections in SCBFs.....	56
Figure 3-14 Fiber section with composite action.....	56
Figure 3-15 Beam models for the testing of composite effects .....	58
Figure 3-16 Test results for beam models: (a) history of cyclic loading and (b) hysteretic loops	59
Figure 3-17 Typical beam model in SMRFs.....	60
Figure 3-18 Panel zone model for beam-column connection .....	60
Figure 3-19 Computation of equivalent area for out-of plane bending (a) original tributary area, (b) equivalent area and (c) composite section with equivalent area .....	63
Figure 3-20 Chord action in diaphragm due to seismic loads .....	66
Figure 3-21 Cyclic loading test for edge chords.....	67
Figure 3-22 Simulation approach for edge collector and chord: (a) analytical model, (b) section A and (c) section B .....	68
Figure 3-23 Fiber stress: (a) stress-strain hysteresis response of Fiber 2, (b) loading history and (c) history of horizontal reaction.....	69
Figure 3-24 Hysteretic loops for (a) W18x46 (X-dir) and (b) W18x46 (Y-dir).....	69
Figure 3-25 Positions of master and slave nodes in rigid diaphragm structures .....	71
Figure 3-26 Tributary areas for gravity loads in columns and moment frames in C1 .....	74
Figure 3-27 Pushover load patterns for rigid and semi-rigid structures .....	77
Figure 4-1 Different assumptions for diaphragm simulation: (a) <b>BF+R</b> , (b) <b>CF+R</b> and (c) <b>CF</b> .	83
Figure 4-2 Elevation of X-braced frame .....	84
Figure 4-3 Analytical results for X-braced frame: (a) capacity curves and (b) deformed shape at 0.05 roof drift ratio.....	85
Figure 4-4 Analytical results including brace fracture: (a) capacity curves and (b) deformed shapes .....	86
Figure 4-5 Capacity curves under different magnitudes of gravity loads: (a) <b>BF+R</b> and (b) <b>CF+R</b> .....	87
Figure 4-6 Elevation of the chevron braced frame .....	88
Figure 4-7 Analytical results of chevron braced frame: (a) capacity curves and (b) deformed shapes .....	89
Figure 4-8 Elevation of 2D SMRF.....	90
Figure 4-9 Analytical results for 2D SMRF: (a) capacity curves ,(b) deformed shapes ,(c) curvature for the left point and right point of the target beam in the 2F and (d) force- displacement relationship of the panelzone in Joint A .....	91

Figure 4-10 One-story 3D frame.....	92
Figure 4-11 Plan layout for shell element simulation.....	93
Figure 4-12 Distance between the centroids in slab and beam: (a) W18x46 and (b) W24x76 ....	94
Figure 4-13 Comparison of capacity curves in the 3D models.....	96
Figure 4-14 Variation of compression axial forces in braces .....	97
Figure 4-15 Variation of imperfection of braces: (a) initial status, (b) imperfection for the structures without elastic shell elements and (c) imperfection for the structures with elastic shell elements .....	97
Figure 4-16 Modified load patterns for the 3D one-story structure.....	98
Figure 4-17 NSA response of one-story structure: (a) capacity curves and (b) <i>TC</i> history.....	99
Figure 5-1 Position of monitor point for the SMRFs and SCBFs in each configuration.....	103
Figure 5-2 Application of $M_{ta}$ for theme structures (C1).....	104
Figure 5-3 Diaphragm force on a rigid diaphragm .....	105
Figure 5-4 $M_{ta}$ on a semi-rigid diaphragm .....	106
Figure 5-5 Re-distribution of diaphragm mass for $M_{ta}$ .....	108
Figure 5-6 Lumped mass model of theme structures (C1 and C2).....	109
Figure 5-7 Additional lateral force distribution based on $M_{ta}$ .....	109
Figure 5-8 Application of additional lumped mass based on the effect of $M_{ta}$ .....	109
Figure 5-9 Movement of master joints for rigid diaphragm structure: (a) C1 and (b) C2.....	111
Figure 5-10 Application of lateral force pattern for pushover analyses .....	112
Figure 5-11 Comparison of capacity curves of C1 with $M_{ta\_1}$ (W=8450kips).....	114
Figure 5-12 Brace buckling and fracture sequence in C1 ( <b>CF+R</b> ): (a) capacity curve and (b) failure sequence .....	114
Figure 5-13 Capacity curves for C1: (a) $M_{ta\_1}$ and (b) $M_{ta\_2}$ .....	116
Figure 5-14 Capacity curves for C1 braced frames with $M_{ta\_1}$ : (a) <b>CF+R</b> and (b) <b>CF</b> .....	118
Figure 5-15 Movement of C.R. in C2.....	118
Figure 5-16 Comparison of capacity curves for C2 structures with $M_{ta\_2}$ (W = 8450kips).....	119
Figure 5-17 Capacity curves for C2: (a) $M_{ta\_1}$ and (b) $M_{ta\_2}$ .....	120
Figure 5-18 Capacity curves of braced frames of C2 with $M_{ta\_1}$ : (a) <b>CF+R</b> and (b) <b>CF</b> .....	121
Figure 5-19 Force redistribution mechanism in structures with rigid diaphragms.....	122
Figure 5-20 Force redistribution mechanism in structures with semi-rigid diaphragms.....	123
Figure 5-21 Rotation of diaphragm during pushover analyses (C2).....	124
Figure 5-22 Rotation stages corresponding to the variation of torsion coefficient.....	126

Figure 5-23 Variation of torsion coefficient of C1: <b>BF+R</b> (a) $M_{ta\_1}$ and (b) $M_{ta\_2}$ .....	127
Figure 5-24 Variation of torsion coefficient of C2: <b>BF+R</b> (a) $M_{ta\_1}$ and (b) $M_{ta\_2}$ .....	127
Figure 5-25 Positions of right and left corner monitor points in each configurations: (a) C1 and (b) C2.....	128
Figure 5-26 Inter-story drift ratio for diaphragm in C1 ( <b>BF+R</b> ) with $M_{ta\_1}$ : (a) Left corner and (b) Right corner .....	129
Figure 5-27 Inter-story drift ratio for diaphragm in C2 ( <b>BF+R</b> ) with $M_{ta\_1}$ : (a) Left corner and (b) Right corner .....	129
Figure 5-28 Individual capacity curves for C1 with $M_{ta\_2}$ : (a) <b>CF+R</b> and (b) <b>CF</b> .....	130
Figure 5-29 Individual capacity curves of C2 with $M_{ta\_2}$ : (a) <b>CF+R</b> and (b) <b>CF</b> .....	131
Figure 5-30 Variation of torsion coefficient for C1 in DBE level ground motion (EI Centro)..	134
Figure 5-31 Variation of rotation angle for C1 at DBE ground motion (EI Centro): (a) entire history and (b) 1.5~5.5 sec.....	136
Figure 5-32 Maximum rotation angles of diaphragms C1 with $M_{ta\_1}$ : (a) DBE and (b) MCE...	137
Figure 5-33 Ratios of Maximum rotation angles of diaphragms for C1 under MCE: (a) $M_{ta\_1}$ and (b) $M_{ta\_2}$ .....	138
Figure 5-34 Ratios of Maximum rotation angles of diaphragms for C2 under MCE: (a) $M_{ta\_1}$ and (b) $M_{ta\_2}$ .....	138
Figure 5-35 History of relative rotation angle for C1 in DBE ground motion (EI Centro): (a) entire history and (b) 2.0~11.0 sec.....	140
Figure 5-36 Maximum relative rotation angle of diaphragms C1: $M_{ta\_1}$ (a) DBE and (b) MCE	141
Figure 5-37 Ratios of Maximum relative rotation angle of diaphragms for C1 under MCE: (a) $M_{ta\_1}$ and (b) $M_{ta\_2}$ .....	142
Figure 5-38 Ratios of Maximum relative rotation angle of diaphragms for C2 under MCE: (a) $M_{ta\_1}$ and (b) $M_{ta\_2}$ .....	142
Figure 5-39 Relative rotation angle history of stories for C1 in DBE ground motion (EI-Centro) .....	143
Figure 5-40 Inter-story drift ratios in C1 (with $M_{ta\_1}$ ) under EI-Centro ground motion at the DBE-level: (a) entire history and (b) 0.0~10.0 sec. ....	144
Figure 5-41 Maximum inter-story drift ratios of C1 with $M_{ta\_1}$ in MCE: (a) Y-dir and (b) X-dir .....	146
Figure 5-42 Maximum inter-story drift ratios of C1 with $M_{ta\_2}$ in MCE: (a) Y-dir and (b) X-dir .....	146
Figure 5-43 Maximum inter-story drift ratios ratio in C1 at MCE-level: (a) $M_{ta\_1}$ and (b) $M_{ta\_2}$	147
Figure 5-44 Maximum inter-story drift ratios ratio in C2 at MCE-level: (a) $M_{ta\_1}$ and (b) $M_{ta\_2}$	147
Figure 5-45 Maximum roof drift ratios vs. $V/W_{max}$ in C1 structures with $M_{ta\_1}$ : (a) DBE and (b) MCE.....	150

Figure 5-46 Maximum roof drift ratios vs. $V/W_{max}$ in C1 structures with $M_{Ia\_2}$ : (a) DBE and (b) MCE.....	150
Figure 5-47 Maximum roof drift ratios vs. $V/W_{max}$ in C2 structures with $M_{Ia\_1}$ : (a) DBE and (b) MCE.....	151
Figure 5-48 Maximum roof drift ratios vs. $V/W_{max}$ in C2 structures with $M_{Ia\_2}$ : (a) DBE and (b) MCE.....	151
Figure 6-1 Nomenclature of roof displacements and reactions of the SMRFs.....	155
Figure 6-2 Normalized base shear vs. drift curves (reaction curves)for SMRFs in C1 with $M_{Ia\_1}$ : (a) $V_{X1}$ vs. $\Delta_{X1}$ and (b) $V_{Y1}$ vs. $\Delta_{Y1}$ .....	157
Figure 6-3 Normalized base shear vs. drift curves (reaction curves) for SMRFs in C1 with $M_{Ia\_2}$ : (a) $V_{X1}$ vs. $\Delta_{X1}$ and (b) $V_{Y1}$ vs. $\Delta_{Y1}$ .....	157
Figure 6-4 Normalized base shear vs. drift curves (reaction curves) for SMRFs in C2 with $M_{Ia\_1}$ : (a) $V_{X1}$ vs. $\Delta_{X1}$ and (b) $V_{Y1}$ vs. $\Delta_{Y1}$ .....	158
Figure 6-5 Normalized base shear vs. drift curves for (reaction curves) SMRFs in C2 with $M_{Ia\_2}$ : (a) $V_{X1}$ vs. $\Delta_{X1}$ and (b) $V_{Y1}$ vs. $\Delta_{Y1}$ .....	158
Figure 6-6 Position of selected section for P-M-M interaction evaluation.....	159
Figure 6-7 P-M-M interaction curves in moment frames in Section <i>A</i> in C2 with $M_{Ia\_1}$ : (a) 3D view and (b) 2D view.....	161
Figure 6-8 Variation of bi-axial bending in Section <i>A</i> in C2: (a) <b>CF+R</b> and (b) <b>CF</b> .....	163
Figure 6-9 P-M-M interaction curves in moment frames in Section <i>A</i> in C2 with $M_{Ia\_2}$ : (a) 3D view and (b) 2D view.....	164
Figure 6-10 Variation of bi-axial bending in Section <i>A</i> in C2 with $M_{Ia\_2}$ : (a) <b>CF+R</b> and (b) <b>CF</b> .....	164
Figure 6-11 Base shear ratio vs. maximum roof drift ratio in MF1 in X-dir. for C1 under MCE-level ground motions: (a) $M_{Ia\_1}$ and (b) $M_{Ia\_2}$ .....	166
Figure 6-12 Base shear ratio vs. maximum roof drift ratio in MF1 in X-dir. for C2 under MCE-level ground motions: (a) $M_{Ia\_1}$ and (b) $M_{Ia\_2}$ .....	166
Figure 7-1 Position of target collectors in each configuration: (a) C1 and (b) C2 .....	171
Figure 7-2 Position of target chords in each configuration: (a) C1 and (b) C2 .....	172
Figure 7-3 Postion of target collectors and chords in the 3D view: (a) collectors and (b) chords .....	172
Figure 7-4 Vertical distribution of seismic design forces for LFRS and diaphragm: (a) C1 and (b) C2.....	173
Figure 7-5 Beam model based on the beam analogy .....	175
Figure 7-6 Collector design axial forces based on ASCE 7: (a) C1 and (b) C2 .....	177
Figure 7-7 Chord design axial forces based on ASCE 7: (a) C1 and (b) C2 .....	178

Figure 7-8 Axial forces in collectors at BF1 in C1: (a) $M_{ta\_1}$ , (b) $M_{ta\_2}$ and (c) sequence of brace failure .....	179
Figure 7-9 Axial forces in collectors at BF4 in C1: (a) $M_{ta\_1}$ , (b) $M_{ta\_2}$ and (c) sequence of brace failure .....	179
Figure 7-10 Axial forces in collectors at BF2 in C2: (a) $M_{ta\_1}$ , (b) $M_{ta\_2}$ and (c) sequence of brace failure .....	180
Figure 7-11 Axial forces in collectors at BF4 in C2: (a) $M_{ta\_1}$ , (b) $M_{ta\_2}$ and (c) sequence of brace failure .....	180
Figure 7-12 Axial forces in chords at MF1 in C2: (a) $M_{ta\_1}$ and (b) $M_{ta\_2}$ .....	181
Figure 7-13 Deformed shape of 2F diaphragm in the C2 structure as the NSA progresses (a) elastic stage, (b) brace buckles in the 1 <sup>st</sup> story in BF1, (c) brace buckles in the 1 <sup>st</sup> story in BF2 and (c) brace buckles in the 1 <sup>st</sup> story in BF3 .....	182
Figure 7-14 Peak axial forces in collectors in C1: (a) BF1, (b) BF2, (c) BF3 and (d) BF4 .....	183
Figure 7-15 Peak axial forces in collectors in C2: (a) BF1, (b) BF2, (c) BF3 and (d) BF4 .....	184
Figure 7-16 Average peak axial forces in chords in C1: (a) MF1 and (b) MF2 .....	185
Figure 7-17 Peak axial forces in chords in C2: (a) MF1 and (b) MF2 .....	186
Figure 7-18 Comparisons of collector and chord axial forces between analytical results and design code in C1: (a) BF1, (b) BF2, (c) BF3, (d) BF4, (e) MF1 and (f) MF2 .....	188
Figure 7-19 Comparisons of collector and chord axial forces between analytical results and design code in C2: (a) BF1, (b) BF2, (c) BF3, (d) BF4, (e) MF1 and (f) MF2 .....	189
Figure 7-20 Comparisons of hysteretic loops, design forces and analytical forces for the edge beams (a) X-dir (edge chords) (b) Y-dir (edge collectors) .....	191
Figure A-1 D/C ratios for braces in SCBFs (C1) .....	207
Figure A-2 D/C ratios for braces in SCBFs (C2) .....	207
Figure A-3 Various spectra from the 3D ground motions scaling process for C1: (a) Unscaled SRSS, (b) Unscaled SRSS and 1.0xdesign, (c) FP SRSS and 1.0xdesign and (d) FP average SRSS and 1.0xdesign .....	214
Figure A-4 Various spectra from the 3D ground motions scaling process for C2: (a) Unscaled SRSS, (b) Unscaled SRSS and 1.0xdesign, (c) FP SRSS and 1.0xdesign and (d) FP average SRSS and 1.0xdesign .....	215
Figure A-5 Combined SRSS and 1.0xdesign: (a) C1 and (b) C2 .....	215
Figure A-6 Un-deformed theme structures in OpenSEES in the initial design .....	216
Figure B-1 Capacity curves of braced frames of C1 with $M_{ta\_1}$ : (a) <b>BF+R</b> , (b) <b>CF+R</b> and (c) <b>CF</b> .....	217

Figure B-2 Capacity curves of braced frames of C1 with $M_{ta\_2}$ : (a) <b>BF+R</b> , (b) <b>CF+R</b> and (c) <b>CF</b> .....	217
Figure B-3 Capacity curves of braced frames of C2 with $M_{ta\_1}$ : (a) <b>BF+R</b> , (b) <b>CF+R</b> and (c) <b>CF</b> .....	217
Figure B-4 Capacity curves of braced frames of C2 with $M_{ta\_2}$ : (a) <b>BF+R</b> , (b) <b>CF+R</b> and (c) <b>CF</b> .....	218
Figure B-5 <i>TC</i> of C1 with $M_{ta\_1}$ : (a) <b>BF+R</b> , (b) <b>CF+R</b> and (c) <b>CF</b> .....	218
Figure B-6 <i>TC</i> of C1 with $M_{ta\_2}$ : (a) <b>BF+R</b> , (b) <b>CF+R</b> and (c) <b>CF</b> .....	218
Figure B-7 <i>TC</i> of C2 with $M_{ta\_1}$ : (a) <b>BF+R</b> , (b) <b>CF+R</b> and (c) <b>CF</b> .....	219
Figure B-8 <i>TC</i> of C2 with $M_{ta\_2}$ : (a) <b>BF+R</b> , (b) <b>CF+R</b> and (c) <b>CF</b> .....	219
Figure B-9 <i>IDR</i> of C1 at left corner with $M_{ta\_1}$ : (a) <b>BF+R</b> , (b) <b>CF+R</b> and (c) <b>CF</b> .....	219
Figure B-10 <i>IDR</i> of C1 at right corner with $M_{ta\_1}$ : (a) <b>BF+R</b> , (b) <b>CF+R</b> and (c) <b>CF</b> .....	220
Figure B-11 <i>IDR</i> of C1 at right corner with $M_{ta\_2}$ : (a) <b>BF+R</b> , (b) <b>CF+R</b> and (c) <b>CF</b> .....	220
Figure B-12 <i>IDR</i> of C2 at left corner with $M_{ta\_1}$ : (a) <b>BF+R</b> , (b) <b>CF+R</b> and (c) <b>CF</b> .....	220
Figure B-13 <i>IDR</i> of C2 at right corner with $M_{ta\_1}$ : (a) <b>BF+R</b> , (b) <b>CF+R</b> and (c) <b>CF</b> .....	221
Figure B-14 <i>IDR</i> of C2 at left corner with $M_{ta\_2}$ : (a) <b>BF+R</b> , (b) <b>CF+R</b> and (c) <b>CF</b> .....	221
Figure B-15 <i>IDR</i> of C2 at right corner with $M_{ta\_2}$ : (a) <b>BF+R</b> , (b) <b>CF+R</b> and (c) <b>CF</b> .....	221
Figure B-16 Capacity curves of each system of C1 with $M_{ta\_1}$ : (a) <b>BF+R</b> , (b) <b>CF+R</b> and (c) <b>CF</b> .....	222
Figure B-17 Capacity curves of each system of C1 with $M_{ta\_2}$ : (a) <b>BF+R</b> , (b) <b>CF+R</b> and (c) <b>CF</b> .....	222
Figure B-18 Capacity curves of each system of C2 with $M_{ta\_1}$ : (a) <b>BF+R</b> , (b) <b>CF+R</b> and (c) <b>CF</b> .....	222
Figure B-19 Capacity curves of each system of C2 with $M_{ta\_2}$ : (a) <b>BF+R</b> , (b) <b>CF+R</b> and (c) <b>CF</b> .....	223
Figure B-20 Variation of <i>RA</i> in C1 with $M_{ta\_1}$ : (a) <i>DBE</i> and (b) <i>MCE</i> .....	223
Figure B-21 Variation of <i>RA</i> in C1 with $M_{ta\_2}$ : (a) <i>DBE</i> and (b) <i>MCE</i> .....	223
Figure B-22 Variation of <i>RA</i> in C2 with $M_{ta\_1}$ : (a) <i>DBE</i> and (b) <i>MCE</i> .....	224
Figure B-23 Variation of <i>RA</i> in C1 with $M_{ta\_2}$ : (a) <i>DBE</i> and (b) <i>MCE</i> .....	224
Figure B-24 Variation of <i>RRA</i> in C1 with $M_{ta\_1}$ : (a) <i>DBE</i> and (b) <i>MCE</i> .....	224
Figure B-25 Variation of <i>RRA</i> in C1 with $M_{ta\_2}$ : (a) <i>DBE</i> and (b) <i>MCE</i> .....	225
Figure B-26 Variation of <i>RRA</i> in C2 with $M_{ta\_1}$ : (a) <i>DBE</i> and (b) <i>MCE</i> .....	225
Figure B-27 Variation of <i>RRA</i> in C2 with $M_{ta\_2}$ : (a) <i>DBE</i> and (b) <i>MCE</i> .....	225
Figure B-28 <i>IDR</i> in C1 with $M_{ta\_1}$ with <i>DBE</i> ground motions: (a) <i>Y-dir</i> and (b) <i>X-dir</i> .....	226

Figure B-29 IDR in C1 with $M_{ta\_1}$ with MCE ground motions: (a) Y-dir and (b) X-dir .....	226
Figure B-30 IDR in C1 with $M_{ta\_2}$ with DBE ground motions: (a) Y-dir and (b) X-dir.....	226
Figure B-31 IDR in C1 with $M_{ta\_2}$ with MCE ground motions: (a) Y-dir and (b) X-dir .....	227
Figure B-32 IDR in C2 with $M_{ta\_1}$ with DBE ground motions: (a) Y-dir and (b) X-dir .....	227
Figure B-33 IDR in C2 with $M_{ta\_1}$ with MCE ground motions: (a) Y-dir and (b) X-dir .....	227
Figure B-34 IDR in C2 with $M_{ta\_2}$ with DBE ground motions: (a) Y-dir and (b) X-dir.....	228
Figure B-35 IDR in C2 with $M_{ta\_2}$ with MCE ground motions: (a) Y-dir and (b) X-dir .....	228
Figure B-36 Axial forces in collectors and chords in C1 under DBE-level ground motions with $M_{ta\_1}$ : (a) BF1, (b) BF2, (c) BF3, (d) BF4, (e) MF1, and (f) MF2.....	229
Figure B-37 Axial forces in collectors and chords in C1 under DBE-level ground motions with $M_{ta\_2}$ : (a) BF1, (b) BF2, (c) BF3, (d) BF4, (e) MF1, and (f) MF2.....	230
Figure B-38 Axial forces in collectors and chords in C1 under MCE-level ground motions with $M_{ta\_1}$ : (a) BF1, (b) BF2, (c) BF3, (d) BF4, (e) MF1, and (f) MF2.....	231
Figure B-39 Axial forces in collectors and chords in C1 under MCE-level ground motions with $M_{ta\_2}$ : (a) BF1, (b) BF2, (c) BF3, (d) BF4, (e) MF1, and (f) MF2.....	232
Figure B-40 Axial forces in collectors and chords in C2 under DBE-level ground motions with $M_{ta\_1}$ : (a) BF1, (b) BF2, (c) BF3, (d) BF4, (e) MF1, and (f) MF2.....	233
Figure B-41 Axial forces in collectors and chords in C2 under DBE-level ground motions with $M_{ta\_2}$ : (a) BF1, (b) BF2, (c) BF3, (d) BF4, (e) MF1, and (f) MF2.....	234
Figure B-42 Axial forces in collectors and chords in C2 under MCE-level ground motions with $M_{ta\_1}$ : (a) BF1, (b) BF2, (c) BF3, (d) BF4, (e) MF1, and (f) MF2.....	235
Figure B-43 Axial forces in collectors and chords in C2 under MCE-level ground motions with $M_{ta\_2}$ : (a) BF1, (b) BF2, (c) BF3, (d) BF4, (e) MF1, and (f) MF2.....	236
Figure C-1 Geometry definition of corrugated slab.....	240
Figure C-2 Geometry and material properties for composite slab.....	241
Figure C-3 Configurations of single-story steel structures.....	243
Figure C-4 Configuration of the structure simulation by using shell elements .....	244
Figure C-5 Beam-truss and shell element model.....	245
Figure C-6 Decomposition of beam-truss model.....	246
Figure C-7 Stiffness matrix of beam system.....	247
Figure C-8 Procedures for determining the beam depth, D .....	248
Figure C-9 The variation of d with different $K_T/K_B$ and E.....	249
Figure C-10 The variation of $A_{truss}$ with different $K_T/K_B$ and E .....	249

Figure C-11 Configuration of the structure simulation by using beam-truss model (simplified structure, TYPE A) .....	251
Figure C-12 Configurations of baseline and simplified structures .....	252
Figure C-13 Comparison of normalized displacement between flexible and rigid diaphragm structures .....	254
Figure C-14 Comparison of normalized displacement between baseline and simplified structures (TYPE A) .....	255
Figure C-15 Comparison of normalized displacement between baseline and simplified model (TYPE A1, B1 and C1) .....	258
Figure D-1 Plan layout of theme structures .....	265
Figure D-2 Orientations of columns in theme structures .....	266
Figure D-3 Elevation layout of vertical frames: (a) Braced frames, (b) Moment frames and (c) gravity frames. ....	266
Figure D-4 Diaphragm force on a rigid diaphragm. ....	268
Figure D-5 Capacity curves: (a) C1SRA <sub>A</sub> and (b) C1SRA <sub>B</sub> .....	272
Figure D-6 Capacity curves: (a) C2SRA <sub>A</sub> and (b) C2SRA <sub>B</sub> .....	273
Figure D-7 <i>TC</i> of each diaphragm: (a) C2SRA <sub>A</sub> and (b) C2SRA <sub>B</sub> .....	275
Figure D-8 <i>TC</i> of each diaphragm: (a) C4SRA <sub>A</sub> and (b) C4SRA <sub>B</sub> .....	275
Figure D-9 Bi-axial NSA in the structures with rigid and semi-rigid diaphragms .....	277
Figure D-10 Capacity curves of each case in C4 structures: (a) C4RA and (b) C4SRA <sub>A</sub> .....	278
Figure D-11 Capacity curves of each braced frame in C4SRA <sub>A</sub> : (a) BF1 and (b) BF2 .....	278
Figure D-12 Maximum <i>RA</i> of each diaphragm in C2SRA <sub>A</sub> : (a) DBE and (b) MCE .....	280
Figure D-13 <i>RRD<sub>max</sub></i> of each diaphragm in C2SRA <sub>A</sub> : (a) DBE and (b) MCE .....	281
Figure D-14 Maximum <i>IDR</i> of the C2 structures with <i>M<sub>ta</sub></i> (a) DBE-level (b) MCE-level .....	283
Figure D-15 Maximum <i>IDR</i> of the C2 structures without <i>M<sub>ta</sub></i> (a) DBE-level (b) MCE-level ...	283

## List of Tables

Table 1-1 Analysis case matrix for this study.....	6
Table 3-1 Material properties for theme structures.....	41
Table 3-2 Gravity loads for theme structures .....	41
Table 3-3 Key seismic design parameters .....	44
Table 3-4 Load combinations of the theme structures.....	44
Table 3-5 Member sizes for LFRS in C1 .....	46
Table 3-6 Member sizes for LFRS in C2.....	46
Table 3-7 Member sizes for gravity frame .....	46
Table 3-8 Comparison of torsion coefficients for rigid diaphragms.....	49
Table 3-9 Period comparison between SAP2000 and OpenSEES (C1) .....	75
Table 3-10 Period comparison between SAP2000 and OpenSEES (C2) .....	75
Table 4-1 Member dimensions for chevron-braced frame .....	88
Table 4-2 Member dimensions for one-story 3D frame .....	93
Table 4-3 Material orthotropic properties for corrugated slab.....	94
Table 5-1 Mass modification parameters of each diaphragm for C1 and C2 .....	108
Table 5-2 Pushover load pattern for rigid diaphragm structures ( <i>BF+R</i> and <i>CF+R</i> ).....	112
Table 5-3 Pushover load patterns for semirigid diaphragm structures ( <i>CF</i> ) .....	112
Table 5-4 Summary of NSA for the C1 structures .....	116
Table 5-5 Summary of NSA for the C2 structures .....	120
Table 5-6 Summary of overstrength for the SCBFs .....	131
Table 5-7 Selected ground motions from PEER Data base .....	132
Table 5-8 Relationship between mean $V/W_{max}$ and $RDR_{max}$ in C1 structure .....	149
Table 5-9 Relationship between mean $V/W_{max}$ and $RDR_{max}$ in C2 structure.....	149
Table 6-1 Plastic moment of columns in braced and moment frames.....	159
Table 6-2 Mean $(V_{x1}/W)_{max}$ vs. $(RDR_{x1})_{max}$ in MF1 for C1 and C2 structures .....	167
Table 7-1 Design force for diaphragm (C1) .....	173
Table 7-2 Design force for diaphragm (C2) .....	173
Table 7-3 Calculation for collector design forces in the C1 structure .....	175
Table 7-4 Calculation for collector design forces in the C2 structure .....	176
Table 7-5 Calculation for chord design forces in the C1 structure.....	177

Table 7-6 Calculation for chord design forces in the C2 structure .....	177
Table A-1 Seismic load coefficients .....	206
Table A-2 Vertical distribution of seismic forces (SCBFs).....	206
Table A-3 Vertical distribution of seismic forces (SMRFs).....	206
Table A-4 Drift and stability check (C1 and C2).....	206
Table A-5 D/C ratios for columns in SCBFs (C1).....	207
Table A-6 D/C ratios for columns in SCBF1 and SCBF4 (C2).....	208
Table A-7 D/C ratios for columns in SCBF2 and SCBF3 (C2).....	208
Table A-8 D/C ratios for beams (C1) .....	208
Table A-9 D/C ratios for beams in SCBF1 and SCBF4 (C2).....	209
Table A-10 D/C ratios for beams in SCBF2 and SCBF3 (C2).....	209
Table A-11 Strong column – weak beam check (2F) .....	210
Table A-12 Strong column – weak beam check (3F) .....	210
Table A-13 Strong column – weak beam check (4F) .....	211
Table A-14 Strong column – weak beam check (RF).....	211
Table A-15 D/C ratios of panel zones.....	212
Table A-16 Spring stiffness of panel zones .....	212
Table A-17 Amplification factors of $CF1$ and $CF2$ .....	213
Table A-18 Amplification factors of $AF1$ (ACI approach) .....	213
Table A-19 Amplification factors of $AF1$ (Equivalent thickness approach) .....	213
Table A-20 Amplification factor of $AF1$ for edge beams.....	214
Table A-21 Selected ground motions from PEER Data base .....	214
Table A-22 Scaling factor for ground motions for C1 and C2 .....	216
Table C-1 Comparison of material properties of different material assumption.....	241
Table C-2 Combination of truss and beam with different stiffness ratio and elasticity of modulus .....	249
Table C-3 Comparison the number of DOF between baseline and simplified structures (TYPE A) .....	251
Table C-4 Structure periods of flexible and rigid diaphragm structures .....	253
Table C-5 Structure periods of baseline and simplified structures (TYPE A) .....	255
Table C-6 Structure period of baseline and simplified structures (TYPE A1, B1 and C1).....	257

Table D-1 Dimension of structural components of theme structures (C1 and C2) .....	266
Table D-2 Dimension of structural components of theme structures (C3 and C4) .....	267
Table D-3 Mass modification parameters of each configuration.....	270
Table D-4 Maximum $TC$ : $C2SRA_A$ , $C2SR_A$ , $C4SRA_A$ and $C4SR_A$ .....	274
Table D-5 Comparison of diaphragm $RRD_{max}$ for the structures with and without $M_{ta}$ ( $C2SR_A$ and $C2SRA_A$ ).....	281

# Chapter 1 Introduction

## 1.1 Background and Motivation

In conventional structural design, a common assumption to simulate the behavior of floor systems is to model those systems as rigid diaphragms. In such models all floor nodes are connected to a master joint by using links with in-plane rigid behavior. This assumption effectively prevents taking into account any in-plane membrane deformations (Figure 1-1). The assumption of rigid diaphragm behavior for the floor plate can significantly reduce the number of degrees of freedom of the structure and thus considerably speed up the analysis. This reduction is particularly valuable when considering non-linear time history and static pushover analyses in the case of seismic design. This assumption is explicitly accepted by design codes such as ASCE 7 (2010) and is almost universally used in preliminary design.

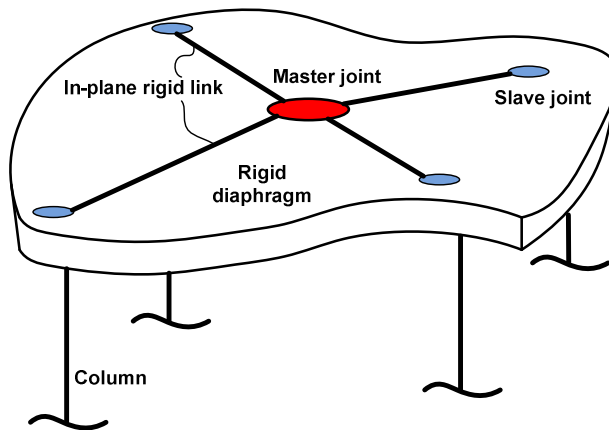


Figure 1-1 Rigid diaphragm model

However, in these analyses the forces in the floor beams connected to the diaphragms do not include the internal axial forces due to the in-plane deformations of the real diaphragm. In addition, the transfer mechanisms for local forces between the horizontal (diaphragms, chords,

collectors, beams and girders) and the vertical members (columns, walls and braces) may not be correctly modeled. Figure 1-2 and Figure 1-3 illustrate the positions of diaphragms, vertical frames, chords and collectors in a structure.

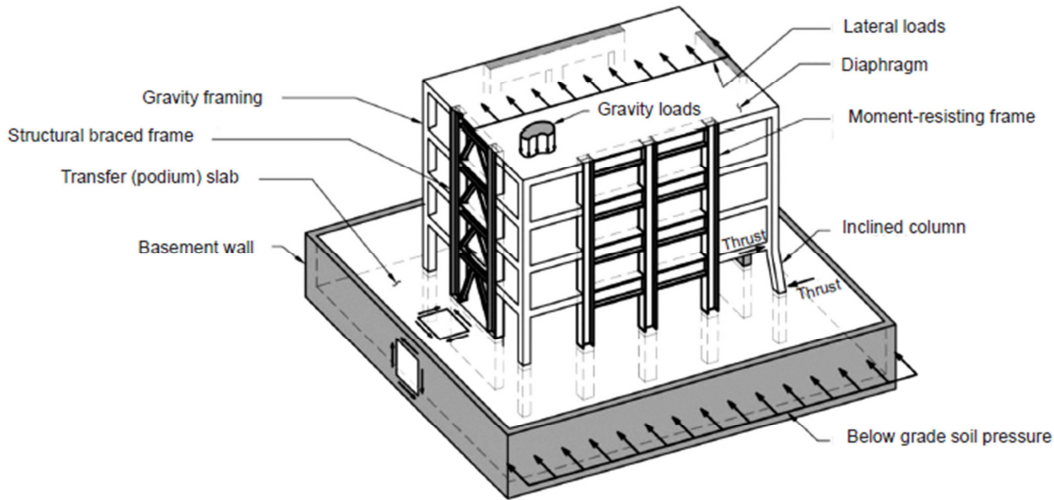


Figure 1-2 Diaphragms and vertical frames in a structure (Sabelli R. et al., 2011)

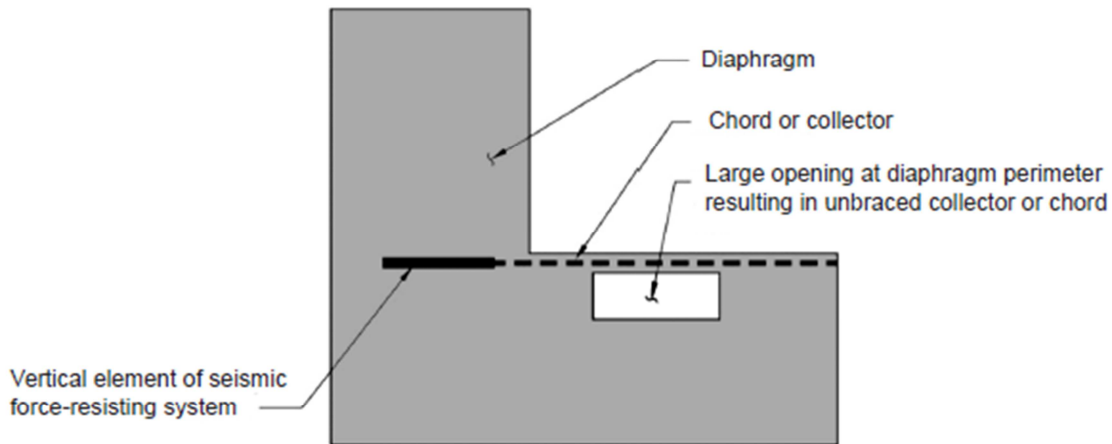


Figure 1-3 Collectors and chords in a diaphragm (Sabelli R. et al., 2011)

Some scenarios where the assumption of rigid diaphragm may not be appropriate for the simulation of diaphragm are as follows:

1. For structures with (a) irregular diaphragms, (b) irregular distributions of vertical systems (i.e. Lateral Force Resisting Systems, LFRS) across the floor plates, or (c) irregular mass distribution on diaphragms, the in-plane behavior of the diaphragm may be important due to the significant in-plane deformation or torsional effects on diaphragms in both the elastic and inelastic stages.
2. For structures in the inelastic stage, the rigid diaphragm assumption may or may not underestimate the internal forces or deformations of structural members, such as collectors and chords. In the inelastic stage, the yielding or failure of elements in the vertical lateral force resisting systems (LFRS) may significantly change the internal load paths in the diaphragms. Here the change of load path may result in an increment of internal axial forces in the structural components of diaphragms, such as collectors and chords.
3. For structures where the efficiency of torsional resistance is influenced by the in-plane stiffness of diaphragms. This will be the cases when 3D modeling is used. This effect may be important for asymmetric structures, where the LFRS perpendicular to the direction of seismic loads also provide resistance for the torsion caused by the mass eccentricities or diaphragm irregularities. This resistance is activated by the in-plane forces transferred from the diaphragms. For this case, different assumptions about the rigidity of diaphragms may lead to different torsional behavior.

These effects may be tied to the levels and types of analyses being considered (elastic or inelastic; small or large deformations; service, ultimate or collapse level; and static or dynamic). In the above scenarios, the assumption of a semi-rigid diaphragm must be used in the analytical models for simulating the in-plane behavior of floor systems.

From the design provisions for seismic design, such as ASCE 7-10 (2010), the diaphragms can be classified as flexible, rigid or semi-rigid. The classification is based on the relative in-plane stiffness of diaphragm compared to the lateral stiffness of the LFRS. Rigid diaphragms are defined as diaphragms consisting of concrete slabs or concrete filled metal deck with span-to-depth ratios of 3 or less in structures that have no horizontal structural irregularities (ASCE 7, Table 12.3-1). In this scenario, the seismic demand on the LFRS depends on the relative lateral rigidity of the LFRS and their distance from the stiffness centroid (i.e. center of rigidity, C.R.) for the structures.

For structures with semi-rigid or flexible diaphragms, however, the seismic demand depends on (a) the tributary mass of the diaphragm supported by the LFRS, and (b) the distance between LFRS and C.R.

Flexible diaphragms are defined as the diaphragms constructed of untopped steel decking or wood panels where the maximum in-plane deformation of the diaphragm is more than two times the average story drift of adjoining vertical LFRS. Semi-rigid diaphragms are defined as those that do not belong to either the rigid or flexible diaphragms categories mentioned above.

There is comparatively little research on the effect of semi-rigid diaphragms in steel structures with different horizontal irregularities in the diaphragms or asymmetric configurations of vertical LFRS in the inelastic stage. The goal of this study is to investigate the influence of different assumptions of diaphragm stiffness on the seismic performance of braced and unbraced frame systems.

## 1.2 Methodology

In this thesis, the nonlinear behavior of the structures with rigid or semi-rigid diaphragms under seismic loads will be addressed primarily from the analytical standpoint. The major steps are:

- (1) Design and analyze symmetric and asymmetric theme steel structures with different in-plane diaphragm stiffness using finite element software (i.e. SAP2000). These structures are intentionally designed to comply with different categories of horizontal structural irregularities based on the definition in ASCE 7 (Table 12.3-1). The member dimensions and strengths in those structures are determined in this step. Initially, all structural components or members will be modeled with linear elastic elements and subjected to equivalent lateral force including the effect of accidental torsion.
- (2) Develop analytical models in OpenSEES after the dimensions of the main structural components are determined in Step 1. For diaphragms with infinite rigidity, constraint equations will be applied to tie the two in-plane translational and the one in-plane rotational degrees of freedom (DOFs) of all slave nodes to the master node at each floor level. For the diaphragms with finite in-plane rigidity, composite beams will be used for describing the in-plane and out-of-plane behavior of the diaphragm system. All of the structural members in the vertical LFRS, such as braces, composite beams and steel columns, are simulated by beam-column elements with inelastic fiber sections.
- (3) Compare the structural response for the structures with different diaphragm assumptions by conducting nonlinear static and dynamic analyses in OpenSEES. In this step, the differences in capacity curves, roof drift ratios, inter-story drift ratios and rotational behavior of diaphragm between the two assumptions will be the main measures of structural response to be investigated.

(4) Compare the torsional performance of structures with horizontal structural irregularities in both the elastic and inelastic stages. By investigating the behavior of the LFRS perpendicular to the direction of seismic loads, the contribution to torsional resistance from those LFRS can be evaluated. In addition, the effect of accidental torsion, which is based on the requirement of ASCE 7 (Section 12.8.4.2), will be considered in the theme structures with different diaphragm assumptions. Table 1-1 shows the analysis matrix in this study.

Table 1-1 Analysis case matrix for this study

Horizontal configurations of vertical LFRS	Aspect ratios of diaphragms	Horizontal Structural Irregularities for archetype structures (ASCE Table 12.3-1)	Diaphragm types	Inclusion of Bi-axial effect	Inclusion of accidental torsion	Analysis approaches
Symmetric	3.0	No Torsional Irregularity	Rigid <sup>(1)</sup>	Yes	Yes	Nonlinear static and dynamic analysis
				No		
			Semi-Rigid	Yes		
				No		
Asymmetric	3.0	Extreme Torsional Irregularity	Rigid <sup>(1)</sup>	Yes		
				No		
			Semi-Rigid	Yes		
				No		

*Note: (1) The structures with rigid diaphragm include (a) bare steel structures with rigid diaphragm constraints and (b) composite structures with rigid diaphragm constraints.*

(5) Evaluate the strength demand on chords and collectors in the structures with semi-rigid diaphragms. The demand will be evaluated using both the traditional method (i.e. beam analogy) and nonlinear static and dynamic analyses.

### 1.3 Objectives and Research Tasks

There are three main goals in the study: (a) evaluating the influence of different simulation assumptions of floor systems on the seismic performance of steel structures, (b) investigating the appropriateness of design criteria mentioned in ASCE 7 for the horizontal structural components

in diaphragms, such as chords and collectors, and (c) evaluating the effect of accidental torsion on steel structures with different diaphragm assumptions. More details of the research objectives are:

- (1) Evaluation of differences in the seismic response for multi-story steel structures with rigid or semi-rigid diaphragms: In the study, groups consisting of six structures corresponding to three different in-plane and out-of plane diaphragm stiffness (i.e. bare frames *with* rigid diaphragm constraint, composite frames *with* rigid diaphragm constraint and composite frames *without* rigid diaphragm constraint) and two horizontal configurations of vertical LFRS (i.e. symmetric and asymmetric configurations) will be examined. Nonlinear static (pushover) and dynamic analyses will be conducted for evaluating the behavior of those structures. By comparing structural behavior among those structures, the differences in response of the structures, such as load-deformation curves, rotational behavior of diaphragm and inter-story drift ratios, will be assessed. In addition, the inelastic behavior of the composite deck is also considered in the structures with composite action.
- (2) Investigate the effect of accidental torsion on multi-story steel structures with rigid and semi-rigid diaphragms: For the theme structures with semi-rigid diaphragms mentioned in Task 1, the effect of accidental torsion can be considered in both nonlinear static and dynamic analyses by modifying the diaphragm mass distribution. For the structures with rigid diaphragms, however, the accidental torsion can be considered in the analyses through changing the position of the master joint (i.e. center of mass) on each diaphragm. In this task, the differences in the structural seismic performance due to accidental torsion will be evaluated by comparing the analytical results from nonlinear static analyses with the ones from nonlinear dynamic analyses. The objectives of the task are to provide guidance for

designers to evaluate the effect of accidental torsion on the structures with different diaphragm assumptions.

- (3) Evaluate the appropriateness of current ASCE 7 seismic design provisions (2010) for the structural components in diaphragms such as chords and collectors: By conducting the nonlinear static and dynamic analyses mentioned in Tasks 1 and 2, the internal axial forces in chords and collectors can be determined under different magnitudes of seismic loads. The appropriateness of traditional method (i.e. beam analogy), which is used for determining the design forces for chords and collectors, will be evaluated in each theme structure. In addition, both the effect of accidental torsion and cracked diaphragms on the design of chords and collectors will be discussed in this task. The goal in this task is to investigate whether the force modification factor for diaphragm design, 1.25, in ASCE 7, to be discussed in Section 7.7, is or is not conservative for the design of collectors and chords.

## **1.4 Organization of the Thesis**

Chapter 2 presents a literature review of past research and topics relevant to the torsional behavior of the structures with rigid and semi-rigid diaphragms.

Chapter 3 presents the design of the prototype structures and the simulation of finite element models in OpenSEES and SAP2000. Simulation details in OpenSEES, such as brace imperfection for buckling and the application of composite effects for simulation of semi-rigid diaphragms, are included in this chapter. In addition, important design criteria for the theme structures based on the requirement of ASCE 7, AISC 341 and 360 are described in the chapter.

Chapter 4 focuses on the evaluation of the inelastic behavior for several 2D frames and a one-story 3D structure through nonlinear static analyses. The two different diaphragm assumptions, rigid and semi-rigid, are imposed in these frames. The content of this chapter primarily corresponds to Task 1.

Chapter 5 investigates the linear and nonlinear behavior of the prototype multi-story steel structures with rigid and semi-rigid diaphragms. Both nonlinear static and dynamic analyses are conducted on the theme structures both with and without bi-axial effects. The effect of accidental torsion is also considered. The differences in the structural behavior between structures with rigid and semi-rigid diaphragms are used to evaluate the validity of the rigid diaphragm assumption. The content of this chapter primarily corresponds to Tasks 1 and 2.

Chapter 6 evaluates the linear and nonlinear behavior of the peripheral or perpendicular frames of the theme structures. By implementing nonlinear static and dynamic analyses, the differences in the peripheral frames behavior with accidental torsion under different diaphragm assumptions are investigated. The content of this chapter corresponds to Task 2.

Chapter 7 concentrates on the strength requirement for the structural components in diaphragms, such as collectors and chords. The internal axial force of those components will be extracted from the nonlinear analyses in Chapters 5 and 6. The appropriateness of conventional analytical procedures for these components in ASCE 7 will be investigated as well. The content of this chapter corresponds to Task 3.

Chapter 8 includes the general conclusions for the behavior of the steel theme structures with and without semi-rigid diaphragms. The appropriateness of rigid diaphragm assumption, the influence of accidental torsion in the structures with semi-rigid diaphragms, and the design requirement of chords and collectors will be discussed.

## **Chapter 2 Literature review**

### **2.1 Introduction**

This chapter focuses on a review of the relevant research on the behavior and design criteria for structures with rigid and semi-rigid diaphragms. Previous analysis and simulation approaches for evaluating the behavior of diaphragms under different scenarios are highlighted. In addition, experimental results on diaphragms relevant to this research are also discussed.

This chapter is organized as follows: Section 2.2 discusses the functions and roles of structural components in diaphragms subjected to horizontal seismic loads. Section 2.3 highlights relevant research topics including the static and dynamic behavior of diaphragms with different in-plane diaphragm stiffness. Section 2.4 introduces the current design procedures for diaphragms based on ASCE 7-10 (2010). Section 2.5 summarizes relevant design and simulation concepts for diaphragms.

### **2.2 Functions of diaphragms**

In general, building structures consist of an assemblage of horizontal elements (slabs and beams), vertical elements (columns, braces and walls), and foundations. For seismic design, the goal is to limit the structure's displacements that result from the inertial forces generated by ground motions to values that can be accommodated by the ductility of the structural elements and their connections. By providing continuous and redundant load paths from horizontal to vertical elements and to the foundations, the structural displacement can be controlled. The floor diaphragms provide the first part of these load paths. The majority of in-plane seismic forces on the diaphragms are generated by the mass of the floor systems, and the forces have to be transferred from diaphragms into the vertical lateral force-resisting systems (LFRS). The

diaphragms carry those forces to the LFRS through collectors, chords and shear connectors. The relationships among collector, diaphragm and shear connectors are illustrated in Figure 2-1 (American Institute of Steel Construction, 2010b). The shear flow in the collector beam caused by in-plane seismic loads is shown in the figure also. These members have to satisfy strength and ductility requirements that arise from compatibility of deformations.

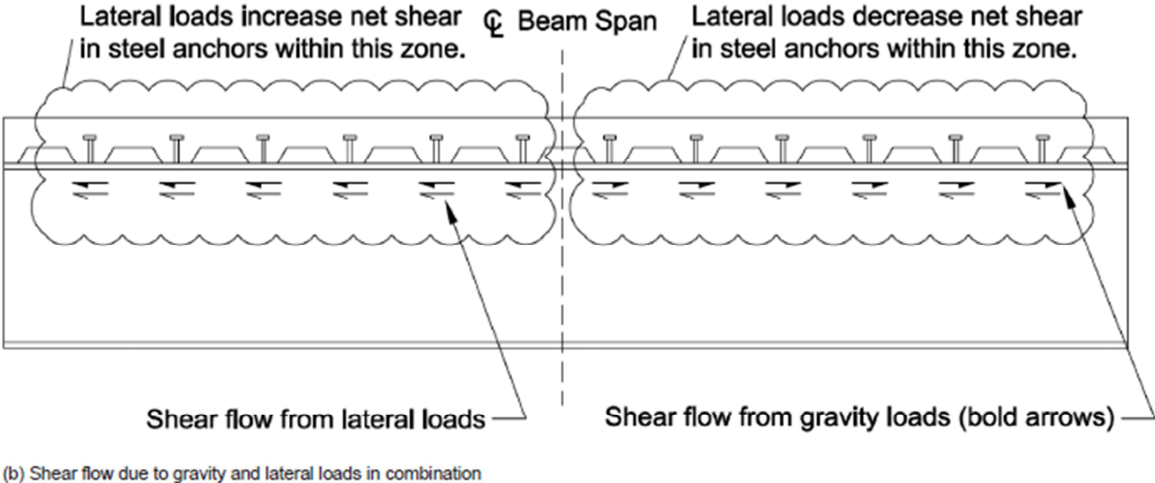


Figure 2-1 Shear flow in collector beams (American Institute of Steel Construction, 2010b)

Therefore, the primary roles that a diaphragm plays in the structural design include (1) transferring internal inertial forces through the diaphragms to chord and collector elements, (2) transferring the forces from the collector and chord elements to the LFRS, and (3) resisting the gravity loads. Several structural components comprise a typical diaphragm, including (a) collectors (or drag struts), (b) chords, (c) slabs (composite slab or bare steel deck), (d) floor beams and girders and (e) shear connectors used to connect girders and decks.

### 2.3 Other relevant topics

A bibliography relative to rigid and semi-rigid diaphragm has been compiled as part of this dissertation. The following is a short compilation of relevant literature on topics germane to this dissertation.

***Diaphragm Strength and Stiffness:*** The importance of diaphragm action was well understood as seismic research in the USA intensified after the 1971 San Fernando earthquake. Davies and Fisher (1979) carried out four full-scale tests on cantilever composite slabs, and the three failure modes were identified. The authors provided relevant design equations for predicting the in-plane strength of composite floor diaphragm. The ABK (1981) initiative conducted full-scale, in-plane quasi-static cyclic displacement and dynamic earthquake shaking on 14 diaphragm specimens ranging from wood to steel deck. The results of test show that typical diaphragms have highly nonlinear stiffness characteristics and produced valuable data for establishing properties for typical diaphragms.

In order to characterize the diaphragm behavior under in-plane shear loading, Easterling and Porter (1994a) and Easterling (1987) conducted a series of full-sized experiments and analytical simulation with different deck types and slab thicknesses. All of the specimens were loaded to failure, and three different limit states or failure modes were identified: diagonal tension, shear transfer, and edge connector failure. The results were utilized to calibrate finite element models that yielded good results, as shown in Figure 2-2. The authors also provided simplified procedures for designers to determine the strength and stiffness of composite diaphragms for each limit state (Easterling W. S. and Porter M. L. (1994b)). The analytical strength and stiffness from these procedures compared satisfactorily with the experimental results.

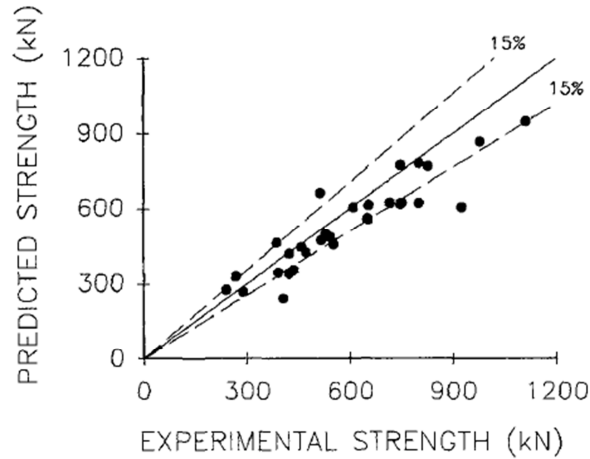


Figure 2-2 Experimental versus analytical strength (Easterling W. S. and Porter M. L., 1994a)

Widjaja (1993) completed analytical simulations for evaluating the in-plane behavior of composite diaphragms with different boundary conditions. Several weld curves and interfacial springs used to simulate the force-displacement relationships between concrete and metal deck elements were utilized in the analytical models. The experimental results were used to calibrate the initial strengths and stiffness of analytical models. The results show that the modified elastic stiffness favorably matched the stiffness from the experimental results.

Hossain and Wright (1998) completed a series of experiments for evaluating the behavior of composite walls under in-plane shear. The results show the yield strengths of composite walls are higher than the summation of profiled concrete walls and steel sheet walls by 30%. Wright and Hossain (1997) conducted several experiments for evaluating the behavior of profiled steel sheeting. The results show the boundary conditions of the sheeting significantly affects the strength, stiffness and failure modes of the composite walls. For instance, the in-plane elastic stiffness of the metal panel with clamped boundaries is 3.16 times higher than those with spot welded boundaries.

**Rigid vs. flexible diaphragms:** A large number of simple analytical studies have been carried out in this area, but until recently the models used were quite simple and the studies very limited in scope. Notable recent work includes that of Ju and Lin (1999) which examined the influence of floor diaphragm flexibility for a large series of low-rise 3D concrete moment structures with and without shear walls, as shown in Figure 2-3.

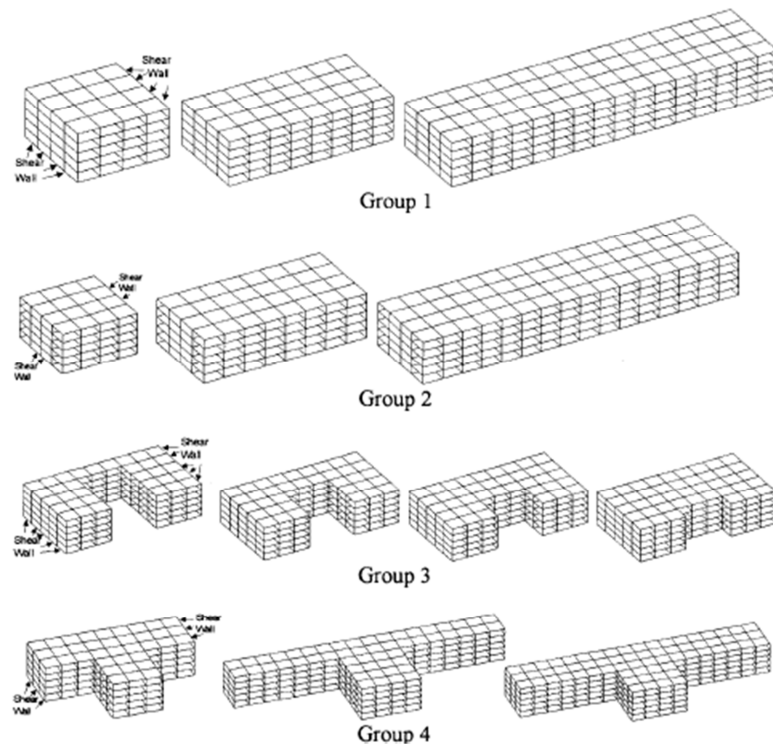


Figure 2-3 Configurations of 3D RC frames (Ju S. H. and Lin M. C., 1999)

For the structures without shear walls, the difference in column moments between semi-rigid and rigid diaphragm models is small regardless of the diaphragm shape. However, for the structures with shear walls, the column moment exhibited large differences between the two assumptions (i.e. rigid and semi-rigid diaphragm). The phenomenon is probably due to the large difference in the in-plane stiffness between shear walls and diaphragms. A comparison of column shear between the RC-wall structures with rigid or flexible diaphragms is shown in Figure 2-4.

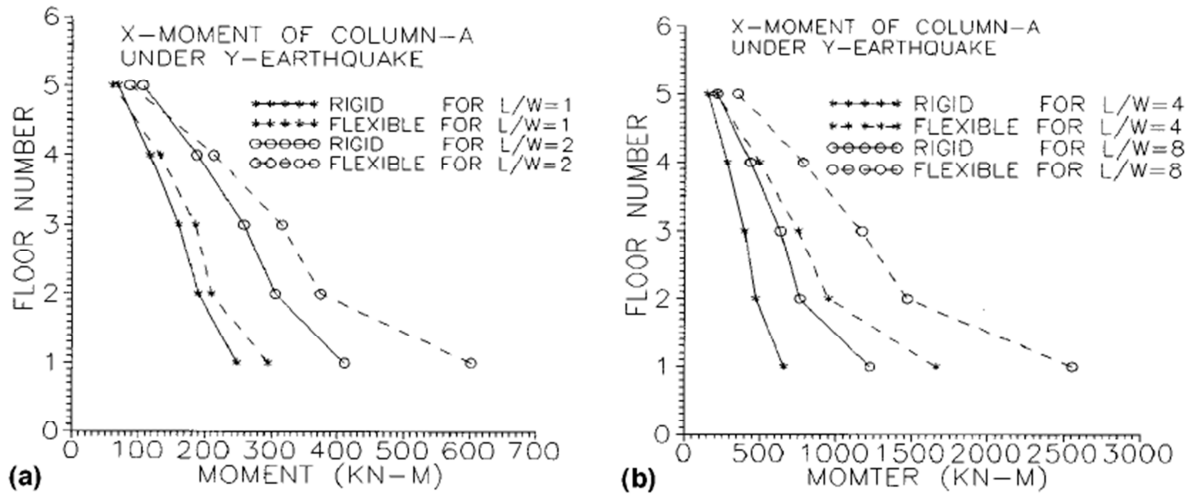


Figure 2-4 Comparison of column shears (Ju S. H. and Lin M. C., 1999)

Saffarini and Qudaimat (1992) analyzed a series of RC buildings with wall systems corresponding to various height, aspect ratios and slab types to investigate the effect of rigid diaphragm assumption on the internal force in vertical structural members. Their results indicate that the difference in lateral displacement and the base shear in walls between the two assumptions are significant in low-rise buildings (i.e. 2-story and 4-story structures). In addition, an error bound between the two assumptions is provided to engineers to evaluate the effect of in-plane stiffness of diaphragm in analytical procedures, as shown in Figure 2-5. The in-plane rigidity factor,  $R_i$ , in Figure 2-5 is defined as the elastic in-plane stiffness of diaphragm divided by elastic lateral story stiffness.

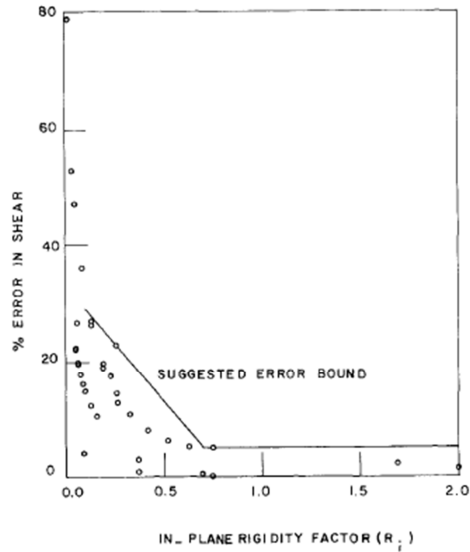


Figure 2-5 Summary of shear error with suggested error bounds (Saffarini H.S. and Qudaimat M.M., 1992)

Moon and Lee (1992) compared the dynamic response between RC structures with rigid and flexible diaphragms. The results showed that higher diaphragm flexibility leads to a longer fundamental period and results in a smaller base shear. Tena-Colunga and Abrams (1995) carried out nonlinear dynamic analyses on three existing buildings, including structures with unreinforced masonry walls and timber floors. The results showed that the torsional forces reduce with the increment of diaphragm flexibility.

**Flexible roof and wood diaphragms:** For the case of roof diaphragms, Essa et al. (2003) conducted quasi-static cyclic experimental and analytical studies on the energy absorbing capacity and inelastic performance of steel deck roof diaphragms. The results show that the current Steel Deck Institute (SDI) method predicts the stiffness and strength of steel diaphragms well if the fasteners are properly installed. The results also show that diaphragms connected to the frames with welded deck-to-frame fasteners without washers have a lower ductility under

cyclic loading. Nailed welded deck-to-frame fasteners with washers have a better energy dissipation performance.

The work also indicates that the 0.91 mm thick steel deck screwed to another deck (i.e. side lap) and nailed to the frame with fasteners have the best inelastic performance. The authors also provided an equivalent viscous damping ratio for the analysis of steel deck diaphragms. The values ranged from 4.1% to 4.6%, and the average of the ratio is 4.5%.

Shresstha et al. (2009) conducted a series of experiments to evaluate the nonlinear dynamic behavior of cold-formed steel corrugated roof diaphragms. The nonlinear truss elements are used for simulating the stiffness and strength degradation behavior of the metal diaphragms, as shown in Figure 2-6. The nonlinear response and the predicted period from analytical models are calibrated based on the experimental results.

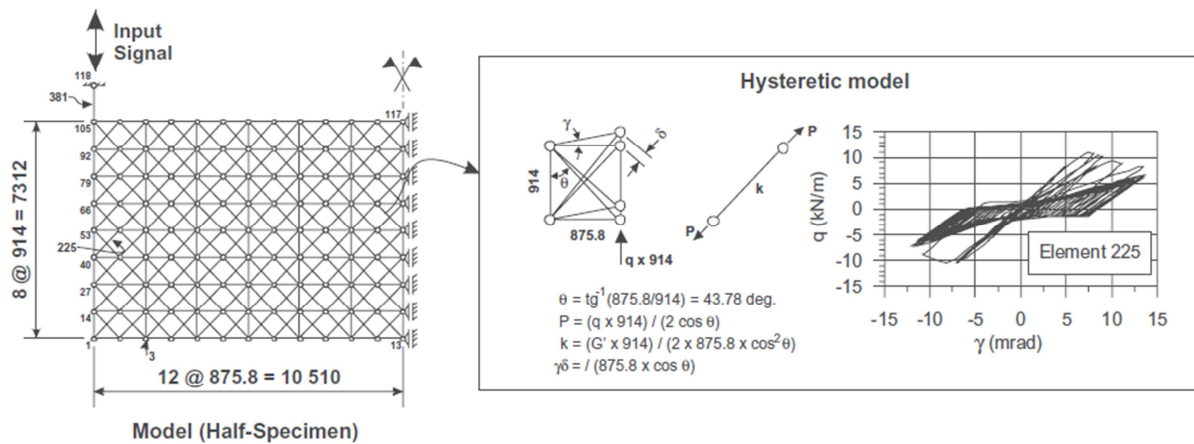


Figure 2-6 Nonlinear truss models for diaphragm simulation in OpenSEES (Tremblay R. and Stierner S. F., 1996)

For understanding the seismic behavior of frames with retrofitted wood diaphragms, Peralta et al. (2003) presented the experimental results from three diaphragm specimens, one floor diaphragm and two typical roof diaphragms, which were built, tested, retrofitted and retested under cyclic

loading. Four different retrofit methods: (1) steel perimeter strapping and enhanced bolted connections (2) a steel truss within enhanced connections (3) an unblocked plywood overlay , and (4) a blocked plywood overlay are utilized for the three frames. The results are extended to estimate seismic response for unretrofitted and retrofitted structure with wood diaphragms.

***Dynamic and static behavior of lateral-systems with flexible or semi-rigid diaphragms:***

Fleischman and Farrow (2001) presented an analytical model to capture the diaphragm behavior in structures with a long span diaphragm and perimeter LFRS by conducting nonlinear dynamic analyses. For the structures with long-floor spans, the in-plane stiffness of the diaphragms is in the flexible range. The dynamic behavior of such structures may not be similar to those with rigid diaphragms. Therefore, the difference may lead to unexpected force and drift patterns in terms of the inelastic behavior for the structures with semi-rigid diaphragms. Such diaphragms may cause failures due to the insufficient ductility stemming from an inaccurate estimation of drift demands in the gravity systems.

The paper also focuses on the difference in the force and displacement patterns between the structures with flexible and rigid diaphragms via defining a diaphragm flexibility ratio,  $\alpha$  (ratio of in-plane diaphragm deformation to the lateral-system absolute drift at the mid-height of the structure). A critical flexibility ratio,  $\alpha=2.0\sim 2.6$ , exists when the remote diaphragm mass and perimeter LFRS act independently, as shown in Figure 2-7. In addition, the largest deformation demand for the diaphragm occurs in the lower levels in the inelastic analysis case.

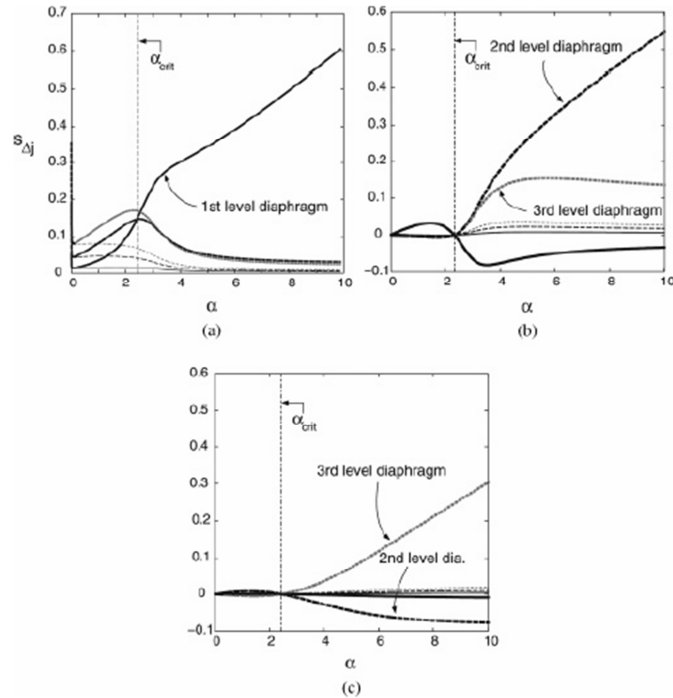


Figure 2-7 Displacement modal static response of UBC design structures as a function of diaphragm flexibility (Fleischman R. B. and Farrow K. T., 2001)

From the above discussion, it is clear that the in-plane stiffness of floor diaphragms is able to influence the building response during horizontal ground motions. To clarify the influence of in-plane stiffness on building dynamic behavior, Sadashiva et al. (2012) presented the results from a series of elastic and inelastic time history analyses with different types of single-story structural systems. According to these results, the variation of in-plane displacement in the single-story elastic structures is sensitive to the diaphragm in-plane stiffness. Moreover, the authors also provided an approach to estimate the increment of peak in-plane diaphragm deformation of the structures with flexible diaphragm based on the lumped mass analytical model shown in Figure 2-8.

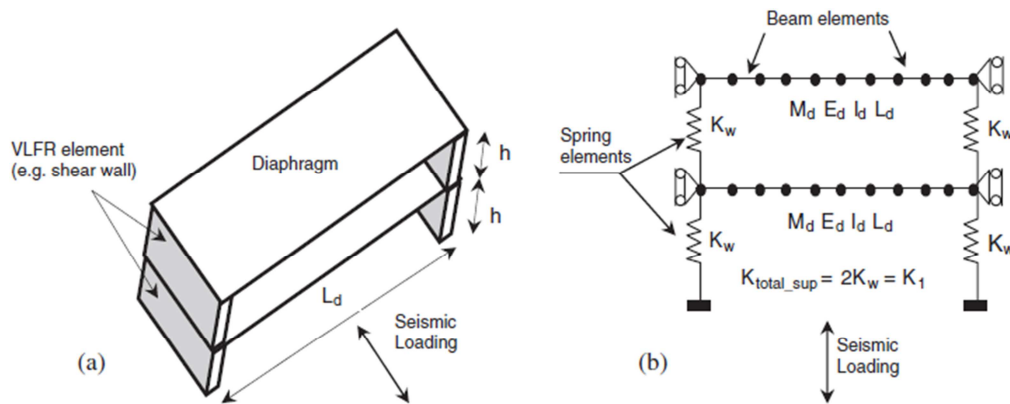


Figure 2-8 Original two-story structure and analytical lumped mass model (Sadashiva V. K. et al., 2012)

For the rigid diaphragm structures, the lateral seismic load is applied at the center of mass on a diaphragm. Therefore, equivalent single degree-of-freedom (SDOF) models are commonly used for the simulation of low-rise buildings with rigid diaphragms. However, for those structures with flexible diaphragms, such as steel deck or wood diaphragms, multiple degree-of-freedom (MDOF) systems are needed for describing the significant in-plane behavior of the diaphragm. A simplified linear static method named structural separation approach was presented by Kim and White (2003) used to separate a 3D MDOF system into several 2D models for the structures with flexible diaphragms. This method can accurately estimate the elastic structural response (i.e. base shear in dynamic analyses) considering the effect of flexible diaphragms. In addition, for investigating the inelastic behavior of structures with flexible diaphragms, Kim and White (2004) provided a 2D approach to predict the 3D nonlinear structural response through applying a calibration process. The comparison results show the structural response predicted by the approach matches favorably with the experimental data.

***The importance of in-plane diaphragm stiffness:*** To investigate the importance of the in-plane diaphragm stiffness in the response of structures, Jain and Jennings (1985) presented an

analytical method to evaluate the dynamic behavior of one- or two-story structures with semi-rigid diaphragms. The method simplifies the diaphragms and shear walls as several discrete deep beam models. The equations of motion can be built based on the analytical model, and thus the natural frequencies can be determined because of the known stiffness and mass matrix. By conducting dynamic analyses, the numerical results show the first two modes provide the largest contribution of total base shear of the structures.

De-la-Colina (1999) carried out nonlinear dynamic analyses for a one-story structure with high horizontal irregularities. The results showed the increment of in-plane diaphragm flexibility may lead to increasing the lateral displacement of the vertical LFRS by 50%. Jain and Mandal (1995) presented the numerical and theoretical analyses for Y-shaped RC buildings with flexible diaphragms. Based on the analytical results, the in-plane flexibility slightly affected the structural periods. Kunnath et al. (1991) proposed a simplified model for evaluating the seismic response of RC buildings considering the effect of inelastic floor diaphragms. In this study, the deep beam models and the shear hysteretic models are used to simulate the elastic and hysteretic behavior of diaphragm, respectively.

To understand the seismic behavior of asymmetric RC buildings with finite flexibility of floor diaphragms, Basu and Jain (2004) present a superposition-based approach for including the effect of inherent and accidental torsion in the structures with semi-rigid diaphragms. The results of comparisons between rigid and semi-rigid diaphragm structures indicate that the torsion significantly affects the structural responses, such as base shear, in the semi-rigid diaphragm structures. However, the individual frames may perform independently when the floor rigidity is very low (i.e. flexible diaphragms). The results show the demands on the strength and ductility of the structures with flexible diaphragms is higher than those with rigid diaphragms.

**Seismic Design of the structures considering accidental torsion:** Erduran and Ryan (2011) assessed the seismic behavior of 3D steel braced structures with rigid diaphragms including the effect of accidental torsion. Nonlinear static and time history analyses were conducted for evaluating the seismic behavior of 3D steel braced frames under various hazard levels. The results show that the structural torsion amplification factor increases when members are yielded in the LFRS, as shown in Figure 2-9. In order to evaluate the accuracy of the structural behavior provided from nonlinear pushover analyses and response spectrum analyses (RSA), response history analyses (RHA) with biaxial excitation and 5% mass eccentricity were conducted in the study. The comparison results indicate that pushover analysis and RSA are not able to predict the story drifts amplified by the accidental torsion.

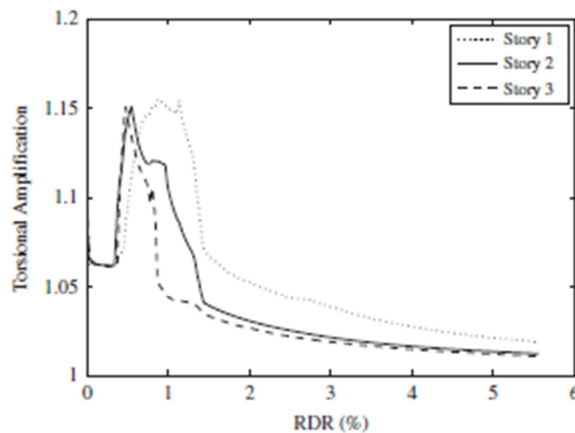


Figure 2-9 Variation of torsional amplification with roof drift ratio from pushover analysis (Erduran E. and Ryan K. L., 2011)

DeBock et al. (2013) discussed the importance for the requirement of design accidental torsion with regard to building collapse capacity. The study evaluated the effect of design accidental torsion based on ASCE 7 on the performance of 230 archetypical structures by comparing the collapse capacity of the structures with and without the consideration of accidental torsion. For

the structures with high torsional flexibility or irregularity, the design accidental torsion can lead a significant change of collapse capacity.

The inherent or accidental torsion is stimulated by the eccentricity between C.M. and C.R. For evaluating the position of center of rigidity (C.R.) in the structures with rigid diaphragms, Tso (1990) presented a simplified plane frame analysis to locate the C.R. Several 2D vertical frames in a 3D structure are connected by rigid links without including the effect of rotation, and thus the story shear in each frame can be determined by applying lateral design forces on the 2D frames. Finally, the position of C.R. can be determined by solving equilibrium equations to equilibrate the in-plane moment stimulated by the story shear and lateral forces. Goel and Chopra (1991) conducted a series of analytical studies comparing the dynamic behavior of asymmetric-plan systems with those of symmetric-plan systems. The results indicate that the effect of asymmetric configurations do not affect the response of inelastic systems significantly.

After considering the application of traditional matrix approach for locating C.R., Goel and Chopra (1993) provided another approach to include the effect of the eccentricity of C.M. without locating the position of C.R. in the multi-story structures with rigid diaphragms. The procedure is available to use directly in commercial computer programs. The method can also be applied in elastic static analysis procedures.

De la Llera and Chopra (1994) presented an approach to include the effect of accidental torsion in the seismic design procedures. The approach utilizes (1) the ratio between uncoupled torsion and lateral fundamental period and (2) plan dimensions to predict the amplified lateral displacements. The design forces of structural components can be determined based on the amplified displacements. Jarrett et al. (2014) carried out the nonlinear dynamic analyses for torsionally-regular structures with accidental torsion. This research indicates that the inelastic

behavior of structures is significantly affected by accidental torsion, and the inclusion of accidental torsion should be considered in the dynamic procedures appropriately.

***Seismic Design of composite steel deck and concrete-filled diaphragms:*** Sabelli et al. (2011) presents general behavior and design concepts for collector and chord elements in composite steel deck diaphragms. Many relevant design issues for these components are discussed in this synthesis of current knowledge. For instance, the design of collector depends on the (1) length of collector, (2) in-plane stiffness of diaphragm and (3) in-plane force distribution. For a short span diaphragm with low shear stiffness such as non-composite steel deck diaphragms, the collector design should focus on the axial ductility due to the development of significant diaphragm shear deformation. For a long collector, however, the diaphragms should have a better shear ductility to accommodate to the significant axial deformation of the collectors. Figure 2-10 presents the distribution of non-uniform in-plane force in diaphragm.

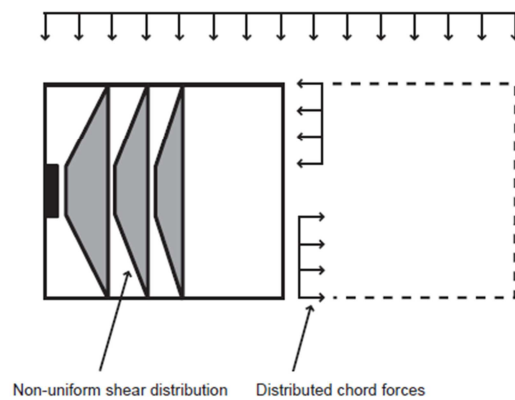


Figure 2-10 In-plane force distribution in a diaphragm (Sabelli R. et al., 2011)

Other important issues include the component design for the openings in diaphragms as well as the simulation details required for proper analysis. While the AISC Seismic Provisions (American Institute of Steel Construction, 2010b) provides some guidance for the design of chord and collectors, this guidance is scant. For example, the seismic behavior of collectors

which consider the effect of eccentric load (accidental torsion) is not discussed in the guide. No significant research had been done for this complex behavior, and this is a primary objective of the research proposed herein.

Cowie et al. (2013) presented suggestions for determining the diaphragm action based on the guidance provided from Sabelli et al. (2011). The axial force distribution of structural components in a diaphragm can be evaluated through using a deep beam analogy, with the peak collector axial force occurring at the connection of nearby LFRS. In order to provide a reliable load path for the collector to deliver the axial force from diaphragms into LFRS, a bolted top flange connection is suggested to use to connect collector/chord and LFRS.

Malone and Rice (2012) provided a series of design examples for the chords/collectors in diaphragms through utilizing deep beam analogy. They provided several design examples for irregular diaphragms or the diaphragms with openings. Taranath (2012) and Naeim et al. (2001) presented seismic design procedures as well as examples for diaphragms with different flexibilities (i.e. timber or RC floor). Fisher et al. (1991) discussed design approaches for several types of connection used for diaphragm chords and collectors. Aghayere and Vigil (2009) presented the design concepts for diaphragm action of roof and floor diaphragms.

***Behavior of semi-rigid diaphragms (Theory of Shell elements):*** For the shell elements used for simulating the semi-rigid or flexible diaphragms in the analytical models. Love (2001) presented the theory of elastic shell element used in OpenSEES. Love utilized a bilinear isoparametric shape function combined with a modified shear interpolation to avoid “shear locking” behavior in the traditional thin-shell elements (Mindlin plate theory, Cook R. D. et al. (2001)). Shear locking is caused by the need of shell elements to include transverse shear to represent their in-

plane bending. When the thickness of bilinear shell element becomes thin, 2 by 2 Gauss quadrature overestimates the in-plane bending stiffness of the shell element.

***3D shear stud and connector behavior:*** A very large number of experiments have been conducted to characterize the shear behavior and strength of headed studs under cyclic and monotonic loads. Pallares and Hajjar (2009a, 2009b), in the most recent comprehensive review of this topic, utilized 391 existing monotonic and cyclic push-out tests to estimate the limit state formulas for headed stud anchors in shear. This work also shows that the ACI 318-08 (American Concrete Institute, 2008) and PCI Design Handbook (Prestressed Concrete Institute, 2004) provide more conservative predictions for the concrete failure than those provided by AISC steel construction manual (2011). Pallares and Hajjar (2009a, 2009b) reported on the behavior of headed studs embedded in solid concrete slabs under monotonic and cyclic load parallel and compare several equations for calculating the nominal strength from a total of 222 experimental results. The scope of this work focuses on the diameters of stud less than 1in, and the yield strengths for typical ASTM A108 Type B stud are 51 and 65 ksi, respectively (American Society of Testing and Materials, 1999). The report indicates that the nominal strength predicted from a concrete capacity design (CCD) approach is more conservative and has a lower scatter than the 45 degree cone method.

***Simulation of steel structures:*** Deierlein et al. (2010) provided a guide for nonlinear structural analyses for seismic design. The authors present the difference in the monotonic and cyclic envelop curve of structural components. For the nonlinear static analysis (i.e. pushover analysis), the nonlinear component models should be simulated based on the degraded cyclic envelope. For the nonlinear dynamic analysis, the simulation of component model depends on how the cyclic degradation behavior is simulated. In addition, ATC-76 (2010) also provided an approach for the

brace simulation. Each brace is suggested to be subdivided into 10 beam-column elements with (1) nonlinear fiber section (2) a minimum of 3 integration points in each element and (3) the initial imperfection from 0.05%~0.1% of effective brace length. Bruneau et al. (2011) discussed the seismic design procedures for special concentrically braced frames. For the design of brace frames, Sabelli et al. (2013) provided a design guide for the steel special concentrically braced frame systems. The failure modes for braces are discussed in the technical report including local strain concentration and brace fracture. The simulation details of braced frame are also discussed in the report, as shown in Figure 2-11.

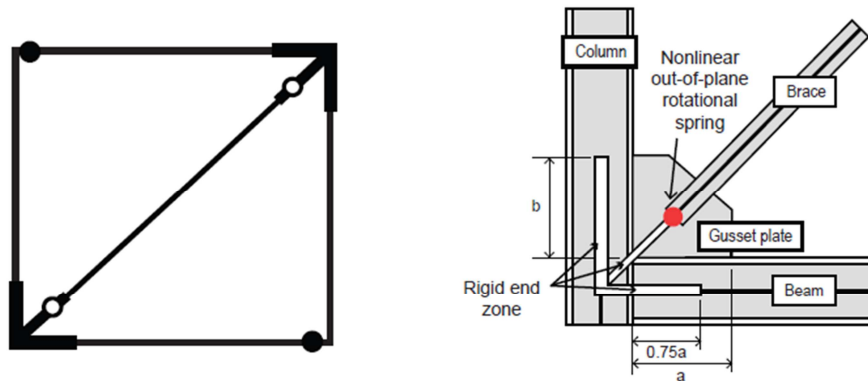


Figure 2-11 Simulation of typical braced frame (Sabelli R. et al., 2013)

## 2.4 Review of design procedures

It was recognized as this thesis was being developed that ASCE 7-16 (2016) would include significant updates for the design of floor diaphragm systems. However, there was considerable uncertainty as to whether these changes would be applicable to composite floors of the type analyzed herein. Therefore, all the discussion in this study is referred to ASCE7-10. Current design procedures for diaphragms as prescribed by ASCE 7 can be briefly summarized as follows

(1) Classification of diaphragm behavior: It is necessary to determine whether the diaphragm flexibility needs to be considered in the analytical procedures. From ASCE7, Section 12.3.1.1 a *Flexible Diaphragm Condition* can be assumed for structures with diaphragms constructed of untopped steel decking or wood structural panels if any of the following conditions exist (American Society of Civil Engineers, 2010):

- a. In structures where the vertical elements are steel braced frames, steel and concrete composite braced frames or concrete, masonry, steel, or steel and concrete composite shear walls.
- b. In one- and two-family dwellings.
- c. In structures of light-frame construction where all of the following conditions are met:
  - i. Topping of concrete or similar materials is not placed over wood structural panel diaphragms except for nonstructural topping no greater than 1 1/2 in. (38 mm) thick.
  - ii. Each line of vertical elements of the seismic force-resisting system complies with the allowable story drift of Table 12.12-1.

A *Rigid Diaphragm Condition* (Section 12.3.1.2) can be used for diaphragms of concrete slabs or concrete filled metal deck with span-to-depth ratios of 3 or less in structures that have no horizontal irregularity. Diaphragms not satisfying the conditions of Sections 12.3.1.1 or 12.3.1.2 are permitted to be idealized as flexible when the computed maximum in-plane deflection of the diaphragm under lateral load is more than two times the average story drift of adjoining vertical elements of the seismic force resisting system of the associated story under equivalent tributary lateral load as shown in Figure 2-12. Structures with horizontal and vertical irregularity need to

comply with the requirements of Tables 12.3-1 and 12.3-2. If horizontal or vertical irregularity exists in structures, diaphragm design force should be increased by 25%. A semi-rigid diaphragm is permitted to use in structural analysis if the diaphragm is not belong to rigid or flexible diaphragm mentioned in Section 12.3.1.1 and 12.3.1.2. In section 12.3.4, the design forces determined from section 12.10.1.1 shall be increased by 25 percent for the design of relative structural components in diaphragms.

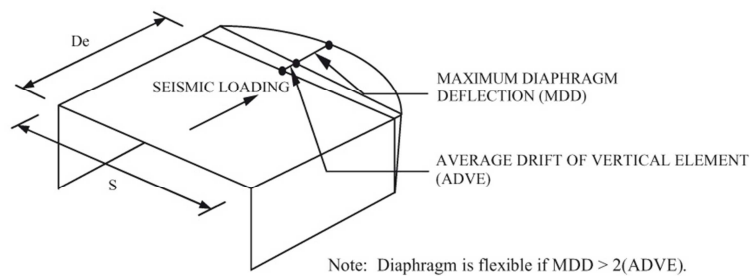


Figure 2-12 Definition of flexible diaphragm by ASCE 7 (American Society of Civil Engineers, 2010)

- (2) Calculation of diaphragm design forces: Diaphragm design force on each floor can be determined based on Equation (12.10.1). The load combinations for collector design are given in Section 12.10.2.1.
- (3) Calculation of internal forces in collectors and chords: The diaphragm design force shall be distributed on the diaphragm based on the distribution of mass tributary area. The internal force of collectors and chords can be determined by using beam analogy in each diaphragm with the distribution. In structures assigned to Seismic Design Category C, D, E, or F, collector elements (see Figure 12.10-1) and their connections including connections to vertical elements shall be designed to resist the maximum of the following:
  - a. Forces calculated using the seismic load effects including overstrength factor of Section 12.4.3 with seismic forces determined by the Equivalent Lateral Force

procedure of Section 12.8 or the Modal Response Spectrum Analysis procedure of Section 12.9.

- b. Forces calculated using the seismic load effects including overstrength factor of Section 12.4.3 with seismic forces determined by Equation 12.10-1.
- c. Forces calculated using the load combinations of Section 12.4.2.3 with seismic forces determined by Equation 12.10-2.

(4) Check capacity of diaphragms and components: The demand-and-capacity ratio of connections between collectors, chords and diaphragms shall be determined, and the shear capacity of diaphragms needs to be checked as well.

## **2.5 Concepts and assumptions for diaphragms in seismic design**

From the simulation standpoint, there are two ways to describe diaphragm behavior. The first one is to consider the diaphragm as having an infinite in-plane rigidity, often called a “rigid diaphragm”. The second to consider the diaphragm as having a finite rigidity, often called a “semi-rigid diaphragm”. Based on the requirements of ASCE 7, the semi-rigid diaphragm can be classified as “flexible diaphragm” once the rigidity cannot satisfy some criteria mentioned in Section 12.3.1.2 and Section 12.3.1.3.

According to Section 12.3.2, the diaphragms of concrete slabs or concrete filled metal deck with span-to-depth ratios of 3 or less in structures without having horizontal irregularities are able to be idealized as rigid. If the span-to-depth ratios of diaphragms cannot satisfy the requirement mentioned in Section 12.3.2, or the maximum in-plane deflection of the diaphragm under lateral load is more than two times the average story drift of adjoining LFRS mentioned in Sec. 12.3.1.3, the diaphragms shall be defined as flexible and the semi-rigid modeling assumption is used for diaphragm simulation.

For structures with rigid diaphragms, the distribution of the design forces is based on the relative lateral stiffness of the LFRS components in the structure. For the structures with flexible and semi-rigid diaphragms, however, the lateral force distribution is based on the tributary area supported by the vertical frames (i.e. LFRS).

According to the design criteria in ASCE 7, two different sets of design forces,  $F_{PX}$  and  $F_X$ , are used for the design of diaphragm and vertical LFRS, respectively. The diaphragm design force,  $F_{PX}$ , is higher than  $F_X$  by 25% because of the inclusion of higher-mode effects. In other words, an empirical force amplification factor of 1.25 is used to reflect the peak response acceleration of the floor systems. In addition, the magnitude of  $F_{PX}$  also depends on the variation of structural periods. Thus, an appropriate simulation of diaphragm stiffness is important to reflect the real diaphragm design forces.

For typical buildings, according to Sabelli et al. (2011), the distribution of diaphragm in-plane force and the corresponding internal forces in the components, such as the axial force in chords and collectors, can be evaluated based on the beam analogy. This approach treats the diaphragm as an elastic “deep beam”, and the LFRS as supports for the deep beam. The design diaphragm force,  $F_{PX}$ , can be distributed on the “deep beam” based on the proportional distribution of diaphragm mass. The internal forces in chords and collectors are able to be determined through calculating the in-plane shear and moment in the “deep beam” shown in Figure 2-13. The shear can be used to evaluate the internal force of collectors, and the in-plane moment can be treated as a couple axial force provided from chords nearby peripheral frames. The internal in-plane force in a diaphragm can be assumed as uniform or non-uniform distribution. Different distributions result in different requirements of axial ductility and strength for collectors due to the deformation compatibility between slabs and collectors.

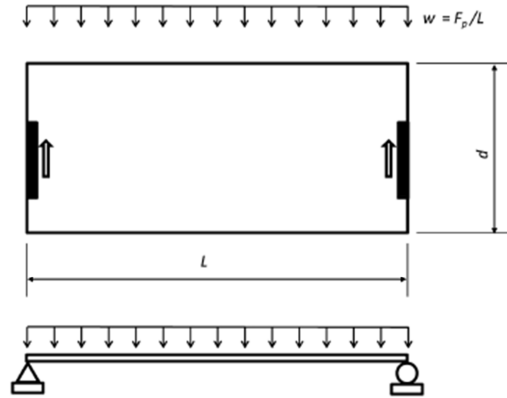


Figure 2-13 Deep beam model for diaphragm design (Sabelli R. et al., 2011)

The above approach is applicable easily and intuitively to diaphragm design, including collectors and chords, in the elastic range. However, it does not consider the interaction between the stiffness variation in the LFRS and the variation of in-plane diaphragm stiffness. In other words, the diaphragm in-plane force may change significantly after inelastic behavior develops in the members of the LFRS. In addition, cracks may be created in the diaphragms due to the lateral or gravity loads; these cracks will lead to stiffness changes that will also lead to the redistribution of in-plane forces in the diaphragms. Moreover, the effect of torsion, such as inherent and accidental torsion, cannot be properly simulated by the beam model. The above problems are not addressed in current ASCE 7 design provisions, and they will be discussed and evaluated in the following chapters. The truss-and-tie (American Concrete Institute, 2008) or stringer-and-panel (Blaauwendraad J. and Hoogenboom P., 1996) models are also possible approaches for addressing the above difficulties. However, both of the approaches are not included in the scope of this study, as they would have required considerable fundamental work to apply to composite floors. In this study, beams with composite action are used for evaluating the real behavior of collectors and chords.

According to ASCE 7, the structural irregularities can be classified as horizontal and vertical ones. Horizontal irregularities, such as an irregular shape of diaphragm, may create an eccentricity between center of mass (C.M.) and center of rigidity (C.R.). In practice, most of the diaphragm inherent torsion comes from the asymmetric distribution of LFRS components in the structures. Vertical irregularities, for instance a soft story, may increase the eccentricity significantly because of the relative movement of C.R between adjacent stories. Both horizontal and vertical irregularity affect the magnitude of inherent torsion. In addition, an accidental torsion is also included in the design procedures by shifting the position of C.M by 5% of diaphragm dimension based on the requirement of ASCE 7.

In seismic design, the torsion in a structure, including inherent and accidental torsion, is resisted by the LFRS which are parallel and perpendicular to the directions of seismic load. The difference in the in-plane stiffness of diaphragms (i.e. rigid or semi-rigid) changes the robustness of in-plane force transfer mechanisms between the vertical LFRS and the horizontal diaphragms. A robust in-plane force transfer mechanism provided by diaphragms can assure the in-plane forces transferred among LFRS efficiently. Thus, the resistance of torsion may be changed by the interaction between in-plane stiffness of diaphragm and lateral stiffness of LFRS. The issue will be discussed in the following chapters.

## **Chapter 3 Structural modeling and design**

This chapter presents the configurations, design procedures and simulation details for the theme structures used in this study. These theme structures have different in-plane diaphragm stiffness and horizontal configurations of vertical frames. The theme structures will be used to investigate the influence of these variables on the seismic behavior by conducting nonlinear static and dynamic analyses. In the study, the structures are simulated through implementations of the Finite Element Method (FEM) in different platforms as discussed in Section 3.2. The overall design at the theme structures is described in Section 3.3. The criteria for the design of the theme structures are taken from ASCE 7 and AISC Seismic Provisions (2010a). These criteria include limitations on horizontal structural irregularity and demand-to-capacity (D/C) ratios of structural components in the LFRS, which are discussed in detail in Section 3.4. The simulation assumptions and limitations for nonlinear static and dynamic analyses in those tools are described in Section 3.5 and Section 3.6. Section 3.7 includes the approach for the simulation of mass and gravity loads in the analytical models. Section 3.8 provides details for both P- $\Delta$  and P- $\delta$  effect on the entire structural systems and individual structural members (i.e. braces). Section 3.9 includes period comparisons among the models with different diaphragm assumptions. Section 3.10 and Section 3.11 discuss the concepts of nonlinear static and dynamic analyses implemented in the study.

### **3.1 Introduction**

In conventional structural design procedures, engineers use the assumption of rigid diaphragms to simulate the floor systems, particularly for preliminary design. The assumption of rigid diaphragm improves the computational efficiency due to constraining the degree of freedoms

(DOFs) to a few specified joints. By applying in-plane rigid constraint equations between a master node and slave nodes in a diaphragm, the constraint creates rigid links between these joints. Therefore, the membrane (in-plane) deformation is kept constant, but the plate (out-of-plane) deformation is still considered in the analyses. The in-plane rotation and deformations of the slave nodes is the same as those of the master node (Computers and Structures Inc., 2009). The other three DOFs of each node, including the two out-of-plane rotation DOFs and one out-of-plane translation DOF, move independently.

This chapter discusses simulation and design issues of the theme structures with and without considering the effect of rigid diaphragm constraints.

### **3.2 Analysis platforms**

To distinguish the behavior of structures under different assumptions of diaphragm stiffness, two multi-story steel prototype structures are developed with different (1) positions of vertical braced frames and (2) in-plane diaphragm stiffness. Horizontal asymmetric and symmetric layouts of vertical concentrically braced frames and rigid/semi-rigid diaphragm assumptions are the two main variables in this study. By comparing the nonlinear seismic response of these theme structures with respect to inter-story drifts, capacity curves, and diaphragm rotations, the possible disadvantages of using conventional rigid diaphragm assumptions can be assessed.

Two main analytical platforms were used in this study, OpenSEES and SAP2000. These two programs correspond to what may be considered conventional and advanced design tools. SAP2000 was considered as an appropriate FEM tool for preliminary design, for which all the structural members were simulated as linear elastic elements. In this step the Equivalent Lateral Force (ELF) method from ASCE 7 was used to dimension the members. OpenSEES was used

for 3D non-linear analyses. For these OpenSEES models, all structural components in both the vertical moment and braced frames were simulated with nonlinear force-based or displacement-based elements (Spacone E. and El-Tawil S., 2004). For the structural members in the diaphragm system, including chords and collectors, linear elastic elements were used in both the SAP2000 and OpenSEES models. The validity of this assumption will be verified in Subsection 7.7.2.

For evaluating the nonlinear behavior of the theme structures, all of the models were simulated in OpenSEES and OpenSEES-MP. The traditional version of OpenSEES (Version 2.4.2) was installed in a personal computer; the multiprocessor version, OpenSees-MP (Version 2.2.1) was installed on Ithaca, a High Performance Computer (HPC) at Virginia Tech (Advanced Research Computing, 2014). The two versions of OpenSEES were used for conducting nonlinear static and dynamic analyses in the study, respectively. The following sections include more details about the structural simulation of the theme structures in OpenSEES and SAP2000.

### **3.3 Description of theme structures**

This section defines the two 4-story, three-dimensional steel structures with different diaphragm types and horizontal layout of the vertical lateral force resisting system (LFRS) used in this study. All the structures have the same story heights, 15 ft. for the 1<sup>st</sup> story and 12.5 ft. for the 2<sup>nd</sup> to 4<sup>th</sup> story. The typical span is 27.5 ft. Figure 3-1 illustrates the typical plan layout for each type of theme structure. Configurations 1 (C1) and 2 (C2) includes diaphragms which comply with the ASCE 7 requirements. (i.e. aspect ratio of 3.0 as the limit by ASCE 7). The LFRS in both structures consists of four braced frames and two moment frames. In the Y-direction, the layout of vertical braced frames in C1 is symmetric and the one in C2 is asymmetric. For both configurations, the LFRS in the X-direction consists of two symmetrically arranged moment

frames. In all cases, the diaphragm consists of corrugated composite decks, as described in detail in Subsection 3.4.6

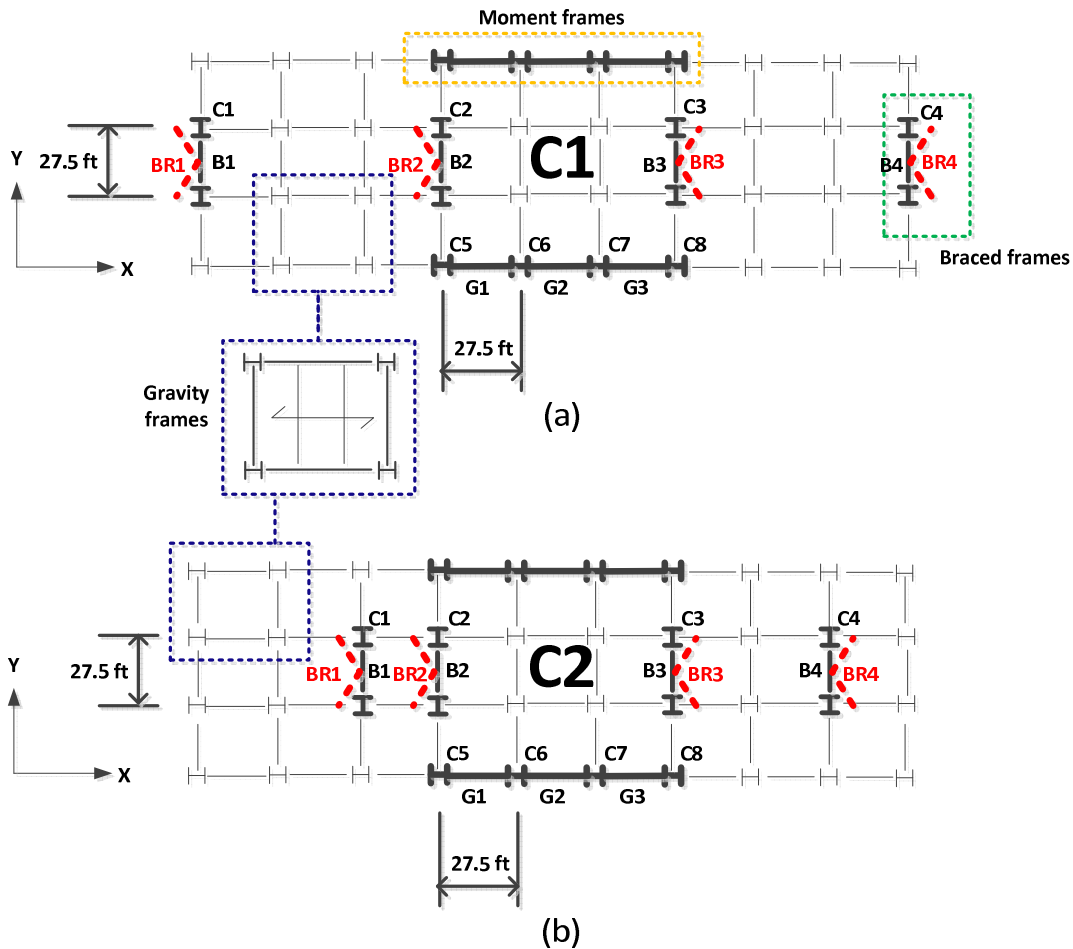


Figure 3-1 Plan layout of these structures (a) C1 (b) C2

In Figure 3-1, the bold black and dotted red lines along the Y-direction in the figure illustrate the position of the four special concentrically X-braced frames (SCBFs), while the bold black lines represent the position of the two special moment resisting frames (SMRFs) along the X-direction. The major structural components in SCBFs and SMRFs, including braces, columns, beams, satisfy the design requirements in ASCE 7 and the AISC Seismic Provisions, as will be discussed in Section 3.4. The columns in both the SMRFs and SCBFs are fixed at the base. In the design,

these columns are assumed to resist lateral forces through bending about their strong-axis. Additional details regarding the released/restrained conditions pertaining to the braced and gravity frames are provided below:

**Special Concentrically Braced Frames (SCBFs):** Pin connections are specified at both ends of braces as well as in all beams. The out-of plane bending effect of gusset plates in braced frames is not included in the analytical models. The column orientations in the SCBFs are shown in Figure 3-1.

**Special Moment Resisting Frames (SMRFs):** Moment connections, which are able to transfer bending moment, shear and axial force, are used for connecting beams and columns in the SMRFs. The column orientations in the SMRFs are shown in Figure 3-1 also. Beams in SMRFs are reduced beam sections (RBS).

**Gravity frames:** The gravity frames resist primarily vertical dead and live loads. All beams in these systems are assumed to be pinned at their ends. Column splices, represented with hinge connections, are assumed to exist at the middle of the third story height. The continuous gravity columns are used above and below the splices. All the columns of the gravity frames are pinned at the base. The orientation of the gravity column section is shown in Figure 3-1. Joists in the gravity systems are not simulated in the analytical models.

The elevations of the theme structures are shown in Figure 3-2.

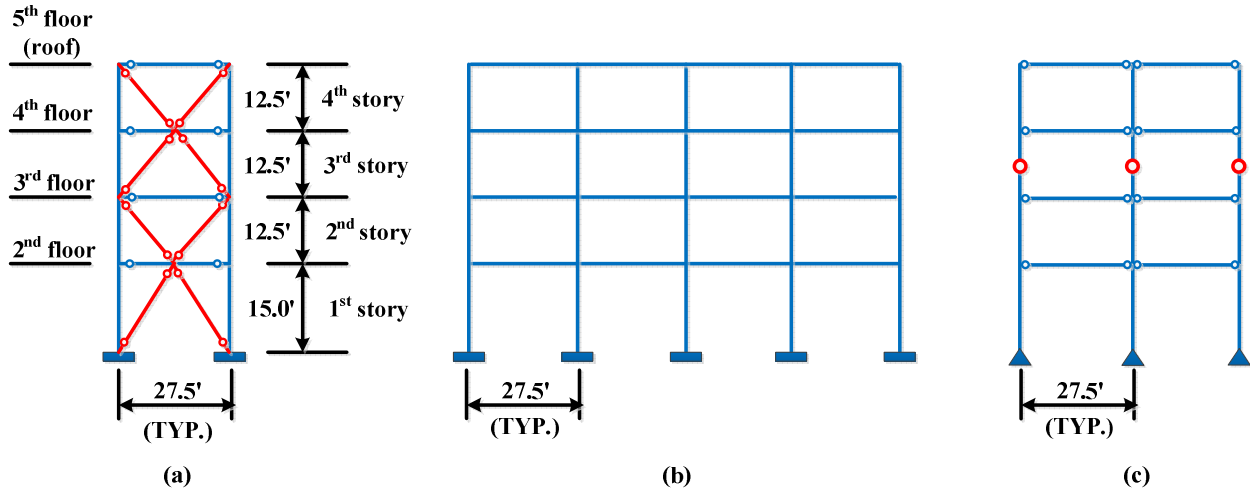


Figure 3-2 Elevation of typical (a) braced frame, (b) moment frame, and (c) gravity frame

### 3.4 Design of the theme structures

This section concentrates on the preliminary design stage according to the requirements of the ASCE 7, AISC 341 (2010a) and AISC 360 (2010b) documents. All the structures are modelled in SAP2000 with the assumption of rigid diaphragms. By conducting analyses based on the Equivalent Lateral Force (ELF) method, including the appropriate seismic load combinations as described in ASCE 7, the maximum forces in the members can be obtained. The demands corresponding to the members can then be checked against the nominal capacities as given in AISC 341 and 360. In this preliminary stage, design seismic lateral forces are applied only in the Y-direction. Some important design criteria related to the study, such as the structural horizontal irregularity and D/C ratios, are investigated in the following sections.

#### 3.4.1 Material properties and gravity loads

Material properties for the two theme structures (i.e. C1 and C2) are summarized in Table 3-1. W-sections with 50 ksi yield strength are used for beam and column members, and HSS-sections with 46 ksi yield strength are used for brace members. Gravity loads for the structure, including

dead load and live load, are summarized in Table 3-2. The dead loads include an average weight of curtain wall of 14.4 psf. The seismic weights of structures C1 and C2 are 8450 kips, which are based on the 4-story prototype structures in ATC 76 (NEHRP, 2010). The equivalent design seismic loads can be determined based on the known structural masses and periods. With regard to the live loads, they are taken as 50 psf for the 2F to 4F, and 20 psf for the RF. The design live load considers the reduction factor according to the requirements of ASCE 7.

Table 3-1 Material properties for theme structures

Steel Section	Material Properties
W Sections	ASTM A992; Fy=50 ksi; Fu=65 ksi
HSS Sections (braces)	ASTM A500 Grade B; Fy=46 ksi; Fu=58 ksi
Concrete (Slab)	f <sub>c</sub> = 3 ksi (Normal weight)

Table 3-2 Gravity loads for theme structures

Dead Load (psf)	C1	C2
Structure	8.0	8.0
Deck+Slab	56.0	56.0
Super-imposed Dead Load	25.0	25.0
Façade	14.4	14.4
Total load	103.4	103.4
Total load (kips)	8449.3	8449.3
Total density (pcf)	7.9	7.9
Live Load (psf)	C1	C2
LL0(office)	50	50
LL(Reduced, 2-4F)	26.1	26.1
LL(Roof)	20	20

### 3.4.2 Site conditions

These theme structures are assumed to be built in a similar location as San Francisco City Hall. The coordinates of the site are 37.78°N, 122.42°W. From the USGS website (U.S. Geological Survey, 2014), the design spectrum as well as the mapped acceleration parameters are

determined as  $S_S=1.50g$  and  $S_1 = 0.63g$ . The site classification is assumed as D, and the importance factor,  $I_e$ , is taken as 1.0. The risk category of the theme structures is I, and thus the allowable story drift is 2% of the height of story. The Seismic Design Category (SDC) for the theme structures based on the importance factor and risk category is taken as “D”. Figure 3-3 and Figure 3-4 shows the design basis (DBE-level) and maximum considered earthquake (MCE<sub>R</sub>-level) spectrums. Related seismic design parameters and the load combinations for the theme structures will be discussed in Subsection 3.4.3.

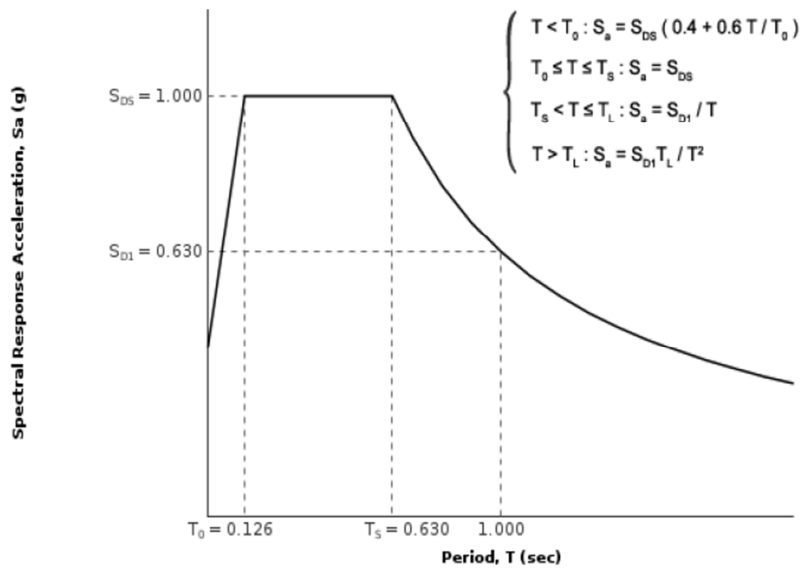


Figure 3-3 Design spectrum

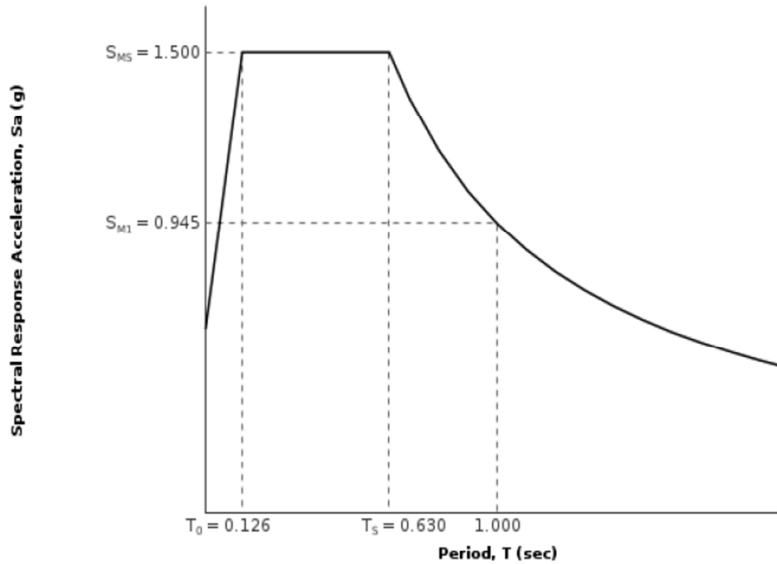


Figure 3-4 Risk-target maximum considered spectrum

### 3.4.3 Seismic design parameters

According to the seismic design requirements in ASCE 7, the response modification coefficient,  $R$ , is 6.0 for SCBFs (Y-direction), and 8.0 for SMRFs (X-direction). Based on these values, the design seismic base shears ( $V$ ) are  $0.167W$  and  $0.084W$  for the SCBFs and SMRFs, respectively (Table A-1). The vertical distribution of seismic loads is based on the portion of the total seismic weight as well as the height of structures given in Table A-2 and Table A-3. The overstrength factors ( $\Omega_0$ ) for the SMRFs and SCBFs are 3.0 and 2.0, respectively.

The determination of the redundancy factors ( $\rho$ ) for the design of the SCBFs and SMRFs is based on the requirements of Table 12.3-3 in ASCE 7. The factor shall be taken as 1.30 if the removal of an individual brace or release of beam-to-column connection results in the existence of extreme torsional irregularity. The redundancy factor,  $\rho$ , is set equal to 1.0 for moment frames in C1 and C2. The  $\rho$  for the braced frames in C1 is selected as 1.0 and as 1.3 in C2. The above key seismic design parameters are summarized in Table 3-3.

Table 3-3 Key seismic design parameters

Parameter	SCBF	SMRF
R	6.0	8.0
$C_d$	5.0	5.5
$\Omega_0$	2.0	3.0
$\rho$	1.0 (C1) ; 1.3 (C2)	1.0 (C1 and C2)

### 3.4.4 Load combinations

Table A-1 to Table A-3, located in Appendix A, show the design seismic lateral forces for SCBFs and SMRFs based on the ELF approach. The effect of accidental torsion is taken into account by the load combinations shown in Table 3-4 in order to verify the demand/capacity (D/C) ratios for both Deformation Controlled Elements (DCEs) and Force Controlled Elements (FCEs). DCEs are the beams and columns in SMRFs, and the braces in SCBFs. FCEs are the columns and beams in SCBFs, and the structural components in diaphragms, such as collectors and chords.

Table 3-4 Load combinations of the theme structures

	Deformation Controlled Elements (DCE)	Force Controlled Elements (FCE)
<b>Load Combination 1</b>	$1.4D \pm \rho(EQ_x \pm 0.3EQ_y) + L$	$1.4D \pm \Omega_0(EQ_x \pm 0.3EQ_y) + L$
<b>Load Combination 2</b>	$1.4D \pm \rho(EQ_y \pm 0.3EQ_x) + L$	$1.4D \pm \Omega_0(EQ_y \pm 0.3EQ_x) + L$
<b>Load Combination 3</b>	$0.7D \pm \rho(EQ_x \pm 0.3EQ_y)$	$0.7D \pm \Omega_0(EQ_x \pm 0.3EQ_y)$
<b>Load Combination 4</b>	$0.7D \pm \rho(EQ_y \pm 0.3EQ_x)$	$0.7D \pm \Omega_0(EQ_y \pm 0.3EQ_x)$

### 3.4.5 Story drift and P-Delta effects

The design check for story drift values and P-Delta effects are based on the requirements of ASCE 7. The values of drift and displacement quantities are multiplied by  $C_d$ , as defined in

Table 3-3. The allowable story drift for SMRFs and SCBFs are limited to 2% story height. Both C1 and C2 satisfy the limitations of story drift and stability as shown in Table A-4.

### 3.4.6 Member sizes

The braced systems are designed to resist at least 30% but not more than 70% of the total seismic forces by braces in tension (AISC 341 Section F2.4a). HSS round sections satisfying the slenderness limitations for SCBF are used in the design. Beams in the SCBFs are assumed to be laterally supported continuously, and thus no lateral torsional buckling can develop in those beams.

W-sections in the columns and beams in SCBFs and SMRFs satisfying the limitations of member slenderness and width-to-depth ratios are used in the design. In addition, the effects of doubler plates (panel zone) and reduced beam sections (RBS) are considered in the design of SMRFs. The related design details for doubler plates are discussed in Subsection 3.4.7. The RBS are designed based on AISC 360, using  $a=0.625b_f$ ,  $b=0.75d_b$  and  $c=0.10b_f$  as the typical dimensions of RBS, where  $b_f$  and  $d_b$  are the flange width and the depth of the original beam section, respectively. Figure 3-5 shows the definitions of the variables,  $a$ ,  $b$  and  $c$ , in a RBS. Table 3-5 and Table 3-6 present the member sizes for C1 and C2, respectively.

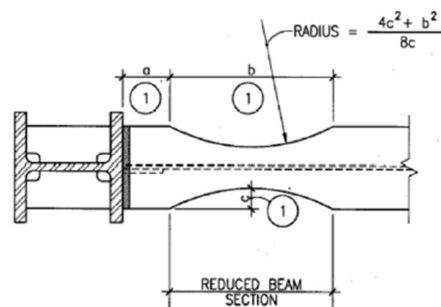


Figure 3-5 Dimensions of RBS (NEHRP, 2010)

Table 3-5 Member sizes for LFRS in C1

Story	Story Height (ft)	Braced frame			Moment frame		
		C1~C4	B1~B4	BR1~BR4	C5~C8	G1~G3	Doubler plate size (in)
4 <sup>th</sup>	12.5	W12x106	W21x57	HSS5x5x1/2	W14x132	W21x44	0.75
3 <sup>rd</sup>	12.5	W12x106	W24x76	HSS5.5x5.5x3/8	W14x132	W24x76	1.25
2 <sup>nd</sup>	12.5	W14x132	W21x57	HSS6x6x1/2	W14x211	W24x84	1.50
1 <sup>st</sup>	15.0	W14x132	W27x114	HSS7x7x1/2	W14x211	W27x114	1.50

Table 3-6 Member sizes for LFRS in C2

Story	Story Height (ft)	Braced frame						Moment frame		
		C1,C4	B1,B4	BR1,BR4	C2,C3	B2,B3	BR2,BR3	C5~C8	G1~G3	Doubler plate size (in)
4 <sup>th</sup>	12.5	W12x106	W21x57	HSS6x6x1/2	W12x106	W21x57	HSS6x6x1/2	W14x132	W21x44	0.75
3 <sup>rd</sup>	12.5	W12x106	W27x114	HSS7x7x1/2	W12x106	W24x103	HSS7x7x1/2	W14x132	W24x76	1.25
2 <sup>nd</sup>	12.5	W14x176	W21x73	HSS8x8x5/8	W14x176	W21x73	HSS7x7x5/8	W14x211	W24x84	1.50
1 <sup>st</sup>	15.0	W14x176	W27x129	HSS9x9x5/8	W14x176	W27x114	HSS8x8x5/8	W14x211	W27x114	1.50

For the gravity frames, both C1 and C2 have the same member sizes for columns and beams in the frames as they have the same magnitudes of gravity loads (i.e. dead load and live load). In addition, the joists have the same size as those of Y-direction interior gravity beams, as illustrated in Figure 3-6 (a). The member sizes for the gravity frames are listed in Table 3-7.

Table 3-7 Member sizes for gravity frame

Story	Story Height (ft)	Gravity frame				
		Column	External beam	Internal beam (X-dir)	Internal beam (Y-dir)	Joists (Y-dir)
4 <sup>th</sup>	12.5	W12x53	W18x46	W24x76	W18x46	W18x46
3 <sup>rd</sup>	12.5	W12x53	W18x46	W24x76	W18x46	W18x46
2 <sup>nd</sup>	12.5	W14x90	W18x46	W24x76	W18x46	W18x46
1 <sup>st</sup>	15.0	W14x90	W18x46	W24x76	W18x46	W18x46

A corrugated fully-composite floor deck is selected as the slab systems in C1 and C2. A 3.0 CD Deck is used to resist the in-plane and out-of plane loads in the slab caused by gravity loads and

seismic loads. The total depth of the corrugated slab is 6.0 inches, which consists of 3.0 inches rib and 3.0 inches flat slab with 3 ksi concrete strength. The distance between two ribs is 12 inches, and the direction of ribs is parallel to X-axis. Figure 3-6 (b) presents the layout of the composite deck used in this study. The shape of the corrugated deck is idealized as the rectangular one. Both (1) the relative slips between beams and composite decks, which in reality is trapezoidal, and (2) contribution of shear studs are neglected in this study because of the assumption of full composite action.

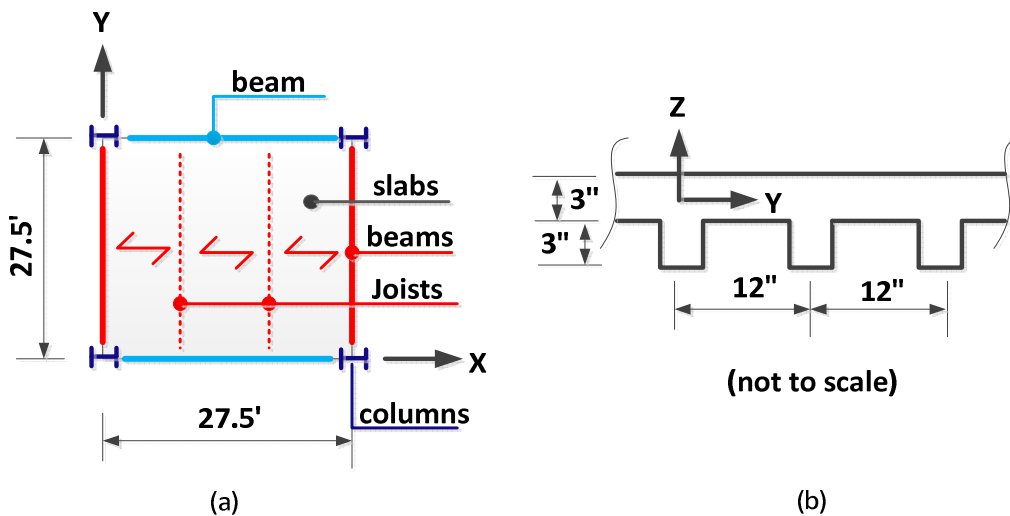


Figure 3-6 Typical layout of (a) slab system and (b) composite deck

### 3.4.7 Demand and Capacity (D/C) ratio check for members

This section focuses on (1) checks of D/C ratios for braces, beams, and columns in braced frames and (2) requirements of strong column-weak-beam and strength of panel-zones in the moment frames. The member internal forces due to seismic loads ( $P_E$ ) include the effect of accidental torsion with 5% shift of the position for the center of mass.

Figure A-1 and Figure A-2 present the D/C ratios of braces in C1 and C2. The ratios in C2 are higher than in C1 because of the design with higher redundancy factors (i.e., 1.30 for SCBFs in

C2) as well as the higher torsional irregularities. Table A-5 to Table A-10 show the results of verification of C1 and C2 including the D/C ratios of beams and columns in braced frames. Both beams and columns satisfy the strength requirement in accordance with a mechanism analysis.

For the design of SMRFs, the design of beam-column joints has to satisfy the limitations of strong column-weak beam. The summation of bending capacity of beams with RBS must be lower than those provided by columns. Table A-11 to Table A-14 shows the D/C ratios for the joints in C1 and C2 structures. All of the ratios are higher than 1.0, which satisfy strong column-weak beam requirement.

In addition, the strength checks for the panel zone, including the doubler plates, are presented in Table A-15. The results show that joint nominal strengths with additional doubler plates satisfy the shear demands due to the development of plasticity in RBS sections.

### **3.4.8 Discussion of horizontal irregularities in the diaphragms**

In the preliminary design stages, the maximum and average story drifts can be determined through ELF analyses. According to the definition of horizontal irregularity mentioned in Table 12.3-1 of ASCE 7, the diaphragm torsional coefficient can be determined by using the maximum story drift divided by the average one, without considering the amplification of accidental torsion. If the coefficient is higher than 1.2 but lower than 1.4, a typical torsional horizontal irregularity exists in the structure. The structures in this range are allowed to be used in SDC E and F. However, if the index is higher than 1.4, the structures are not allowed for SDC E and F due to the existence of an extreme horizontal torsional irregularity.

According to Table 12.3.1 in ASCE 7, typical and extreme torsional irregularities are allowed in the structures belonging to SDC D. The theme structures, belonging to SDC D, are intentionally

designed for categories corresponding to different horizontal irregularities. Table 3-8 shows the diaphragm torsional coefficients ( $TC$ ) in each configuration including the effect of accidental torsion. The results show that the index for C2 is higher than that for C1 because C1 is a symmetric structure and C2 is asymmetric. Based on the classification in Table 12.3-1, C1 belongs to the *no torsional irregularity* category, and C2 to the *extreme* irregularity category. The  $TC$  in C2 are higher than 1.40. Thus, they cannot be used for the structures in SDCs E and F. In other words, the two configurations correspond to the upper and lower limitations of horizontal torsional irregularity.

Table 3-8 Comparison of torsion coefficients for rigid diaphragms

	Torsion Coefficient (TC)	
	C1	C2
<b>RF</b>	<b>1.17</b>	<b>1.47</b>
<b>4F</b>	<b>1.17</b>	<b>1.47</b>
<b>3F</b>	<b>1.18</b>	<b>1.48</b>
<b>2F</b>	<b>1.14</b>	<b>1.51</b>

### 3.5 Simulation details for structural components in OpenSEES

The section concentrates on the simulation details of columns, beams and braces for the FEM 3D analytical models in OpenSEES.

#### 3.5.1 Columns in LFRS

For the columns in moment frames (i.e. SMRFs) and braced frames (i.e. SCBFs), each frame section is subdivided into fibers, each fiber is assigned a uniaxial material properties. For column sections, the flange and web of each column sections are divided into 32 fibers and 16 fibers, respectively, as shown in Figure 3-7.

The element type “ForceBeamColumn” element (FBC) is used for simulating the column elements in moment and braced frames. Some characteristics of force-based elements (Terzic V., 2011) are:

- a. Equilibrium between element and section forces is exact by conducting iterative procedures.
- b. Section forces are determined from the basic forces by interpolation within the basic system. The variation of axial force is constant and moment linear without the application of additional load along the element.
- c. The Principle of Virtual Force (PVF) is used to satisfy the compatibility in the element.

According to the suggestions for the simulation of FBCs from the OpenSEES Forum (OpenSeesWiki), the accuracy and convergence efficiency can be improved with increasing the number of integration points (NIPS) for each FBE. In this study 8 NIPs are used in each column and beam element. For the selection of material for those columns, Steel02 (i.e. Giuffre-Menegotto-Pinto Model in OpenSEES) with isotropic strain hardening effect is specified for the material properties of each fiber. The strain hardening ratio is taken as 0.1%. To consider the effect of expected strength, the nominal yield stress is increased by 10%, based on ASCE 41 (2013), to 55 ksi in the analytical OpenSEES models.

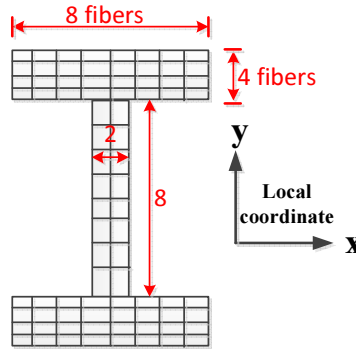


Figure 3-7 Fiber beam and column sections in 3D OpenSEES models

### 3.5.2 Braces

For the 3D braced steel structures with horizontal irregularities, buckling of the braces and its sequence influence the rotation of the diaphragms significantly. The sequential brace buckling creates series of “load redistribution” among vertical lateral load resisting members, creating an unexpected demand on the diaphragm and its components. Thus simulating buckling is a key part of the model.

There are several ways to simulate the buckling behavior of braces. In this study, all the braces are HSS sections with 46 ksi yield strength with the strain hardening ratio of the material taken as 0.1%. The expected strength, 50 ksi, is used in the analytical brace models based on the recommendations of ASCE 41 (2013). The buckling of the brace is stimulated by a brace imperfection and the 2<sup>nd</sup> order (P-Δ) effect. Results from ATC 76 (NEHRP, 2010) document suggest the initial imperfection of brace should be between 0.05% and 0.1% of the effective brace length.. In the thesis, a 0.1% imperfection is imposed at the middle point of each brace and the effect of residual stress is not considered in the analyses. A co-rotational transformation is used to track the effects of brace buckling with large deformations. Fiber sections with

Menegotto-Pinto material model (Steel02 in OpenSEES) are also used to describe the hysteretic behavior of each fiber. Each brace section is subdivided into 50 fibers as shown in Figure 3-8.

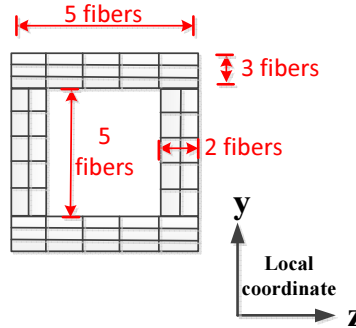


Figure 3-8 Fiber brace section in 3D models

Uriz and Mahin (2008) suggested at least two force-based nonlinear beam column elements (FBC) can be used to simulate the behavior of a single brace. To investigate the accuracy of the combinations of element types and numbers for the brace simulation in the 3D models, the hysteretic behavior of an individual brace (HSS7x7x1/2), simulated by either “ForceBeamColumn (FBC)” elements or “DispBeamColumn (DBC)” elements, is investigated by conducting cyclic loading tests. This simple analytical model is illustrated in Figure 3-9.

The hysteretic loops corresponding to different number of elements (2, 4 and 6) with different element types (FBC or DBC) are presented in Figure 3-10. The results show the model with 6 DBC elements provides the best match for the hysteretic loops provided by the 6 FBC elements model. In addition, all the models simulated by 2, 4 and 6 elements perform similarly compression and tension strength. To improve the computational efficiency in the 3D model, two DBC elements model with  $L/1000$  imperfection are selected as the typical analytical brace model in the 3D models.

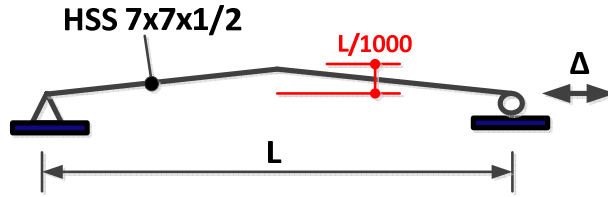


Figure 3-9 Individual brace model with imperfection

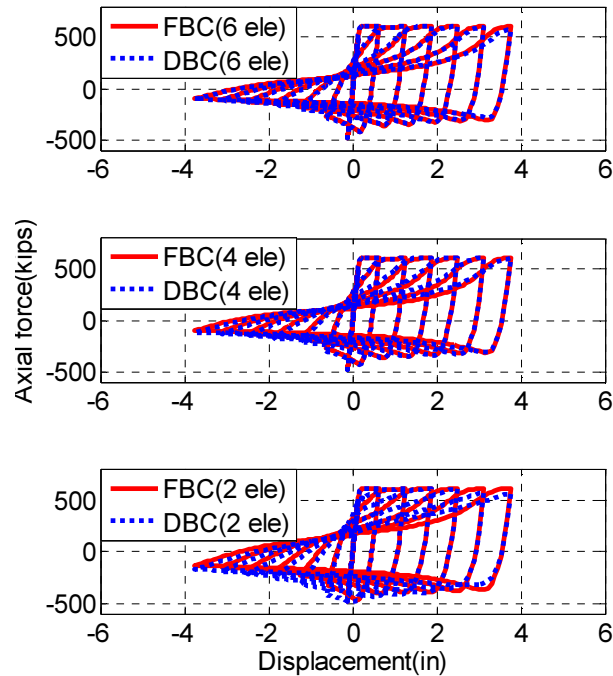


Figure 3-10 Hysteretic loops for brace simulated by different element types and numbers

In addition, both brace fracture and fatigue are modeled in the braces simulation, such behavior can be captured in OpenSEES models by assigning MinMax and Fatigue uniaxial material properties in the brace elements, respectively. For the nonlinear static (pushover) analyses, the effect of brace fracture is included by setting a tensile strain cap of 0.05 in the Menegotto-Pinto material model. The fiber stress is released when the tensile strain achieves this limitation.

For the nonlinear dynamic analyses, the effect of material low-cycle fatigue is included in the Menegotto-Pinto material model. The related fatigue material properties of the brace based on

coupon test are defined in OpenSEES models according to the Coffin-Manson relationship. For these studies, the required parameters ( $m$  and  $\epsilon_0$ ) are selected as -0.458 and 0.190, respectively, based on the recommendations from Uriz and Mahin (2008). The definition of  $m$  and  $\epsilon_0$  are defined as follows:

- $m$  is the material parameter that describes the sensitivity of the log of the total strain amplitude to the log of the number of cycles to failure.
- $\epsilon_0$  is the material parameter that roughly indicates the strain amplitude at which one cycle on a virgin material will cause failure.

Figure 3-11 shows the hysteretic loops of the same brace model considering the effect of fracture and fatigue, respectively.

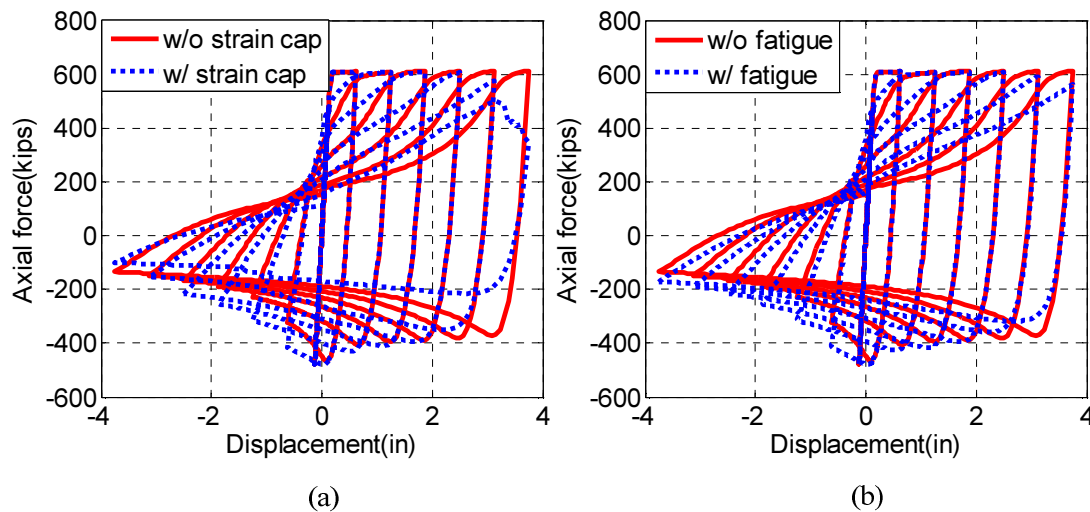


Figure 3-11 Hysteretic loops of brace with (a) fracture and (b) fatigue effects

On the basis of the suggestions provided by Mahin and Uriz in the ATC-76 (NIST, 2010) document, rigid offsets have to be incorporated into the beam-column connections as well as brace-to-framing connections. Such offsets provide the physical length and stiffness of the braces.

The assumed effective length of the brace is 75% of the work-point-to-work-point length. The effective lengths are subdivided into 2 nonlinear DBC elements considering fatigue or fracture effects. Each brace element has 6 NIPs. The geometric configuration of brace with imperfection is illustrated in Figure 3-12.

To simplify the analysis of structure, the contribution of gusset plate is not considered in this study. Zero length elements with a very low out-of plane rotational stiffness (rotation stiffness about local z axis as shown in Figure 3-12) are used to describe the behavior of the pin connections between rigid offsets and brace elements as shown in Figure 3-12.

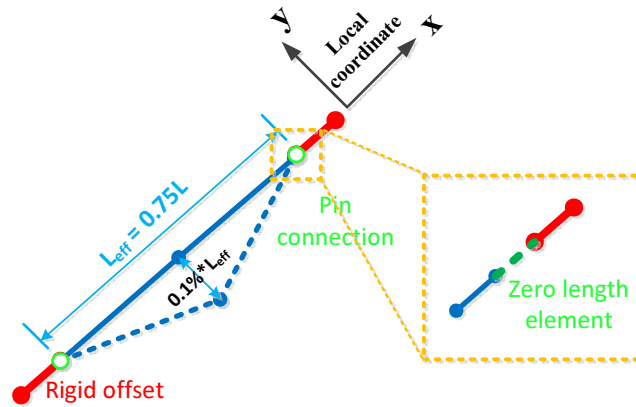


Figure 3-12 Simulation of brace including imperfection

### 3.5.3 Beams in SCBFs

For the beams in SCBFs, pin connections are used at both ends of beams. In addition, full lateral supports are provided to all beams and thus no lateral torsional buckling can develop. Both flanges and web are divided into 16 fibers. Figure 3-13 illustrates the configurations of fiber section of those beams.

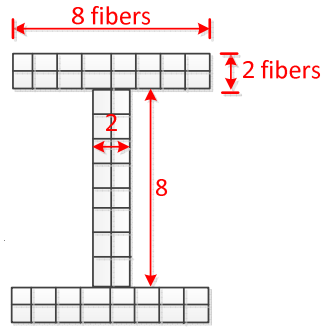


Figure 3-13 Fiber sections for beam sections in SCBFs

To include (1) the inelastic material behavior of the diaphragm, such as the strength softening in the concrete, and (2) the composite action in the analytical models, the composite slabs with an effective width,  $b_E$ , are modeled by 16 concrete fibers, as illustrated in Figure 3-14. In addition, a single lumped steel rebar fiber in each composite beam section is used at the middle of slab. The dimensions  $t_{eq}$  and  $d$  are both selected as 3.0 inches for the composite beams in the SCBFs as the rib of slab is parallel to X-axis shown in Figure 3-6.

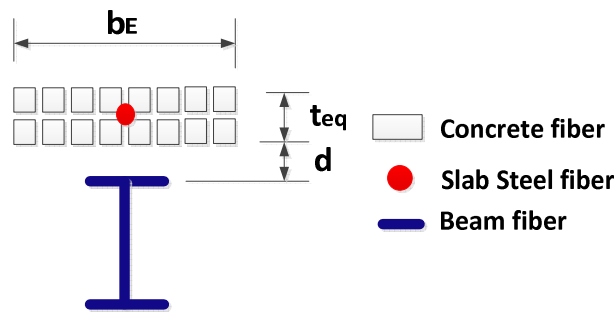


Figure 3-14 Fiber section with composite action

The effective width of slab,  $b_E$ , is determined by the conventional AISC equations.

For an interior beam,

$$b_E \leq L / 4 \tag{Equation 3-1}$$

For an exterior beam,

$$b_E \leq L/8 \quad \text{Equation 3-2}$$

where  $L$  is the span of the beam (i.e. 27.5 ft).

For the stress-strain behavior of concrete fibers, the concrete model proposed by Kent and Park (1971) is implemented in OpenSEES (i.e. Concrete01) and used in the 3D models. The related material parameters are (1) concrete compressive strength  $f'_c = 3$  ksi (2) strain corresponds to compressive strength,  $\epsilon_c = 0.002$  (3) crushing strain  $\epsilon_{cu} = 0.006$  and (4) crushing strength,  $f'_{cu} = 0.6$  ksi. The concrete tensile strength is neglected in this model. The neglect of concrete tensile strength yields a smaller strength and stiffness of the entire structures.

To consider the strength provided by metal wire and the additional rebars in the composite section, the steel ratio,  $\rho_s$ , is assumed as 0.5%. The yield strength of rebars is 60 ksi with 0.1% strain hardening ratio. In the study, the rebars are lumped at the middle of slab as a single fiber, as shown in Figure 3-14. The area of the single fiber is determined by the following equation.

$$A_s = \rho_s \times b_E \times t_{eq} \quad \text{Equation 3-3}$$

where  $\rho_s$  is the steel ratio of the slab and  $t_{eq}$  is the equivalent thickness of the slab.

To investigate the composite effect of the beam section, an individual W-section analytical beam model (W18x46) is tested by applying vertical cyclic loading at the middle of beams, as illustrated in Figure 3-15. Three scenarios corresponding to different combinations of composite effects and restraint conditions are considered. Those are:

(1) bare frame with axial restraint (**BF+R**): In this model the concrete slabs are not included and pin supports are used at both ends to restrain the axial deformation of the beam.

(2) composite frame with axial restraint (**CF+R**): In this model, the composite effect is included in the beam model with pin supports at both ends.

(3) composite frame (**CF**): In this model, the composite effect is included in the beam model with but axial deformations are permitted by the use of a roller support at one end. .

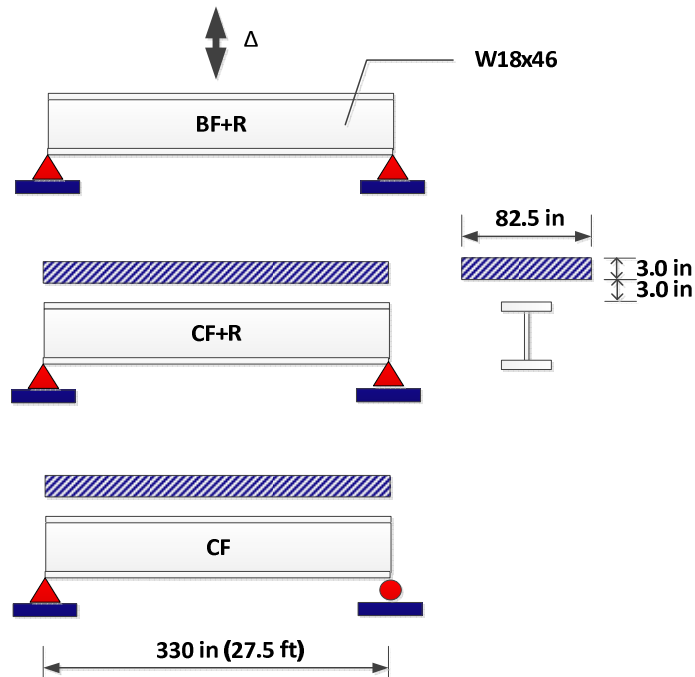


Figure 3-15 Beam models for the testing of composite effects

The relationships between vertical displacement and reaction among the three models are shown in Figure 3-16. For the **CF** beam, the magnitude of vertical reactions increases significantly due to the composite action when it undergoes downward deflection. However, the hysteretic behavior of the **CF** beam is similar as those of **BF+R** beam when the beams undergo upward deflection. This indicates the cracking of the slab caused by the upward deflection diminishes the strength of **CF** beam. For the **CF+R** beam, the model performs symmetrically because the cracking in the slab is restrained by the pin supports.

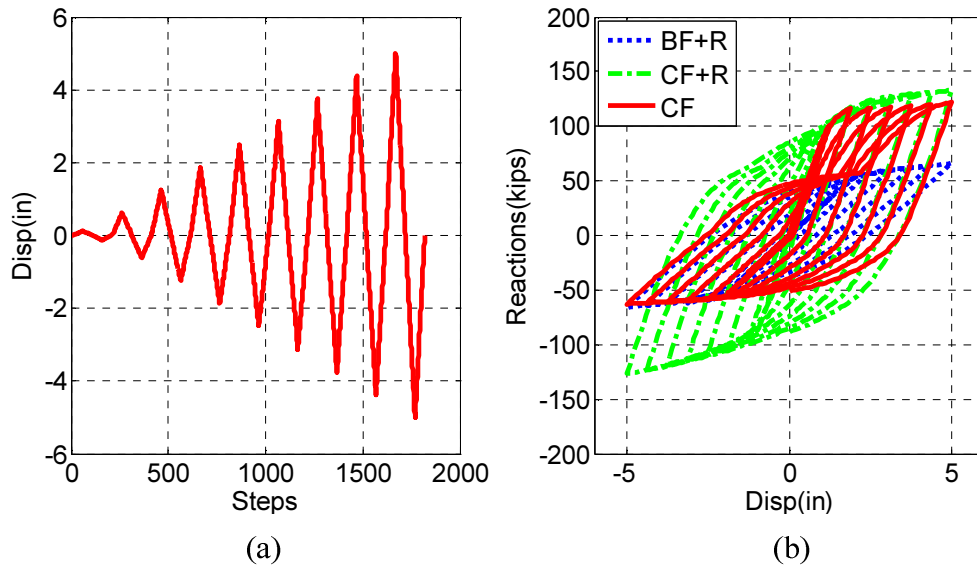


Figure 3-16 Test results for beam models: (a) history of cyclic loading and (b) hysteretic loops

### 3.5.4 Beams in SMRFs

The beams in the SMRFs for C1 and C2 also consider the (1) inelasticity of the composite action and (2) inelasticity of RBS. To include composite action, the layout and material properties of the composite beam sections will be the same as those of the three models discussed in Subsection 3.5.3. However, the equivalent thickness,  $t_{eq}$ , is selected as 4.5 inches in these beams by including half of the concrete in the rib as an average for the two directions. The gap,  $d$ , which is the distance between the bottom of slab and the top of beam, is 1.5 inches.

For the RBS, the related dimensions have been defined in Figure 3-5, with the *maximum* reduction of the width in each RBS permitted set at  $0.40b_f$ . To simplify the simulation procedures of the 3D model, a reduction of the width to  $0.20b_f$ , is selected as the typical flange width for the entire length of each RBS.

In this study, the “beamwithHinges” elements in OpenSEES are used to model the nonlinear beam behavior in the SMRFs. The length of plastic hinges is equal to the length of the RBS

region (i.e.  $0.75d_b$ ) with the reduction of the flange width,  $0.20b_f$ . The elastic part of the beam includes the composite effect which will be discussed in Subsection 3.5.7. Figure 3-17 shows the layout of the composite beam in SMRFs.

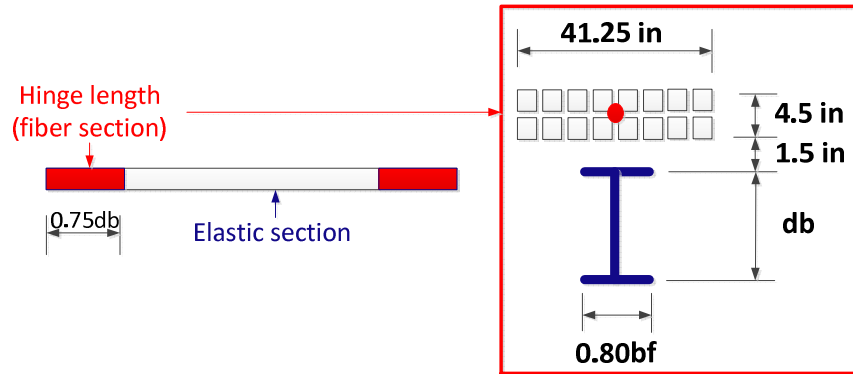


Figure 3-17 Typical beam model in SMRFs

### 3.5.5 Panel zones

The effects of panel zones are considered in the 3D analytical models, in accordance with Charney and Down (2004). Specifically, the panel zone is modeled with 8 rigid bar and 2 elastic-perfectly plastic rotational springs. One rotational spring is used to simulate the in-plane shear behavior of the panel zone, while the other is used to simulate the bending behavior of the flanges. The layout of typical panel zone simulation is presented in Figure 3-18.

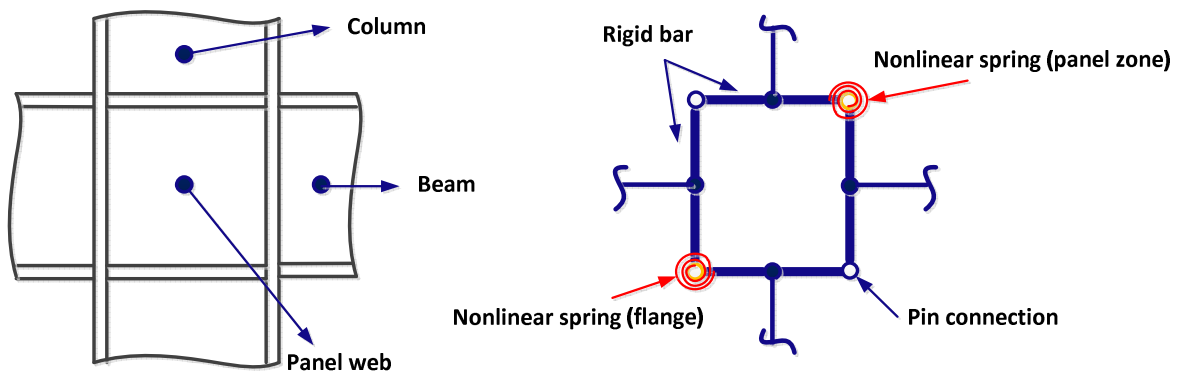


Figure 3-18 Panel zone model for beam-column connection

The initial strength and stiffness of the rotational spring for the simulation of panel zone can be evaluated as (Charney F. A. and Down W. M., 2004):

$$S_p = GV_p \quad \text{Equation 3-4}$$

$$M_{YP} = 0.58F_YV_p \quad \text{Equation 3-5}$$

where  $S_p$  is the initial stiffness of panel zone;  $G$  is the steel shear modulus;  $V_p$  is the volume of panel zone;  $M_{YP}$  is the yielding strength of panel zone; and  $F_Y$  is the yielding strength of steel.

The initial strength and stiffness of the rotational spring for the simulation of the flanges can be evaluated as (Charney F. A. and Down W. M., 2004):

$$S_F = 0.75Gb_{cf}t_{cf}^2 \quad \text{Equation 3-6}$$

$$M_{YF} = 1.80F_Yb_{cf}t_{cf}^2 \quad \text{Equation 3-7}$$

where  $S_F$  is the initial spring stiffness of flanges;  $b_{cf}$  is the flange width of column; and  $t_{cf}$  is the flange thickness of column.

Table A-16 includes the spring stiffnesses for the panel zones simulation in the SMRFs.

### 3.5.6 Composite action of the beam in internal gravity beams

The beams in gravity frames are simulated by elastic beam-column elements. To include the slab in-plane, out-of plane and axial behavior in these bare beam-column elements, three amplification factors ( $CF1$ ,  $CF2$  and  $AF1$ ) are applied to the section properties of the elastic beam-column elements. The details of the amplification factors are discussed as follows.

**Out-of plane bending:** According to AISC 360 (2010a), the effective moment inertia is based on the cracked transformed section considering the degree of composite action. In this study, the

effective moment inertia is taken as the average value of the moment inertia of bare steel beam and the full composite beam. For the internal full composite beam, the effective width,  $b_E$ , is selected as 82.50 inches for internal gravity beams. The following equation defines the effective moment inertia.

$$I_{avg} = \frac{I_{comp} + I_{steel}}{2} \quad \text{Equation 3-8}$$

where  $I_{avg}$  is the average out-of plane moment inertia of the internal beams in gravity frames;  $I_{comp}$  is the out-of plane moment inertia of the elastic composite section for positive moment; and  $I_{steel}$  is the out-of plane moment inertia for bare beam section for negative moment.

The amplification factor of the steel bare beam,  $CFI$ , can be determined as follows:

$$CFI = \frac{I_{avg}}{I_{steel}} \quad \text{Equation 3-9}$$

The  $CFI$  for the interior beams in the gravity frames are presented in Table A-17.

**In-plane bending:** This amplification factor of in-plane bending is used to model the slab in-plane bending behavior. The slab area which is enclosed by four gravity beams can be distributed on each beam uniformly based on their triangular tributary areas, as shown in Figure 3-19 (a). Therefore, the equivalent slab width of each beam can be determined as illustrated in Figure 3-19 (b). In Figure 3-19 (b), the equivalent width of each beam is  $0.25L$ . Therefore, the in-plane bending moment inertia of the gravity beams,  $I_{comp,z}$ , can be computed accordingly (Figure 3-19 (c)).

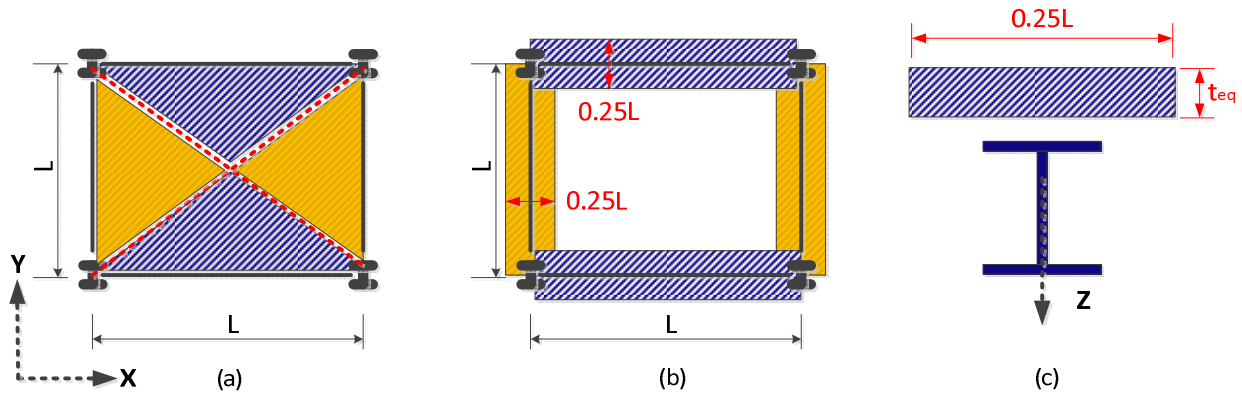


Figure 3-19 Computation of equivalent area for out-of plane bending (a) original tributary area, (b) equivalent area and (c) composite section with equivalent area

The amplification factor for considering the effect of in-plane bending,  $CF2$ , can be determined as follows:

$$CF2 = \frac{I_{comp,z}}{I_{steel}^z} \quad \text{Equation 3-10}$$

where  $I_{comp,z}$  is the in-plane bending moment inertia of elastic composite section about the  $z$  – axis and  $I_{steel}^z$  is the moment inertia of steel beam about the  $z$ -axis.

The  $CF2$  for the interior beams in gravity frames are presented in Table A-17.

**Compression and tension:** Cracking may develop in the slab due to the in-plane seismic loads and out-of plane gravity loads, resulting in decreases of the axial stiffness of the diaphragm. The evaluation of an amplification factor for the axial stiffness has to consider the effect due to cracks. The amplification factor is used to amplify the axial stiffness of the elastic bare steel beam for considering the composite action. In this study, this factor can be computed by using either the (1) ACI approach or (2) Equivalent thickness approach. The details regarding the two approaches are as follows:

**(1) ACI approach:** The moment inertia of slab is reduced by 75% due to the cracks in slab based on ACI 318-08 (2008). The equivalent slab thickness,  $t_{eq,2}$ , can be determined accordingly. Equations 3-11 and 3-12 show the relationship between the reduced moment inertia and equivalent slab thickness.

$$I_{slab} = \left( \frac{b_E \times t_{eq}^3}{12} \right) \quad \text{Equation 3-11}$$

$$t_{eq,2} = \left( \frac{0.25 \times I_{slab}}{b_E} \right)^{1/3} \quad \text{Equation 3-12}$$

where  $t_{eq}$  is the original equivalent thickness of slab (i.e. 4.5 in or 3.0 in);  $t_{eq,2}$  is the equivalent thickness of slab corresponding to reduced moment inertia; and  $I_{slab}$  is the original moment inertia corresponding to  $t_{eq}$ .

The amplification factor,  $AFI$ , can be determined based on the known  $t_{eq,2}$ , as defined in the Equation 3-13.

$$AFI = \frac{\left( \frac{b_E}{n} \right) \times t_{eq,2} + A_{steel}}{A_{steel}} \quad \text{Equation 3-13}$$

where  $n$  is taken as 9, a common ratio between the elastic moduli of steel ( $E_s$ ) and concrete ( $E_c$ ).  $A_{steel}$  is the area of the bare steel beam.

**(2) Equivalent thickness approach:** This method calculates the equivalent thickness,  $t_{eq,3}$ , based on the known average out-of plane moment inertia ( $I_{avg}$ ) which can be determined by Equation 3-8. The equivalent thickness,  $t_{eq,3}$ , can be computed by calculating the position of neutral axis through conducting an iteration processes within Equation 3-15. The  $t_{eq,3}$  may be significantly

smaller than  $t_{eq,2}$  when the deeper steel beam is used. Equation 3-14 defines the position of neutral axis.

$$\bar{Y} = \frac{A_{steel} \times (d_b / 2 + t_{eq,3}) + (b_E / n) \times t_{eq,3}^2 / 2}{A_{steel} + (b_E / n) \times t_{eq,3}} \quad \text{Equation 3-14}$$

$$I_{avg} = I_{steel} + A_{steel} \times (d_b / 2 + t_{eq,3} - \bar{Y})^2 + \left(\frac{1}{12}\right) \times \left(\frac{b_E}{n}\right) \times t_{eq,3}^3 + \left(\frac{1}{12}\right) \times \left(\frac{b_E}{n}\right) \times \left(\bar{Y} - \frac{t_{eq,3}}{2}\right)^2 \quad \text{Equation 3-15}$$

where  $\bar{Y}$  is the position of neutral axis and  $d_b$  is the depth of steel beam.

Similarly, the amplification factor,  $AFI$ , can be determined based on the known  $t_{eq,3}$ , as shown in Equation 3-16.

$$AFI = \frac{\left(\frac{b_E}{n}\right) \times t_{eq,3} + A_{steel}}{A_{steel}} \quad \text{Equation 3-16}$$

Table A-18 and Table A-19 present the  $AFI$  determined by the ACI approach and the Equivalent thickness approach. In the study, the  $AFI$ s provided by the ACI approach, 2.16 for W14x76 and 2.28 for W18x46, are used in the 3D analytical models.

### 3.5.7 Composite action of the beam in external gravity beams

The section properties of the external beams in the gravity frame also include the amplification factors,  $CF1$ ,  $CF2$  and  $AFI$ . However, the determination of  $AFI$  is different when compared with those discussed in Subsection 3.5.6 because of the diaphragm chord influence. Details regarding the determination of these factors are provided below.

**Out-of plane bending:** The approach used to determine the  $CFI$  is same as the approach mentioned in Subsection 3.5.6. The only difference is the effective width,  $b_E$ , for the external gravity beams is 41.25 inches. The  $CFI$ s for external gravity beams are listed in Table A-17.

**In-plane bending:** The approach used to determine the  $CF2$  is same as the approach mentioned in Subsection 3.5.6. The  $CF2$  for external gravity beams are listed in Table A-17.

**Compression and tension:** For the external gravity beams, the slab can crack severely due to the obvious chord action in the diaphragm, as shown in Figure 3-20. This phenomenon may become dominant when the structures have an extremely torsional irregularity. Therefore, the ACI approach or equivalent thickness approach discussed in Subsection 3.5.6 may not be appropriate for the determination of  $AFI$  for such members in this scenario.

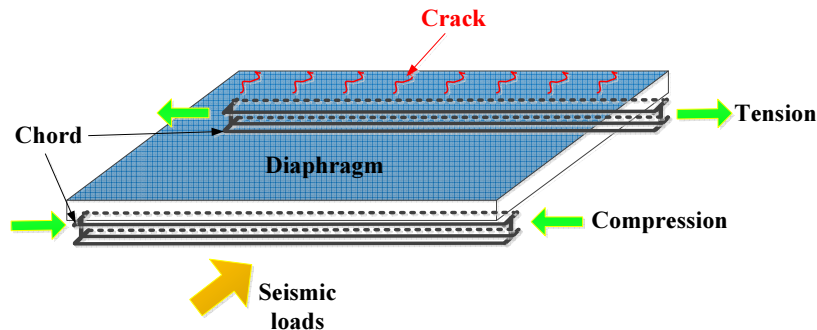


Figure 3-20 Chord action in diaphragm due to seismic loads

To address this issue, one can select a typical edge composite beam and conduct a cyclic displacement test along the beam as shown in Figure 3-21. The composite beam with a typical span (i.e., 27.5 ft) and  $b_E$  behaves like a chord when the seismic loads applied in the Y-direction. According to this figure, this steel beam is pinned at both ends. In other words, moment in the steel beam can not be transferred in the columns. However, the slab is able to transfer both in-plane and out-of plane forces to the vertical members (i.e., columns) due to its continuity.

The analytical model illustrated in Figure 3-22 (a) is used to simulate the axial cyclic behavior of this chord member shown in Figure 3-21. Fully fixed and fixed vertical displacement and rotation are imposed at the two ends (Points A and C) of this beam, respectively. The rotation restraints at the two ends are used to simulate the out-of bending stiffness provided by the slab. The steel beam and concrete slab are both modeled by inelastic fiber sections as mentioned in Subsection 3.5.3 and Subsection 3.5.4. In addition, the section aggregator command in OpenSEES is used to combine the uncoupled elastic torsional stiffness in the composite section. The gravity load,  $1.05D+0.25L$ , is applied along the members before conducting the cyclic loading in the model as shown in Figure 3-22 (a). The cyclic displacement is applied at Point C in this analytical composite beam model. To investigate the variation of fiber stress at the top of slab as the cyclic displacement progresses, Fiber 1 in Section A and Fiber 2 in Section B shown in Figure 3-22 (b) and (c) are selected as the target fibers for this propose.

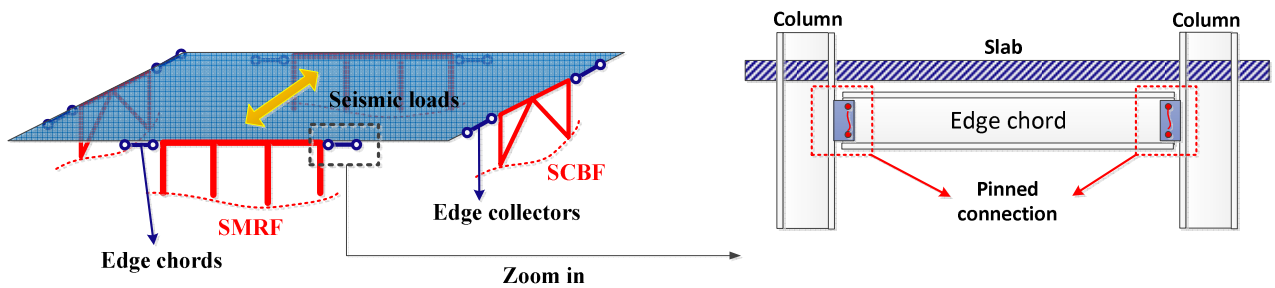


Figure 3-21 Cyclic loading test for edge chords

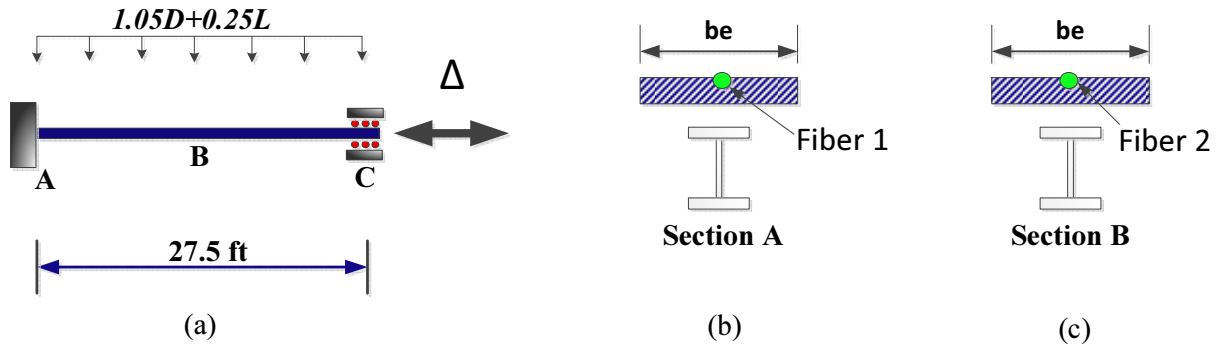


Figure 3-22 Simulation approach for edge collector and chord: (a) analytical model, (b) section A and (c) section B

The tension and compression stiffness of the composite edge beam are different because of the cracks in slab. Figure 3-23 (a) shows the stress-strain hysteretic response for Fiber 2 in Section B. Figure 3-23 (b) and (c) presents the loading and reaction history of the beam. The stress in Fiber 2 located at the middle of the chord varies from 0.0 to -3.0 ksi corresponding to the different direction of applied loads (positive or negative displacement) as illustrated in Figure 3-23 (a) and (b). Point 4 and 6 in Figure 3-23 (a) and (b) show the peak compression stress of Fiber 2 in the 3<sup>rd</sup> and 4<sup>th</sup> load cycles. The magnitude of loads indicates concrete crushing at the top of slab. Similarly, the cyclic loading test can be implemented at the edge collector illustrated in Figure 3-21 (a).

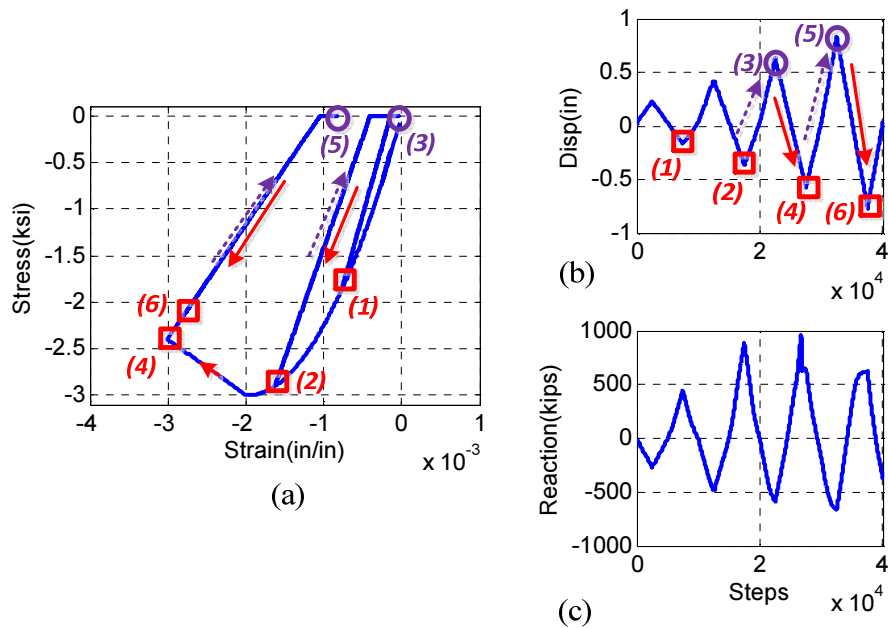


Figure 3-23 Fiber stress: (a) stress-strain hysteresis response of Fiber 2, (b) loading history and (c) history of horizontal reaction

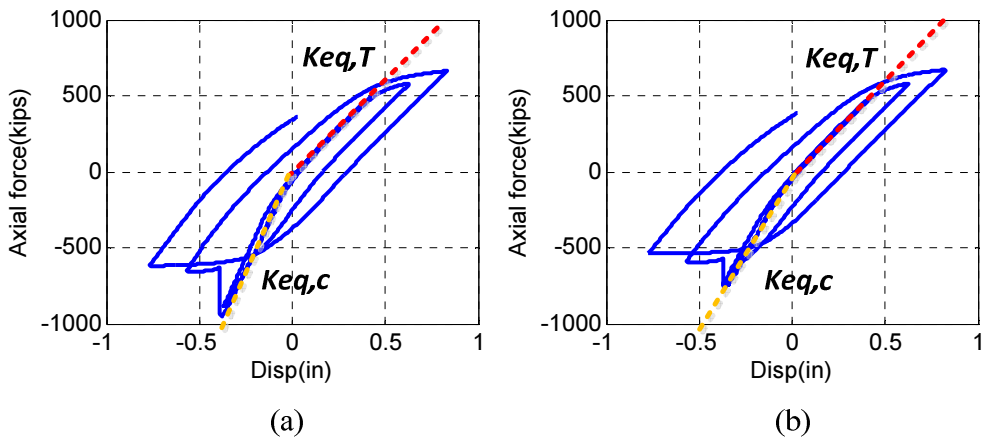


Figure 3-24 Hysteretic loops for (a) W18x46 (X-dir) and (b) W18x46 (Y-dir)

The axial hysteretic loops of edge beams W18x46 (X-dir, edge chords) and W18x46 (Y-dir, edge collectors) are shown in Figure 3-24, respectively. The equivalent elastic stiffness under compression or tension action,  $K_{eq,T}$  and  $K_{eq,C}$ , of the two members are listed in Table A-20. One can observe that compression stiffness is higher than the tensile stiffness because of the cracks in

slab. In addition, the equivalent thickness,  $t_{eq,4}$ , of the slab corresponding to these equivalent elastic stiffnesses can be determined by the Equation 3-17 and Equation 3-18. Therefore, the axial stiffness amplification factor can be determined according to Equation 3-19. These factors are listed in Table A-20.

$$K_{eq} = K_{steel} + K_{slab} = \frac{E_s A_{steel}}{L_s} + \frac{\left(\frac{A_c}{n}\right) E_s}{L_s} \quad \text{Equation 3-17}$$

$$t_{eq,4} = A_c / b_E \quad \text{Equation 3-18}$$

$$AF1 = \frac{\left(\frac{b_E}{E_s / E_c}\right) \times t_{eq,4} + A_{steel}}{A_{steel}} \quad \text{Equation 3-19}$$

The average value of  $AF1$ , which is computed by the average of  $AF1$  of compression and tensile stiffness, are conservatively selected as the axial stiffness amplification factors for the edge beams in the gravity frames in the 3D model. These factors are higher than those extracted from the ACI approach or the Equivalent thickness approach discussed in Subsection 3.5.6.

### 3.6 Simulation details for semi-rigid and rigid diaphragms in OpenSEES

To compare the seismic response between the structures with different in-plane stiffness of floor diaphragms is a main goal in the study. This section includes the simulation details for rigid and semi-rigid diaphragms in the 3D theme structures in OpenSEES.

#### 3.6.1 Rigid diaphragms

In OpenSEES, the constraint command “RigidDiaphragm” is used in the 3D models to impose an in-plane rigid constraint in each floor.

No shell or plate elements are built in the analytical models with rigid diaphragms in OpenSEES. After defining the master node (i.e., the C.M.) on each rigid diaphragm, the slave nodes are constrained by including the “RigidDiaphragm” command. In the theme structures with rigid diaphragms, the slave nodes correspond to the intersection nodes among columns and beams. The typical floor plans for rigid diaphragm structures are illustrated in Figure 3-25.

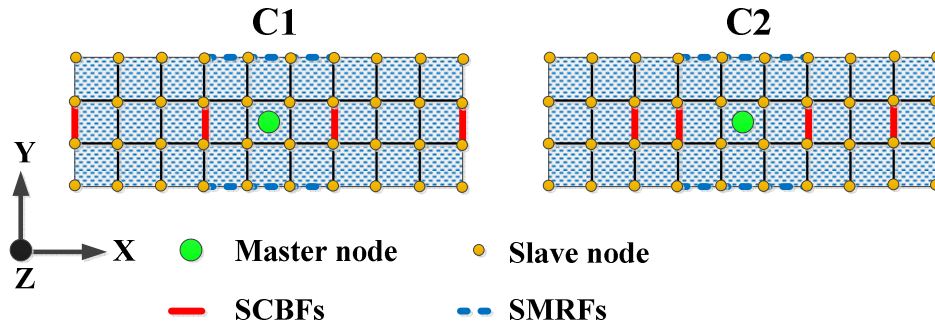


Figure 3-25 Positions of master and slave nodes in rigid diaphragm structures

In this study, two types of rigid diaphragm constraints are investigated, as follows:

- (1) Bare steel structures with rigid diaphragm constraint (**BF+R**): The analytical **BF+R** models *do not* include the composite effect of beams in either the LFRS or the gravity frames. A rigid diaphragm constraint is imposed on each diaphragm. In such structures, the lateral resistance of LFRS is provided by the nonlinear steel beam-column elements only. This is the current conventional assumptions for design of steel frame.
- (2) Composite steel structures with rigid diaphragm constraint (**CF+R**): Both LFRS and gravity frames include the composite properties, and the rigid diaphragm constraint is applied as for the (**BF+R**) models. The lateral stiffness of these **CF+R** structures is provided by the LFRS including the composite action.

### 3.6.2 Semi-rigid diaphragms

For the structures with semi-rigid diaphragms, the effect of in-plane deformation has to be considered in the analytical models. The rigid diaphragm constraint cannot be used in such structures. In the study, two ways are used to implement the effect of semi-rigid diaphragms:

(1) Composite frames without rigid diaphragm constraint (*CF*): The frame includes the in-plane and out-of plane effect of slab in the beams without using rigid diaphragm constraints. Both simulation approach and the analytical model are the same as the *CF+R* structure; the only difference between *CF* and *CF+R* is the imposition of rigid diaphragm constraints.

(2) Shell elements without rigid diaphragm constraints: The element “ShellMITC4” in OpenSEES is used in those theme models to simulate the in-plane and out-of plane behavior of semi-rigid diaphragms. The “ShellMITC4” element is an isotropic, 4-node shell element including finite in-plane and out-of-plane stiffness based on Mindlin plate theory. There are 6 DOFs, three for translation and three for rotation, at each node. The stress resultants, such as membrane, bending and shear stress can be determined by integrating the stresses through the thickness. The ShellMITC4 element includes a bilinear isoparametric shape function in combination with modified shear shear-displacement matrices ( $\bar{B}_I^S$ ) to avoid “shear locking” (Love E., 2001) in the thin-plates. However, some limitations of the ShellMITC4 element for the simulation of semi-rigid diaphragms when the structures steps into the inelastic stages, need to be considered:

a. The nonlinear material properties could not be included in the analytical 3D models directly. In a 3D environment, OpenSEES provides few choices for the selections of 3D concrete nonlinearity simulation. One possible way is to use the “Concrete damage model”, which used

with 3D plate fiber sections. However, this material model has not been released in several versions of OpenSEES (version 2.4.1, 2.4.2 and 2.4.6), even though it is listed in the OpenSEES Manual.

b. Low computational efficiency: The computational demand for the 3D analytical model with shell elements is high, especially for the nonlinear dynamic analysis (NDA). For the nonlinear analyses for the 3D model with elastic shell elements, each NDA needed at least 2000 CPU hours in the ARC High Performance Computers using over 20 processors (2.26 GHz Intel Nehalem processors). In other words, at least 100 hours (i.e. 2000 CPU hours/20 processors) is needed to complete one NDA.

Based on the above two reasons, the study selects the composite frames with amplification factors (*CF*) as the simulation approach for investigating the behavior of the structures with semi-rigid diaphragms.

### **3.7 Application of vertical loads and mass**

This section concentrates on the distribution of the vertical loads and mass on the 3D models for the nonlinear static and dynamic analysis. The gravity loads, including dead loads and live loads acted on the diaphragm, are lumped at the columns based on their own tributary area in the SCBFs and gravity frames. However, for the SMRFs, the corresponding vertical loads are distributed on the beams uniformly, using the load combination suggested by ATC-76 for non-linear analysis,  $1.05D+0.25L$  (i.e. D=Dead load; L=Live load). Figure 3-26 illustrates the tributary areas of gravity loads for the columns in gravity frames and SMRFs in C1.

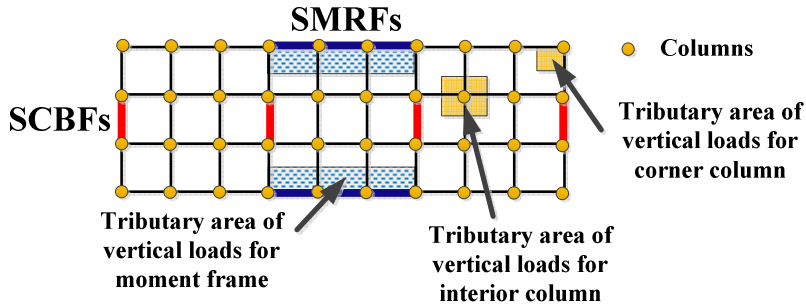


Figure 3-26 Tributary areas for gravity loads in columns and moment frames in C1

The structural mass computed from the seismic weight is taken as a lumped mass at each beam-column intersection point, with the loads initially distributed uniformly.

### 3.8 Consideration of effect of nonlinear geometry

All nonlinear analyses consider the effect of nonlinear geometry. For the brace elements, a co-rotational transformation in OpenSEES is imposed due to the expected large buckling deformations. For the other members, such as the columns and beams in the LFRS and gravity frames, the standard P-Delta transformation in OpenSEES is imposed in these members.

### 3.9 Period comparison between SAP2000 and OpenSEES

To verify the consistency of the analytical models, this section shows the comparison of structural periods of the different structural configurations simulated in SAP2000 and OpenSEES. Comparisons of the first five periods for the models built in SAP2000 and OpenSEES are listed in Table 3-9 to Table 3-10. One can observe that the structures with composite action and rigid diaphragm constraints ( $CF+R$ ) lead to the lower periods. This indicates that the effect of composite action slightly increases the lateral stiffness of the entire structures. For the structures without rigid diaphragm constraint ( $CF$ ), the periods increase slightly when compared with those

in **CF+R** models. The fifth mode in the **CF** structures in both configurations is a torsional mode, which is different from those in **BF+R** and **CF+R**.

Table 3-9 Period comparison between SAP2000 and OpenSEES (C1)

C1	SAP2000 (BF+R)	OpenSEES (BF+R)	OpenSEES (CF+R)	OpenSEES (CF)	Direction	Type
1	1.72	1.73	1.63	1.63	X	T <sup>(1)</sup>
2	0.61	0.58	0.57	0.62	Y	T
3	0.58	0.57	0.54	0.56	Z	R <sup>(2)</sup>
4	0.56	0.52	0.52	0.55	Y	T
5	0.27	0.26	0.25	0.33 <sup>(3)</sup>	X	T

Table 3-10 Period comparison between SAP2000 and OpenSEES (C2)

C2	SAP2000 (BF+R)	OpenSEES (BF+R)	OpenSEES (CF+R)	OpenSEES (CF)	Direction	Type
1	1.72	1.73	1.62	1.64	X	T
2	0.65	0.61	0.60	0.71	Z	R
3	0.53	0.56	0.53	0.55	X	T
4	0.51	0.48	0.47	0.50	Y	T
5	0.24	0.25	0.24	0.42 <sup>(3)</sup>	X	T

Unit: sec

Note: <sup>(1)</sup> T: Transverse mode (X or Y-dir); <sup>(2)</sup> R: Torsional mode (Z-dir); <sup>(3)</sup> Torsional modes (Z-dir) for CF structures only.

### 3.10 Nonlinear static (Pushover) analyses

Nonlinear static (pushover) analyses are used for evaluating the monotonic nonlinear behavior of structures. In a pushover analysis, the lateral loads are the product of a constant force load pattern vector and a scalar load factor. The magnitude of load pattern increases gradually until the monitored roof drifts reaches a target displacement. This results in a capacity curve for the structure that allows the behavior of structural component to be investigated at various

magnitudes of lateral displacement. The modification of lateral load patterns due to accidental torsion will be discussed in Chapter 5.

### 3.10.1 Lateral load pattern in rigid diaphragm structures

For the structures with a rigid diaphragm assumption (i.e. **BF+R** and **CF+R**), the corresponding pushover load pattern is a set of concentrated forces applied at the master nodes of the diaphragms. In this study, the position of master joint is same as the one of center of mass (C.M.) shown in Figure 3-27. The vertical distribution of pushover load patterns across the height of rigid diaphragm structures are based on the following formula specified in FEMA-356 (2000).

$$F_x = \frac{W_x h_x^k}{\sum W_x h_x^k} V \quad \text{Equation 3-20}$$

where  $F_x$  is the force applied at  $x$ -level;  $W_x$  is the story weight at  $x$ -level;  $h_x$  is the story height;  $k$  is the coefficient related to the structural period.

The above equation indicates that the pushover load pattern across the height of building is an inverted triangular shape if  $k$  is one.

### 3.10.2 Lateral load pattern in semi-rigid diaphragm structures

For the structures with semi-rigid diaphragms (i.e. **CF**), there is no master joint. Thus, the horizontal distribution of pushover loads should be based on the distribution of the diaphragm mass as per Sabelli et al (2011). In this study, the shape of all diaphragms is rectangular, and thus the horizontal distribution of pushover loads is uniform. Figure 3-27 shows the application of pushover load patterns for rigid and semi-rigid diaphragm structures. For the pushover load patterns considering the effect of accidental torsion due to the eccentricity of mass, a modified

load patterns shall be applied in the pushover analyses. The corresponding modification approach will be discussed in Chapter 5.

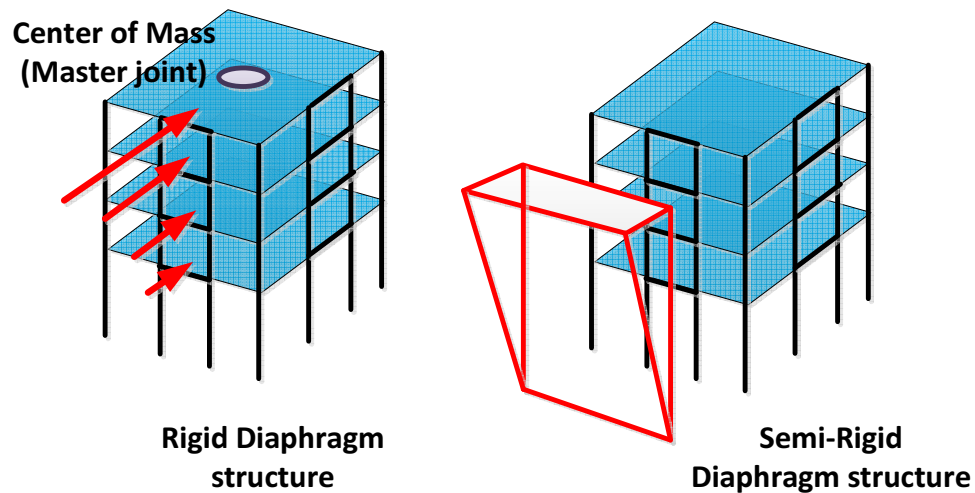


Figure 3-27 Pushover load patterns for rigid and semi-rigid structures

### 3.11 Nonlinear dynamic analyses

Nonlinear Dynamic Analyses (NDA) is the other important approach to evaluate the difference in structural behavior for the structures with different in-plane diaphragm stiffness. On the basis of the analytical requirements of NDA in ASCE 7, seven ground motions are used for evaluating the dynamic behavior of structures. The original earthquake records provided by PEER (Pacific Earthquake Engineering Research Center, 2014) will be used in the analytical models in OpenSEES. Parallel computation is used in these NDA improve the computational efficiency.

#### 3.11.1 Direct integration analysis

The Newmark method is chosen as the direct integration method for NDA. In the method, the variation of displacement and velocity based on time-stepping can be defined as the following equations (Chopra A.K., 2007):

$$\dot{u}_{i+1} = \dot{u}_i + [(1-\gamma)\Delta t]\ddot{u}_i + (\gamma\Delta t)\ddot{u}_{i+1} \quad \text{Equation 3-21}$$

$$u_{i+1} = u_i + (\Delta t)\dot{u}_i + [(0.5-\beta)(\Delta t)^2]\ddot{u}_i + [\beta(\Delta t)^2]\ddot{u}_{i+1} \quad \text{Equation 3-22}$$

In the above equations, the parameters  $\gamma$  and  $\beta$  are used to define the variation of acceleration between two time steps. Those parameters can be also used for determining the stability and accuracy of the method. For all the NDA cases in the study, the assumption of average acceleration (i.e.  $\gamma=1/2$ ;  $\beta=1/4$ ) over a time step are applied for determining the dynamic behavior of the structures. This assumption can provide numerical stability for any  $\Delta t$ .

### 3.11.2 Damping ratios

A classical damping matrix is used in NDA for all configurations. Rayleigh proportional damping,  $\mathbf{c}$ , is applied in the study to construct the classical damping matrix. It is recognized that this may not be the best approach, but it was used here for its simplicity and common use. The damping matrix is specified as a combination of stiffness and mass proportional damping matrices (Charney F.A., 2008; Chopra A.K., 2007). The tangent stiffness matrix,  $\mathbf{k}$ , at *current state* determination is used to build the damping matrix. The definition of damping matrix and damping ratio can be expressed as follows,

$$\mathbf{c} = a_0 \mathbf{m} + a_1 \mathbf{k} \quad \text{Equation 3-23}$$

$$\zeta_n = \frac{a_0}{2} \frac{1}{\omega_n} + \frac{a_1}{2} \omega_n \quad \text{Equation 3-24}$$

where  $\mathbf{c}$  is the damping matrix of the structure.  $\mathbf{m}$  and  $\mathbf{k}$  is the known mass and tangent stiffness matrix (*at current state*) of the structure.  $a_0$  and  $a_1$  is the constants to construct the damping matrix.  $\zeta_n$  and  $\omega_n$  is the damping ratio and structural frequency corresponding to the *n-th* mode.

In order to prevent very high damping ratios in the higher modes, which lead to the underestimation of higher mode effects on the response, the second period used in computing the Rayleigh damping matrix shall be small. Based on the recommendation provided by Charney (2008), the full ( $\omega_1$ ) or reduced 1<sup>st</sup> mode frequency ( $0.707\omega_1$ ) and  $T=0.2$  sec (31.41 rad/sec), can be the 1<sup>st</sup> and 2<sup>nd</sup> mode for determining the Rayleigh damping matrix, respectively. Erduran (2012) suggested that the reduced 1<sup>st</sup> mode frequency ( $\omega_r=0.707\omega_1$ ) and  $T=0.2$  sec ( $\omega_j=31.41$  rad/sec) seems to be the best option for composing the damping matrix for midrise steel structures. This frequency combination (i.e.,  $\omega_r=0.707\omega_1$ ,  $\omega_j=31.41$  rad/sec) is used in this study for composing the Rayleigh damping matrix.

### **3.11.3 Selection and scaling of Ground Motions**

Seven ground motions are applied in the NDA for evaluating the nonlinear dynamic behavior of each structure according to the requirements of ASCE 7. Seven ground motion records from historical California earthquakes (Pacific Earthquake Engineering Research Center, 2014) have been used for the NDA. The modification records are presented in Table A-21. The selection of ground motions is generally based on the magnitudes, fault distances, site conditions in accordance with the probabilistic seismic hazard deaggregation of the site.

For the ground motion scaling for the 3D models, the process based on ASCE 7 is to scale each square root of sum of squares (SRSS) of the spectra for each pair of horizontal components at the structural fundamental period, which matches 1.0 times the design spectrum. Therefore, the scale factor,  $FP_i$ , corresponding to each ground motion can be determined. Because the combined average SRSS spectrum shall not be lower than the design spectrum in the period range of  $0.2T_{small}$  to  $1.5T_{large}$ , the  $S$  factor shall be applied to match the point corresponding to the period

of  $0.2T_{small}$ . In this study,  $T_{large}$  and  $T_{small}$  are the periods corresponding to primarily transverse modes at X and Y-direction. Figure A-3 to Figure A-5 presents the various spectra of 3D ground motions scaling process. Table A-22 lists the scaling factors of each ground motions.

It is currently no consensus on how to appropriately scale and choose the ground motions for the evaluation of seismic performance of buildings using NDA. Although NEHRP (2011) has provided some guidance for scaling and selection the ground motions, the approach suggested by ASCE 7 was used herein for the selection and scaling of the ground motions.

### **3.12 Initial designs**

The preliminary designs of this study included four theme structures, labelled C1 to C4, with different (1) diaphragm span-to-depth ratios (i.e. 3.0 for C1 and C2 and 2.0 for C3 and C4), (2) in-plane diaphragm stiffness of diaphragm (i.e. rigid and semi-rigid) and (3) horizontal configurations of vertical braced frames (i.e. symmetric and asymmetric). For the final studies only redesigns of the C1 and C2 structures were used. Thus the influence of the diaphragm aspect ratio is not included. The initial structures were designed for lower dead loads and utilizing linear elastic diaphragms with the intent to maximize chord and collector forces. The performance of these structures was evaluated through both NSA and NDA similar to those in latter chapters of this thesis. The four theme structures are illustrated in Figure A-6.

In the initial designs, the seismic weights (dead loads) were taken as 4.31 pcf for the C1 and C2 structures and 4.22 pcf for the C3 and C4 structures, respectively. The seismic weights for the initial C1 and C2 structures are lower than those in the new design listed in Table 3-2. With regard to the live loads, they were taken as 50 psf for the 2F to 4F, and 26.13 psf for the RF, which are the same as listing in Table 3-2. The redundancy factor, 1.30, was used in the design

of the member sizes in both the SCBFs and SMRFs. Because these structures were not fully compliant with ASCE 7 design criteria, their performance will not be described in detail in the main body of the thesis.

For simulation of these theme structures with the assumption of rigid diaphragm in OpenSEES, the command “RigidDiaphragm” was used in the models to impose the in-plane rigid constraint at each floor level. No plate or shell elements were built into these analytical models. For the structures with semi-rigid diaphragms, however, the element “ShellMITC4” in OpenSEES was used in these models to simulate the elastic behavior of both the in-plane and out-of plane stiffness of diaphragm. The composite action was not considered in both the rigid and semi-rigid diaphragm structures in the initial designs.

The analytical results of the structures in the initial designs from NDA and NSA, which are summarized in Appendix D, result in similar conclusions as those given by the new thesis will be discussed in Chapter 4 to Chapter 7. Although the designs were not strictly code compliant, the initial C1 and C2 structures exhibited behavior very similar to the redesigned C1 and C2 ones. As the differences in behavior had been much larger between the initial C1 and C2 cases (aspect ratio at the ASCE 7 limit of 3) than for the initial C3 and C4 cases (aspect ratio of 2.0), only the C1 and C2 structures were redesigned. However, it is expected that the conclusions for initial C3 and C4 structures would have stood if those had also been redesigned.

## Chapter 4 The behavior of the steel structures considering the effects of semi-rigid diaphragms

### 4.1 Introduction

In conventional analytical procedures, the strength and ductility of a structure is determined by 2D analyses. This chapter investigates the monotonic behavior of two types of steel structures by conducting nonlinear static (pushover) analyses. The first type includes four story 2D (1) X-braced frame (SCBF), (2) chevron-braced frame (SCBF), and (3) moment frame (SMRF). The second type is the single-story 3D structure with SCBFs in one direction and SMRFs in the other. To distinguish the diaphragm effect on those frames, the (1) composite effects and (2) rigid diaphragm constraints are or are not included in the analytical models. The frame strength and stiffness under different diaphragm assumptions are investigated in this chapter. Section 4.2 presents the classification of the structures with different diaphragm assumptions. Section 4.3 to Section 4.6 discuss the pushover responses of X-braced frame, Chevron-braced frame, moment frame and single-story 3D frame, respectively. Section 4.7 provides the conclusions of these analytical results. An objective of this chapter is to develop a 2D benchmark for the 3D analysis to be discussed in latter chapters.

### 4.2 Classifications

For the 2D and 3D frames in this study, there are three different diaphragm types corresponding to different combinations of rigid constraints and composite effects:

1. The bare steel frame with rigid constraints (***BF+R***) where the rigid constraints imposed at the ends of beams prevent the development of axial deformations and corresponding internal force in the beams as shown in Figure 4-1(a).

2. Composite frame with rigid constraints (**CF+R**) where the composite properties of the beam effects are included in the frame but the rigid constraints are preserved as illustrated in Figure 4-1 (b).
3. Composite frame (**CF**) where the composite effects are included in the frame without rigid constraints, and axial forces and deformations are allowed to be developed in the beams, as shown in Figure 4-1 (c).

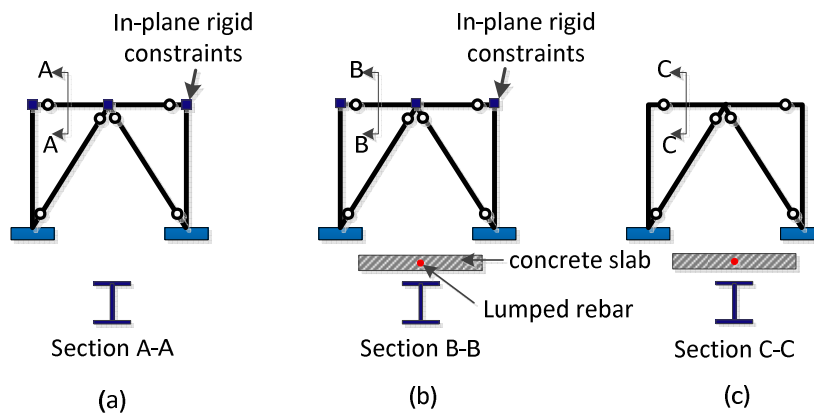


Figure 4-1 Different assumptions for diaphragm simulation: (a) **BF+R**, (b) **CF+R** and (c) **CF**

### 4.3 X-braced frame

This section focuses on the monotonic behavior of a 2D X-type braced frame with the vertical layout of bracing units and member dimensions similar to the braced frames in the C1 configuration listed in Table 3-5. There are four braced frames used to resist the lateral loads in the 3D analytical model in the considered direction (i.e. Y-dir). Therefore, the total gravity load applied on this 2D frame is 25% of the total gravity loads of the 3D model.

#### 4.3.1 Related simulation details

For the beams, columns and braces in this braced frame, the modeling is the same as those in the 3D model discussed in Section 3.5. However, to include the P-Delta effect in the 2D braced

frames appropriately, a leaning rigid column is connected to the braced frame by a co-rotational truss at each story level. Pin connections are imposed in the leaning column at each floor level. The gravity loads are applied on the leaning rigid columns at each floor level before conducting the pushover analyses. The effective width of the 2D X-type braced frame is selected as 82.5 inches, which assumes this 2D SCBF is an interior frame in the 3D model. Figure 4-2 shows the elevation layout of this X-braced frame.

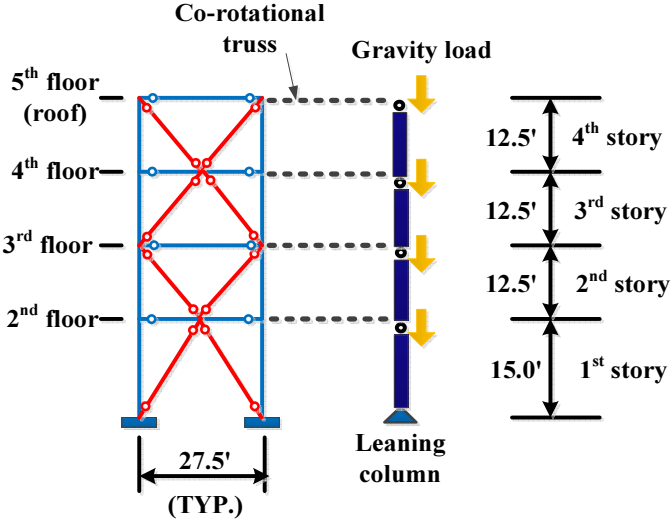


Figure 4-2 Elevation of X-braced frame

**4.3.2 Capacity curves**

Figure 4-3 (a) shows the capacity curves of **BF+R**, **CF+R** and **CF** for the frame in Figure 4-2. One can observe that the capacity curves among the three cases do not have a significant difference. This indicates the inclusion of composite effect and rigid constraints may not be sensitive with regard to the lateral stiffness and strength of the X-type braced frames in a 2D analysis. One of the possible reasons for this phenomenon is that the unbalanced forces generated by the buckling of the braces are transferred to the columns directly. Therefore, the in-plane and out-of plane stiffness of the beams do not play an important role in the transfer

mechanism of unbalanced force. Figure 4-3 (b) shows the deformed shape of the braced frame corresponding to 0.05 roof drift.

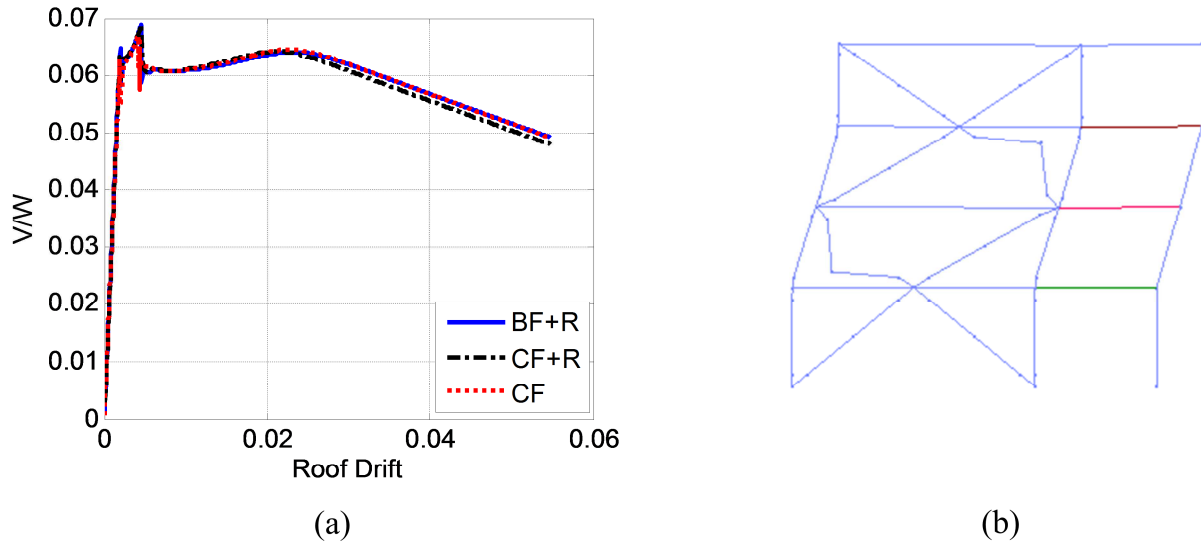


Figure 4-3 Analytical results for X-braced frame: (a) capacity curves and (b) deformed shape at 0.05 roof drift ratio

Figure 4-4 presents the capacity curves for the braced frame considering the fracture effect. The strength of the braced frame reduces significantly (i.e. over 50%) because of the fracture of the brace in the 3<sup>rd</sup> story at 0.032 roof drift. The story stiffness and strength of the 3<sup>rd</sup> story drops over 90% after the brace fractures. However, the overall behavior between **BF+R**, **CF+R** and **CF** is still similar.

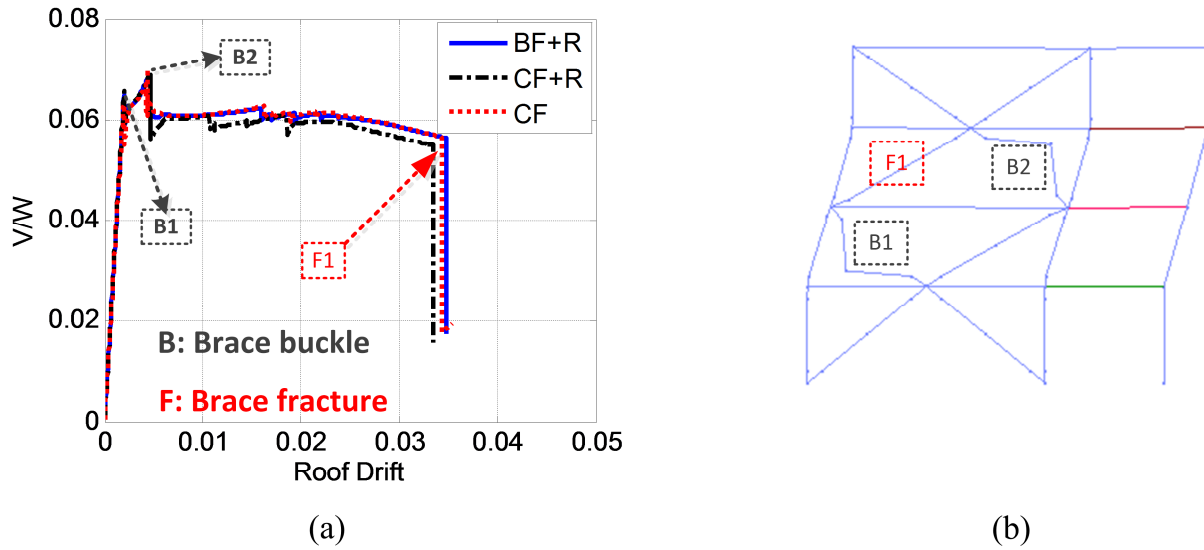


Figure 4-4 Analytical results including brace fracture: (a) capacity curves and (b) deformed shapes

### 4.3.3 P-Delta effect

The P-Delta effects for the X-type braced frame under different magnitudes of gravity loads are investigated in this section. Three magnitudes used to amplify the original gravity loads (1.0, 2.0 and 2.5) are considered in this section. These gravity loads are applied on the leaning column in **BF+R** and **CF+R** X-braced frames, respectively. The results are shown in shown in Figure 4-5. It is obvious that the change of magnitudes of gravity loads significantly affects the post-buckling strength of the braced frame. In the case of  $2.5 \times$  Gravity load, this load leads to the highest negative post buckling stiffness of the braced frame. However, the inclusion of composite action (i.e. **CF+R**) does not result in a significant change in terms of stiffness and strength when compared with those in the **BF+R** model when the magnitude of gravity loads increases.

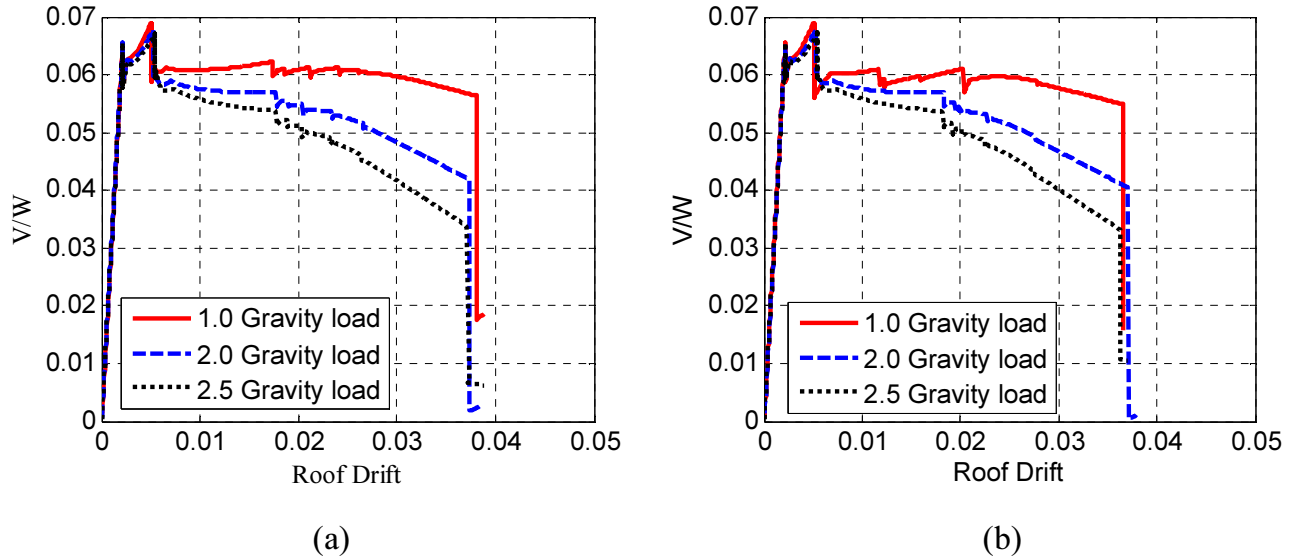


Figure 4-5 Capacity curves under different magnitudes of gravity loads: (a) **BF+R** and (b) **CF+R**

#### 4.4 Chevron-braced frame

To evaluate the effect of rigid diaphragm constraints and composite action in the braced frames with different elevation layouts, a 2D chevron-braced frame is modeled in this section. This braced frame is designed to replace the X-type braced frame in C1. In other words, the demand-to-capacity ratios (D/C) of the structural members, including braces, beam and columns in this frame also satisfy the requirements of the design of SCBFs in the 3D analytical models. The simulation approach and the magnitudes of gravity loads are the same as the one in X-braced frame. Table 4-1 lists the member dimensions of this frame. Figure 4-6 illustrates the elevation layout of this chevron braced frame.

Table 4-1 Member dimensions for chevron-braced frame

Story	Story Height (ft)	Braced frame		
		C1	B1	BR1
4 <sup>th</sup>	12.5	W12x120	W21x57	HSS5x5x3/8
3 <sup>rd</sup>	12.5	W12x120	W24x146	HSS5.5x5.5x3/8
2 <sup>nd</sup>	12.5	W12x120	W27x194	HSS6x6x3/8
1 <sup>st</sup>	15.0	W12x120	W30x292	HSS7x7x1/2

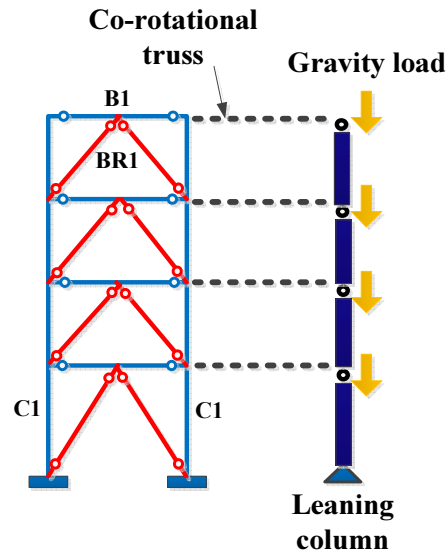


Figure 4-6 Elevation of the chevron braced frame

#### 4.4.1 Capacity curves

Figure 4-7 presents the capacity curves for the chevron-braced frames with the three different diaphragm assumptions. There are significant local differences in strengths among the three cases. The ultimate strength of *CF+R* is slightly higher than the other two cases. This indicates that the transfer mechanism of unbalanced force released from braces may be different from those in X-braced frame. The unbalanced forces released from braces have to transfer to the columns via beams in this layout. If the out-of plane and in-plane stiffness of the beams are increased by the rigid constraints or composite action, the frame can be strengthened slightly.

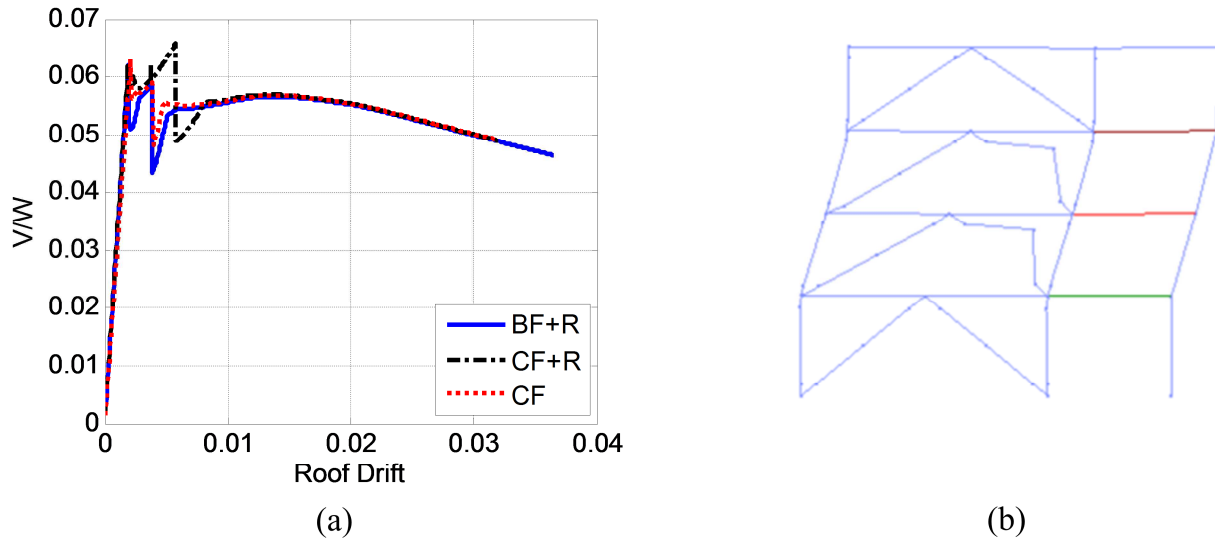


Figure 4-7 Analytical results of chevron braced frame: (a) capacity curves and (b) deformed shapes

#### 4.5 Moment frame

This section focuses on the evaluation of monotonic behavior for a 2D SMRF. The member dimensions in the 2D SMRF are the same as those in 3D model shown in Table 3-5. The distributed gravity loads applied on the beams are based on the distribution area of gravity loads for the beams only. The magnitudes of this gravity loads are the same as the one in 3D model. The 2D frames are taken from the LFRS at the X-direction in the 3D models (Figure 3-1(a) and (b)). For the gravity loads used to evaluate the P-Delta effect of the SMRF, half of total gravity load of the entire 3D structure (i.e.  $0.5 \times (1.05D + 0.25L)$ ) is applied on the leaning column. Figure 4-8 illustrates the elevation layout of the 2D SMRF.

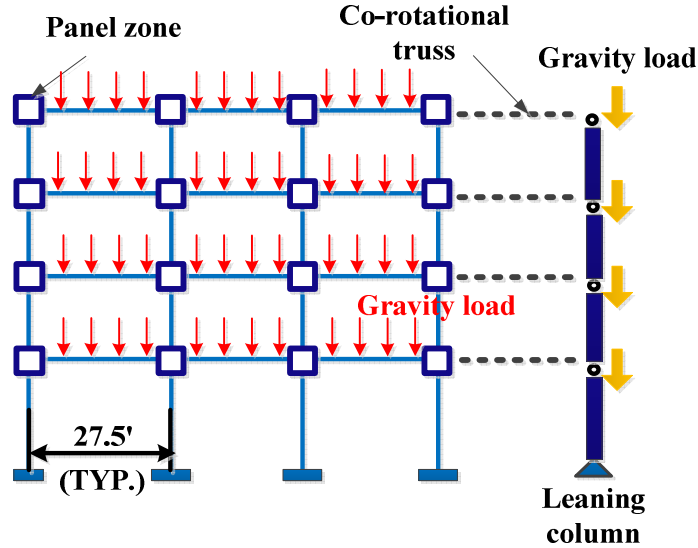


Figure 4-8 Elevation of 2D SMRF

#### 4.5.1 Capacity curves

Figure 4-9 (a) shows the capacity curves of the 2D SMRF with and without composite action and in-plane rigid constraints. The ultimate strength in **CF+R** structure is higher than the other two cases, and the ultimate strength in **BF+R** structure is the lowest one. The design base shear based on ASCE 7 for the single SMRF is  $0.042V/W$  (Subsection 3.4.3). Therefore, the overstrength factors of these three structures are:  $\Omega_{CF+R} = 2.27$ ,  $\Omega_{CF} = 2.19$ , and  $\Omega_{BF+R} = 2.02$ , respectively. The difference in the overstrength factor between **CF+R** and **BF+R** is 12.3%, and the difference between **CF+R** and **CF** is 3.6%. In addition, the elastic stiffness of the **CF+R** is the highest one also, which is slightly higher than those of **CF** structure but also significantly higher than those of **BF+R**. The phenomenon indicates that the inclusion of composite action in the SMRF is more significant than those in SCBF.

Figure 4-9 (c) illustrates the curvature variations of the target beam in the 2F. The left and right points on the target beam are shown in Figure 4-9 (b). The composite action on the left side of beam, corresponding to the positive moment, leads to stronger and stiffer behaviors as compared

to the right side with negative moment. Based on the known yield strength of the reduced beam section (i.e.  $M_y=1140$  kips-ft, Figure 4-9(c)) at the 2F, the ratios of composite action at the left and right sides are 1.62 (i.e.  $M_{comp,left}/M_y$ ) and 1.23 (i.e.  $M_{comp,right}/M_y$ ) in this target beam, respectively. Figure 4-9 (d) shows the force-displacement relationships of the panel zone spring in the Joint A at the 2F. One can observe that the spring yields complying with a significant spring inelastic rotation.

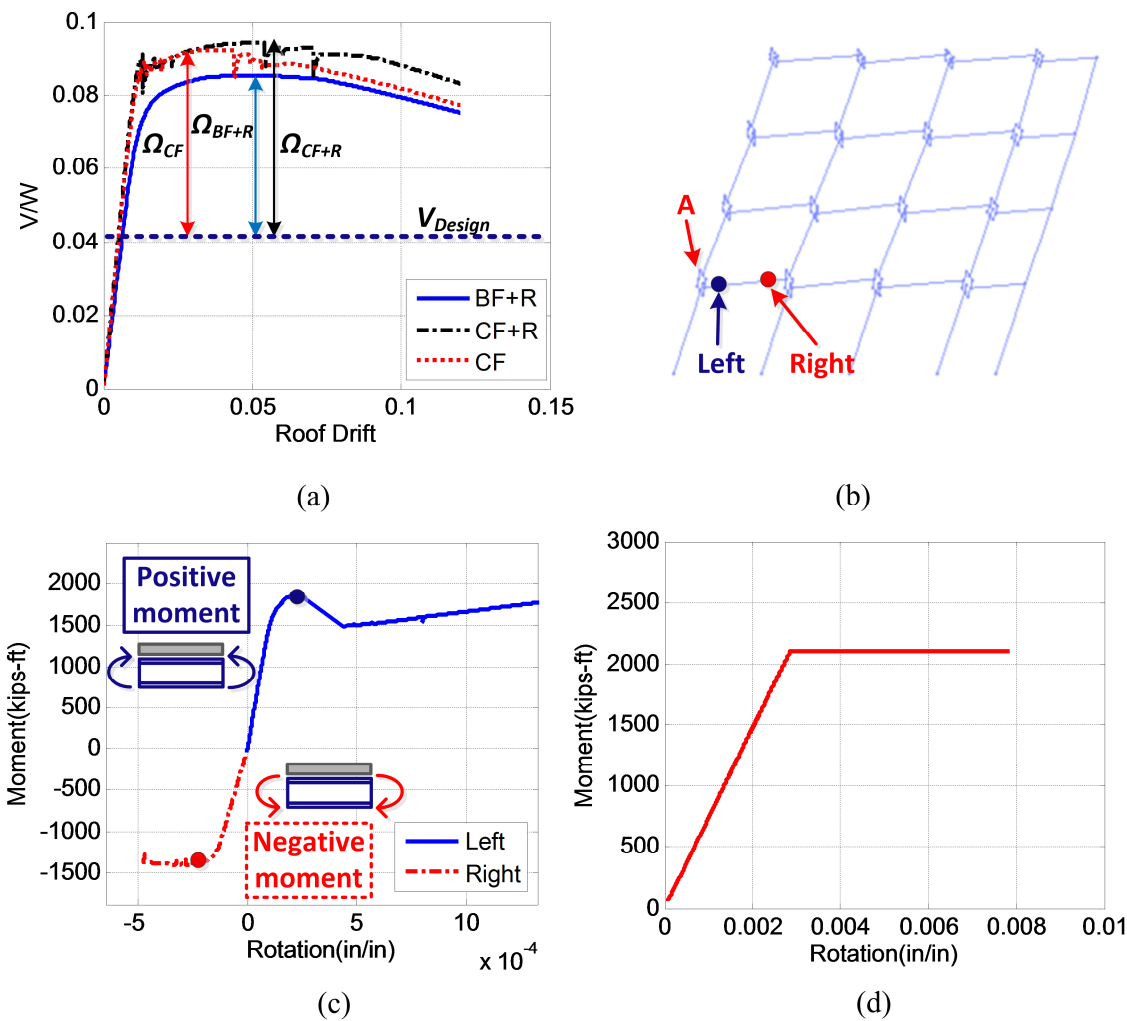


Figure 4-9 Analytical results for 2D SMRF: (a) capacity curves ,(b) deformed shapes ,(c) curvature for the left point and right point of the target beam in the 2F and (d) force-displacement relationship of the panelzone in Joint A

## 4.6 Single-story 3D structure

A 3D, one-bay, one-span and one-story structure is investigated in this section. In addition to the three cases corresponding to *BF+R*, *CF+R* and *CF* as mentioned in Section 4.2, an elastic diaphragm including the composite and orthotropic behavior are selected as the fourth case for the comparison of the pushover analyses. For this one-story 3D frame, the pushover load pattern is applied at the Y-direction and the two braced frames provide the primary lateral resistance against seismic loads. The monitor point for the pushover analyses is located in the middle of diaphragm. Figure 4-10 shows the layout of the 3D model.

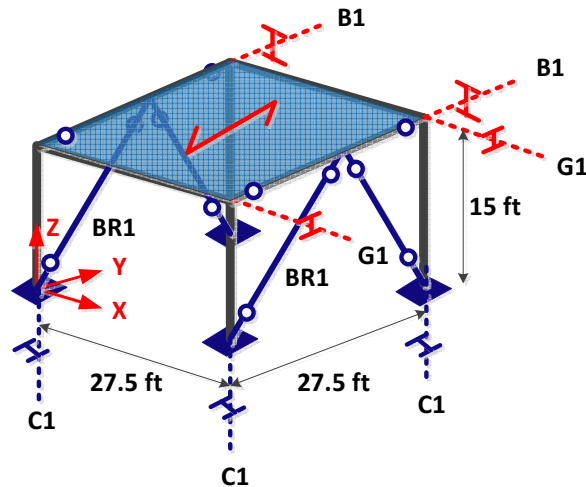


Figure 4-10 One-story 3D frame

### 4.6.1 Description of the structure

In this simple 3D analytical model, the moment frames are located in the X-direction, and the braced frame in the Y-direction. The span at each direction is 27.5 ft, and the story height is 15 ft. The member sizes of this model are based on the 2-story braced frame archetypes in ATC-76 (2010) with some modifications. The dimensions are listed in Table 4-2. The orientations of these members are shown in Figure 4-10. Corrugated composite slabs are used as the slab system

in this model. The ribs of the slab are along the Y-direction, and the dimension of the composite slab is the same as those shown in Figure 3-6.

Table 4-2 Member dimensions for one-story 3D frame

Story	Story Height (ft)	C1	B1	G1	BR1
1 <sup>st</sup>	15.0	W14x61	W18x46	W24x76	HSS6x6x3/8

The simulation approach of the structural members in this model, such as beams, columns, braces, and composite action are the same as the approaches for the 3D modeling shown in Section 3.5. The gravity loads are taken as 7.9 pcf based on Table 3-2 and are applied at the intersections of beams and columns.

#### 4.6.2 Shell element simulation

The additional case in this section is the semi-rigid diaphragms simulated by shell elements. The “ShellMITC4” elements discussed in Subsection 3.6.2 are used in this model. The floor, which dimension is 27.5 ft by 27.5 ft, are divided into and modeled by 16 shell elements with the average thickness of slab, 4.5 inches. The concrete elastic modulus,  $E_c$ , is selected as 3122 ksi, which corresponds to the concrete ultimate compressive strength of 3.0 ksi. Figure 4-11 illustrates the layout of the slab simulation of this model.

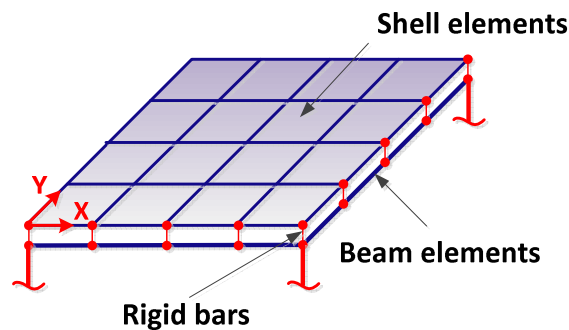


Figure 4-11 Plan layout for shell element simulation

To include the composite action in this model, the position along the Z-axis (i.e. out-of-plane direction) of shell elements shall be different from those of the beam elements. Rigid elements are used between the shell elements and beam elements to describe the composite action. The length of the rigid elements is selected as 16.1 inches, which is determined as the average height from the centroid of the steel beam to the centroid of the concrete slabs of the beams in X-direction (W24x76) and Y-direction (W18x46), respectively. Figure 4-12 shows the position of the centroids of beams and slabs. For the beams in Y-direction (W18x46), the distance between the two centroids in steel beam and concrete slab is 12.8 inches; for the beams in X-direction (W24x76), the distance is 19.5 inches.

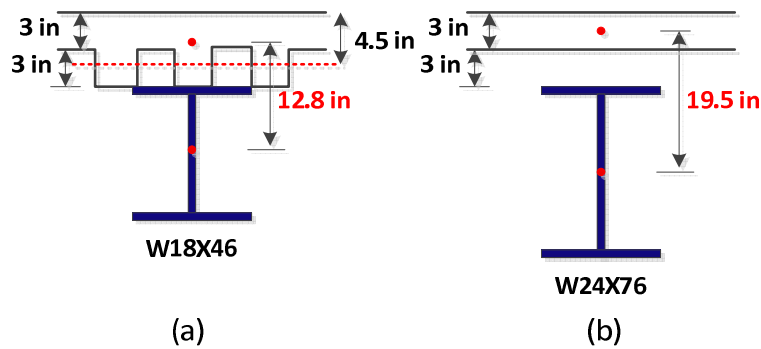


Figure 4-12 Distance between the centroids in slab and beam: (a) W18x46 and (b) W24x76

The orthotropic behavior of the corrugated behavior is considered in the slab material properties also. Saffaini H.S. (1992) provided the formulas to estimate the material properties ( $E_{x,c}$ ,  $E_{y,c}$ ,  $G_c$ ) of the concrete slab within rib as shown in Equations C-1 to C-3. Therefore, the material properties including the orthotropic behavior can be determined accordingly (Table 4-3).

Table 4-3 Material orthotropic properties for corrugated slab

<b><math>E_c</math></b>	3122	ksi	<b><math>\mu_c</math></b>	0.200
<b><math>E_{x,c}</math></b>	3184	ksi	<b><math>\mu_{x,c}</math></b>	0.136
<b><math>E_{y,c}</math></b>	4683	ksi	<b><math>\mu_{y,c}</math></b>	0.200
<b><math>G_c</math></b>	1631	ksi		

### 4.6.3 Capacity curves

The comparison of capacity curves among the four cases in 3D model is shown in Figure 4-13. It is obvious that the ultimate strength and the post buckling strength of the structure with elastic-orthotropic shell elements are significantly higher 20% than those of the other three cases. The ultimate strengths of the structures without shell elements (i.e. **CF+R**, **CF** and **BF+R**) are similar to each other. The structure with composite action and rigid diaphragm constraints (**CF+R**) displays a higher post-buckling strength. In addition, the structure without composite action (**BF+R**) has the lowest post-buckling strength. The biggest overall behavior difference is that the structure with elastic shell elements shows a very large and stable recovery of strength after buckling. At the roof drift of 15 inches, the strength of the structure with shell elements is almost double that of the other three structures. While it is unlikely that elastic behavior could be maintain for such large drift, it is nevertheless important to recognize that some of this strengthening effect will be present at low roof displacement (say, less than 5 inches). For example, tests by Leon (1998) show that this composite action is maintained slab up to chord rotation of 0.04 or 7.2 inches in this case. In the future, it will be important to verify this conclusion by full scale experimental tests.

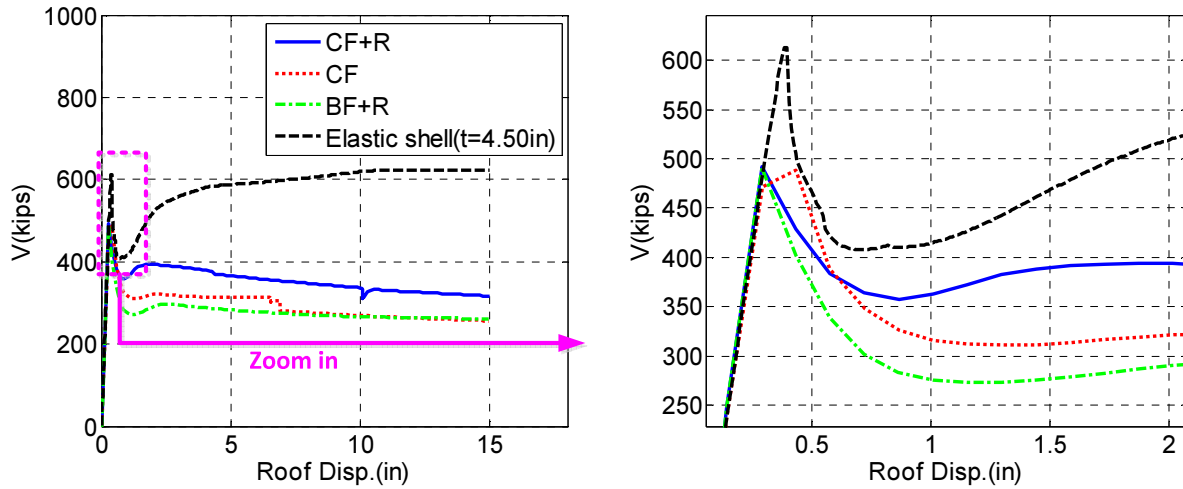


Figure 4-13 Comparison of capacity curves in the 3D models

To investigate this phenomenon, the variations of brace axial forces in the four structures are shown in Figure 4-14. One can observe that the compressive brace axial force in the model with *elastic shell elements* is the highest one. The peak axial force corresponding to the buckling of the brace are 205 kips (Elastic shell model), 180 kips (**CF+R**), 179 kips (**BF+R**) and 166 kips (**CF**), respectively. The difference in the magnitude of the buckling load is related to the different effect of initial imperfection as shown in Figure 4-15. For the structures without elastic shell elements, the vertical displacement at the middle point of the beam does not perform a significant change before the occurrence of brace buckling as shown in Figure 4-15 (b).

However, for the structure with elastic shell elements, the middle vertical displacement of beam moves upward when the structure is still in the elastic range. Such movement leads to the reduction of the imperfection of the brace (i.e. Imperfection 2) before the occurrence of buckling, as illustrated in Figure 4-15 (c). Therefore, the buckling strength of the brace increases significantly if vertical deformation is permitted.

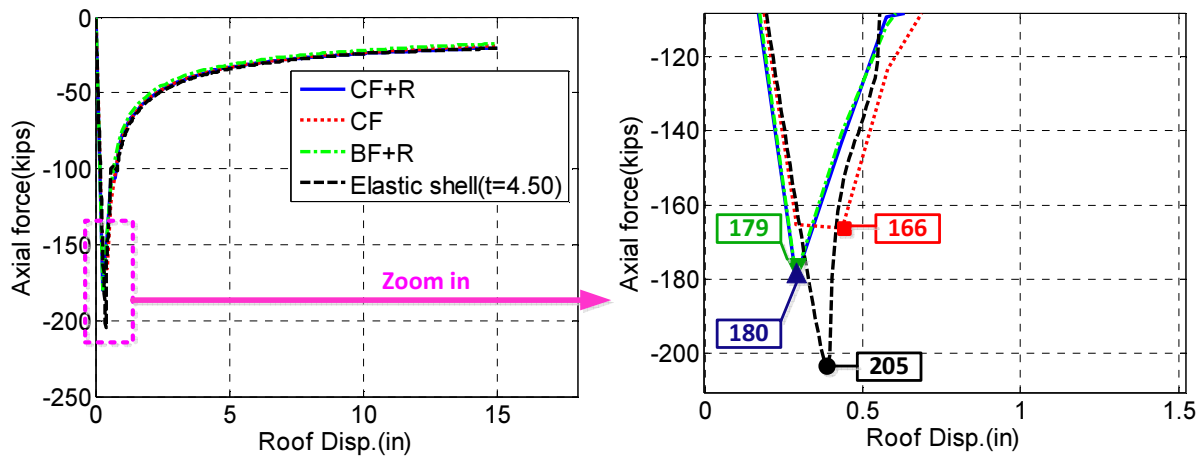


Figure 4-14 Variation of compression axial forces in braces

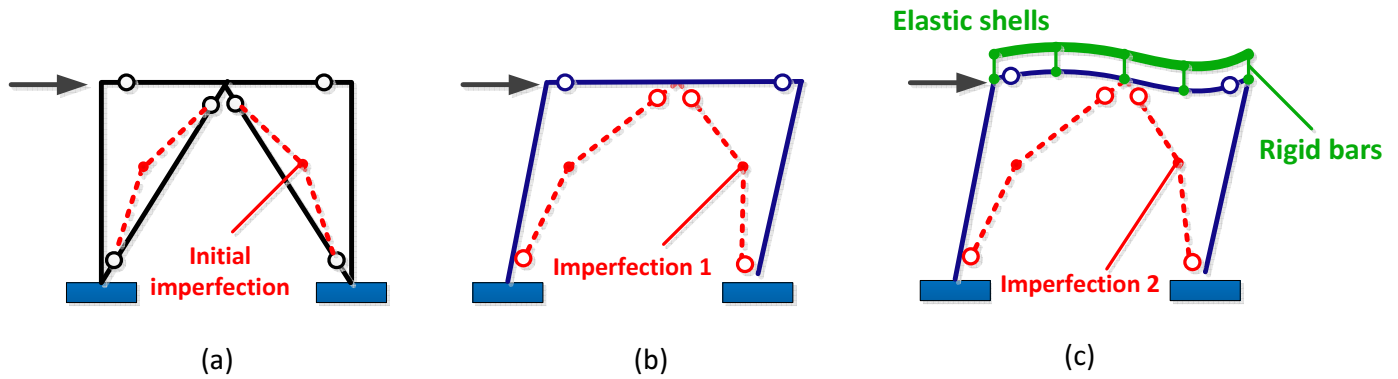


Figure 4-15 Variation of imperfection of braces: (a) initial status, (b) imperfection for the structures without elastic shell elements and (c) imperfection for the structures with elastic shell elements

#### 4.6.4 Rotational deformation of the 3D structure

To investigate the rotational behavior of the 3D structure in NSA, the modified pushover load patterns, based on the magnitude of accidental torsion ( $M_{ta}$ ) was applied in this model. The magnitude of  $M_{ta}$  is generated by shifting the master joint by 5% of the diaphragm dimension (i.e.  $0.05L$ ). This can be equally generated by the application of an asymmetric load pattern (0.55 and 0.45) at the two corners (Points A and B) of diaphragm in NSA, as shown in Figure 4-16.

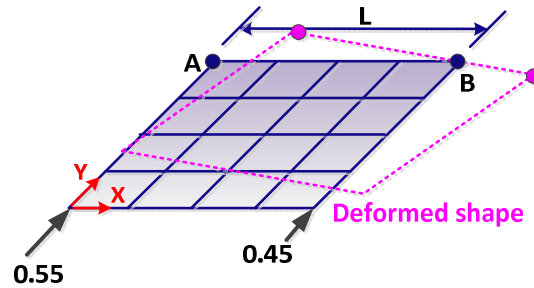


Figure 4-16 Modified load patterns for the 3D one-story structure

Figure 4-17 depicts (1) the capacity curves and (2) the variation of torsional coefficient ( $TC$ ) defined in ASCE 7 (Table 12.3-1) as the NSA progresses. In Figure 4-17 (a), one can observe that two distinct peaks are developed in the  $CF+R$ ,  $BF+R$  and Elastic shell models. The 1<sup>st</sup> and 2<sup>nd</sup> peaks indicate the 1<sup>st</sup> and 2<sup>nd</sup> occurrence of brace buckling. The model with elastic shells shows the highest pre-buckling strength as well as the post-buckling strength. The  $BF+R$  structure shows the lowest strengths corresponding to the two peaks when compare with the other three cases. The 2<sup>nd</sup> peak is not evident in the  $CF$  structure due to the higher magnitudes of diaphragm rotation.

In Figure 4-17 (b), the magnitudes of  $TC$  in the  $CF$  structure are the highest one because only one brace buckles. For the other three structures ( $BF+R$ ,  $CF+R$  and Elastic shell model), this magnitude ( $TC$ ) reduces significantly when the both braces buckle, which corresponds to the 2<sup>nd</sup> peaks in Figure 4-17 (b). This difference in behavior is related to the snap back of diaphragms that will be discussed in detail in Subsection 5.4.3 and Figure 5-21.

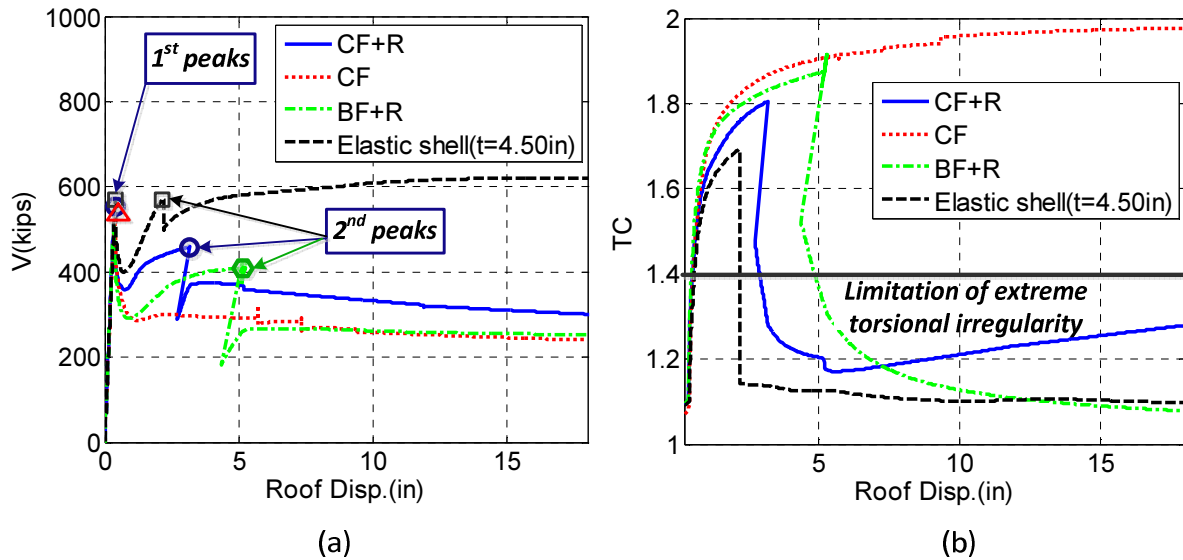


Figure 4-17 NSA response of one-story structure: (a) capacity curves and (b)  $TC$  history

#### 4.7 Conclusions

This chapter focused on the monotonic behavior of the 2D X-braced frame, Chevron-braced frame, moment frame and a one-story 3D frame by conducting pushover analyses. The following are the conclusions extracted from the nonlinear analyses in this chapter:

1. The chevron-braced frame shows a higher ultimate strength than that of the X-braced frame due to the composite action: The different unbalanced force transfer mechanisms at different elevations of the braced frame results in the different lateral stiffness and strength because of the composite action. The composite beams in the chevron-braced frame resist the unbalanced force before the forces are transferred in to columns. Therefore, the composite action affects the ultimate strength of braced frames locally.
2. The inclusion of composite action and in-plane rigid constraints results in a higher ultimate strength for the SMRFs: The results show that the ultimate strength of **CF+R** structure is higher than the strength of **BF+R** by 12.3%, and higher than **CF** by 3.6%.

This indicates both composite action and rigid diaphragm constraints are able to increase the strength of SMRFs, but the contribution to the strength from composite action is more significant than those provided by rigid constraints.

3. The performance of braces are significantly affected by the out-of-plane stiffness provided by the diaphragm system: A higher out-of-plane stiffness of the diaphragm, such as is the case for the elastic shell elements, leads to the smaller brace imperfection and results in higher brace buckling strengths.

The 3D model with elastic shell elements overestimates the ultimate strength and post-buckling strength: According to the analytical results in the one-story 3D model, both ultimate strength and post-buckling stiffness are higher than the other three cases (i.e. ***BF+R***, ***CF+R*** and ***CF***). This means such model may not be appropriate to evaluate the inelastic behavior of the 3D model with semi-rigid diaphragms. However, the results show that the structure is very sensitive to the modeling of diaphragm: the development of shell element capable of tracking the strength and stiffness degradation of diaphragm is needed.

## Chapter 5 The behavior of 3D steel structures with semi-rigid and rigid diaphragms with accidental torsions

### 5.1 Introduction

The chapter concentrates on the evaluation of inelastic behavior of the two theme structures with different in-plane diaphragm stiffness (i.e. semi-rigid and rigid diaphragms) and subjected to the effects of accidental torsion. Based on the requirement of ELF approach in ASCE 7-10 (12.8.4.2 and 12.8.4.3), the evaluation of the behavior of structural systems and components should consider the effect of both inherent torsion ( $M_t$ ) and accidental torsion ( $M_{ta}$ ) in the ELF method. The  $M_t$  is typically caused by the plan or mass irregularities of the structure, while the  $M_{ta}$  is used to account for the inevitable eccentricities in nominally regular structures. The  $M_{ta}$  is generated by shifting the position of C.M. by 5 percent of the dimension of the diaphragm perpendicular to the direction of considered seismic loads. The  $M_{ta}$  requirement is intended to account for the fact that the exact location of the center of rigidity is difficult to determine even in regular structures as it depends on many variables, including the loading and distributions of strength and stiffness in adjacent stories . By modifying the distribution of mass on the diaphragm, a technique described in the commentary to ASCE 7 (C12.8.4.2), the effect of  $M_{ta}$  on the structures with semi-rigid diaphragms can be evaluated under both NDA and NSA.

For nonlinear dynamic analysis, the effect of accidental torsion ( $M_{ta}$ ) should be included in the models in accordance with the upcoming ASCE 7-16 (2016) documents. This is a significant change from previous practice. However, ASCE-16 states that if the earthquake forces are applied in two orthogonal directions simultaneously, the required shift of the center of mass need not to be applied in both directions. A number of the advanced analyses in this study were

conducted with  $M_{ta}$  and bi-axial ground motion effects in order to study the effects of potential amplified torsional effects. The effects of diaphragm rigidity on parameters used in the ELF, such as the structural horizontal irregularity, inter-story drift ratios, are all discussed in this chapter. In addition, the contribution provided by each system (i.e. SCBFs, SMRFs, gravity systems) in each theme structure is also evaluated.

In this chapter, Section 5.2 introduces the notation used to represent the theme structures in the study. Section 5.3 includes an evaluation approach for including the effect of  $M_{ta}$  in the analytical models. Section 5.4 discusses the rotation and nonlinear behavior of the theme structures under NSA. Section 5.5 describes the analytical results of theme structures from NDA.

## 5.2 Classification and notation of the theme structures in nonlinear analyses

In the NSA and NDA studies, the theme structures are divided into several groups corresponding to different scopes in terms of design and analysis parameters. These include: (1) the two horizontal configurations of vertical LFRS, C1 and C2, with three different in-plane diaphragm stiffness shown in Figure 5-1, which are denoted by  $BF+R$  and  $CF+R$ , and  $CF$  as described in Section 4.2, and (2) different combinations of accidental torsion, which are denoted by  $M_{ta\_1}$  and  $M_{ta\_2}$ .  $M_{ta\_1}$  is used to represent the consideration of accidental eccentricity by shifting the location of center of mass by 5% of the diaphragm dimension perpendicular to the considered direction of earthquake forces (i.e. Y-dir.).  $M_{ta\_2}$  is used to represent the consideration of the bi-axial effects due to the application of ground motions in the two principal directions. More details with regard to  $M_{ta\_1}$  and  $M_{ta\_2}$  are discussed in Section 5.3.

Additionally,  $MF$  and  $BF$  are used to represent the LFRS for C1 and C2 in this study as follows:

- **MF1** and **MF2**: These represent the two special moment frames in each theme structures. The direction of MF1 and MF2 is perpendicular to the direction of the considered seismic loads (Y-dir), as shown in Figure 5-1.
- **BF1~BF4**: These represent the four SCBFs in prototype structures. The longitudinal direction of these SCBFs is all parallel to the direction of considered seismic loads (Y-dir), as shown in Figure 5-1.

The seven ground motions with magnitude scaling as shown in Table A-1 are used for NDA. Two different magnitudes corresponding to the DBE and  $MCE_R$  levels are considered in the analytical processes. In the study, “DBE” and “MCE” are used to represent the response extracted from design basis earthquake and maximum considered earthquake in the NDA, respectively.

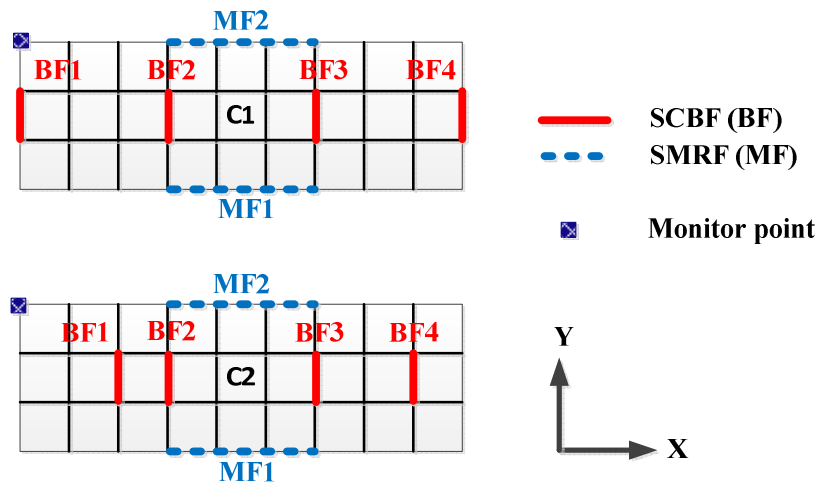


Figure 5-1 Position of monitor point for the SMRFs and SCBFs in each configuration

### 5.3 Nonlinear analyses for the structures with $M_{ta}$

Based on the approach suggested by ASCE 7 (C12.8.4.2 and C12.9.5), the dynamic characteristics of 3D model due to accidental torsion can be considered directly by modifying the horizontal distribution of diaphragm mass. This section describes a simplified approach used to

calculate the modified mass distribution that reflects the magnitude of  $M_{ta}$  in the nonlinear analyses. This modification of mass distribution generates the  $M_{ta}$ , which increases the clockwise rotation for all these structures as illustrated in Figure 5-2. For the analysis of semi-rigid diaphragm structures with  $M_{ta}$ , the distribution of mass has to be modified based on the magnitude of eccentricity between the old C.M. and the new C.M. so that the effect of  $M_{ta}$  can be included in the analyses automatically.

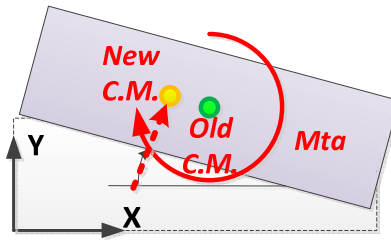


Figure 5-2 Application of  $M_{ta}$  for these structures (C1)

The following steps show the modification of mass distribution corresponding to the mass eccentricity in a specified diaphragm with an arbitrary shape. This approach assumes that the  $M_{ta}$  in both the semi-rigid and rigid diaphragms have the same magnitudes.

**Step 1- Define the position of the C.M. and the magnitude of  $M_{ta}$  for each rigid diaphragm:**

The derivation for a rigid diaphragm with an arbitrary shape (Figure 5-3) is based on shifting the position of the C.M. by a specified distance  $\beta L$  as shown in Figure 5-3:

$$M_{ta} = F\beta L \quad \text{Equation 5-1}$$

where  $M_{ta}$  is the accidental torsion,  $\beta$  is the ratio of C.M. eccentricity (0.05 based on ASCE 7),  $L$  is the dimension perpendicular of the direction of seismic loads, and  $F$  are the seismic loads applied on the diaphragm. The relationships between  $F$ ,  $\beta L$  and C.M.s are illustrated in Figure 5-3.

The position of the old C.M. can be evaluated by calculating the centroid of mass of the rigid diaphragm. The position of C.M. depends on the shape of the rigid diaphragm with the uniform thickness, which is the same as the position of the centroid of the diaphragm. The distributed seismic loads are then lumped at the new C.M. as a concentrated load ( $F$ ) as defined by Equation 5-2:

$$F = F_A \times A + F_B \times B \quad \text{Equation 5-2}$$

where  $F_A$  and  $F_B$  are the distributed seismic loads based on the proportional mass distribution and  $F$  is assumed as a concentrated load applied on the new C.M.

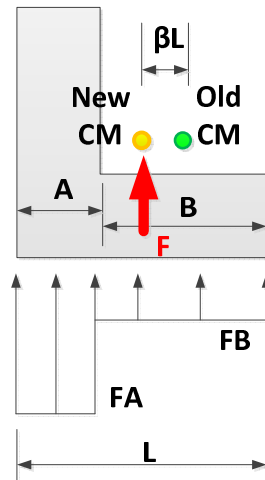


Figure 5-3 Diaphragm force on a rigid diaphragm

**Step 2 – Define  $M_{ta}$  for each semi-rigid diaphragm:** By assuming the same magnitude of  $M_{ta}$  between the structures with rigid and semi-rigid diaphragms, the corresponding diaphragm mass modification can be determined for the semi-rigid diaphragms. For the structures with semi-rigid diaphragms, the  $M_{ta}$  (Figure 5-3) can be generated by assuming two triangular distributed forces on the diaphragms (Figure 5-4). The two distributed forces generate a couple, creating a  $M_{ta}$  that causes rotation about C.M. of the semi-rigid diaphragm; the “old” C.M. is the same as the one in

the structure with rigid diaphragms. In this step, one assumes the peak magnitudes of the distributed seismic load are  $f_1$  and  $f_2$ , respectively as given by Equation 5-3.

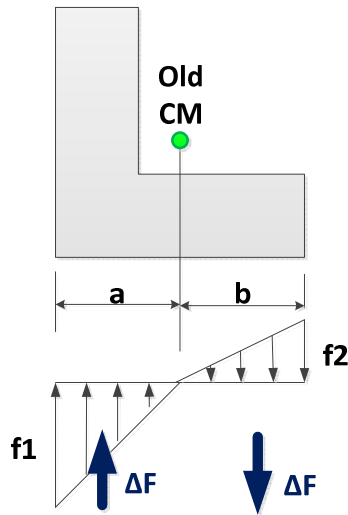


Figure 5-4  $M_{ia}$  on a semi-rigid diaphragm

$$M_{ia} = \frac{1}{2} f_1 \left( \frac{2}{3} L \right) a = \frac{1}{2} f_2 \left( \frac{2}{3} L \right) b \quad \text{Equation 5-3}$$

where  $a$  and  $b$  are the distances used to define the location of the old C.M., and  $f_1$  and  $f_2$  are the two peak magnitudes of the linear triangular distributed forces.

**Step 3 – Build the relationships between the structures with rigid and semi-rigid diaphragms:**

By combining Equation 5-2 and Equation 5-3 under the assumption of the same magnitude of  $M_{ia}$  in both the rigid and semi-rigid diaphragm structures, one can build the relationship between  $M_{ia}$  and the distributed force as shown in Equation 5-4:

$$F\beta L = f_1 \left( \frac{L}{3} \right) a = f_2 \left( \frac{L}{3} \right) b \quad \text{Equation 5-4}$$

Therefore, based on Equation 5-4,  $f_1$  and  $f_2$  can be re-expressed as follows:

$$f_1 = 3F\beta/a \quad \text{Equation 5-5}$$

$$f_2 = 3F\beta/b \quad \text{Equation 5-6}$$

Both Equation 5-5 and Equation 5-6 indicate that the magnitude of  $M_{ta}$  is affected by the seismic loads, the eccentricity ratios of the C.Ms and the shape of diaphragm.

**Step 4 – Modify the mass distribution on a diaphragm:** For including the effect of  $M_{ta}$  in the analytical procedures automatically, the relationship between total diaphragm mass,  $M$ , and the linear triangular couple distributed forces,  $f_1$  and  $f_2$ , has to be developed. One can use Equation 5-7 to bridge the two items.

$$F = MA \quad \text{Equation 5-7}$$

where  $M$  is the total mass of the specified diaphragm and  $A$  is the horizontal acceleration of the diaphragm generated by ground motions. By combining Equation 5-5 and Equation 5-7, the relationship between the couple distributed forces and diaphragm mass can be re-defined as follows:

$$f_1 = (3M\beta/a)A \quad \text{Equation 5-8}$$

$$f_2 = (3M\beta/b)A \quad \text{Equation 5-9}$$

Form Equation 5-8 and Equation 5-9, one can observe that the force distribution can be expressed by the combination of the mass distribution as well as the horizontal acceleration on diaphragms. Therefore, by modifying the mass distribution of the diaphragm, the effect of  $M_{ta}$  can be automatically accounted in the NDA. Figure 5-5 illustrates the distribution of diaphragm mass before and after considering the effect of  $M_{ta}$ . Subsection 5.3.1 shows the application of Step 1 to Step 4 for the theme structures.

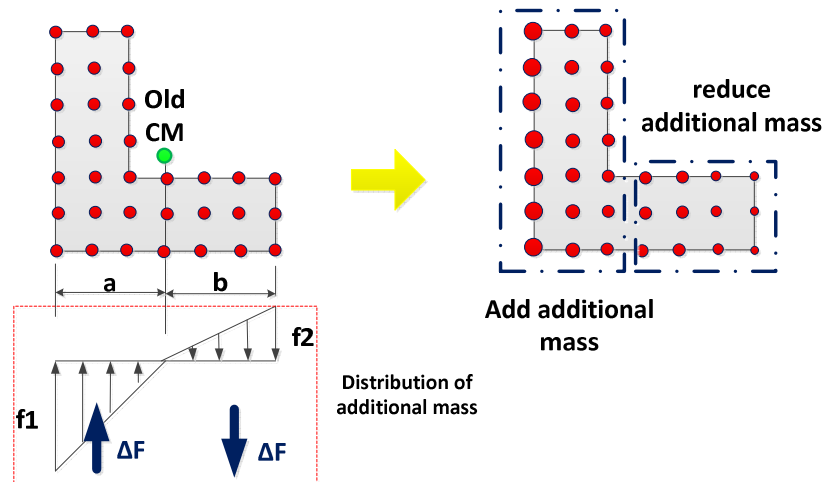


Figure 5-5 Re-distribution of diaphragm mass for  $M_{ta}$

### 5.3.1 Modification of diaphragm mass distribution for these structures

Based on Equation 5-8 and Equation 5-9, the redistribution of mass depends on the diaphragm mass ( $M$ ), eccentricity ratio ( $\beta$ ), and the position of C.M. ( $a$  and  $b$ ) can be determined. In the study,  $\beta$  is kept at 0.05 in all configurations. The parameters for each diaphragm in the two configurations are listed in Table 5-1.

Table 5-1 Mass modification parameters of each diaphragm for C1 and C2

Types of Configuration	$W$ (kips)	$M=W/g$ (k-s <sup>2</sup> /in)	$\beta$	$a$ (ft)	$b$ (ft)	$3M\beta/a$
C1/C2	2113	5.49	0.05	123.8	123.8	0.00662

Note:  $g = \text{gravity acceleration} = 386.4 \text{ in/sec}^2$

In order to implement the effect of  $M_{ta}$ , the total diaphragm mass,  $M$ , can be lumped separately at the column points as a series of discrete lumped masses. For the C1 and C2 groups, there are 40 column points in each diaphragm (Figure 5-6).

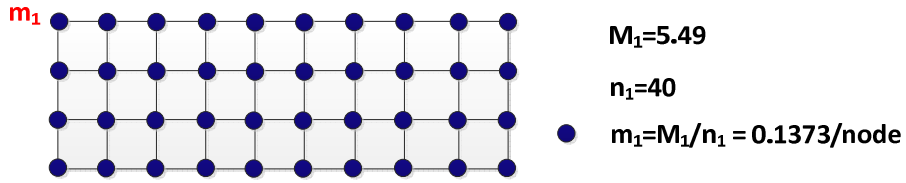


Figure 5-6 Lumped mass model of theme structures (C1 and C2)

Figure 5-7 shows the distribution of the additional masses for the C1 and C2 configuration in accordance with Table 5-1. From Figure 5-7, one can observe that the direction of the mass distribution indicates that  $M_{ta}$  is applied clockwise. Therefore, the original discrete lumped mass system on the left side of the diaphragm is added to the additional mass, while on the right side the original mass is subtracted.

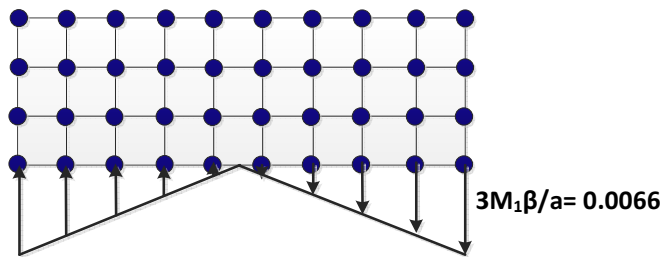


Figure 5-7 Additional lateral force distribution based on  $M_{ta}$

The next step is to combine the original lumped mass with the additional masses at each column point to generate a new distribution of lumped masses. Figure 5-8 illustrates the discrete models for considering the  $M_{ta}$  in the analytical procedures of the C1 and C2 structures.

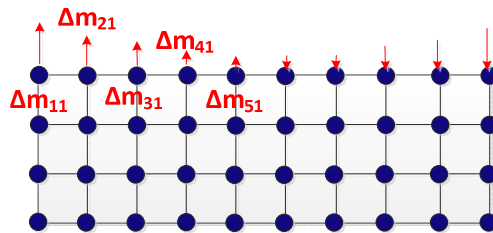


Figure 5-8 Application of additional lumped mass based on the effect of  $M_{ta}$

Taking C1 as an example, for column 21, the distribution of additional mass can be calculated as follows:

$$CI: \Delta m_{21} = (0.004 + 0.003) \times (27.5) \times (1/2) / 4 = 0.02410 \text{ kips-sec}^2/\text{in}$$

After modifying the diaphragm masses for considering the effect of  $M_{ta}$ , the new analytical models will be used in the NDA discussed in Section 5.5. In addition, the modified pushover load patterns considering the effect of  $M_{ta}$  will be determined based on the modified distributed mass system.

#### 5.4 Nonlinear static (Pushover) analyses (NSA)

According to both FEMA 750 (2009) and ASCE 7-10 (2010), NSA are not one of the permitted analysis procedures (Table 12.6.1). However, some of the other analysis approaches allowed in these provisions, such as the ELF, Modal Response Spectrum Analysis (MRA) and Linear Response History Analysis (LRHA) methods, cannot capture all relevant features of the inelastic behavior of structures. In particular, the NSA can be used to determine if the sequence of hinge formation and the overall structural performance reflect the desired performance in terms of  $R$ ,  $C_d$  and  $\Omega_0$  as mentioned in ATC-76. (2010). In this section, NSA will be used to gain insight into the general performance of the theme structures including the effect of accidental torsions.

##### 5.4.1 Pushover load patterns for the structures with $M_{ta_1}$ and $M_{ta_2}$

For the nonlinear static analyses (NSA) of the structures with rigid diaphragms (**CF+R** and **BF+R**), a set of concentrated lateral loads are applied to the master joints of the rigid diaphragms (i.e. center of mass) along the major axis (+Y-dir) as discussed in Subsections 3.10.1 and 3.10.2. A shift of the position of the master joints (i.e. C.Ms) on each diaphragm by a specified distance is used to include the effect of  $M_{ta_1}$ . According to the ELF methodology in ASCE 7 (Section 12.8.4.2), the earthquake forces shall be applied in the direction that produces the greater effect.

Therefore, the position of master joints is shifted to the left of the original C.M. by 5 percent of the diaphragm dimension,  $L$ , as illustrated in Figure 5-9.

For considering the effects of  $M_{ta_2}$ , the bi-axial effect is generated by applying the two seismic load patterns along the two principal axes of the structure simultaneously. The magnitude of seismic loads along the minor axis (-X-dir) is 30% of the considered seismic loads along the major axis (+Y-dir) applied at the new C.M. In this scenario, the design provision (ELF) indicate that the 5% eccentricities does not need to be applied in both of the directions (12.8.4.2) simultaneously as illustrated in Figure 5-10.

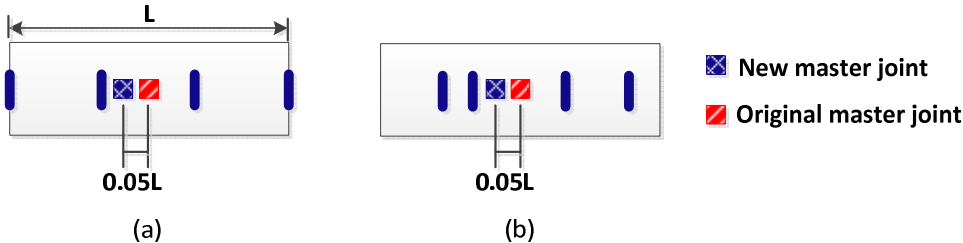


Figure 5-9 Movement of master joints for rigid diaphragm structure: (a) C1 and (b) C2

For the structures with semi-rigid diaphragms, the pushover loads at along the major axis must be applied as discussed in Subsection 3.10.2 with the modification of the diaphragm mass based on the magnitude of eccentricities for including the effect of  $M_{ta_1}$ . For the inclusion of  $M_{ta_2}$ , 30% of the major axis pushover loads is applied simultaneously along the minor axis (-X-dir) as the orthogonal load. Figure 5-10 illustrates the adjusted pushover load patterns for the semi-rigid diaphragm structures with  $M_{ta_1}$  and  $M_{ta_2}$ . Table 5-2 to Table 5-3 show the pushover loads applied to the different column lines ( $CLi$ ) for including  $M_{ta_1}$  or  $M_{ta_2}$  in the rigid or semi-rigid diaphragm structures.

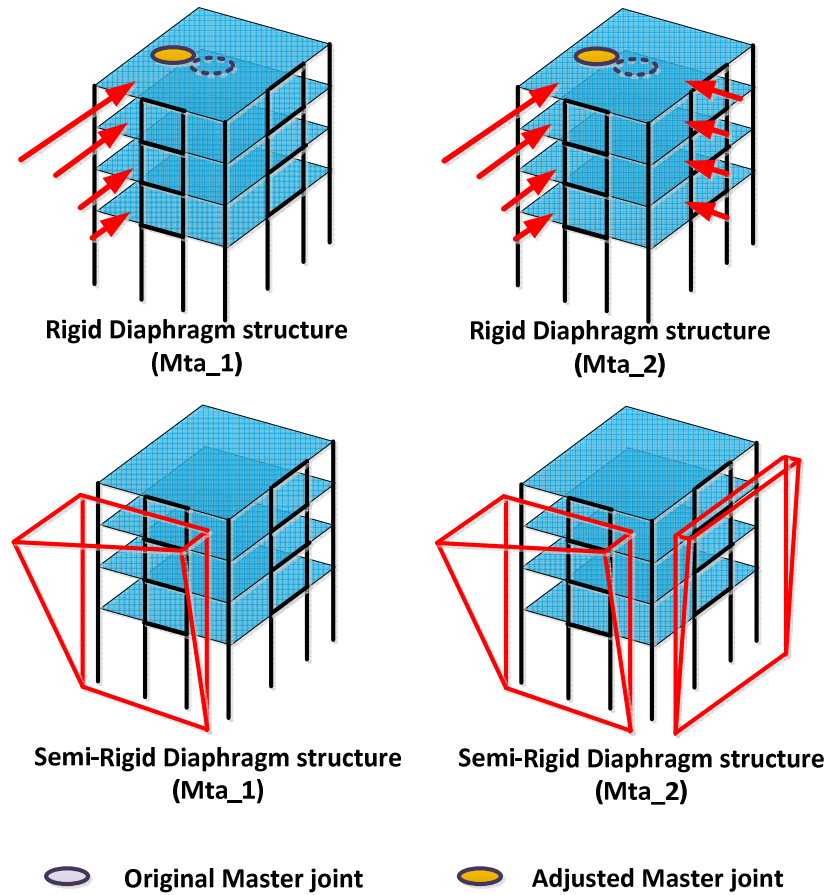


Figure 5-10 Application of lateral force pattern for pushover analyses

Table 5-2 Pushover load pattern for rigid diaphragm structures (*BF+R* and *CF+R*)

Level	Pushover load pattern (Y-dir)	Pushover load pattern (X-dir)
RF	1.00	0.30
4F	0.79	0.24
3F	0.50	0.15
2F	0.23	0.07

Table 5-3 Pushover load patterns for semirigid diaphragm structures (*CF*)

Level	Pushover load pattern (Y-Direction)										Pushover load pattern (X-Direction)			
	CL1	CL2	CL3	CL4	CL5	CL6	CL7	CL8	CL9	CL10	CLA	CLB	CLC	CLD
RF	0.92	1.00	0.94	0.88	0.82	0.76	0.71	0.65	0.59	0.67	0.30	0.30	0.30	0.30
4F	0.73	0.79	0.74	0.70	0.65	0.60	0.56	0.51	0.46	0.53	0.24	0.24	0.24	0.24
3F	0.46	0.50	0.47	0.44	0.41	0.38	0.35	0.32	0.29	0.33	0.15	0.15	0.15	0.15
2F	0.21	0.23	0.21	0.20	0.19	0.17	0.16	0.15	0.13	0.15	0.07	0.07	0.07	0.07

Note: *CLi* are column lines corresponding to the acting points of pushover load patterns

### 5.4.2 Capacity curves for each configuration

For the capacity curves from NSA, the monitor points for lateral displacement are located at the left corner of the roof diaphragms as shown in Figure 5-1. The magnitudes of lateral displacement at these monitor points are higher than at any other joint in the diaphragm. The target roof drift for the structures in C1 and C2 is 6% of the structure height (52.5 ft) in each NSA. Figure 5-11 includes the comparison of capacity curves for the structures in the C1 group. In these capacity curves, “Roof Drift Ratio” is defined as the ratio equal to the lateral displacement in the +Y-direction at the monitor point on the roof divided by the height of the structure.

Observations from the capacity curves are:

**CI:** The comparison of capacity curves between **BF+R**, **CF+R** and **CF** with  $M_{ta\_1}$  is shown in Figure 5-11. The three structures step into inelastic stages when the brace buckles in the 3<sup>rd</sup> story. One can observe that the post buckling behavior is different between the structures with semi-rigid (**CF**) and rigid diaphragms (**BF+R**, **CF+R**). The overstrength factors for the three structures are:  $\Omega_{CF+R}=2.08$ ,  $\Omega_{BF+R}=2.03$ ,  $\Omega_{CF}=2.01$  based on the known design base shear for SCBFs (0.167 V/W). Therefore, the **CF+R** structure has a higher post buckling stiffness as well as ultimate strength. The lowest ultimate resistance is obtained for the BF+R structure.

Note that because this is a four-story X-type braced frame and because buckling occurs in the 3F. The capacity curves do not show the typical rapid degradation of chevron braced frames with buckling in the first floor. This result is analogous to Erduran et al (2011) and Uriz et al (2008).

The **CF+R**, structure reaches its ultimate strength when the fracture of two braces (F1 and F2) develops in the 3<sup>rd</sup> story, resulting in a noticeable drop of global strength shown in Figure 5-12.

This figure illustrates the sequences of the brace buckling and fractures as the lateral displacement progresses. A slight decrease in the strength develops when the braces buckle in BF4 (i.e. B10 and B11). This decrease is not significant because the other two tension braces in the 2<sup>nd</sup> and 3<sup>rd</sup> story have not reached yield yet, and thus can pick up the loss of the strength due to the buckling of the two braces.

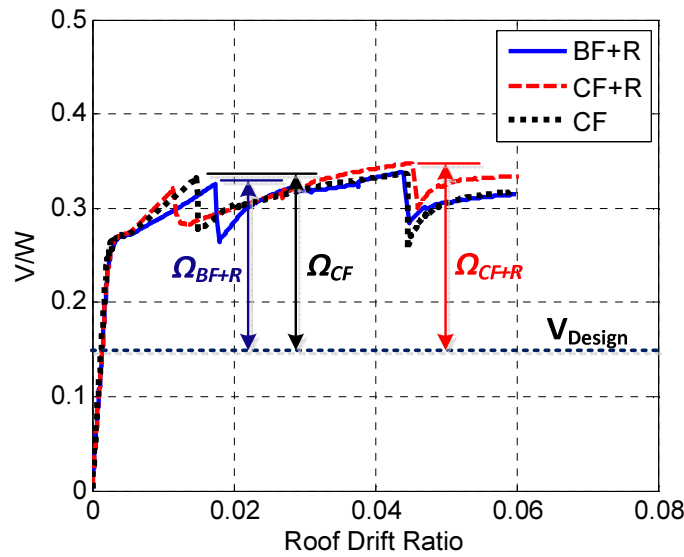


Figure 5-11 Comparison of capacity curves of C1 with  $M_{ta_1}$  ( $W=8450\text{kips}$ )

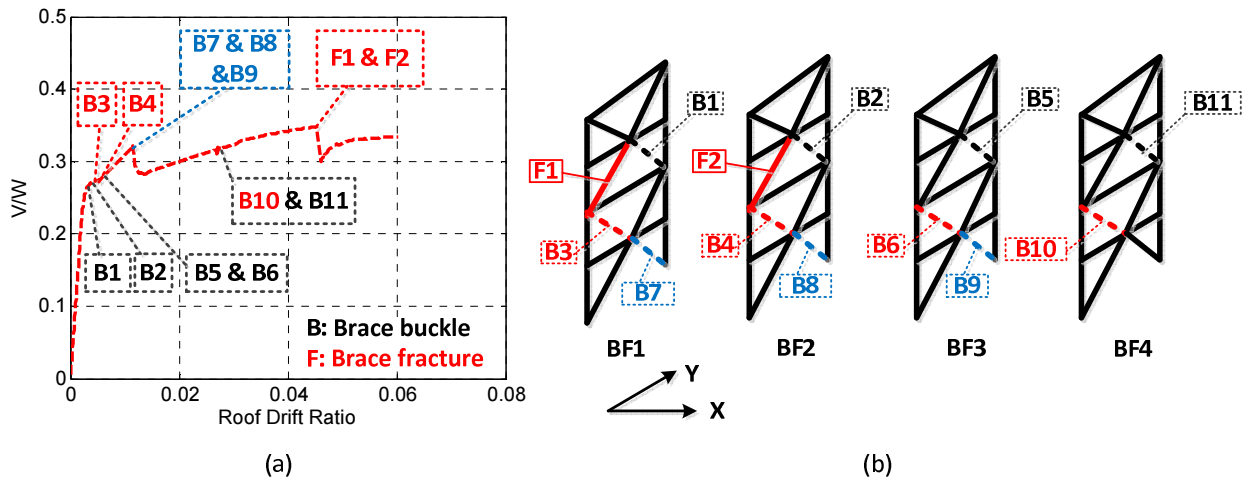


Figure 5-12 Brace buckling and fracture sequence in C1 ( $CF+R$ ): (a) capacity curve and (b) failure sequence

By comparing Figure 5-13 (a) ( $M_{ta\_1}$  or one-axial) with Figure 5-13 (b) ( $M_{ta\_2}$  or bi-axial), one can evaluate the effect of the different combinations of the input of ground motions on the capacity curves of each system in the C1 structures. Three points, represented as 1, 2 and 3, are marked in each capacity curve in Figure 5-13. The three points represent the occurrence of maximum elastic strength (pre-buckling strength), 1<sup>st</sup> peak strength and 2<sup>nd</sup> peak strength of those structures, respectively. The strengths and the corresponding roof drift ratios are listed in Table 5-4. Based on the results shown in this table, the ultimate base shears in the three systems in structures with  $M_{ta\_2}$  are lower than those with  $M_{ta\_1}$  by 1.5%~7.7%. The **CF+R** structure suffers the highest reduction of the strength due to the bi-axial effect (7.7%). For the **CF+R** structure with  $M_{ta\_1}$ , “snap back” develops in the diaphragms at Point 3 (BF+R<sub>3</sub>, CF+R<sub>3</sub> and CF<sub>3</sub>) marked in Figure 5-13. Therefore, the base shear is larger because of the smaller structural rotation. However, for the **CF+R** structure with  $M_{ta\_2}$ , the snap back behavior does not develop as a result of the larger structural rotation. In this scenario, the lateral deformation of the SMRFs is higher than those for  $M_{ta\_1}$ . This leads to a lower base shear ratio for the entire structure. The phenomenon indicates that the inclusion of bi-axial ground motion effect decreases the capacities of the three systems.

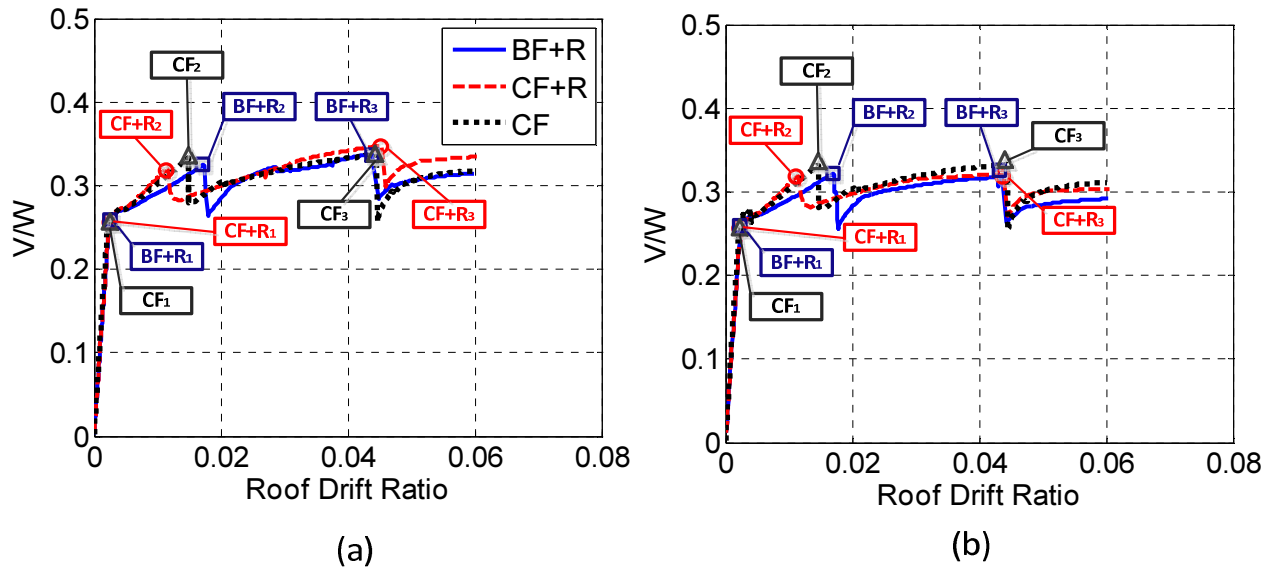


Figure 5-13 Capacity curves for C1: (a)  $M_{ta_1}$  and (b)  $M_{ta_2}$

Table 5-4 Summary of NSA for the C1 structures

$M_{ta_1}$		1	2	3	$\Omega_o$
<b>BF+R</b>	$V/W_{max}^{(1)}$	0.230	0.321	<b>0.339</b>	2.03
	$RDR_{max}^{(2)}$	0.002	0.012	0.044	
<b>CF+R</b>	$V/W_{max}$	0.230	0.325	<b>0.348</b>	2.08
	$RDR_{max}$	0.002	0.017	0.045	
<b>CF</b>	$V/W_{max}$	0.232	0.332	<b>0.337</b>	2.01
	$RDR_{max}$	0.002	0.015	0.045	
$M_{ta_2}$		1	2	3	$\Omega_o$
<b>BF+R</b>	$V/W_{max}$	0.234	<b>0.322</b>	0.317	1.93
	$RDR_{max}$	0.002	0.017	0.043	
<b>CF+R</b>	$V/W_{max}$	0.234	0.319	<b>0.320</b>	1.92
	$RDR_{max}$	0.002	0.011	0.044	
<b>CF</b>	$V/W_{max}$	0.231	0.331	<b>0.332</b>	1.98
	$RDR_{max}$	0.002	0.015	0.045	

Note: <sup>(1)</sup> $RDR_{max}$  is defined as the peak roof drift ratio (Peak roof drift/structural height) <sup>(2)</sup>

$V/W_{max}$  is defined as the peak base shear ratio (Peak base shear/structural seismic weight)

The individual capacity curves of each braced frame in each configuration can be used to evaluate the variation of lateral stiffness and resistance provided by these braced frames in NSA.

Given the variation of capacity curves of the individual braced frames (i.e. BF1~BF4), a significant difference exists between the curves that consider the effect of diaphragm rigidity, as illustrated in Figure 5-14. It is obvious that the pre-buckling and ultimate capacities of the three individual braced frames, BF1~BF3, are similar in the **CF+R** case but not in **CF** case. The pre-buckling strength of the structures is defined as the strength corresponding to the 1<sup>st</sup> occurrence of the brace buckling. BF3 in **CF** reaches its ultimate strength significantly after the other two configurations (**BF+R** and **CF+R**) as illustrated in Figure 5-14 (b). This phenomenon demonstrates that the *in-plane diaphragm rigidity* does influence the behavior of the LFRS.

In Figure 5-14 (a), BF1~BF3 reach their ultimate strengths almost at the same drift; however, BF4 reaches its peak strength significantly after the first three. The reason is that the floor diaphragms rotate significantly after the first three braced frames reach their own pre-buckling strengths. The structure rotates about BF4 due to the loss of lateral stiffness from BF1 to BF3 at this stage. In other words, the C.R. of the structure moves to a position near BF4. The phenomenon is the same as the one that will be discussed in Subsection 5.4.3. The braced frame capacity curves for C1 with different assumptions of diaphragm and accidental torsion combinations are shown in Figure B-1 to Figure B-2.

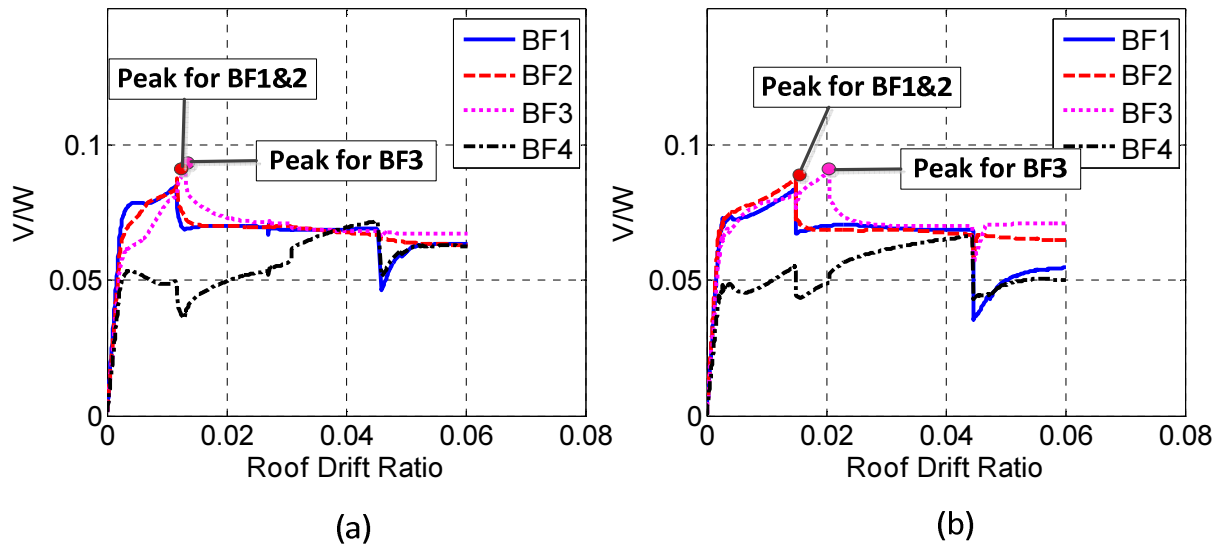


Figure 5-14 Capacity curves for C1 braced frames with  $M_{t\alpha_1}$ : (a)  $CF+R$  and (b)  $CF$

**C2:** For the structures in C2 group, their asymmetric structural configurations generate an inherent torsion in both the elastic and inelastic stages. The center of rigidity (C.Rs) of the diaphragms in the C2 group structures moves away from the center of mass (C.Ms) toward the right side of diaphragms after braces buckle as shown in Figure 5-15. Accordingly, the inherent torsion increases due to the movement of the C.R. Therefore, the pre-buckling and ultimate strengths of individual braced frames in the C2 structures do not develop simultaneously due to the rotation of the structure. The comparison of capacity curves between  $BF+R$ ,  $CF+R$  and  $CF$  is shown in Figure 5-16.

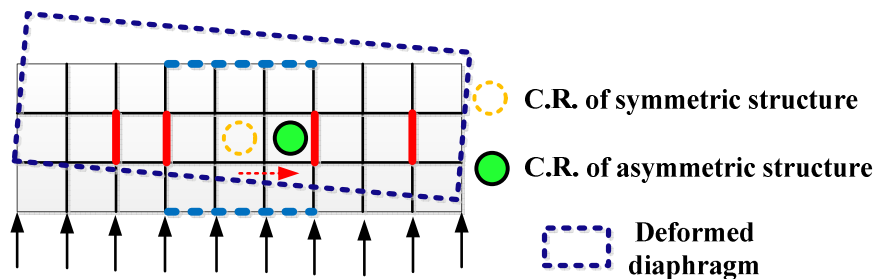


Figure 5-15 Movement of C.R. in C2

According to Figure 5-16, the elastic stiffness of **CF+R** (1520 ksi) and **BF+R** (1498 ksi) structures are significantly higher than those in the **CF** structure (980 ksi) because of the existence of rigid diaphragm constraints. This indicates that structures with rigid diaphragm constraints show higher elastic lateral stiffnesses. In addition, the overstrength factors for the three models in the C2 are:  $\Omega_{CF+R}=2.72$ ,  $\Omega_{BF+R}=2.94$ ,  $\Omega_{CF}=2.66$ . Note that all the C1 structures (Figure 5-11) had similar initial stiffness (1430 ksi). The overstrength factors in the C2 structures are higher than those of the C1 structure because of a higher redundancy factor,  $\rho=1.30$ , is used in the design of the C2 structures. The use of a higher  $\rho$  factor results in a larger size of braces, which leads to a higher overstrength factor of the structures. Moreover, also the moment frame and gravity systems both provide a portion of the entire strength. More details about the latter contributions will be discussed in Subsection 5.4.5.

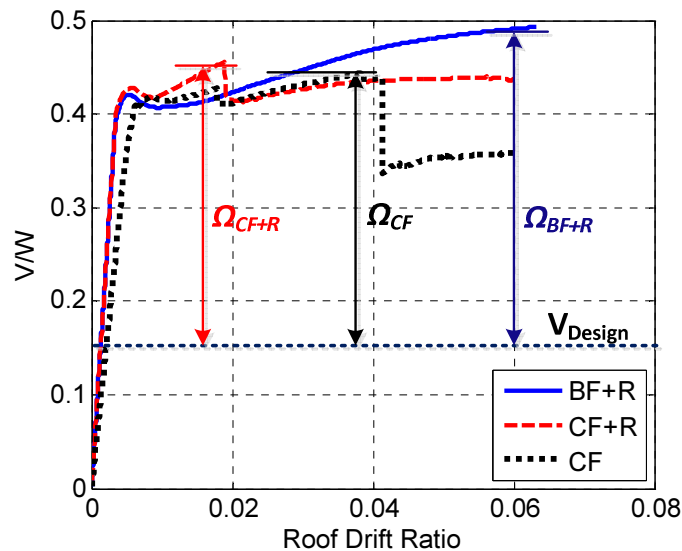


Figure 5-16 Comparison of capacity curves for C2 structures with  $M_{ta,2}$  ( $W = 8450$  kips)

Similar to C1 (Figure 5-13), one can use three points to mark the elastic strength, the 1<sup>st</sup> peak and the 2<sup>nd</sup> peak strength in each capacity curve as shown in Figure 5-17. The corresponding base shears and roof drifts are shown in Table 5-5. One can observe that the reductions in

overstrength factor for the structures with bi-axial effect are more significant than the ones in C1 structures (2.3%~14.7%). This indicates that the inclusion of bi-axial effect decreases the capacities of the three systems significantly for the asymmetric structures. In addition, the *CF* structure with  $M_{ta\_2}$  exhibits a higher overstrength factor, which is different from those with  $M_{ta\_1}$ . The phenomenon is caused by the change in the sequence of brace failure due to the removal of rigid diaphragm constraints. The un-identical development of ultimate strength of braced frames lead to a smaller P-Delta effect on the entire structure as compared with those with rigid diaphragm constraints. The braced frame capacity curves for C2 with different assumptions of diaphragm and accidental torsion combinations are shown in Figure B-3 to Figure B-4.

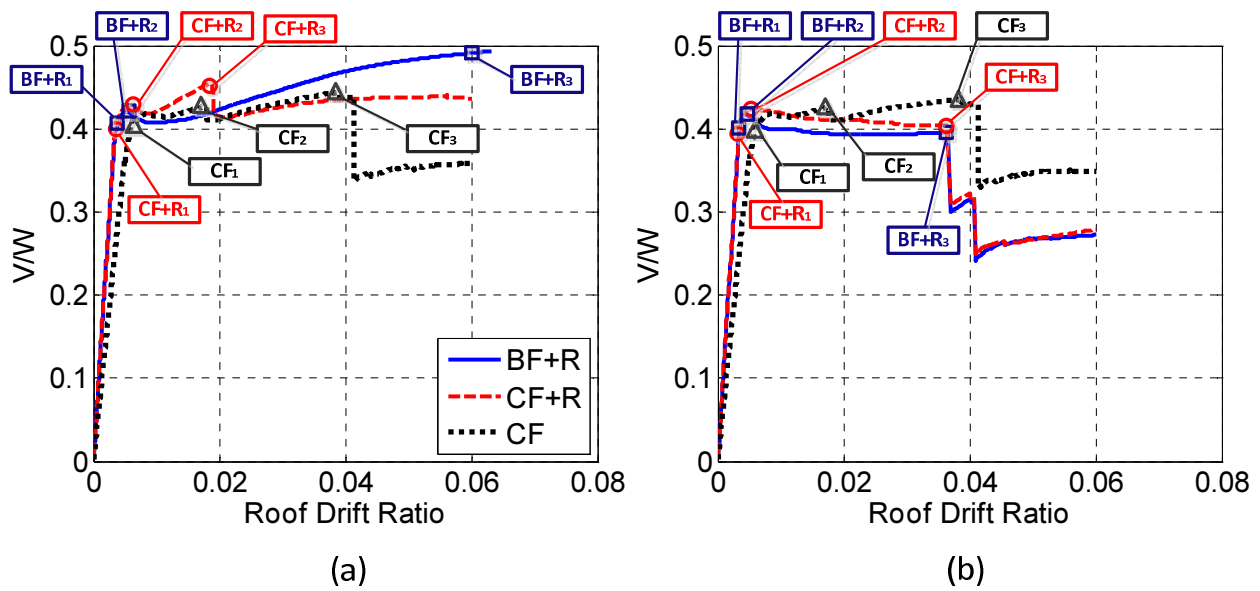


Figure 5-17 Capacity curves for C2: (a)  $M_{ta\_1}$  and (b)  $M_{ta\_2}$

Table 5-5 Summary of NSA for the C2 structures

$M_{ta\_1}$		1	2	3	$\Omega_0$
<b>BF+R</b>	$V/W_{max}$	0.393	0.421	<b>0.491</b>	2.94
	$RDR_{max}$	0.003	0.005	0.060	
<b>CF+R</b>	$V/W_{max}$	0.393	0.427	<b>0.455</b>	2.72
	$RDR_{max}$	0.003	0.006	0.019	
<b>CF</b>	$V/W_{max}$	0.365	0.427	<b>0.445</b>	2.66
	$RDR_{max}$	0.005	0.018	0.038	
$M_{ta\_2}$		1	2	3	$\Omega_0$
<b>BF+R</b>	$V/W_{max}$	0.410	<b>0.418</b>	0.395	2.50
	$RDR_{max}$	0.004	0.005	0.036	
<b>CF+R</b>	$V/W_{max}$	0.410	0.425	<b>0.404</b>	2.54
	$RDR_{max}$	0.004	0.006	0.036	
<b>CF</b>	$V/W_{max}$	0.363	0.426	<b>0.435</b>	2.60
	$RDR_{max}$	0.005	0.018	0.038	

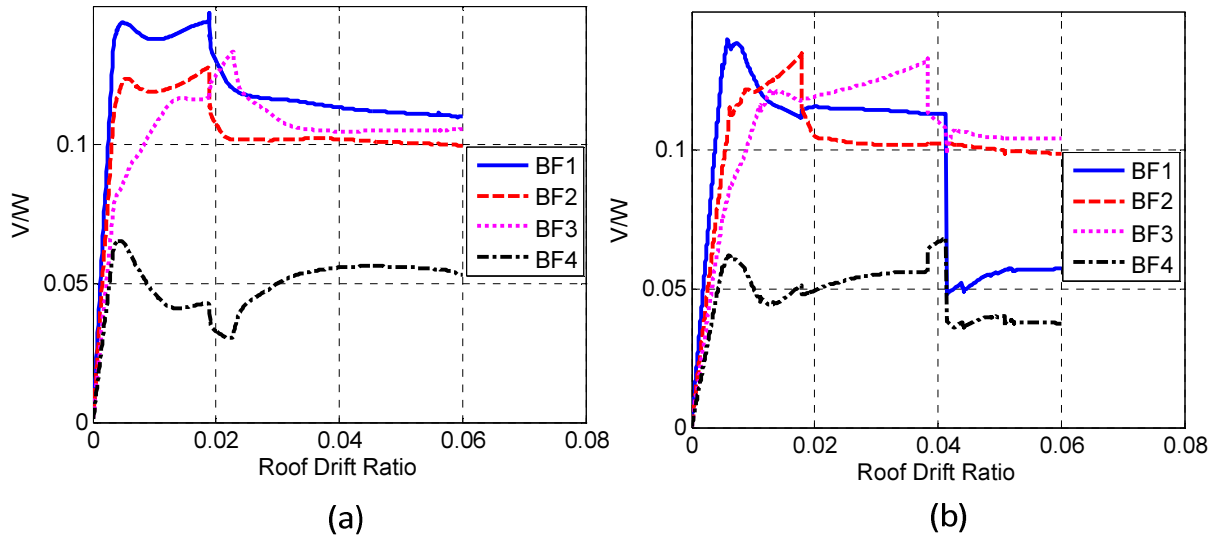


Figure 5-18 Capacity curves of braced frames of C2 with  $M_{ta\_1}$ : (a) **CF+R** and (b) **CF**

From the results of NSA for the different configurations, one can observe that the ultimate strength in the structures with rigid diaphragms (**CF+R** and **BF+R**) are slightly higher (5~10%) than the ones with semi-rigid diaphragms (**CF**) for the structures with  $M_{ta\_1}$ . A possible explanation for this phenomenon is that the in-plane diaphragm stiffness affects the transfer mechanism of in-plane forces among structural members in the diaphragms.

For the structures with rigid diaphragms, the braced frames and moment frames are connected via in-plane rigid links shown in the Stage 1 in Figure 5-19. The braced and moment frames deform because of the external (seismic) loads. Stage 2 in Figure 5-19 illustrates the deformed LFRS before the structures step into the inelastic stages. Once the braces buckle or fracture, the force redistribution is generated as shown in Stage 3. In this study, the force redistribution in a braced frame is caused by the difference in the magnitude of axial force in the two braces connected at the same point in a beam. These vertical and horizontal redistributed forces must be transferred to other LFRS through these links in diaphragms. This mechanism is robust in rigid diaphragms since the links have infinite in-plane rigidity and leads to higher strengths of such structures.

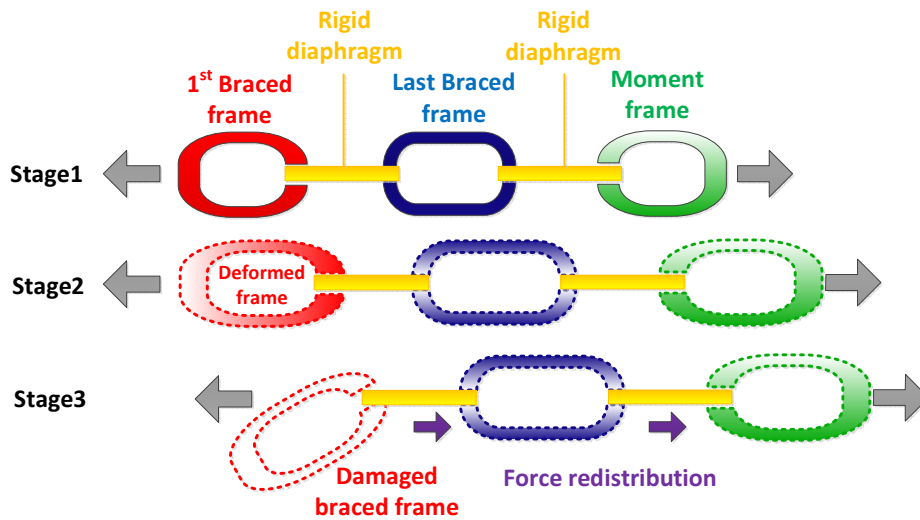


Figure 5-19 Force redistribution mechanism in structures with rigid diaphragms

For the structures with semi-rigid diaphragms, however, these links are not as strong. The semi-rigid diaphragms are able to deform due to the in-plane and out-of plane forces in earthquakes. The in-plane and out-of plane stiffness of diaphragm between LFRS can be different because of the differences in the diaphragm spans as well as boundary conditions of diaphragm. Accordingly, the diaphragm deformation is different, as presented in Stage 2 in Figure 5-20. In

addition, the force redistribution cannot be delivered to the other undamaged vertical LFRS as simply and efficiently as in the structures with rigid diaphragms. This may lead to the local failure of damaged vertical LFRS, as well as a decrease of the overall structural ductility and strength. Stage 3 in Figure 5-20 illustrates this mechanism schematically.

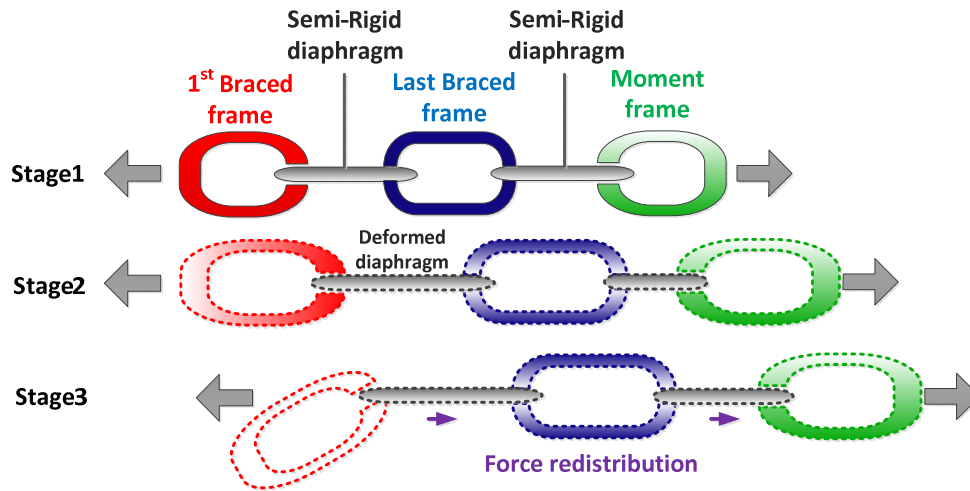


Figure 5-20 Force redistribution mechanism in structures with semi-rigid diaphragms

### 5.4.3 Rotation behavior of diaphragms

This section focuses on the rotational behavior of diaphragms for the symmetric and asymmetric structures. The rotation the structure is stimulated by the changes in eccentricity between C.M. and C.R. as the NSA progresses. In the inelastic stages, the magnitude of torsional moment is strongly dependent on the sequence of brace buckling. In other words, the movement of the C.R. in each diaphragm depends on the variation of lateral stiffness in the SCBFs, which, in the inelastic range, can also be strongly dependent on modeling assumptions.

Figure 5-21 depicts several stages corresponding to different rotational behavior, or movement of the C.R., on the 2F diaphragm (Figure 3-2) of the C2 structures. The movement can be divided into five stages. The structure has an initial inherent torsion due to the asymmetric horizontal configuration of LFRS (Stage 1) in the elastic range. As elements of the braced frames begin to

buckle, starting with in the 1<sup>st</sup> story in BF1 (the positions are defined in Figure 5-21), the lateral stiffness of these braced frames reduces in sequence accordingly. The 2F diaphragm rotates significantly corresponding initially to the buckling of braces in the 1<sup>st</sup> story of the braced frames (Stage 2~Stage 3). In these two stages, the position of C.R. moves towards the right side of the diaphragm, and thus the magnitude of torsional moment keeps accumulating because of the increment of eccentricity.

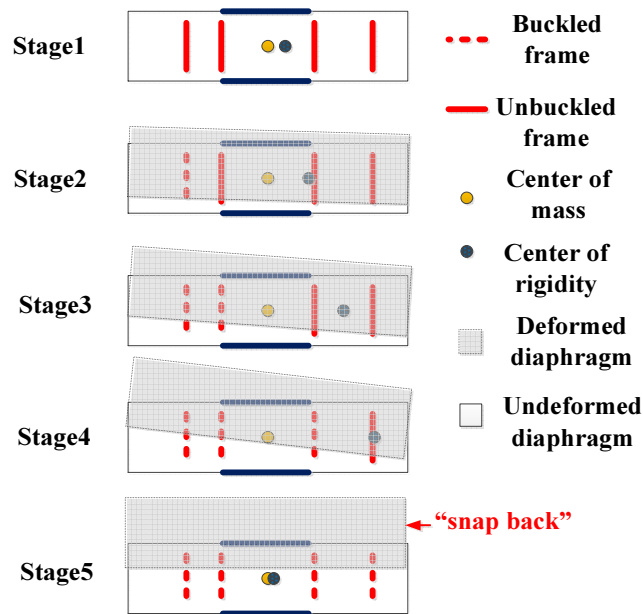


Figure 5-21 Rotation of diaphragm during pushover analyses (C2)

The extreme case of the rotation behavior of diaphragm is generated at the instant corresponding to the development of pre-buckling strength in the last braced frame (BF4, Stage4). In this scenario, the position of C.R. is close to BF4. Afterwards, the diaphragm “snaps back” while all SCBFs develop their pre-buckling capacities subsequently (Stage5). In Stage 5, the C.R. moves back near the center of diaphragm because the lateral inelastic stiffness of each SCBF in the first floor is similar. It is obvious that the magnitude of inherent torsional moment reduces significantly in Stage 5. Note that the other floors will not necessarily be following this pattern

concurrently and that therefore significant differences will exist between the torsional deformations at each floor.

Based on the definition of the horizontal torsional irregularities of structures in ASCE 7, a Torsion Coefficient ( $TC$ ) will be used for evaluating the degree of irregularity as shown in Equation 5-10. Based on ASCE 7, the  $TC$  is defined by the following equation:

$$TC_j = \frac{D_{max}^j}{D_{avg}^j} \quad \text{Equation 5-10}$$

where  $TC_j$  is the torsional coefficient at  $j$ -level,  $D_{max}^j$  is the maximum story drift at the  $j$ -level and  $D_{avg}^j$  is the average story drift at  $j$ -level.

Note that the in general the maximum value of  $TC$  is 2.0; however, if negative displacement occurs at one of the monitor point, this value can be greater than 2.0. Figure 5-22 illustrates the variation of the  $TC$  in the C1 structure corresponding to each stage mentioned in Figure 5-21. The  $TC$  increases sharply from Stage 2 to 4, accompanying the sequence of brace buckling in the SCBFs. The figure also shows that the magnitude of  $TC$  in the 2F is higher than in the other floors in Stages 4 and 5. This indicates the 2F diaphragm in the theme structure has the highest magnitude of torsional irregularity in the inelastic stages. In addition, “snap back” behavior occurs in the 2~4F due to the buckling of braces in the 2<sup>nd</sup> and 3<sup>rd</sup> story of BF4.

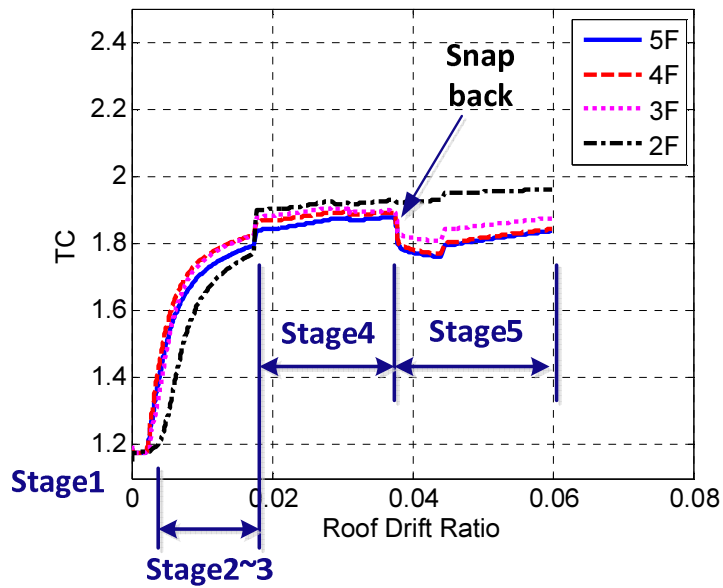


Figure 5-22 Rotation stages corresponding to the variation of torsion coefficient

Figure 5-23 and Figure 5-24 show the variation of  $TC$  of each diaphragm for the C1 and C2 structures with rigid diaphragm constraints ( $BF+R$ ) under  $M_{ta_1}$  and  $M_{ta_2}$ . One can observe that the magnitude of  $TC$  varies significantly after the inelastic behavior develops. For instance, the peak  $TC$  in C1 for  $BF+R$  with  $M_{ta_1}$  (shown in Figure 5-23 (a)) is 1.96 in Stage 5. This value is higher than 1.4, the boundary of the existence of extreme torsional irregularity given in ASCE 7, by 38%. On the other hand, the peak  $TC$  for C1 for  $BF+R$  with  $M_{ta_2}$  is higher than the limitation by 42% (shown in Figure 5-23 (b)). In other words, a significant increment of horizontal torsional irregularity can be generated in the analyses by the sequence of brace buckling in the vertical SCBFs.

From Figure 5-23 and Figure 5-24, one can observe that the magnitude of  $TC$  in the structures with  $M_{ta_1}$  is lower than those with  $M_{ta_2}$ . The phenomenon indicates that the structures considering bi-axial effects will probably suffer a higher magnitude of horizontal torsional irregularity due to the diaphragms with infinite in-plane rigidity. In addition, Figure 5-24 shows

that the “snap back” behavior of each diaphragm cannot be developed in C2. This means the Stage 5 disappears in those structures. The variation of  $TC$  for C1 and C2 with different assumptions of diaphragm and accidental torsion combinations are shown in Figure B-5 to Figure B-8.

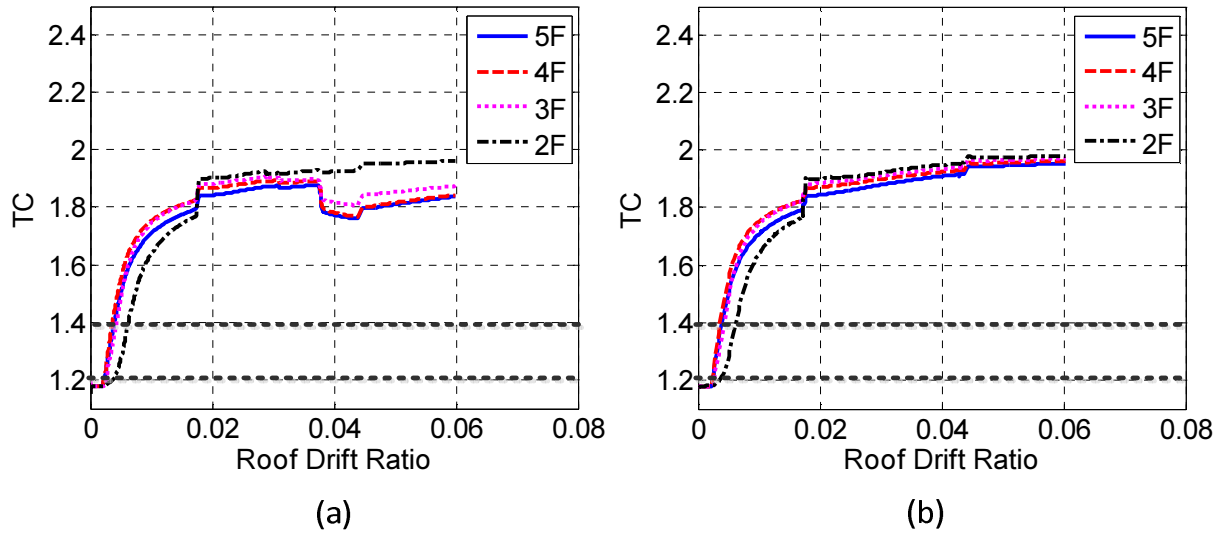


Figure 5-23 Variation of torsion coefficient of C1:  $BF+R$  (a)  $M_{ta_1}$  and (b)  $M_{ta_2}$

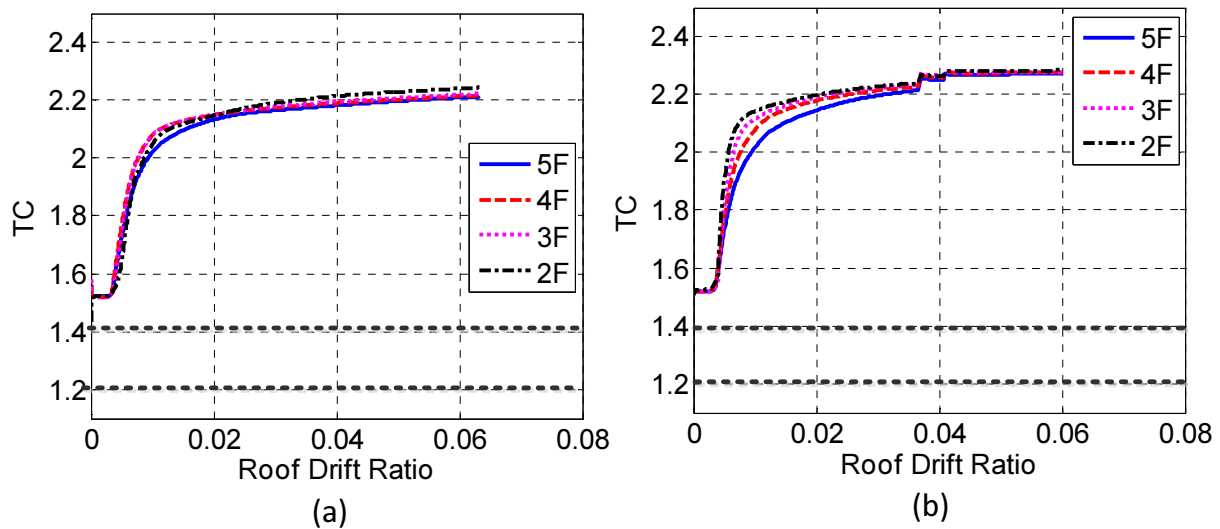


Figure 5-24 Variation of torsion coefficient of C2:  $BF+R$  (a)  $M_{ta_1}$  and (b)  $M_{ta_2}$

#### 5.4.4 Inter-story drift ratios

This section describes the variation of inter-story drift ratios (IDR) of the theme structures considering the effect of  $M_{ta_1}$  and  $M_{ta_2}$ . The IDRs corresponding to the corners of each diaphragm are evaluated in this section. The locations of left and right corners of these structures are marked in Figure 5-25.

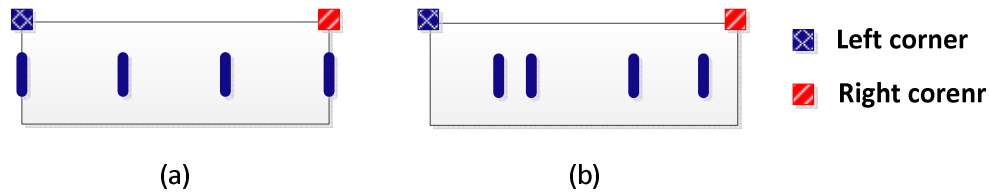


Figure 5-25 Positions of right and left corner monitor points in each configurations: (a) C1 and (b) C2

For the C1 and C2 structures, the relationships between the IDR and roof drift ratio at the monitor joints are shown in Figure 5-26 and Figure 5-27. One can observe that (1) the magnitude of IDR at the left corner (i.e. Figure 5-26 (a) and Figure 5-27 (a)) increase significantly in the 1<sup>st</sup>, 2<sup>nd</sup> and 3<sup>rd</sup> story after the structures move into the inelastic stages, and (2) the IDR in the 2<sup>nd</sup> and 3<sup>rd</sup> story at right corner (i.e. Figure 5-26 (b)) has a significant increment when “snap back” behavior occurs. The variation of IDR for C1 and C2 with different assumptions of diaphragm and accidental torsion combinations are shown in Figure B-9 to Figure B-15.

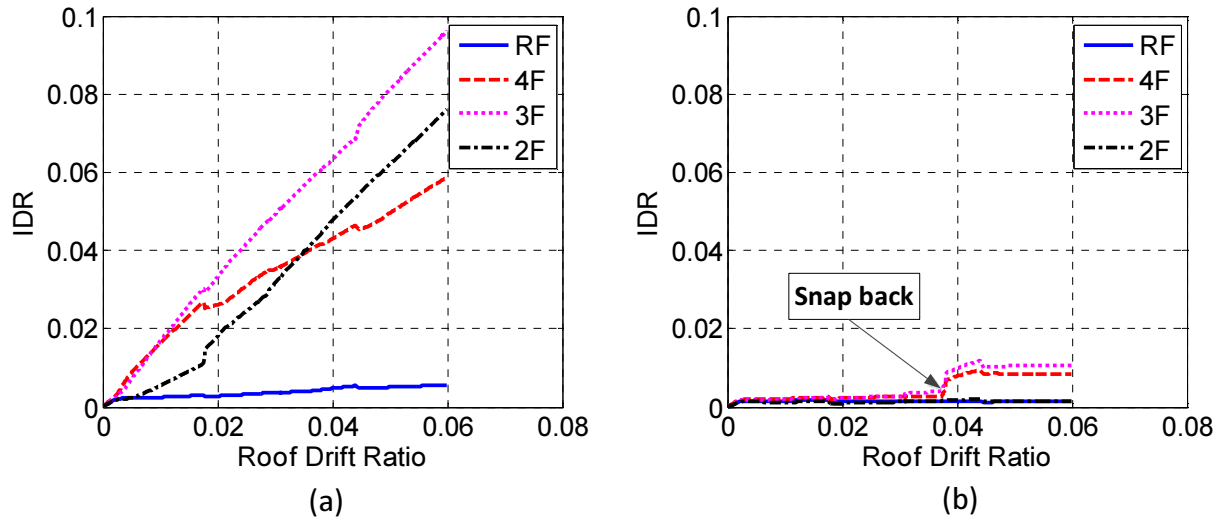


Figure 5-26 Inter-story drift ratio for diaphragm in C1 (**BF+R**) with  $M_{t1_1}$ : (a) Left corner and (b) Right corner

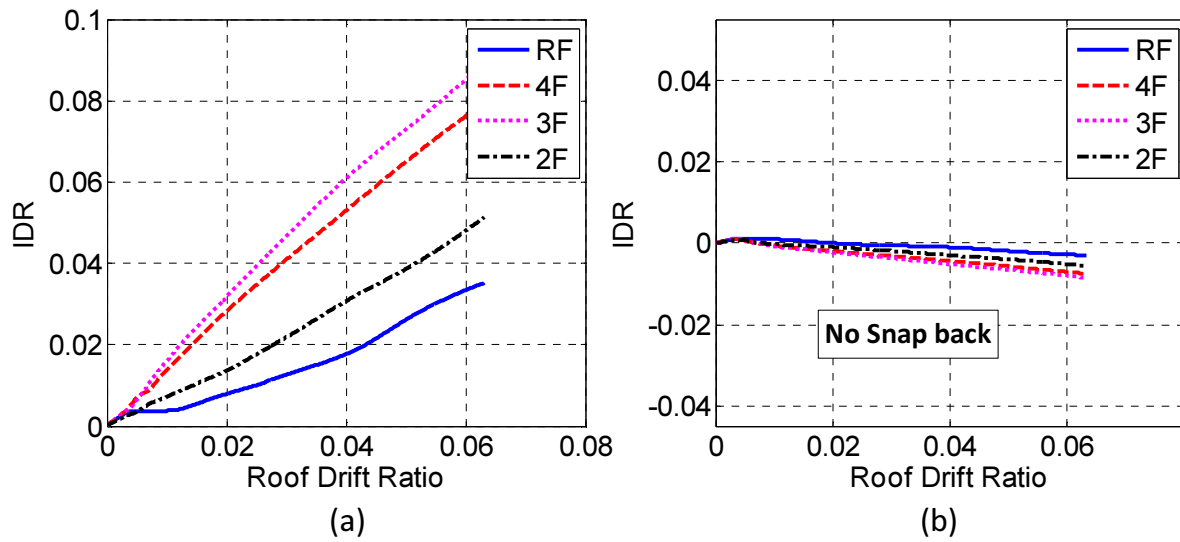


Figure 5-27 Inter-story drift ratio for diaphragm in C2 (**BF+R**) with  $M_{t1_1}$ : (a) Left corner and (b) Right corner

#### 5.4.5 Contribution of individual systems

This section concentrates on the contribution provided by the individual systems to the overall response. Figure 5-28 to Figure 5-29 show the individual capacity curves for braced frames, moment frames and gravity systems for C1 and C2 with  $M_{t2_2}$ , respectively. One can observe the

contribution of SCBF systems is significant. The overstrength factors for the SCBFs alone are about 1.80 for C1 and 2.50 for C2. These factors are smaller than the ones for the entire structures mentioned in Subsection 5.4.2 because the SMRFs and gravity frames also provide a portion of the overall strength. Table 5-6 lists the overstrength factors of SCBFs in both configurations. In this table, the reduction of overstrength factor considering the bi-axial effect in the C2 structures is more significant than the ones in the C1 structures.

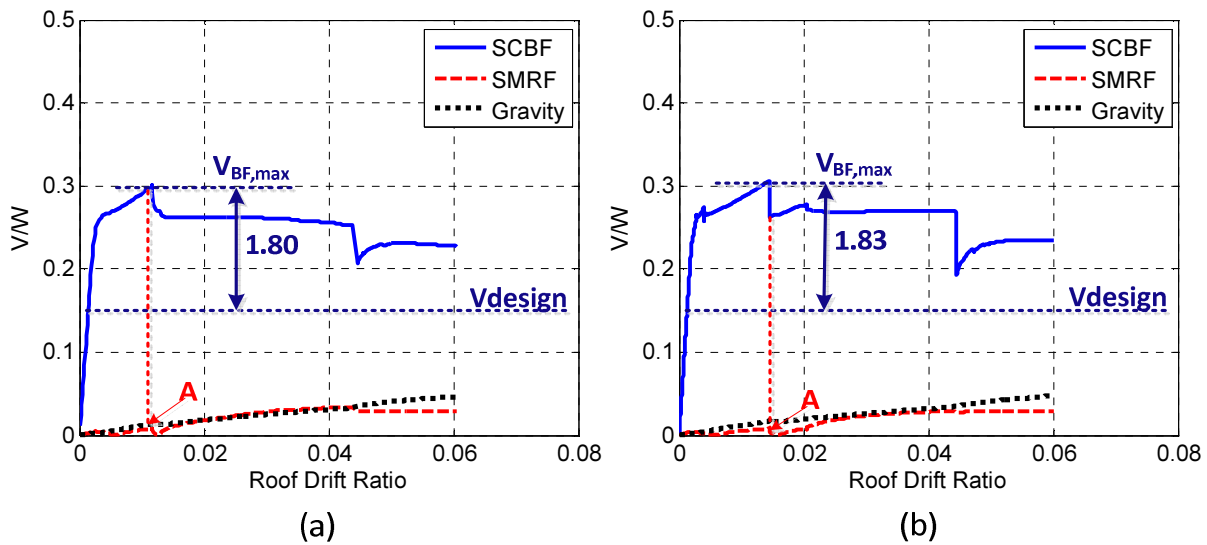


Figure 5-28 Individual capacity curves for C1 with  $M_{ta_2}$ : (a)  $CF+R$  and (b)  $CF$

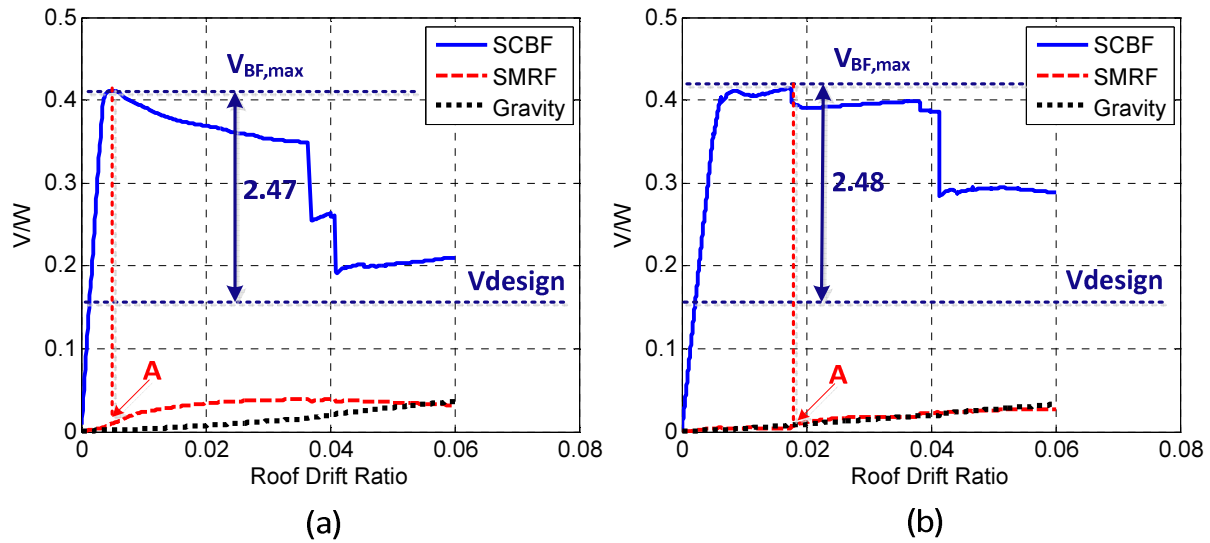


Figure 5-29 Individual capacity curves of C2 with  $M_{ta\_2}$ : (a)  $CF+R$  and (b)  $CF$

Table 5-6 Summary of overstrength for the SCBFs

$\Omega_0$	C1		C2	
	$M_{ta\_1}$	$M_{ta\_2}$	$M_{ta\_1}$	$M_{ta\_2}$
$BF+R$	1.81	1.79	2.59	2.44
$CF+R$	1.79	1.80	2.59	2.47
$CF$	1.84	1.83	2.49	2.48

The contribution of SMRFs to base shear in each configuration is significant when (1) the structures steps into the inelastic stages and (2) the SCBFs reach their ultimate strengths. In other words, the magnitude of base shear provided by the SMRFs becomes significant after the development of “Point A” in Figure 5-28 and Figure 5-29. The behavior of these moment frames play an important role as will be discussed in Chapter 6.

The contribution of gravity systems (i.e. base shear provided from gravity systems) can be neglected when the structures are elastic (Stage1 in Figure 5-21). Comparing the magnitude of base shear in the gravity systems with those in SMRFs, the increment of magnitude in the gravity systems is close to constant. This indicates the contribution of gravity system is insensitive to the

strength variation in the SCBFs and SMRFs and roughly proportional to interstory drift. The variation of strength of individual systems for C1 and C2 with different assumptions of diaphragm and accidental torsion combinations are shown in Figure B-16 to Figure B-19.

### 5.5 Nonlinear dynamic analyses (NDA)

To investigate the nonlinear dynamic behavior of the structures with different in-plane diaphragm stiffness, Nonlinear Dynamic Analyses (NDA) are used to evaluate the dynamic behavior when subjected to the seven target earthquakes discussed in Subsection 3.11.3. For the NDA in this chapter, the effect of accidental torsion,  $M_{ta\_1}$  and  $M_{ta\_2}$ , are both included in the simulation procedures. The approach for modeling the accidental torsion in the models with rigid (**BF+R and CF+R**) or semi-rigid diaphragm (**CF**) was given in Subsection 5.3.1. The accidental torsion develops as a result of the redistribution of diaphragm mass. The inclusion of  $M_{ta\_1}$  is represented by the redistributed diaphragm masses. When including the bi-axial effect in the analytical models, the  $M_{ta\_2}$  is represented as the ground motions applied along the Y and X-directions simultaneously. The ground motions in direction 2 listed in Table 5-7 are applied in the X-direction with magnitudes reduced by 70%. The effect of  $M_{ta}$  in the structural behavior for the three diaphragm assumptions will be characterized by the rotation angles of the diaphragms, inter-story drift ratios and roof drift ratios.

Table 5-7 Selected ground motions from PEER Data base

Ground Motions	PEER NGA ID	Year	Site Class	Magnitude	Fault type	Epicentral distance (km)	Direction 1	Direction 2
Northridge - 01	1078	1994	D	6.7	Reverse	14.66	090	000
Imperial Valley - 02	6	1940	D	7	Strike slip	12.98	270	180
San Fernando	68	1971	D	6.6	Reverse	39.49	090	180
Loma Prieta	758	1989	D	6.9	Reverse Oblique	96.5	260	350
Northern Calif - 03	20	1954	D	6.5	Strike slip	30.79	044	314
Superposition	723	1987	D	6.5	Strike slip	15.99	225	315
Hollister	23	1961	D	5.6	Strike slip	20.6	271	181

### 5.5.1 Variation of torsion coefficients

In the static analysis procedures such as NSA or ELF, the torsion coefficient ( $TC$ ) was a useful index to evaluate the rotational behavior or horizontal irregularities of the structure. However, it may or may not be appropriate to use the  $TC$  from the NDA because:

1. The index may not be able to reflect the change of magnitude for the horizontal irregularities under different intensities of ground motions. In other words, the conventional definition of  $TC$  defined in ASCE 7 may generate a similar magnitude under the ground motions with different hazard levels, and
2. The  $TC$  may not capture the rotational behavior of a diaphragm with low in-plane stiffness because of the significant in-plane deformation.

Therefore, this section discusses the appropriateness of application for  $TC$  in NDA and provides a method to remedy the potential shortcomings mentioned above.

Figure 5-30 shows the variation of  $TC$  based on the definition in ASCE 7 from the NDA of structure C1 with  $M_{ta_1}$  for the DBE-level EI Centro ground motion. The  $TC$  of each diaphragm ranges from 1.0 to 2.0 during the ground motion, with the limits being a direct consequence of the definition  $TC$  shown in Equation 5-10. A  $TC$  of 1.0 indicates that the average diaphragm displacement is close to the maximum diaphragm displacement, meaning that little or no rotation is occurring. A  $TC$  of 2.0 indicates that the maximum lateral displacement of diaphragm is two times greater than the average displacement. The upper and lower bounds are 1.0 and 2.0 regardless of the amplification applied to the different ground motions or the rigidity of the diaphragm. Occasionally, the  $TC$  might be higher than 2.0 when the movement at left and right corner is in opposite directions. This may lead to a relative small magnitude of average

displacement of the diaphragm and result in an unreasonable high magnitude of  $TC$  in the NDA. The definition of the  $TC$  probably should change if the diaphragm is not rectangular in plan by using a weighted average of several lateral displacements along the diaphragm; this will highlight differences between rigid and semi-rigid diaphragms.

Therefore, while the  $TC$  is appropriate to use in the NSA or ELF to detect the horizontal irregularity of diaphragm, it is probably not appropriate for evaluating the irregularities in NDA. Subsection 5.5.2 proposes a new index to detect the horizontal irregularities of diaphragm in NDA.

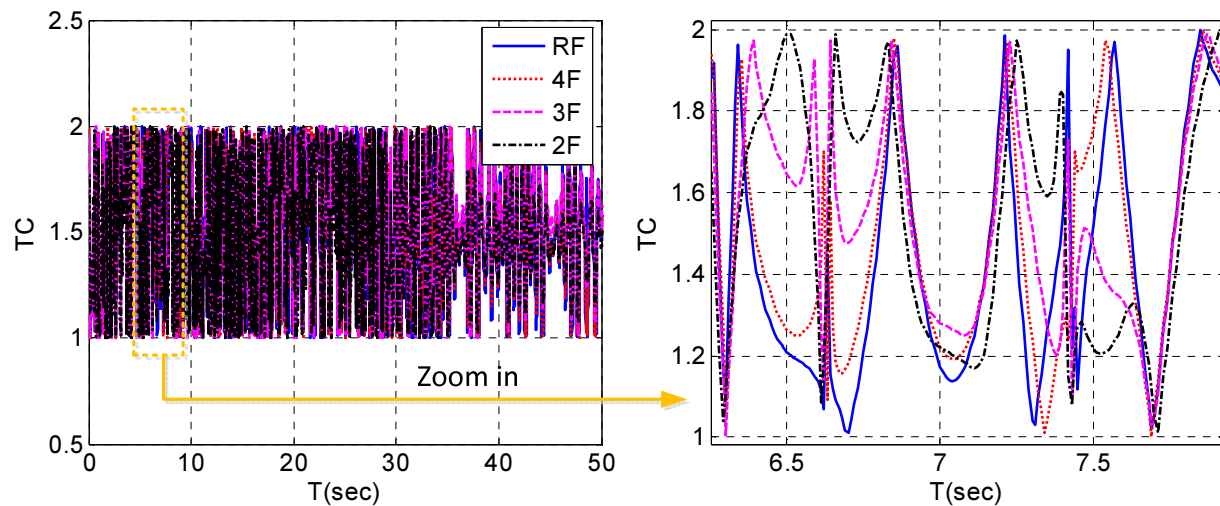


Figure 5-30 Variation of torsion coefficient for C1 in DBE level ground motion (EI Centro)

### 5.5.2 Absolute and relative maximum rotational angles for diaphragms

This section discusses the use of rotation angles as an alternate index to the conventional  $TC$  to identify the influence of horizontal irregularities in non-linear dynamic analyses. For the structures in groups C1 and C2, the rotation of diaphragms is caused by the eccentricities between center of mass (C.M.) and center of rigidity (C.R.). Under this scenario, the magnitude

of the rotational angle of the diaphragm depends on (1) the configuration of the vertical LFRS and (2) the sequence of inelastic behavior in the LFRS.

The rotational angle of the diaphragm can be simply defined as the difference in the lateral displacement between the two corners of a diaphragm divided by the dimension of diaphragm perpendicular to the direction of considered seismic loads (Equation 5-11):

$$RA_j = \frac{\Delta_j^R - \Delta_j^L}{L_j} \quad \text{Equation 5-11}$$

where  $RA_j$  is the rotation angle (in degree) at  $j$ -th level,  $L_j$  is the dimension of diaphragm at  $j$ -th level perpendicular to the direction of seismic loads,  $\Delta_j^R$  is the lateral displacement at the right corner of diaphragm at  $j$ -th level and  $\Delta_j^L$  is the lateral displacement at the left corner of diaphragm at  $j$ -th level.

Figure 5-31 shows the variation of  $RA$  in each floor under the DBE-level El Centro ground motion. One can observe that the magnitude of  $RA$  in the roof is typically higher than those in other floors. The residual  $RA$  detected at the end of this ground motion may also be a useful index for determining the repairability of the structure. Figure 5-32 (a) and Figure 5-32 (b) shows the maximum  $RA$  of the diaphragms in the C1 structures with rigid or semi-rigid diaphragms under the DBE and the MCE-level ground motions including  $M_{Ia-1}$ . The figures show the result for rigid (**BF+R** and **CF+R**) and semi-rigid (**CF**) for the seven ground motions.

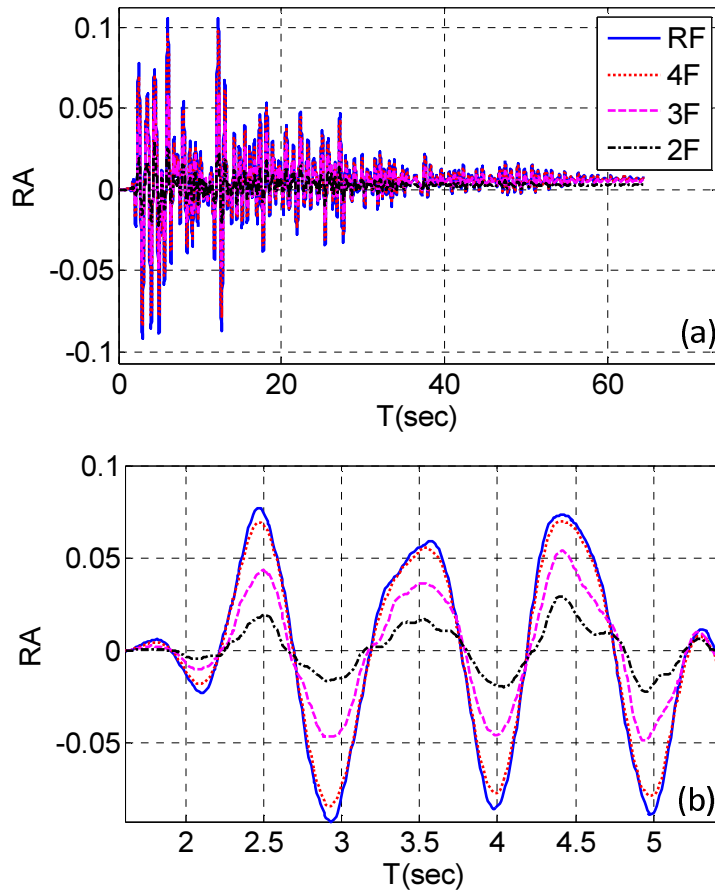


Figure 5-31 Variation of rotation angle for C1 at DBE ground motion (EI Centro): (a) entire history and (b) 1.5~5.5 sec.

The  $RA_{max}$  is defined as the absolute maximum value of  $RA$ . The ratios of  $RA_{max}$  between (1)  $CF+R$  and  $BF+R$ , (2)  $CF$  and  $BF+R$ , and (3)  $CF$  and  $CF+R$  in C1 and C2 are shown in Figure 5-33 and Figure 5-34, respectively. One can observe that the differences in  $RA_{max}$  between the structures with and without composite action (i.e.  $CF+R/BF+R$ ) in C1 are not significant because the ratios are close to 1.0. However, these ratios in C2 are smaller than those in C1, ranging between 0.80 and 0.95 as shown in Figure 5-34. This indicates that  $RA_{max}$  is more sensitive to the composite action in asymmetric rigid diaphragm structures than the one in symmetric structures.

For *CF* structures, the CF/CF+R ratios are lower than 1.0 in C1, as shown in Figure 5-33 (a) and (b). This indicates the symmetric structures have lower rotation angles when the rigid diaphragm constraints are not imposed. This phenomenon becomes obvious when the bi-axial effect included in the models (Figure 5-33 (b)).

However, for the asymmetric structures shown in Figure 5-34, the ratios (CF/CF+R) are higher than 1.0. For example, the CF/CF+R ratio is 1.19 at 2F. The phenomenon indicates that the rigid diaphragm constraints may play an important role in influencing the magnitudes of  $RA_{max}$  in the asymmetric structures. The ratios (CF/CF+R) in C2, which is higher than those in C1, is probable caused by the effect of higher modes. The effect of higher mode is caused by the yielding and buckling of structural members in the inelastic range. This considerably changes the deformed shape from the first mode one assumed in the elastic analyses used for the design.

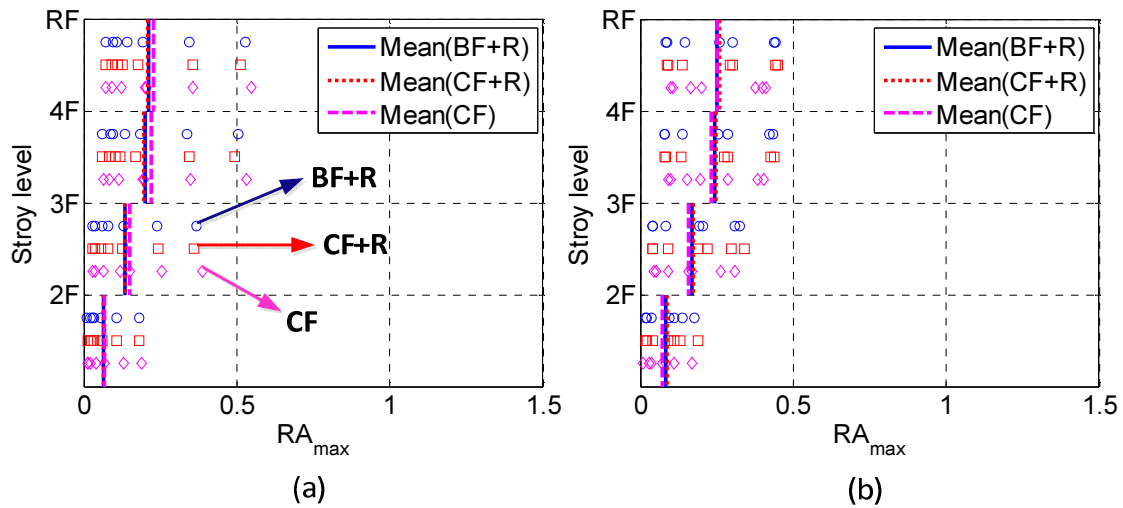


Figure 5-32 Maximum rotation angles of diaphragms C1 with  $M_{1a_1}$ : (a) DBE and (b) MCE

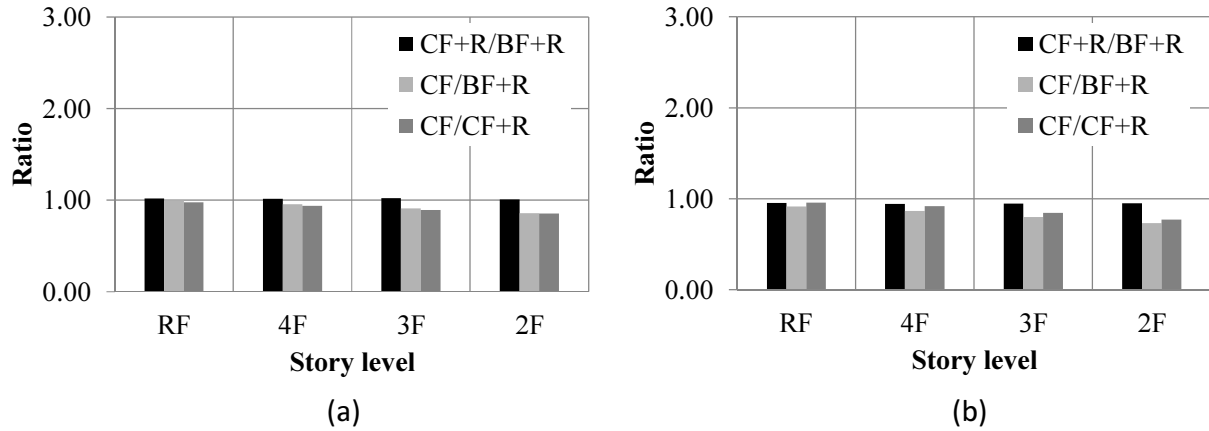


Figure 5-33 Ratios of Maximum rotation angles of diaphragms for C1 under MCE: (a)  $M_{1a_1}$  and (b)  $M_{1a_2}$

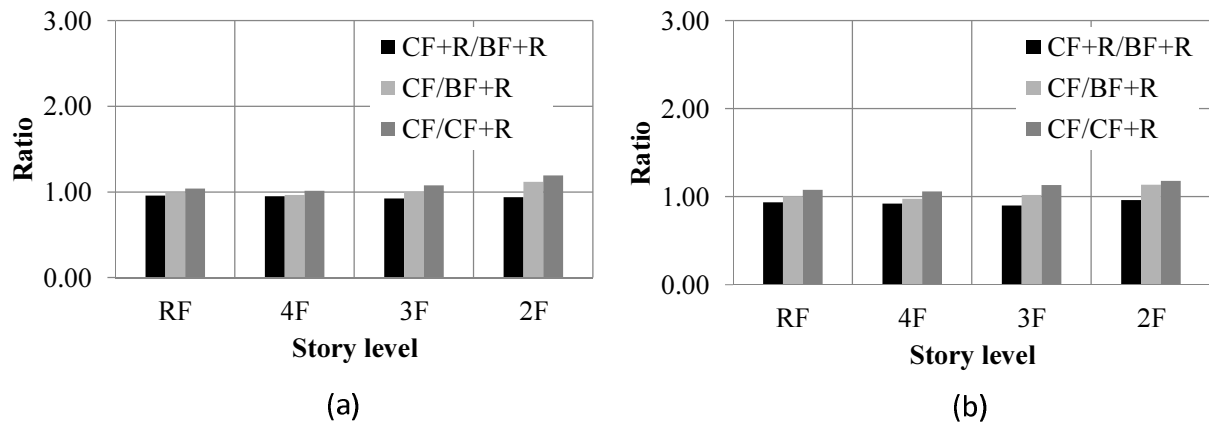


Figure 5-34 Ratios of Maximum rotation angles of diaphragms for C2 under MCE: (a)  $M_{2a_1}$  and (b)  $M_{2a_2}$

The rotation angle as described so far is related to the global displacements of the floors. By measuring the relative rotation angles ( $RRA$ ) between two contiguous diaphragms, a measure akin to the inter-story drift can be developed. The  $RRA$  is probably a better measure of the instantaneous horizontal irregularity between floors and thus of the torsional forces on individual diaphragms. The definition of  $RRA$  is:

$$RRA^j = RA_{j+1} - RA_j$$

where  $RRA^j$  is the relative rotation angle in the  $j^{\text{th}}$  story,  $RA_{j+1}$  is the maximum relative rotation angle in the  $j+1^{\text{th}}$  diaphragm and  $RA_j$  is the relative rotation angle in the  $j^{\text{th}}$  diaphragm

Figure 5-35 exhibits the history of  $RRA$  for each story in the NDA for the symmetric structure with  $M_{ta\_1}$ . The magnitude of  $RRA$  in the 3<sup>rd</sup> and 4<sup>th</sup> story is higher than those in other stories indicating that the structural components in this story suffer a higher magnitude of story rotation. This matches the results from the NSA that indicate a higher magnitude of  $TC$  in stages 2~3 in the 4F and 3F as illustrated in Figure 5-21 and Figure 5-22. In addition, the history of  $RRA$  of each story shown in Figure 5-35 also illustrates the residual  $RRA$  at the end of earthquake due to the inelastic behavior (yielding and buckling) of structural members in the LFRS.

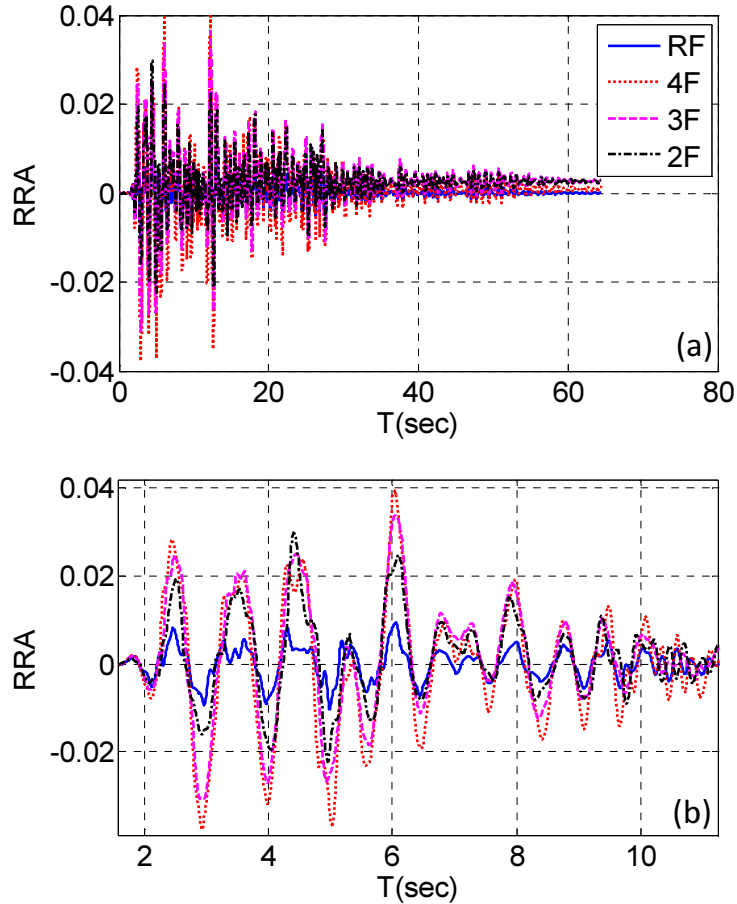


Figure 5-35 History of relative rotation angle for C1 in DBE ground motion (EI Centro): (a) entire history and (b) 2.0~11.0 sec.

The  $RRA_{max}$  is defined as the absolute maximum value of  $RRA$ . The ratios of  $RRA_{max}$  between (1)  $CF+R$  and  $BF+R$ , (2)  $CF$  and  $BF+R$ , and (3)  $CF$  and  $CF+R$  in C1 and C2 are shown in Figure 5-37 and Figure 5-38. According to the two figures, the differences in  $RRA_{max}$  between the structures with and without rigid diaphragm constraints (i.e.  $CF/CF+R$ ) are significant in C2 because these ratios are higher than 1.0. For instance, the highest  $CF/CF+R$  ratio in C2 is 1.70 (RF) as shown in Figure 5-38 (b). In addition, the  $RRA_{max}$  in RF is the highest one among the other stories in the both configurations. This indicates the asymmetric structures (i.e. C2) have a significant increment of  $RRA_{max}$  when the rigid diaphragm constraints are not imposed. Therefore, the rigid diaphragm constraints may play an important role in influencing the magnitudes of

$RRA_{max}$  in asymmetric structures. The larger magnitudes of the ratio (CF/CF+R) of RF in C2 are probably caused by (1) the high mode effects and (2) the in-plane deformation of diaphragm.

The ratios in the structures with  $M_{ta\_2}$  are higher than those with  $M_{ta\_1}$  in both configurations especially for the roof level (RF). The phenomenon shows that the inclusion of bi-axial input of ground motions leads to a higher magnitude of  $RRA_{max}$  in RF while the rigid diaphragm constraints are removed from the analytical models. In addition, the variation of CF+R/BF+R ratio in the both configurations shows that the inclusion of composite action decreases the magnitude of  $RRA_{max}$ . This reduction is more significant in the structures with bi-axial effects.

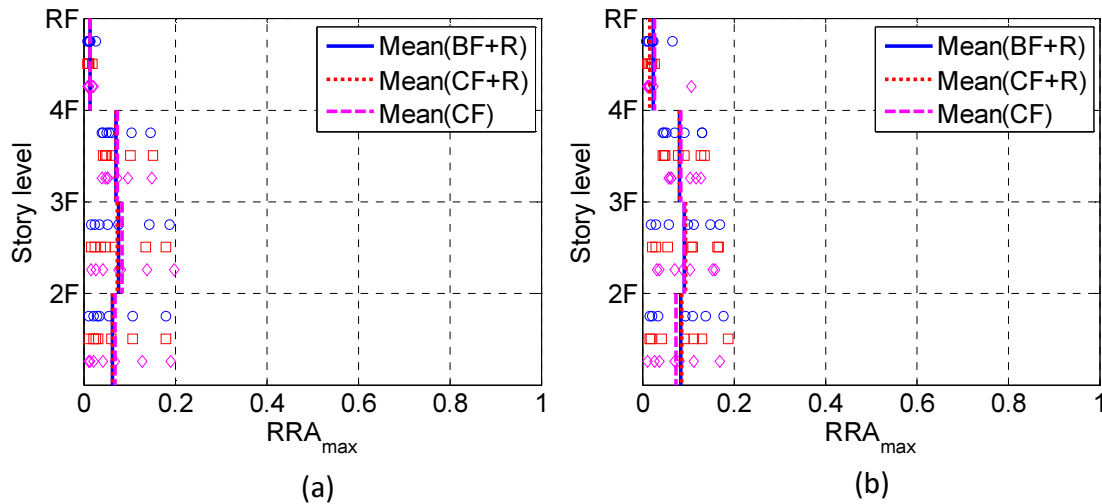


Figure 5-36 Maximum relative rotation angle of diaphragms C1:  $M_{ta\_1}$  (a) DBE and (b) MCE

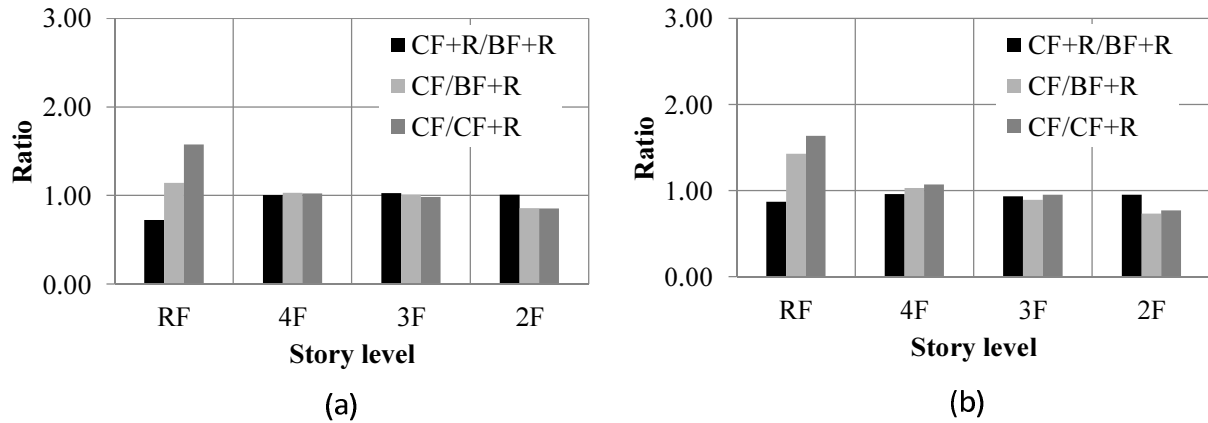


Figure 5-37 Ratios of Maximum relative rotation angle of diaphragms for C1 under MCE: (a)  $M_{Ia_1}$  and (b)  $M_{Ia_2}$

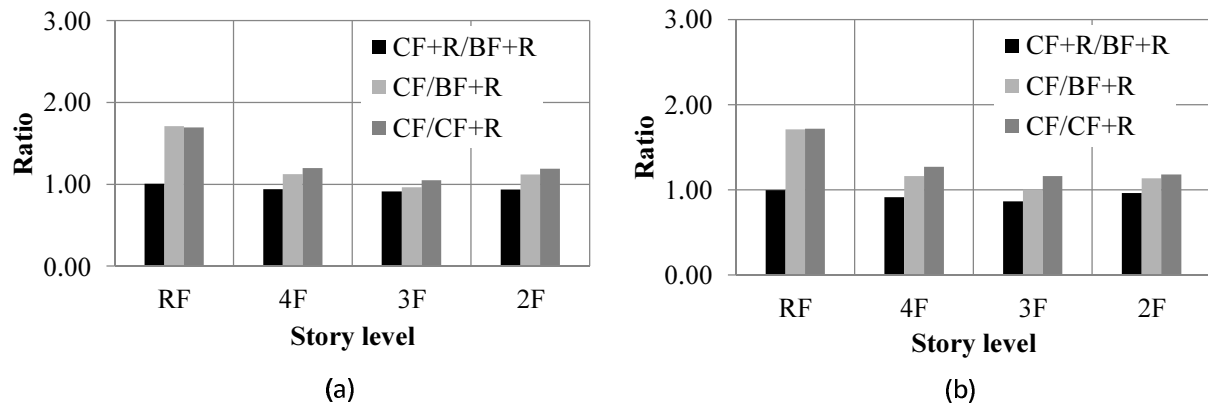


Figure 5-38 Ratios of Maximum relative rotation angle of diaphragms for C2 under MCE: (a)  $M_{Ia_1}$  and (b)  $M_{Ia_2}$

Figure 5-39 (a) illustrates the history of  $RRA$  for C1 during the EI Centro-DBE-level ground motion. The magnitude of  $RRA$  for each story from 0.0 to 2.2 sec is roughly the same, indicating that the diaphragms are rotating without developing inelastic behavior in the entire structure. However, the  $RRA$  in the 2<sup>nd</sup> and 3<sup>rd</sup> story increases significantly after 2.2 sec. because of the buckling of braces. Once inelasticity has been developed in a story, the corresponding lateral stiffness reduces. Therefore, the “period” of the  $RRA$  of these two stories becomes lower than that of the other stories.

In this scenario, the behavior of out-of phase rotation between the two stories (2<sup>nd</sup> and 3<sup>rd</sup> story) can be detected from 2.2 sec. to 4.0 sec. as shown in Figure 5-39 (b). If braces buckle in other stories, the differences in the lateral stiffness among the stories diminish, and the magnitude of the out-of phase behavior reduces. This phenomenon can be detected in *RRA* history after 30.0 sec. shown in Figure 5-39 (c).

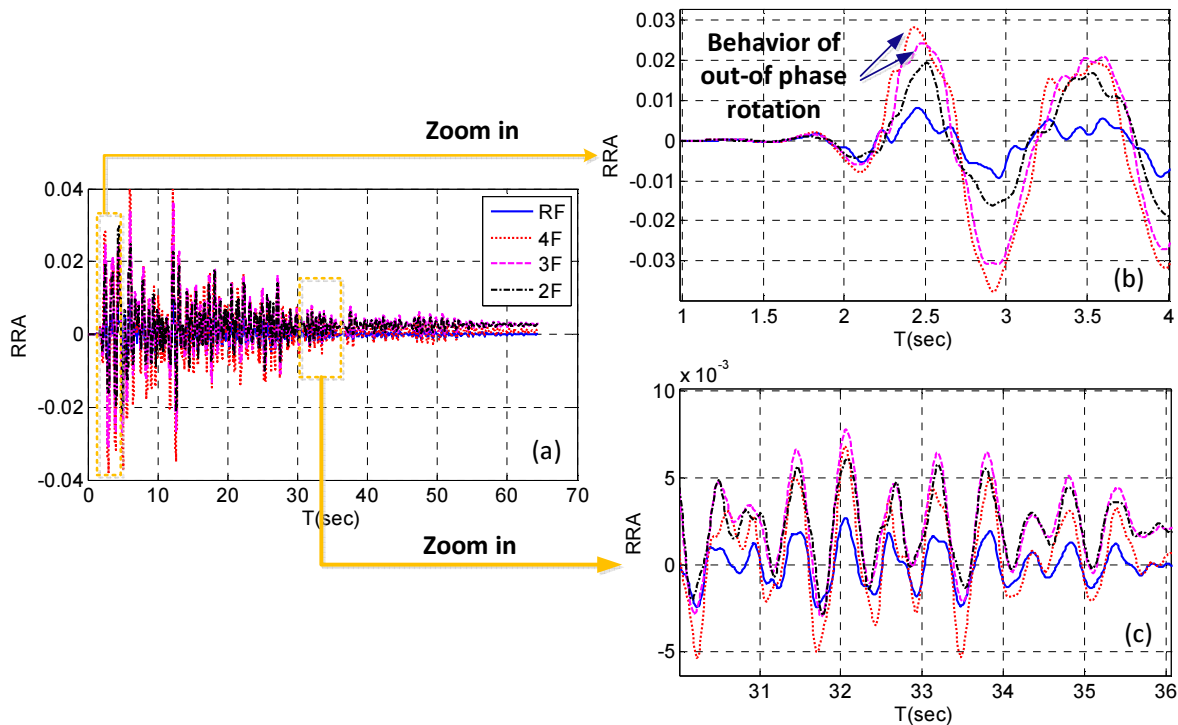


Figure 5-39 Relative rotation angle history of stories for C1 in DBE ground motion (EI-Centro)

### 5.5.3 Maximum inter-story drift ratios

The maximum inter-story drift ratio ( $IDR_{max}$ ) obtained from an NDA is one of the most important used to evaluate the seismic performance of structures. In this study, both the *IDR* and the *RRA* are the two independent indexes used to evaluate the elastic and inelastic behavior of the theme structures. The *RRA* is used to assess the relative horizontal irregularity of the target stories, while the *IDR* is used to evaluate the relative vertical irregularity of the structures. Another important goal for this study is the comparison of the  $IDR_{max}$  between the structures

with rigid (**BF+R** and **CF+R**) and semi-rigid diaphragms (**CF**) as this ratio may be significantly affected by the in-plane stiffness of diaphragm as well as the structural configurations.

To understand the influence on the *IDR* caused by the  $M_{ta\_1}$  or  $M_{ta\_2}$ , this section includes a comparison result of *IDR* between the structures with (1)  $M_{ta\_1}$  and  $M_{ta\_2}$  and (2) the effect of in-plane diaphragm stiffness. Figure 5-40 illustrates the history of *IDR* in C1 structures under the EI Centro ground motion.

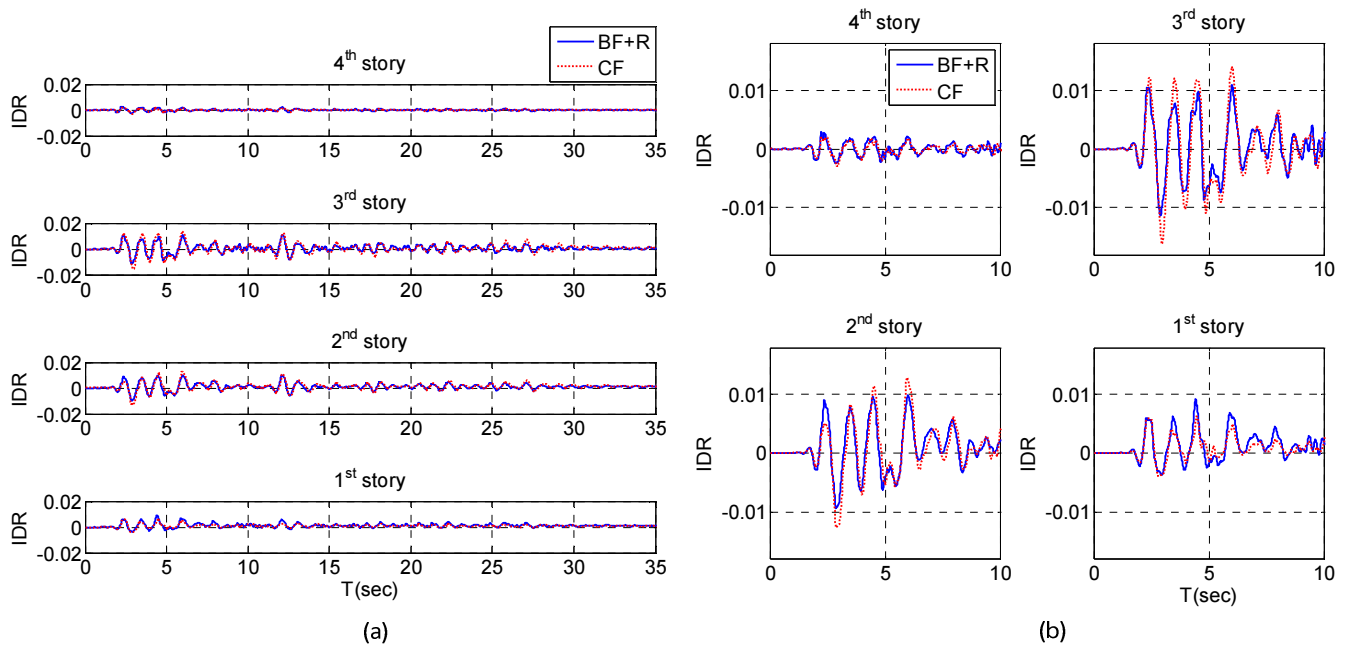


Figure 5-40 Inter-story drift ratios in C1 (with  $M_{ta\_1}$ ) under EI-Centro ground motion at the DBE-level: (a) entire history and (b) 0.0~10.0 sec.

For the inter-story drift ratios along the X-dir and Y-dir in the C1 structures shown in Figure 5-41, the ratios between rigid and semi-rigid structures do not evidence a significant difference. The  $IDR_{max}$  in X-direction is caused by the effect of  $M_{ta\_1}$ . The mean of  $IDR_{max}$  along major (Y-dir) and minor direction (X-dir) among **BF+R**, **CF+R** and **CF** are similar. However, for the C1 structure with bi-axial ground motion inputs (i.e  $M_{ta\_2}$ ) as illustrated in Figure 5-42, the average  $IDR_{max}$  along Y-dir in the 1<sup>st</sup> and 2<sup>nd</sup> story in the semi-rigid diaphragm structures (i.e **CF**) is

significantly lower than the one with rigid diaphragms at the MCE-level. However, the Y-dir  $IDR_{max}$  at 4<sup>th</sup> story in CF is higher than the other two structures with rigid diaphragm constraints. The phenomenon is caused by the development of significant higher mode effects in the C1 structures with semi-rigid diaphragms structures.

The ratios of  $IDR_{max}$  between (1) **CF+R** and **BF+R** (2) **CF** and **BF+R** and (3) **CF** and **CF+R** in C1 and C2 are shown in Figure 5-43 and Figure 5-44. The ratio (CF/CF+R) is higher than the corresponding ratio (CF+R/BF+R) in most of the stories. For example, (CF/CF+R) is 1.50 (Roof) and 2.00 (Roof) for the C1 and C2 configurations, respectively. However, (CF+R/BF+R) is around 1.00 for both the C1 and C2 configurations. This indicates the effects of rigid diaphragm constraints on the both theme structures are higher than those from composite action in terms of the magnitudes of  $IDR_{max}$ . In addition, the ratios (i.e. CF/BF+R and CF/CF+R) at the roof level are significantly higher than the ones at the other stories indicating that the higher modes are contributing. Moreover, the (CF+R/BF+R) ratios are smaller than 1.0 meaning that the composite action reduces the  $IDR_{max}$  slightly in both configurations.

The inclusion of bi-axial ground motions also plays a role in terms of  $IDR_{max}$ . The structures with  $M_{ta\_2}$  have higher (CF/BF+R and CF/CF+R) ratios than those with  $M_{ta\_1}$  particularly for the roof level. This indicates the inclusion of  $M_{ta\_2}$  may stimulate larger contributions of higher modes.

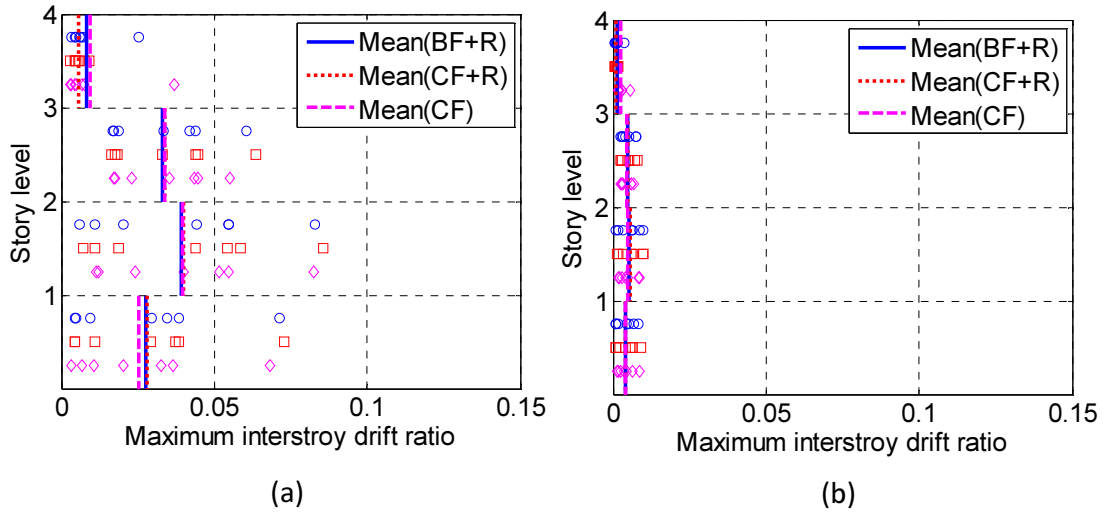


Figure 5-41 Maximum inter-story drift ratios of C1 with  $M_{ta_1}$  in MCE: (a) Y-dir and (b) X-dir

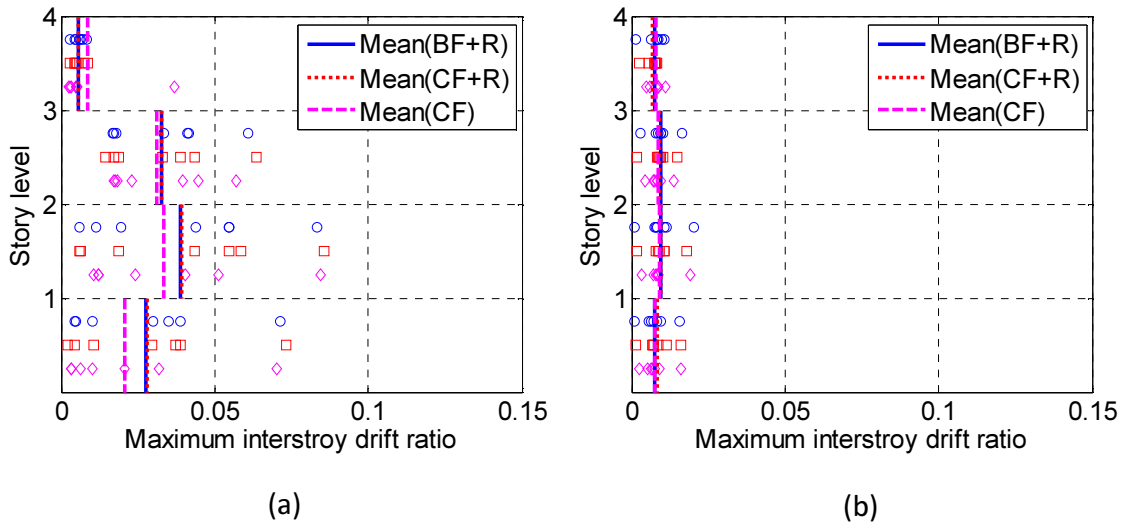


Figure 5-42 Maximum inter-story drift ratios of C1 with  $M_{ta_2}$  in MCE: (a) Y-dir and (b) X-dir

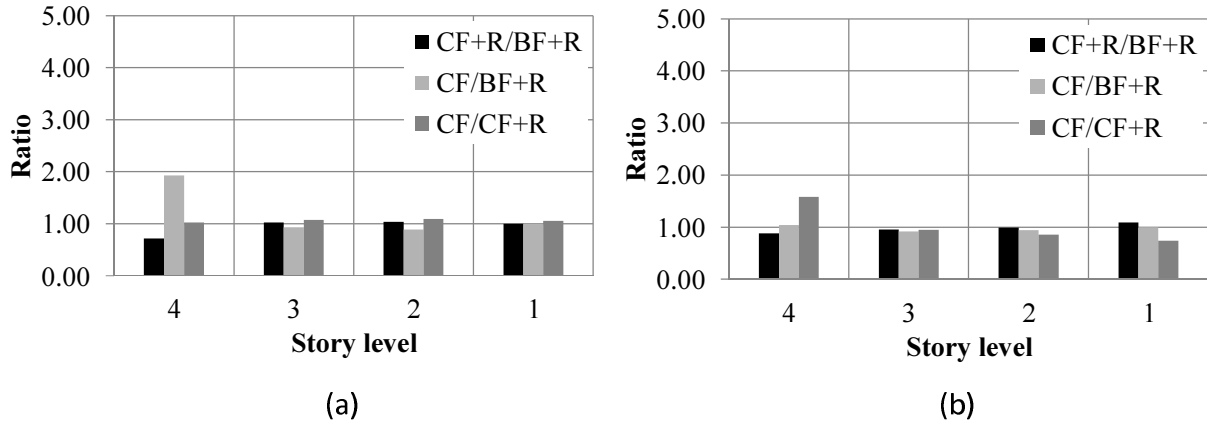


Figure 5-43 Maximum inter-story drift ratios ratio in C1 at MCE-level: (a)  $M_{ta\_1}$  and (b)  $M_{ta\_2}$

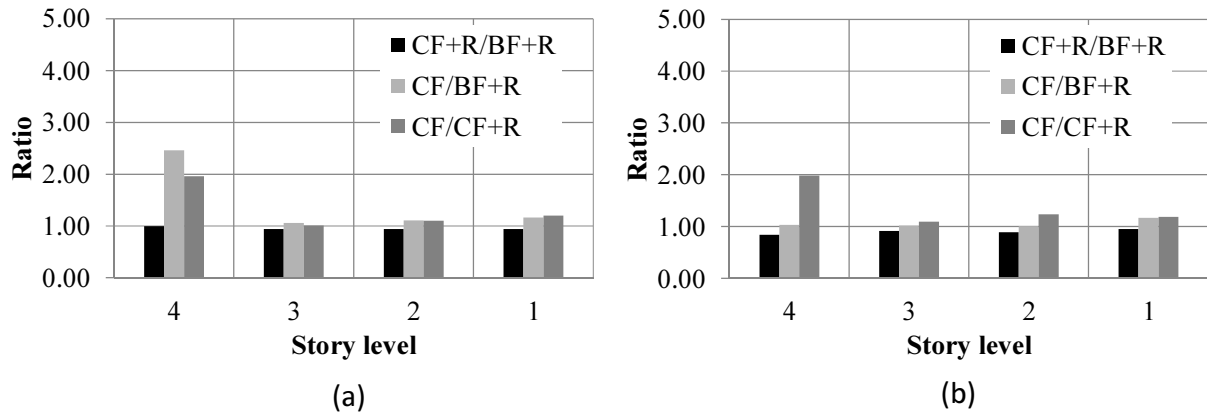


Figure 5-44 Maximum inter-story drift ratios ratio in C2 at MCE-level: (a)  $M_{ta\_1}$  and (b)  $M_{ta\_2}$

### 5.5.4 Maximum roof drift ratios and base shears

This section compares maximum roof drift ratios ( $RDR_{max}$ ) and base shear ( $V/W_{max}$ ) for the theme structures along the Y-direction. These results are summarized in Table 5-8 and Table 5-9. The actual results are given in Figure 5-45 to Figure 5-48, where the three solid and dotted lines correspond to the mean  $V/W_{max}$  and the mean  $RDR_{max}$  extracted from the NDA under the seven selected ground motions.

One can observe that most of the  $RDR_{max}$  in the semi-rigid diaphragm structures ( $CF$ ) are higher than those with rigid diaphragm ( $BF+R$  and  $CF+R$ ) under both the DBE and MCE-level motions. In addition, the magnitude of base shear in the structures with semi-rigid diaphragms ( $CF$ ) is

lower than those with rigid diaphragms (**BF+R** and **CF+R**). Synthesis of these results leads to the following conclusions:

- (1) The magnitudes of base shear ratios are higher for the structures with rigid diaphragms than for those with semi-rigid diaphragms for the two configurations. For instance, the (CF/BF+R) ratio for base shear in C1 ranges between 0.96 to 0.98 as shown in Table 5-8. This is due to the contribution of the infinite in-plane diaphragm stiffness, which is included in the simulation of 3D analytical models with rigid diaphragms. Therefore, the global structural lateral stiffness of the structures with rigid diaphragms is increased by the assumption and leads to a higher base shear.
- (2) The difference in the  $RDR_{max}$  between rigid and semi-rigid structures is significant. For example, (CF/BF+R) ratio for  $RDR_{max}$  in configuration C2 ranges from 1.15~1.04 as shown in Table 5-9. This indicates that the removal of rigid diaphragm constraint significantly increases the  $RDR_{max}$  in the asymmetric structure. In other words, the robust in-plane force transfer mechanism in the rigid diaphragms results in a lower magnitude of  $RDR_{max}$ .
- (3) The composite action improves the strength of structures very slightly. Comparing the base shear ratios of (CF+R/BF+R) for the C1 and C2 configurations, one can observe the magnitudes of base shear ratio are increased by 1~3%. The possible reason is the seismic loads are resisted by SCBFs primarily in these analytical models. The ultimate strength of 2D X-braced frames is not influenced by the composite action significantly as illustrated in Figure 4-3. Therefore, the SCBFs are slightly affected by the composite action in the 3D models. The composite action is important on the SMRFs in the 3D models when the

structures rotate, but this effect is not significant because the SMRFs are the secondary systems to resist the seismic loads.

- (4) For the inclusion of the bi-axial ground motion inputs, the  $V/W_{max}$  and  $RDR_{max}$  in the models with  $M_{ta\_2}$  is slightly lower than those with  $M_{ta\_1}$ . The results indicate the variations of these two parameters may not be significantly influenced by the ground motions applied in the minor direction.

Table 5-8 Relationship between mean  $V/W_{max}$  and  $RDR_{max}$  in C1 structure

<b>Mta_1</b>		<b>BF+R</b>	<b>CF+R</b>	<b>CF</b>	<b>CF+R/BF+R</b>	<b>CF/BF+R</b>
<b>DBE</b>	$V/W_{max}$	0.317	0.3252	0.3054	<b>1.03</b>	<b>0.96</b>
	$RDR_{max}$	0.0162	0.0161	0.0173	<b>0.99</b>	<b>1.07</b>
<b>Mta_2</b>		<b>BF+R</b>	<b>CF+R</b>	<b>CF</b>	<b>CF+R/BF+R</b>	<b>CF/BF+R</b>
<b>DBE</b>	$V/W_{max}$	0.3169	0.3252	0.3059	<b>1.03</b>	<b>0.97</b>
	$RDR_{max}$	0.0162	0.0161	0.017	<b>0.99</b>	<b>1.05</b>
<b>Mta_1</b>		<b>BF+R</b>	<b>CF+R</b>	<b>CF</b>	<b>CF+R/BF+R</b>	<b>CF/BF+R</b>
<b>MCE</b>	$V/W_{max}$	0.3235	0.3271	0.3165	<b>1.01</b>	<b>0.98</b>
	$RDR_{max}$	0.025	0.0255	0.0252	<b>1.02</b>	<b>1.01</b>
<b>Mta_2</b>		<b>BF+R</b>	<b>CF+R</b>	<b>CF</b>	<b>CF+R/BF+R</b>	<b>CF/BF+R</b>
<b>MCE</b>	$V/W_{max}$	0.3238	0.327	0.3166	<b>1.01</b>	<b>0.98</b>
	$RDR_{max}$	0.0251	0.0252	0.0218	<b>1.00</b>	<b>0.87</b>

Table 5-9 Relationship between mean  $V/W_{max}$  and  $RDR_{max}$  in C2 structure

<b>Mta_1</b>		<b>BF+R</b>	<b>CF+R</b>	<b>CF</b>	<b>CF+R/BF+R</b>	<b>CF/BF+R</b>
<b>DBE</b>	$V/W_{max}$	0.484	0.489	0.476	<b>1.01</b>	<b>0.98</b>
	$RDR_{max}$	0.006	0.006	0.007	<b>0.94</b>	<b>1.15</b>
<b>Mta_2</b>		<b>BF+R</b>	<b>CF+R</b>	<b>CF</b>	<b>CF+R/BF+R</b>	<b>CF/BF+R</b>
<b>DBE</b>	$V/W_{max}$	0.484	0.489	0.475	<b>1.01</b>	<b>0.98</b>
	$RDR_{max}$	0.0062	0.0058	0.007	<b>0.94</b>	<b>1.13</b>
<b>Mta_1</b>		<b>BF+R</b>	<b>CF+R</b>	<b>CF</b>	<b>CF+R/BF+R</b>	<b>CF/BF+R</b>
<b>MCE</b>	$V/W_{max}$	0.5095	0.5103	0.5121	<b>1.00</b>	<b>1.01</b>
	$RDR_{max}$	0.0126	0.0123	0.0132	<b>0.98</b>	<b>1.05</b>
<b>Mta_2</b>		<b>BF+R</b>	<b>CF+R</b>	<b>CF</b>	<b>CF+R/BF+R</b>	<b>CF/BF+R</b>
<b>MCE</b>	$V/W_{max}$	0.5095	0.51	0.5117	<b>1.00</b>	<b>1.00</b>
	$RDR_{max}$	0.0126	0.0121	0.0131	<b>0.96</b>	<b>1.04</b>

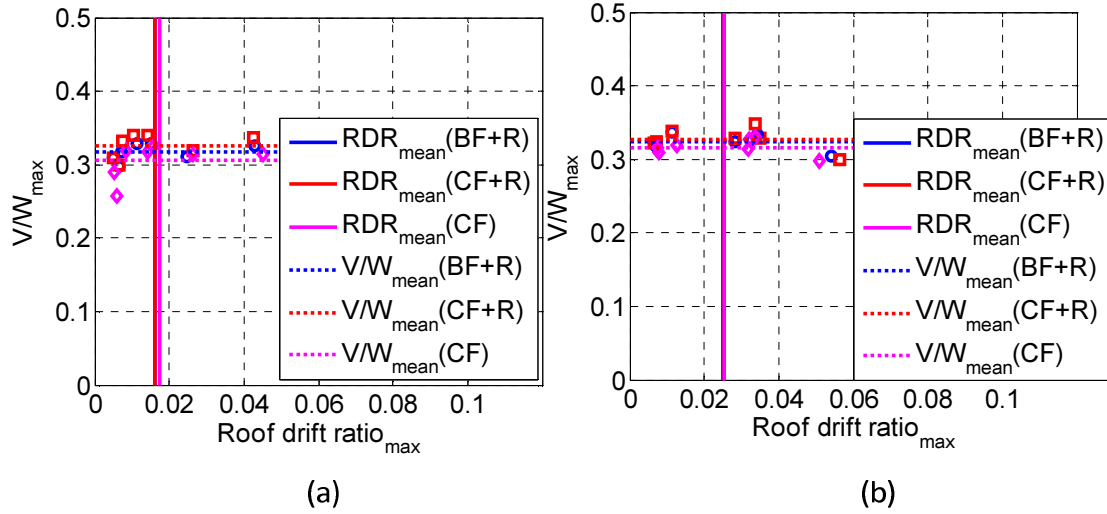


Figure 5-45 Maximum roof drift ratios vs.  $V/W_{max}$  in C1 structures with  $M_{ta_1}$ : (a) DBE and (b) MCE

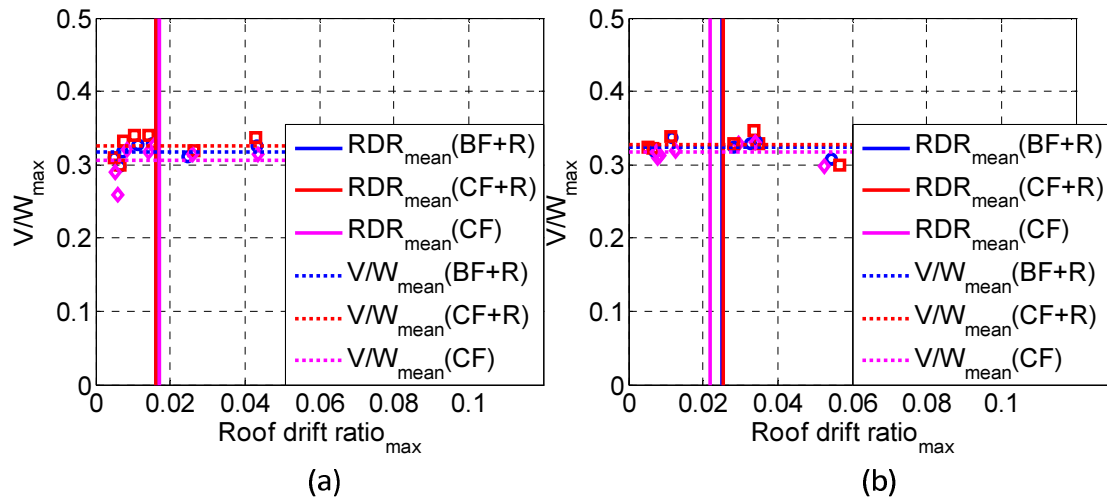


Figure 5-46 Maximum roof drift ratios vs.  $V/W_{max}$  in C1 structures with  $M_{ta_2}$ : (a) DBE and (b) MCE

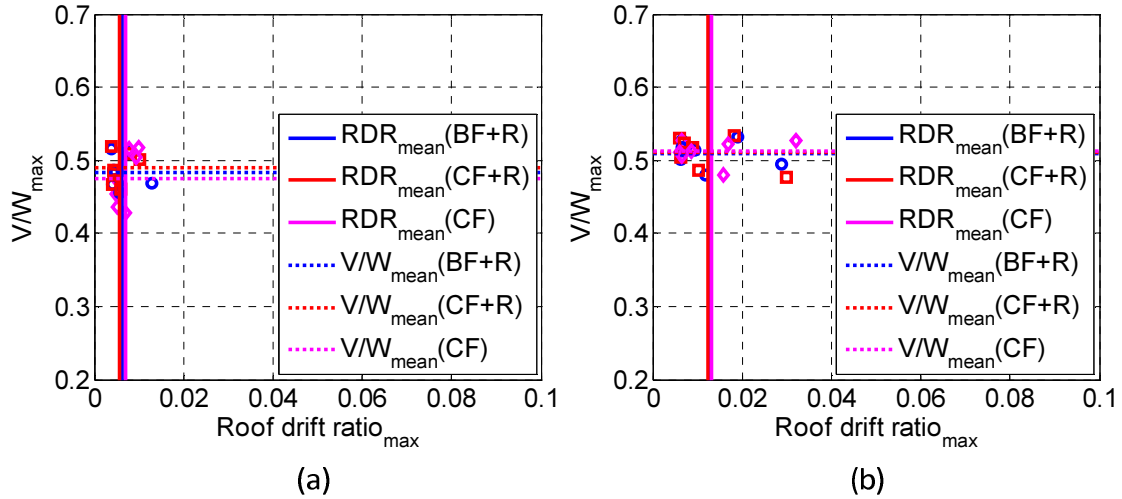


Figure 5-47 Maximum roof drift ratios vs.  $V/W_{max}$  in C2 structures with  $M_{ta_1}$ : (a) DBE and (b) MCE

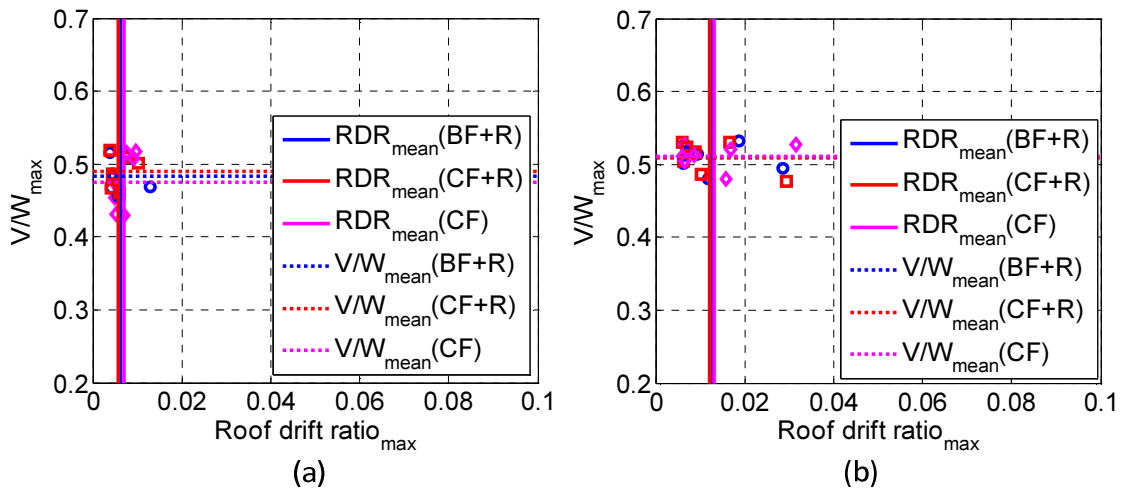


Figure 5-48 Maximum roof drift ratios vs.  $V/W_{max}$  in C2 structures with  $M_{ta_2}$ : (a) DBE and (b) MCE

## 5.6 Conclusions

The nonlinear behavior of the theme structures considering (1) the effect of  $M_{ta}$  and (2) different in-plane diaphragm stiffness can be evaluated can be summarized as follows:

1. The inelastic behavior of the LFRS significantly affects the torsional irregularity of the structures: For the C1 and C2 structures, an inherent and accidental torsion exists in the

structures in the elastic stage due to the asymmetric configurations of (1) vertical LFRS and (2) mass distribution. In this scenario, the inelastic behavior initially develops in some structural components at one of the SCBF first, leading to the development of a soft story in that vertical LFRS. A significant increment of torsional irregularities in the structures is generated in both NSA and NDA by the resulting structural rotation. The magnitude of the  $TC$  in the inelastic stage is significantly higher than that from the boundary defining the existence of the extreme torsional irregularity as given by ASCE7. In other words, the position of C.R on each diaphragm may diverge significantly from that assumed in design when the structure enters into the inelastic stage.

2. The inclusion of bi-axial effect leads to an increment of the  $TC$  as well as to the decrease in ultimate strength: According to the results from NSA, the magnitudes of  $TC$  increase slightly due to the application of the load patterns along the minor axis. In addition, the ultimate strengths of analytical models decrease slightly due to the bi-axial effects. This indicates the strength demands in structural members of the LFRS increases as well.
3. The ultimate strength of the structures with rigid diaphragm constraints ( $BF+R$  and  $CF+R$ ) is slightly higher than the one with semi-rigid diaphragms ( $CF$ ): The inclusion of infinite in-plane diaphragm stiffness leads to a higher strengths of structures in the both NSA and NDA. In other words, the change of diaphragm assumptions affects the pre-buckling and ultimate strengths of the structures.
4. The effect of composite action in terms of lateral stiffness and strength is more significant in the asymmetric structures (C2): By implementing NDA in the 3D structures with rigid or semi-rigid diaphragms, the inclusion of composite action was shown to increase the structural capacity and reduce the maximum roof drift slightly.

5. The higher mode effects are significant in the semi-rigid models under bi-axial loading in the asymmetric structures: Based on the analytical results of NDA with  $M_{ta\_2}$  in the asymmetric  $CF$  structure, the increments of  $RRA_{max}$  and  $IDR_{max}$  are significant when compared with those of asymmetric  $CF$  structure with  $M_{ta\_1}$ . This indicates that the effect from higher modes is increased due to the removal of rigid diaphragm constraints in such structures.
6. The structures with rigid diaphragms have a higher torsional response in the NSA: For the structures with asymmetric configurations (i.e. C2), the assumption of rigid diaphragm may cause a higher magnitude of torsional irregularities. The difference in the (a) robustness of in-plane force transfer mechanisms and (b) pushover load patterns (i.e. concentrated loads or distributed loads) between the structures with rigid and semi-rigid diaphragms are the two possible reasons that cause the phenomenon.
7. From the results from NDA, the average  $RDR_{max}$  and  $IDR_{max}$  in the asymmetric structures with semi-rigid diaphragms ( $CF$ ) are higher than the one with rigid diaphragms ( $CF+R$ ): This indicates that the global ductility requirement of the structures with semi-rigid diaphragms is larger. A possible explanation is that significant higher mode effects due to the finite in-plane diaphragm rigidity can be developed in such models.
8. The contribution of base shear from moment frames in the structure increase after the SCBFs reach their ultimate capacities: From the NSA, the results show that the reactions in SMRFs increases significantly after the ultimate strengths develops in SCBFs. In addition, the contribution of gravity systems to the base shear is similar as those provided by SMRFs. In this scenario, the lateral resistance of the entire structure is primarily provided by these three systems instead of the SCBFs only.

## **Chapter 6 Behavior evaluation of peripheral frames in the 3D models**

### **6.1 Introduction**

This chapter concentrates on the behavior of the peripheral frames (SMRFs) in the 3D analytical models. In conventional seismic design procedures, such as the ELF procedure, the contribution of peripheral LFRS perpendicular to the direction being considered is generally not included. However, for (1) the asymmetric structures with horizontal torsional irregularity as defined in ASCE 7, and (2) the structures with accidental torsion, the effect of these peripheral LFRS on the global inelastic behavior and collapse resistance of the structures may be significant. These peripheral LFRS provide a primary resistance mechanism against the increment of inherent torsion ( $M_t$ ) and accidental torsion ( $M_{ta}$ ) in the inelastic range generated by the progressive damage to the principal LFRS. To investigate above issues, this chapter focuses on the evaluation of behavior of the peripheral moment frames (SMRFs) in the symmetric and asymmetric steel structures with rigid and semi-rigid diaphragms by conducting nonlinear static and dynamic analyses (NSA and NDA) in OpenSEES.

Section 6.2 discusses the global static behavior of the peripheral frames as gleaned from the NSA. Section 6.3 focuses on the P-M-M interaction behavior of the columns in the frames. Finally, Section 6.4 concentrates on the dynamic response of the peripheral frames from the NDA.

### **6.2 Behavior of peripheral moment frames in asymmetric structures**

In conventional design, the contribution of structural systems perpendicular to the direction of considered seismic loads is not included. However, when structures move into the inelastic range, the capacity provided by any structural system aligned in the perpendicular direction may play an important role. In this study, such system consists of ductile SMRFs, and as such, is assumed to

provide a significant contribution as the structure approaches its incipient collapse stage. In the case of symmetric structures, the SMRFs initially contribute resistance mostly through bending about the weak axis of the columns in the SMRFs. For the structures with asymmetric configurations and accidental torsion, however, the SMRFs contribute their capacity through in-plane frame action and out-of plane column flexure. This phenomenon (bi-axial bending in columns) is significant because of the increment of inherent torsion ( $M_t$ ) and accidental torsion ( $M_{ta}$ ) due to the structural horizontal irregularities and the shift in the center of mass.

Figure 6-1 illustrates the nomenclature and relationships between the roof lateral displacement and reactions for the longitudinal and transverse direction of the SMRFs in the symmetric (C1) and asymmetric (C2) structures. The considered seismic loads are applied in the Y-direction. The reactions and lateral displacement in the X-direction ( $\Delta_{X1}$ ,  $\Delta_{X2}$ ,  $V_{X1}$ ,  $V_{X2}$ ) in both SMRFs is generated by the  $M_t$  and  $M_{ta}$ . The monitor points for horizontal displacements in the SMRFs that will be used in the discussions in this chapter are also marked in Figure 6-1.

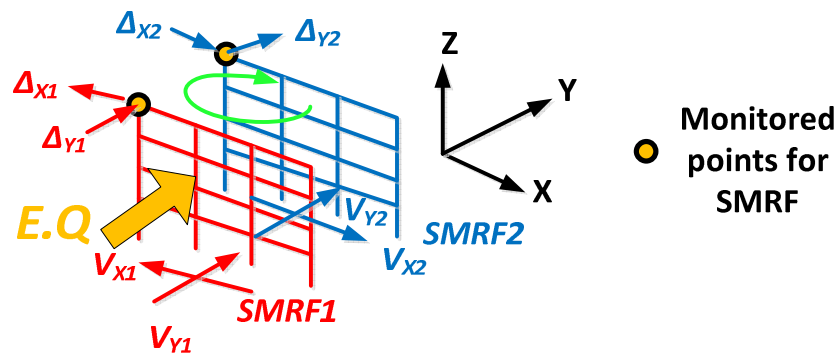


Figure 6-1 Nomenclature of roof displacements and reactions of the SMRFs

### 6.2.1 Discussion of the reaction curves for SMRFs

Figure 6-2 to Figure 6-5 illustrate the normalized base shear vs. interstory drift (or “reaction curves”) of the SMRFs in the transverse direction (X-direction) for the C1 and C2 structures.

Both roof drift ratios and reaction ratios are measured in the X-direction ( $\Delta_{X1}$ ,  $\Delta_{X2}$ ,  $V_{X1}$ ,  $V_{X2}$ ) and Y-direction ( $\Delta_{Y1}$ ,  $\Delta_{Y2}$ ,  $V_{Y1}$ ,  $V_{Y2}$ ) while the NSA loading is applied only in the Y-direction. Note that all quantities in the Y-direction refer exclusively to the SMRFs; the contributions of the SCBFs to the base shear in the Y-direction are not included in the figures.

In these figures, one can observe that the peak base shear for the SMRFs in the X-direction ( $V_{X1}$ ) in all structures is significantly higher than the base shear in the Y-direction ( $V_{Y1}$ ). The maximum  $V_{X1}$  in the C1 in the structures with semi-rigid diaphragms subjected to either  $M_{ta\_1}$  or  $M_{ta\_2}$  are  $0.062V_{X1}/W$  and  $0.073V_{X1}/W$ , respectively. The corresponding overstrength achieved with respect to the design base shears in the X-direction are 1.48 and 1.74, respectively. This compares with an  $\Omega_0$  of 2.27 for the SMRF in C1. For the C2 structures, the corresponding values are  $0.069V_{X1}/W$  and  $0.081V_{X1}/W$  for the base shears and 1.64 and 1.93 for the overstrength, respectively. This means that the SMRFs reach about 75% of their capacity even if the loads are applied in the perpendicular direction.

For both the C1 and C2 structures, their overstrength factors are significantly higher than 1.0. These high overstrength factors show that the rotation of the structures stimulated by asymmetric configurations as well as accidental torsion dominate the performance of peripheral frames. This also indicates the SMRFs are able to develop inelastic behavior even if the loads are applied perpendicularly if extreme torsional horizontal irregularities exist in the structure. In addition, the overstrength factors in C2 are higher than those in C1. This means the asymmetric structures result in higher magnitudes of both diaphragm rotation and base shears in the peripheral frames of the C2 structures.

From these figures, one can also observe the overstrength factors in the structures without rigid diaphragm constraints (**CF**) are higher than those of the other two structures (**BF+R** and **CF+R**).

The phenomenon indicates the peripheral moment frames may provide more torsional resistance in the 3D analyses when the rigid diaphragm constraints are removed, especially for asymmetric structures. This indicates that assuming rigid diaphragm action may not be a conservative assumption when looking at 3D behavior.

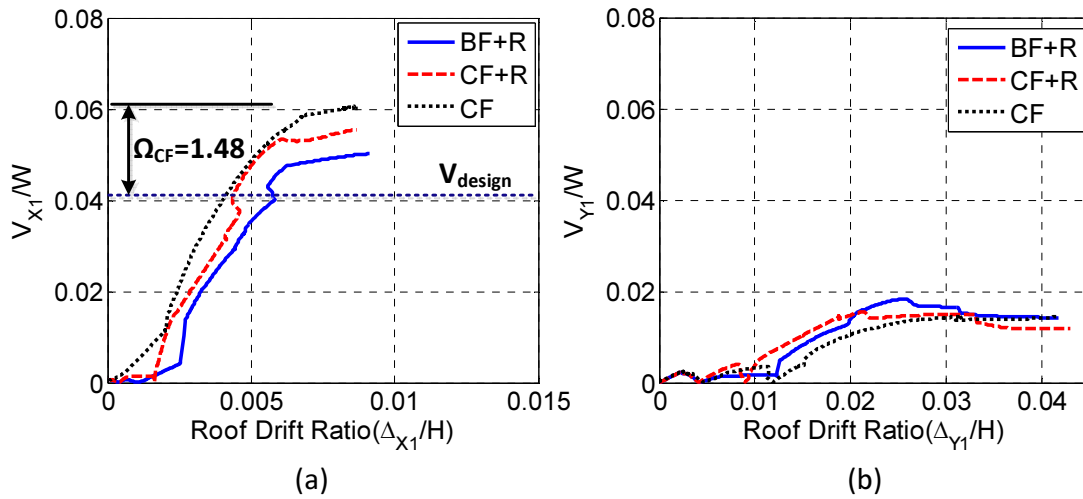


Figure 6-2 Normalized base shear vs. drift curves (reaction curves) for SMRFs in C1 with  $M_{ta\_1}$ :  
 (a)  $V_{X1}$  vs.  $\Delta_{X1}$  and (b)  $V_{Y1}$  vs.  $\Delta_{Y1}$

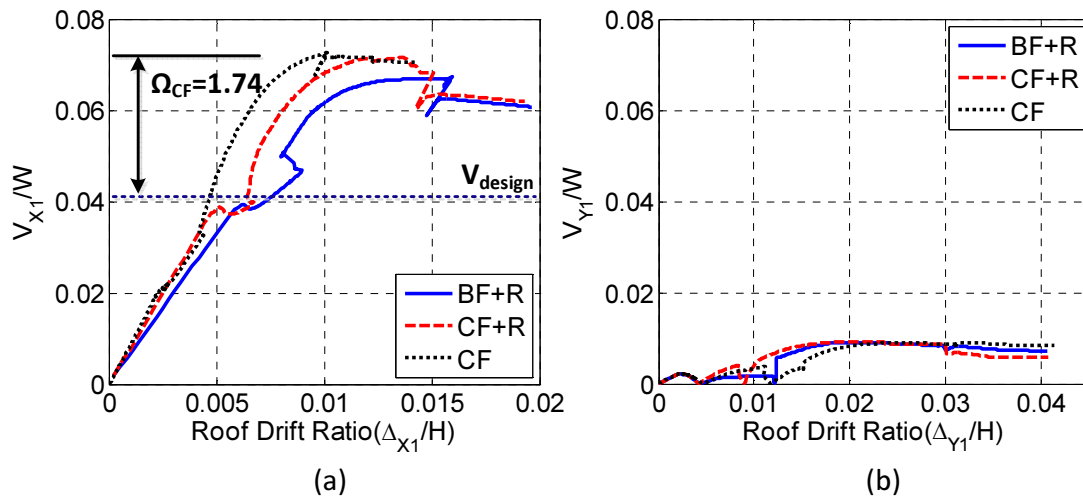


Figure 6-3 Normalized base shear vs. drift curves (reaction curves) for SMRFs in C1 with  $M_{ta\_2}$ :  
 (a)  $V_{X1}$  vs.  $\Delta_{X1}$  and (b)  $V_{Y1}$  vs.  $\Delta_{Y1}$

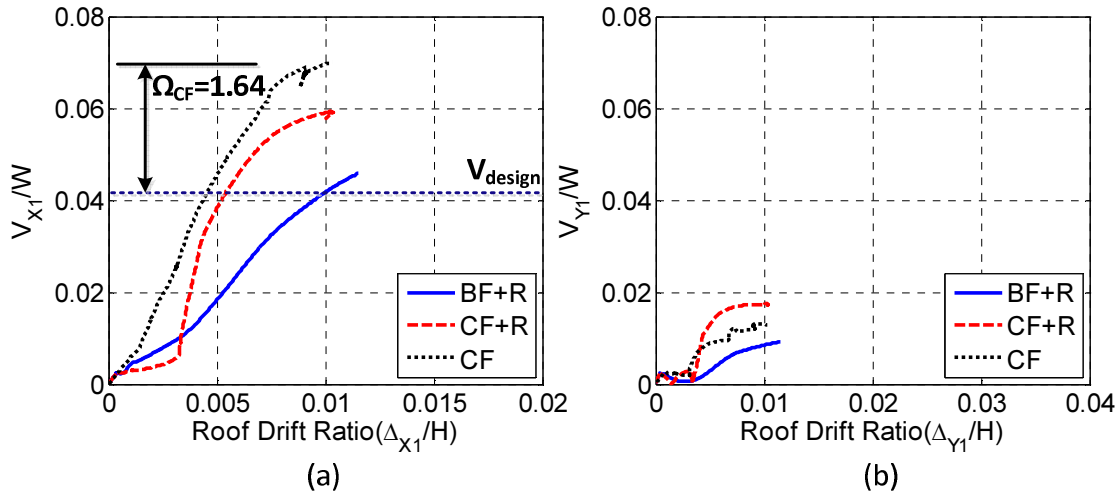


Figure 6-4 Normalized base shear vs. drift curves (reaction curves) for SMRFs in C2 with  $M_{ta\_1}$ :  
 (a)  $V_{X1}$  vs.  $\Delta_{X1}$  and (b)  $V_{Y1}$  vs.  $\Delta_{Y1}$

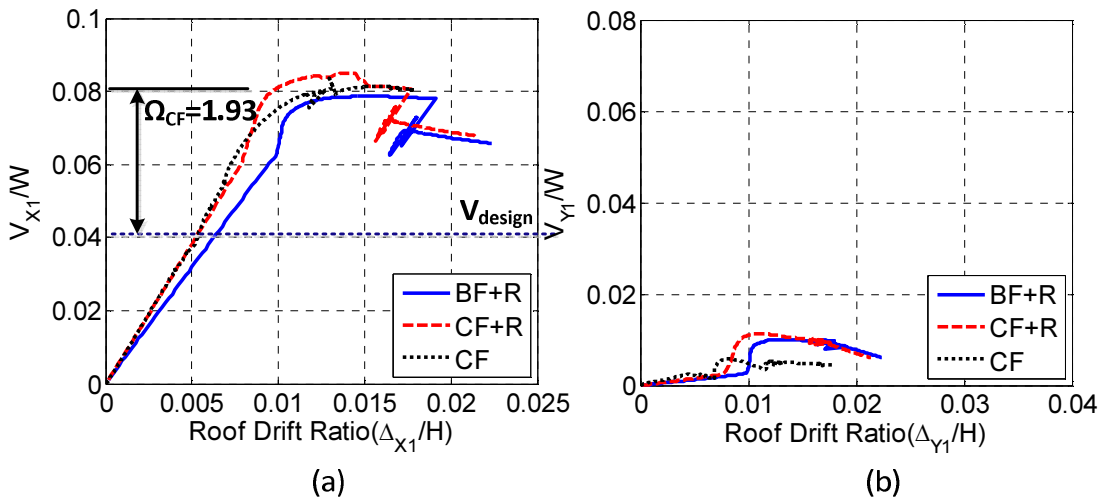


Figure 6-5 Normalized base shear vs. drift curves for (reaction curves) SMRFs in C2 with  $M_{ta\_2}$ :  
 (a)  $V_{X1}$  vs.  $\Delta_{X1}$  and (b)  $V_{Y1}$  vs.  $\Delta_{Y1}$

### 6.3 P-M-M interaction of the columns in moment and braced frames

In Section 6.2, the reaction curves of SMRFs corresponding to the principal direction (Y-dir) were determined from 3D pushover analyses. The results indicated that the moment frames in the structures of C1 and C2 structures are able to develop significant inelastic behavior. This section

evaluates the evaluation of inelastic behavior of the columns in the SMRFs by examining the interaction between axial force and bending moment (i.e. P-M-M interaction curves) in 3D.

Section *A*, located at the bottom of the left corner column in the moment frames as shown in Figure 6-6, is selected as the target section to evaluate the variation of P-M-M interaction. Section *A* is assumed as the most critical if structural rotation is considered. The bi-axial effect is considered in the evaluation also, as shown in Figure 6-6 (b). Table 6-1 lists the plastic moment capacities about both the strong and weak axis for Section *A*. The definitions of local strong (x) and weak (y) axis for Section *A* are shown in Figure 6-6 (c).

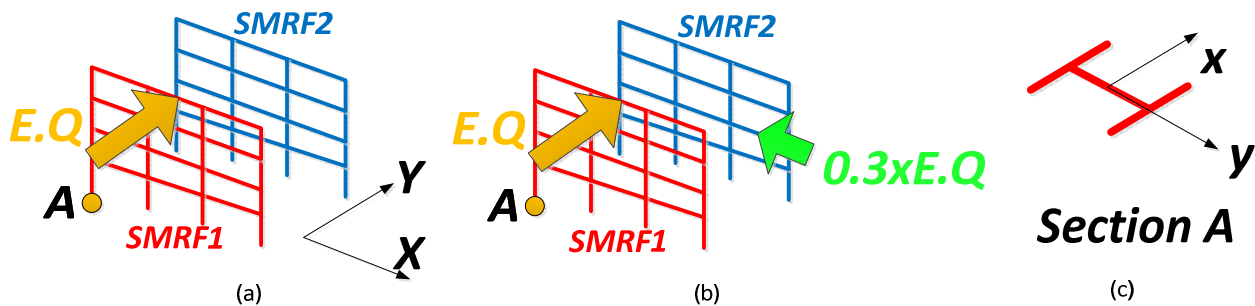


Figure 6-6 Position of selected section for P-M-M interaction evaluation

Table 6-1 Plastic moment of columns in braced and moment frames

Column at the 1 <sup>st</sup> story	SMRFs					
	Z <sub>x</sub>	F <sub>y</sub>	M <sub>px</sub>	Z <sub>y</sub>	F <sub>y</sub>	M <sub>py</sub>
	(in <sup>3</sup> )	(ksi)	(kips-in)	(in <sup>3</sup> )	(ksi)	(kips-in)
W14X211	390	50	21450	198	50	10890

The 3D yield surfaces (envelop) of W-shaped columns (Section *A*), including the interaction of axial force and bi-axial bending moment, can be described by Equation 6-1 [Orbison et al (1982)]. This equation was determined through a combination of experiments and curve fitting.

$$1.15\left(\frac{P}{P_y}\right)^2 + \left(\frac{M_x}{M_{px}}\right)^2 + \left(\frac{M_y}{M_{py}}\right)^4 + 3.67\left(\frac{P}{P_y}\right)^2 \left(\frac{M_x}{M_{px}}\right)^2 + 3.0\left(\frac{P}{P_y}\right)^6 \left(\frac{M_y}{M_{py}}\right)^2 + 4.65\left(\frac{M_x}{M_{px}}\right)^4 \left(\frac{M_y}{M_{py}}\right)^2 = 1.0$$

Equation 6-1

where  $P/P_y$  is the ratio of the axial force to the squash load.  $M_x/M_{px}$  is the ratio of the strong axis bending moment to the corresponding the expected plastic moment.  $M_y/M_{py}$  is the ratio of the weak axis bending moment to the corresponding the expected plastic moment.

For comparisons in this study, the nominal strong and weak axis plastic moment capacities of the columns in the SMRFs are amplified by 10% (i.e.  $R_y=1.10$ ) to the expected plastic moment. For the columns in the 1<sup>st</sup> story of SMRF (W14x211), the expected plastic moments about strong axis (X-axis) corresponds to the steel strain ranging from 0.18 to 0.20 of the extreme fiber in the section. Thus, the nominal plastic moments in Equation 6-1 are amplified accordingly, as follows:

$$M_{px} = R_y \times Z_x \times F_Y \quad \text{Equation 6-2}$$

$$M_{py} = R_y \times Z_y \times F_Y \quad \text{Equation 6-3}$$

where  $M_{px}$  and  $M_{py}$  are the expected plastic moment about the strong and weak axis of the columns in SMRFs.  $Z_x$  and  $Z_y$  are the plastic modulus about strong and weak axis of the columns in SMRFs, respectively.  $R_y$  is the yield stress adjustment factor selected as 1.10.

By comparing the 3D theoretical yield surface (envelope) extracted from Equation 6-1 with the variation of analytical P-M-M forces in Section A as the NSA progresses, one can determine the occurrence of inelasticity in these sections. The development of inelasticity is discussed in the following paragraphs. This discussion is meant to clarify the 3D behavior of the columns and to verify that the yield surfaces are not breached.

Figure 6-7 illustrates the P-M-M interaction for Section *A* in the C2 structures with  $M_{ta\_1}$  corresponding to the three different diaphragm assumptions. Points A, B and C are used to distinguish the different stages in terms of P-M-M interaction in the **CF+R** structures. Points 1, 2 and 3 are used to distinguish the different stages in terms of P-M-M interaction in the **CF** structures.

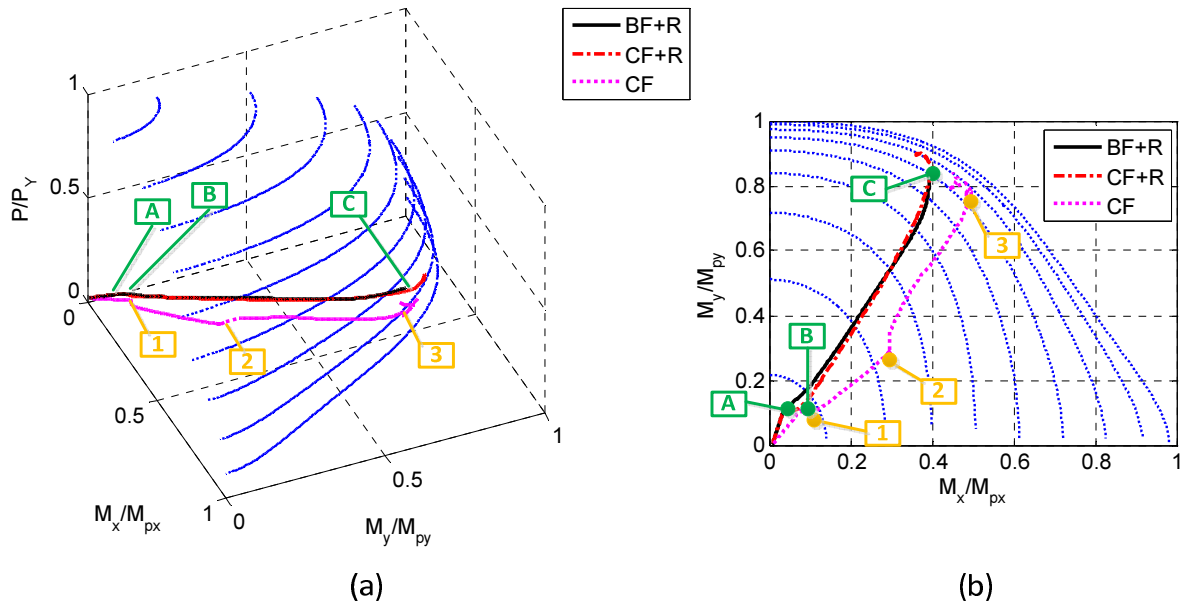


Figure 6-7 P-M-M interaction curves in moment frames in Section *A* in C2 with  $M_{ta\_1}$ : (a) 3D view and (b) 2D view

According to Figure 6-7, the interaction curve starts for the **CF** structure at the end of the gravity loading, for which the forces are small ( $0.037P/P_y$ ,  $0.0023M_x/M_{px}$ ,  $0.0023M_y/M_{py}$ ). In this curve, Point 1 corresponds to the development of the buckling of the 1<sup>st</sup> brace in the 3<sup>rd</sup> story, and Points 2 to 3 correspond to the buckling of the braces in BF1~BF3 in the 1<sup>st</sup> story, in sequence. The brace buckling in the 1<sup>st</sup> story leads to the significant increment of diaphragm rotation and results in similar magnitudes of  $M_x/M_{px}$  and  $M_y/M_{py}$  in Section *A* (i.e. Points 2 and 3). Point 3 corresponds to the brace fracture in the 3<sup>rd</sup> story for BF1, which results in a decrease of  $M_x/M_{px}$  in the column. The variation of  $M_x$  and  $M_y$  for Section *A* in C2 corresponds to the each stage is

shown in Figure 6-8 (b). One can observe that the force point motion stays on the yield surfaces after the development of Point 3. This indicates the Section *A* reaches its section expected strength.

The variation of P-M-M interaction of **CF+R** is also shown in Figure 6-7. A significant increment of  $M_y$  can be observed after Point B due to the simultaneous buckling of three braces in the 1<sup>st</sup> story in BF1~BF3. Therefore, the sharp increment of  $M_y$  that develops in Section *A* is caused directly by the severe rotation of the diaphragm. This phenomenon results in the difference in slopes between **CF** and **CF+R** after Point 1 and B as illustrated in Figure 6-7 (b).

Figure 6-8 illustrates the variations of  $M_x$  and  $M_y$  for structure C2 with different diaphragm stiffness. Both yield strengths of the section corresponding to the two principal axes ( $M_{y,yield}/M_{py}$ ,  $M_{x,yield}/M_{px}$ ) are marked in Figure 6-8. The magnitudes of  $M_y/M_{py}$  in both **CF+R** and **CF** structures are eventually larger than  $M_{y,yield}/M_{py}$  (0.790) as the NSA progresses. However, because biaxial bending is occurring, the representation in Figure 6-7 (b) is more realistic.

The axial force in this column (Figure 6-7 (a)), which is going into tension as the rotation starts, is small until initial buckling occurs (Point A and Point 1) and the SMRF begins to take significant loads. The trend of axial force ratio ( $P/P_y$ ) in Section *A* is shown as follows: Points A, B and C are 0.035, 0.050 and 0.090; Point 1, 2 and 3 are 0.036, 0.056 and 0.085 $P/P_y$ , respectively. This trend indicates the magnitude of axial force is small. Therefore, the axial force does not dominate the elastic and inelastic behavior of the section. This is consistent with the design assumption that the columns in the SMRF are flexural elements used to control drift.

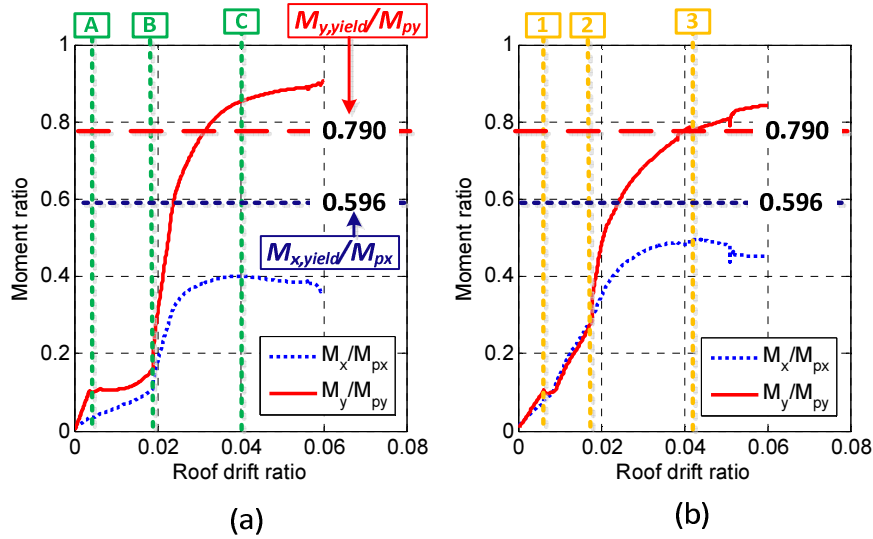


Figure 6-8 Variation of bi-axial bending in Section *A* in C2: (a) *CF+R* and (b) *CF*

Figure 6-9 and Figure 6-10 illustrate the P-M-M interaction of Section *A* in the C2 structure with  $M_{ta\_2}$ . For the *CF+R* and *CF* structures, the force point motion stays on the yield surfaces after the development of Points B and 3, respectively. This indicates the Section *A* reaches its section expected strength. One can observe that  $M_x$  dominates the section behavior in all structures with different diaphragm in-plane stiffness. The magnitude of  $M_x$  is significantly higher than the one of  $M_y$  before Point A and Point 1 in *CF+R* and *CF* structures. The magnitudes of  $M_x$  decrease as the lateral displacement along the Y-direction increases due to the rotation of the structure, which corresponds to Point 1~3 in *CF* and Point A~C in *CF+R*, respectively. The zigzags in the P-M-M interaction curves after Point C and Point 3 are caused by brace fractures. The results indicate the inclusion of bi-axial effect affect the inelastic behavior significantly.

In addition, both yield strengths of the section corresponding to the two principal axes ( $M_{y,yield}/M_{py}$ ,  $M_{x,yield}/M_{px}$ ) are marked in Figure 6-10. The magnitudes of  $M_x/M_{px}$  in both *CF+R* and *CF* structures are eventually higher than  $M_{x,yield}/M_{px}$  (0.596) as the NSA progresses.

Comparing Figure 6-10 with Figure 6-8, it is clear that for C2 bending about the strong axis is dominant.

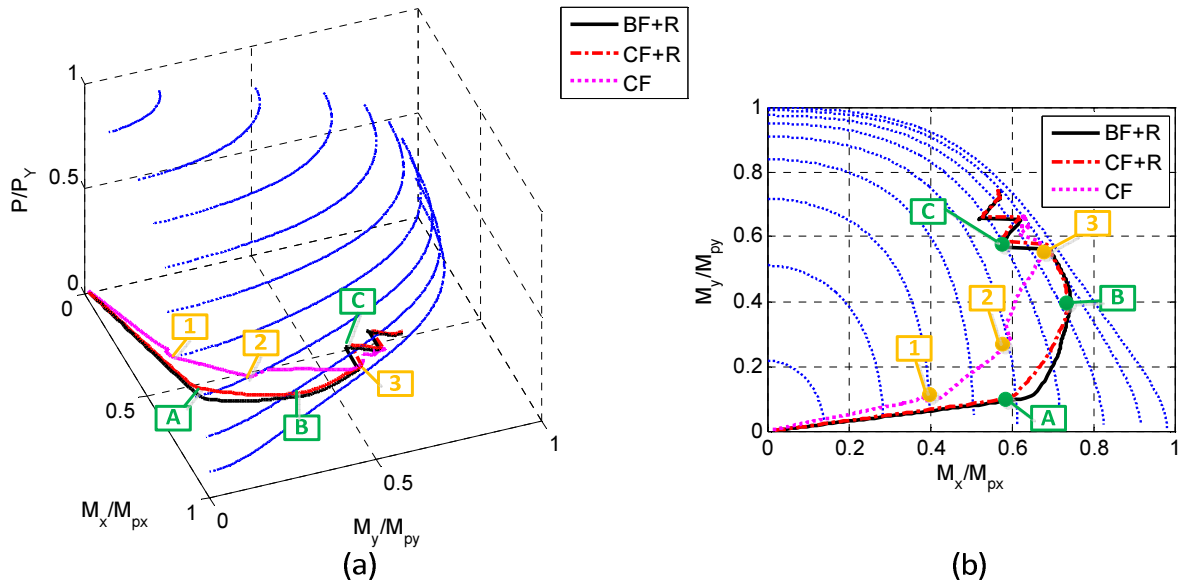


Figure 6-9 P-M-M interaction curves in moment frames in Section *A* in C2 with  $M_{ta_2}$ : (a) 3D view and (b) 2D view

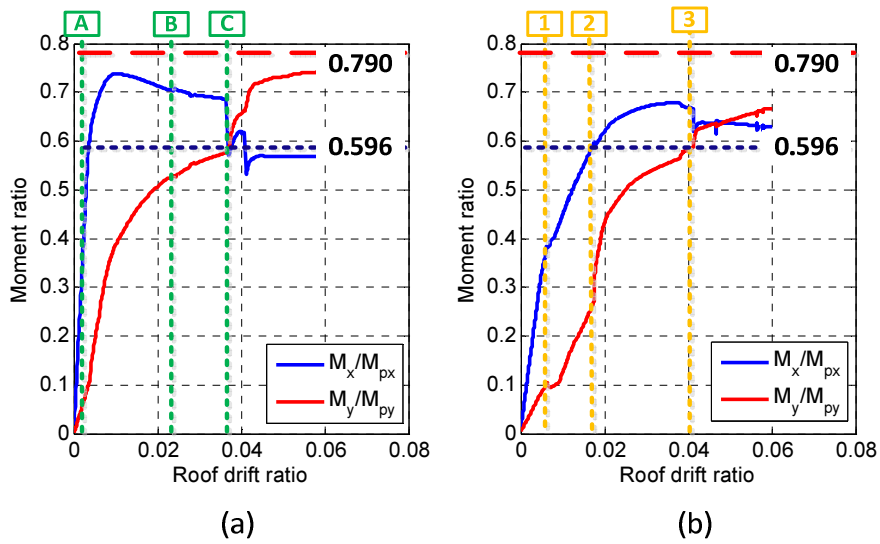


Figure 6-10 Variation of bi-axial bending in Section *A* in C2 with  $M_{ta_2}$ : (a) *CF+R* and (b) *CF*

#### 6.4 Dynamic response for peripheral frames

To investigate the dynamic behavior of moment frames (MF1) in the C1 and C2 structures, the relationships between peak base shear ratio and maximum roof drift ratios in the X-direction are extracted from NDA with the inclusion of  $M_{ta\_1}$  and  $M_{ta\_2}$ . Figure 6-11 and Figure 6-12 present the results of these relationships for the 7 ground motions studied (Subsection 3.11.3). For all structures, the increment of base shear in the X-direction is significant due to the bi-axial effect (i.e.  $M_{ta\_2}$ ). For instance, the mean base shear of **CF** in C2 increases from 0.0351 to  $0.0615V_{x1}/W$ , which is higher than the design base shear ( $V_{design}$ ) of  $0.042 V_{x1}/W$  for a SMRF. The results are listed in Table 6-2. The phenomenon shows the inclusion of bi-axial effect significantly increases the base shears in the peripheral frames of asymmetric structures.

The C2 structures without rigid diaphragm constraints (**CF**) show the largest increment for both the mean  $(V_{x1}/W)_{max}$  and the mean  $(RDR_{x1})_{max}$ . The difference in mean ratio of base shear  $(V_{x1}/W)_{max}$  and the mean ratio of roof drift  $(RDR_{x1})_{max}$  among **CF**, **BF+R** and **CF+R** is significant for the C2 structures as illustrated in Figure 6-12. The mean  $(V_{x1}/W)_{max}$  of the three structures with  $M_{ta\_2}$  are 0.0484, 0.0561 and 0.0615, respectively (Table 6-2). This indicates the in-plane rigidity of diaphragm plays an important role for the behavior of peripheral frames in the asymmetric structures.

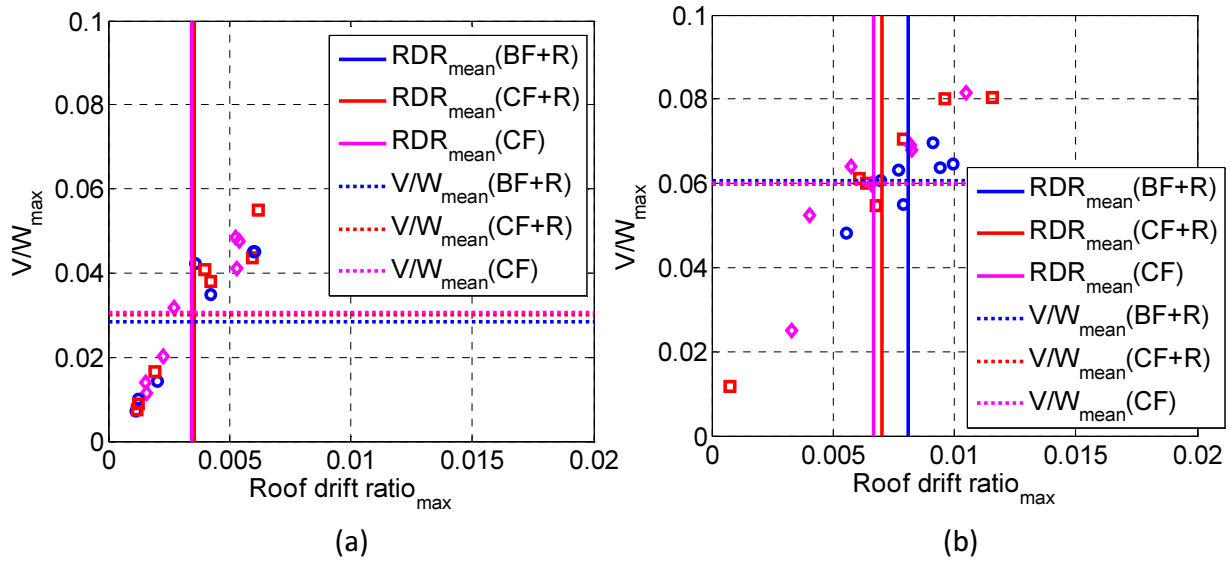


Figure 6-11 Base shear ratio vs. maximum roof drift ratio in MF1 in X-dir. for C1 under MCE-level ground motions: (a)  $M_{Ia_1}$  and (b)  $M_{Ia_2}$

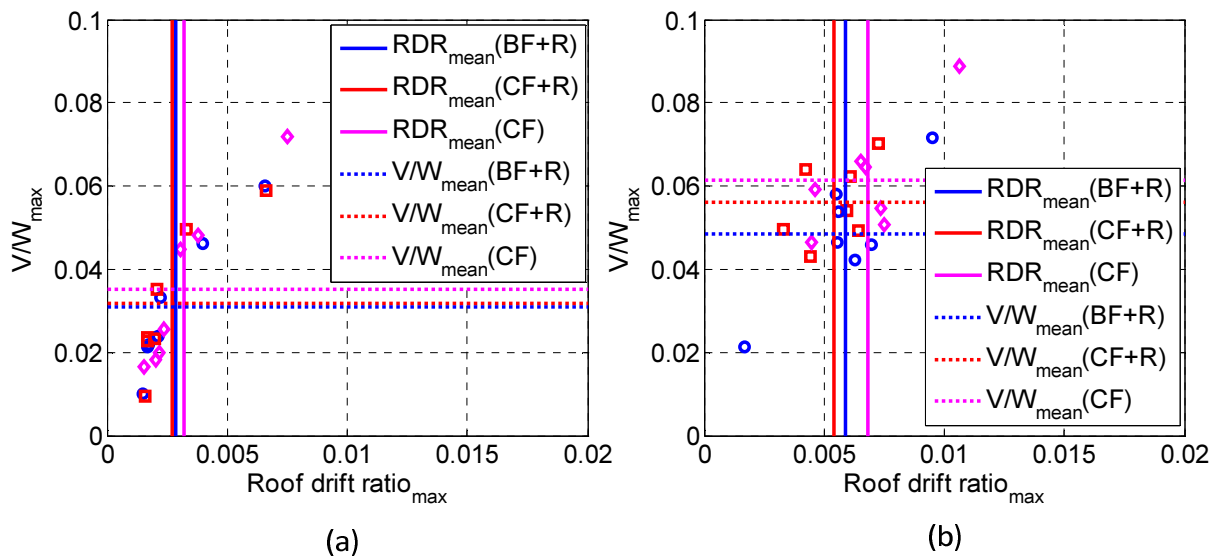


Figure 6-12 Base shear ratio vs. maximum roof drift ratio in MF1 in X-dir. for C2 under MCE-level ground motions: (a)  $M_{Ia_1}$  and (b)  $M_{Ia_2}$

Table 6-2 Mean  $(V_{x1}/W)_{max}$  vs.  $(RDR_{x1})_{max}$  in MF1 for C1 and C2 structures

MCE		BF+R		CF+R		CF	
		$M_{ta\_1}$	$M_{ta\_2}$	$M_{ta\_1}$	$M_{ta\_2}$	$M_{ta\_1}$	$M_{ta\_2}$
C1	$(V_{x1}/W)_{max}$	0.0284	0.0607	0.0300	0.0598	0.0306	0.0600
	$(RDR_{x1})_{max}$	0.0035	0.0081	0.0035	0.0070	0.0034	0.0067
C2	$(V_{x1}/W)_{max}$	0.0309	0.0484	0.0318	0.0561	0.0351	0.0615
	$(RDR_{x1})_{max}$	0.0028	0.0059	0.0027	0.0054	0.0032	0.0068

## 6.5 Conclusions

This chapter concentrated on the behavior of the peripheral moment resisting frames by through both NSA and NDA with loads applied along the Y-direction. Both  $M_{ta\_1}$  and  $M_{ta\_2}$  are included in the 3D model. The following are the conclusions extracted from the nonlinear analyses in the chapter:

1. The peripheral frames show higher demands on the asymmetric (C2) than in the symmetric (C1) configuration: According to the analytical results from the NSA, the peak base shear ratios along the X-direction in the C2 SMRFs are higher than those in the C1 SMRFs for both the  $M_{ta\_1}$  and  $M_{ta\_2}$  cases. This indicates the peripheral frames have higher magnitudes of base shear due to the larger diaphragm rotation in the asymmetric structures.
2. The columns in the 1<sup>st</sup> story in the LFRS (SMRFs) perpendicular to the direction of considered seismic loads may show inelastic behavior during the NSA for the C2 configuration. For this column, the inelasticity is developed at the base of the column due to the effect of bi-axial bending caused by the considered seismic loads as well as the irregular configurations. For the C2 structures with  $M_{ta\_1}$ , the inelasticity of the columns is dominated by the weak-axis bending. However, for the C2 structures with  $M_{ta\_2}$ , the section behavior is dominated by the strong-axis bending.

3. The asymmetric structures without rigid diaphragm constraints (**CF**) show the largest increment of the mean  $V_{x1}/W_{max}$  and the mean  $RDR_{x1,max}$  when such structures include the effect of  $M_{ta\_2}$ . The difference in mean  $V_{x1}/W_{max}$  and the mean  $RDR_{x1,max}$  among **CF**, **BF+R** and **CF+R** is significant for the C2 configuration. This indicates the in-plane rigidity of diaphragm provides a stronger in-plane constraint for the peripheral frames when the C2 structures rotate significantly. This leads to a smaller magnitude of base shear in the peripheral frames.

## Chapter 7 Seismic Behavior of Collectors and Chords

### 7.1 Introduction

This chapter focuses on the evaluation of forces on chords and collectors for the structures with semi-rigid diaphragms. Horizontal structural components in diaphragms, such as chords and collectors, are used for transferring the in-plane forces from diaphragms into the vertical LFRS. The collectors and chords may develop significant axial strengths and ductility demands to satisfy the compatibility of deformations between the diaphragms and horizontal structural components. Such behavior will result in chords and collectors behaving like beam-column elements. It is important to understand that the concept of chords and collectors is a useful abstraction for design purposes, but the actual load paths may be far more complex. The behavior of diaphragms idealized as deep beams may be better treated using structures bits models.

Current design provisions [AISC 360 (2010a)] suggests that the beam analogy can be used to evaluate the axial force demands in chords and collectors in regular rigid diaphragms regardless of the development of inelastic behavior in the LFRS and the effect of accidental torsion. In this approach, the seismic loads are distributed to the beams based on the diaphragm mass distribution, while the elastic supports of the beams are provided by the lateral stiffness of the vertical LFRS. In such a beam model, the internal forces in the beam, such as shears, are used to evaluate the axial forces in collectors. Two assumptions, either a uniform or a non-uniform distribution of the in-plane diaphragm shear, can be used for evaluating the magnitudes of axial force in the collectors.

However, because of the effects of on the distribution of in-plane diaphragm forces of (1)  $M_t$  and  $M_{ta}$ , (2) the potential cracking of the diaphragm and (3) the inelastic behavior of the LFRS, the elastic forces calculated for design using the beam analogy may not be the correct ones. To clarify the behavior of collector and chord under seismic loads, the two theme structures (C1 and C2) described in Chapter 3 are used for evaluating the variation of axial forces in collectors and chords. By comparing the analytical results with those from the beam analogy, the appropriateness of the latter can be evaluated.

In this chapter, Section 7.2 describes the diaphragm design based on ASCE 7. Section 7.3 and Section 7.4 discuss the behavior of collectors and chords from the NSA with considering the effect of  $M_{ta_1}$  and  $M_{ta_2}$ . The behavior of chords and collector from the NDA is discussed in Sections 7.5 and 7.6, respectively. In addition, the variation of the axial forces for collectors and chords is evaluated in Section 7.7, where the appropriateness of conventional beam analogy is discussed.

## **7.2 Diaphragm design based on ASCE 7**

This section concentrates on the design philosophy of collectors and chords based on the requirements of ASCE 7.

### **7.2.1 Collectors and chords**

The function of collectors and chords is to transfer the in-plane seismic forces from diaphragms into the vertical LFRS. On the basis of this definition, one can select several horizontal structural components in the diaphragms for each configuration as the target chords and collectors for investigating the variation of their axial forces. The beams near the LFRS are often defined as the primary collectors and chords for a specified direction of the seismic loads. In this study, the

primary direction of seismic loads is the same as the one in the previous chapters (i.e. Y-direction). Under this assumption, the beams connected to the braced frames are defined as collectors, and the other beams connected to the moment frames are chords. The approaches used for including of the effect of accidental torsion (i.e.  $M_{ta\_1}$  and  $M_{ta\_2}$ ) are the same as those shown in Figure 5-10. Figure 7-1 and Figure 7-2 illustrate the position of these members in each configuration. In addition, the notation for each vertical frame (BF1~BF4, MF1~MF2) is the same as defined in Figure 5-1. Figure 7-3 illustrates the positions of chords and collectors in a 3D view.

From the point of view of the analytical simulation, collectors and chords are part of the gravity system in a structure. Pinned connections at both ends of each collector and chord are used for connecting to the vertical LFRS, simulating conventional bolted shear tab connections. In the OpenSEES models, elastic beam-column elements with composite action are used for simulating the behavior of collectors and chords. The simulation details for chords and collectors in the internal and external vertical gravity frames are discussed in Subsections 3.5.6 and 3.5.7. The weak links in the chord and collector system are the axial resistance of the shear connections between the beams and columns; the possibility of shear bolt failure due to combined shear and axial forces is not built into the model and will be spot-checked manually.

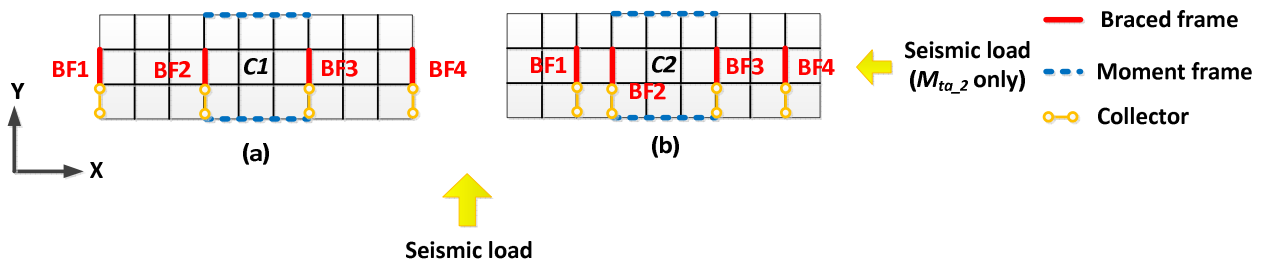


Figure 7-1 Position of target collectors in each configuration: (a) C1 and (b) C2

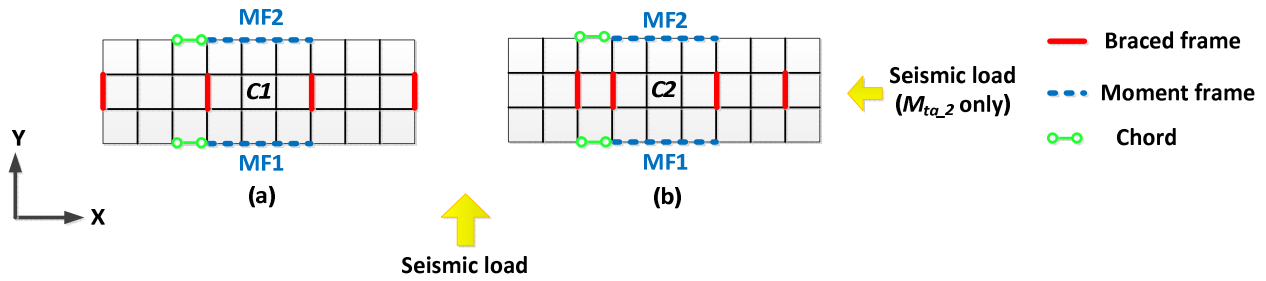


Figure 7-2 Position of target chords in each configuration: (a) C1 and (b) C2

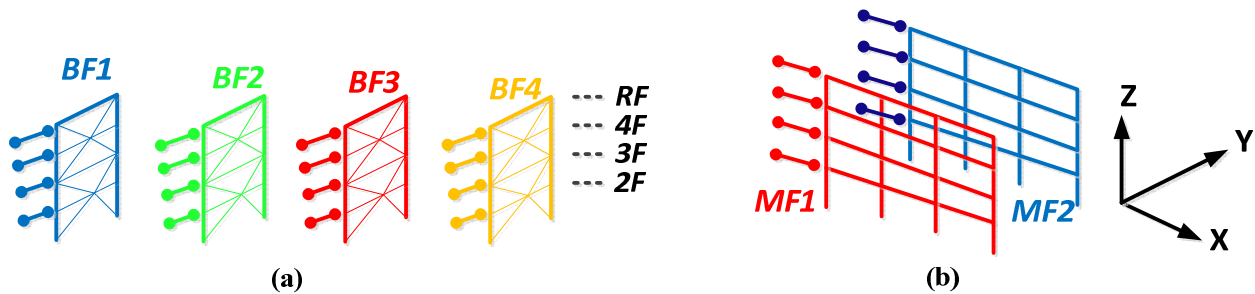


Figure 7-3 Position of target collectors and chords in the 3D view: (a) collectors and (b) chords

### 7.2.2 Diaphragm design forces based on ASCE 7-10

In Section 3.4, the appropriateness of structural members in the vertical braced frames was verified. According to ASCE 7, for the horizontal structural members in the diaphragm such as chords and collectors, the design forces for those components (i.e.,  $F_{PX}$ ) should be increased by 25% from the design forces of the LFRS (i.e.,  $F_X$ ) if vertical or horizontal irregularity exists in the structures. This amplification is used to include the effect of higher-order modes of the diaphragm. The results in Table 7-1 to Table 7-2 show the diaphragm design forces. For C1, the torsion coefficient of each diaphragm, considering the effect of accidental torsion, is smaller than 1.20, indicating that the design diaphragm forces do not need to be amplified by 25%. However, for C2, the amplification factor, 1.25, has to be included in the diaphragm design because of the existence of extreme torsional irregularity. The internal forces in chords and collectors can be determined under the known diaphragm design forces based on the beam analogy. The evaluation of axial force in those members will be discussed in Subsection 7.2.3. Figure 7-4

displays the vertical distribution of design seismic loads for LFRS and diaphragm. One can observe the magnitudes of diaphragm design forces are higher than the one for LFRS design.

Table 7-1 Design force for diaphragm (C1)

C1	F <sub>x</sub>	∑F <sub>x</sub>	∑F <sub>x</sub> /∑w <sub>x</sub>	F <sub>px</sub>	Ω <sub>0</sub> F <sub>px</sub>	0.2S <sub>Ds</sub> I <sub>wpx</sub>	0.4S <sub>Ds</sub> I <sub>wpx</sub>	L	1.00 * F <sub>px</sub> /L
	(kips)	(kips)		(kips)	(kips)	(kips)	(kips)	(ft)	(kips/ft)
5F	552.63	552.63	0.26	552.63	1105.27	422.50	845.00	247.50	2.23
4F	418.77	971.41	0.23	485.70	971.41	422.50	845.00	247.50	1.96
3F	285.76	1257.16	0.20	419.05	838.11	422.50	845.00	247.50	1.71
2F	153.99	1411.15	0.17	352.79	705.58	422.50	845.00	247.50	1.71
	1411.2			1810.2					

Table 7-2 Design force for diaphragm (C2)

C2	F <sub>x</sub>	∑F <sub>x</sub>	∑F <sub>x</sub> /∑w <sub>x</sub>	F <sub>px</sub>	Ω <sub>0</sub> F <sub>px</sub>	0.2S <sub>Ds</sub> I <sub>wpx</sub>	0.4S <sub>Ds</sub> I <sub>wpx</sub>	L	1.25 * F <sub>px</sub> /L
	(kips)	(kips)		(kips)	(kips)	(kips)	(kips)	(ft)	(kips/ft)
5F	546.85	546.85	0.26	546.85	1093.70	422.50	845.00	247.50	2.76
4F	417.78	964.63	0.23	482.32	964.63	422.50	845.00	247.50	2.44
3F	288.30	1252.94	0.20	417.65	835.29	422.50	845.00	247.50	2.13
2F	158.21	1411.15	0.17	352.79	705.58	422.50	845.00	247.50	2.13
	1411.2			1799.6					

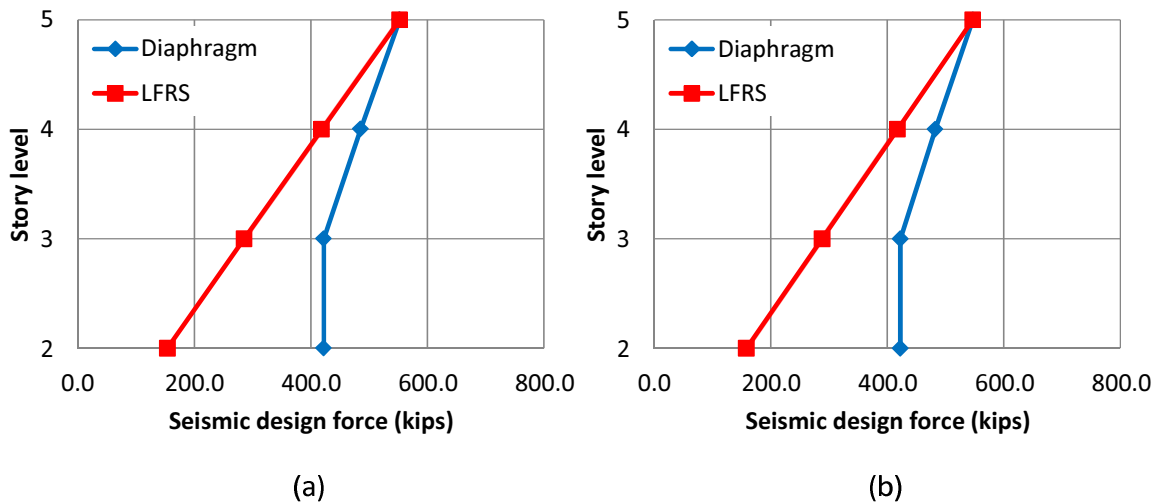


Figure 7-4 Vertical distribution of seismic design forces for LFRS and diaphragm: (a) C1 and (b) C2

### 7.2.3 Beam analogy for the design of chords and collectors in diaphragms

The beam analogy is a common method for determining the axial forces of chord and collector in a diaphragm (Sabelli R. et al., 2011). By treating the diaphragm as an elastic deep beam, the LFRS used to resist the seismic diaphragm design loads, can be simplified as the supports of the deep beam. These analytical beam models corresponding to each diaphragm in the C1 and C2 structures is simulated in SAP2000. The shear and moment diagrams of each “beam” can be determined from elastic static analysis. Figure 7-5 illustrates the typical beam model in the C2 structure. A typical beam element (i.e., Euler-Bernoulli beam) is used in the simulations and subjected to the diaphragm design forces listed in Table 7-1 and Table 7-2. The beam moments and shears can be used for evaluating the internal axial forces in chords and collectors.

The discussion on the strength requirements for chords and collectors concentrates on the seismic loads applied in one direction of each theme structure (i.e., Y-direction). Figure 7-5 illustrates the application of beam analogy for the diaphragm in the C2 structures. The axial force of collector and chord can be evaluated by the following equations:

Collector:

$$P_{collector} = v \times L \quad \text{Equation 7-1}$$

Chords:

$$P_{chord} = M / D \quad \text{Equation 7-2}$$

where  $P_{collector}$  is the axial force in the collector,  $P_{chord}$  is the axial force in the chord,  $v$  is the in-plane shear distribution along the collector,  $L$  is the length of the collector,  $M$  is the internal beam moment in the beam model, and  $D$  is the dimension of the diaphragm parallel to the seismic loads

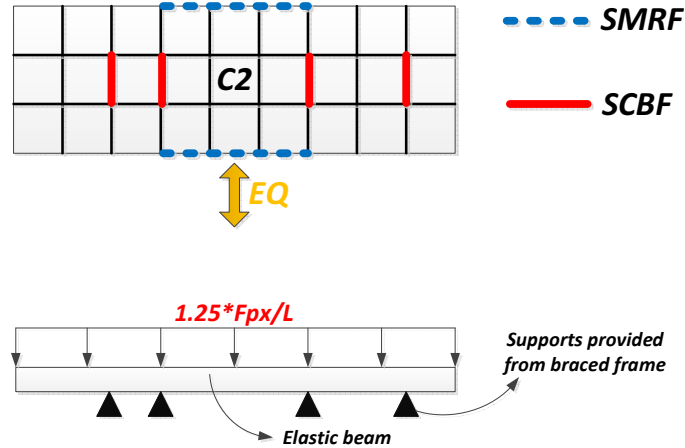


Figure 7-5 Beam model based on the beam analogy

Table 7-3 and Table 7-4 list the axial forces in the collectors based on the beam analogy for the C1 and C2 structures. The diaphragm in-plane shears near the supports (i.e., braced frames),  $V_L$  and  $V_R$ , are determined by the beam models. The collector design axial forces,  $P_{collector}$ , can be determined based on the known collector length ( $L$ ) as well as the assumed constant in-plane shear distribution ( $v_L, v_R$ ).

Table 7-3 Calculation for collector design forces in the C1 structure

<i>RF</i>	$V_L$	$V_R$	$B$	$v_L=V_L/B$	$v_R=V_R/B$	$L$	$P_{collector}$ (kips)	$\Omega_0 P_{collector}$
	(kips)	(kips)	(ft)	(kips/ft)	(kips/ft)	(ft)	$(v_L + v_R)*L$	(kips)
<b>BF1</b>	0	77.7	82.5	0.00	0.94	27.5	25.90	52
<b>BF2</b>	106.7	92.0	82.5	1.29	1.12	27.5	66.23	132
<b>BF3</b>	92.0	106.7	82.5	1.12	1.29	27.5	66.23	132
<b>BF4</b>	77.7	0	82.5	0.94	0.00	27.5	25.90	52
<b>4F</b>	$V_L$	$V_R$	$B$	$v_L=V_L/B$	$v_R=V_R/B$	$L$	$P_{collector}$ (kips)	$\Omega_0 P_{collector}$
	(kips)	(kips)	(ft)	(kips/ft)	(kips/ft)	(ft)	$(v_L + v_R)*L$	(kips)
<b>BF1</b>	0	68.3	82.5	0.00	0.83	27.5	22.77	46
<b>BF2</b>	93.3	80.9	82.5	1.13	0.98	27.5	58.07	116
<b>BF3</b>	80.9	93.3	82.5	0.98	1.13	27.5	58.07	116
<b>BF4</b>	68.3	0	82.5	0.83	0.00	27.5	22.77	46
<b>3F/2F</b>	$V_L$	$V_R$	$B$	$v_L=V_L/B$	$v_R=V_R/B$	$L$	$P_{collector}$ (kips)	$\Omega_0 P_{collector}$
	(kips)	(kips)	(ft)	(kips/ft)	(kips/ft)	(ft)	$(v_L + v_R)*L$	(kips)
<b>BF1</b>	0	59.6	82.5	0.00	0.72	27.5	19.87	40
<b>BF2</b>	81.5	70.5	82.5	0.99	0.85	27.5	50.67	101
<b>BF3</b>	70.5	81.5	82.5	0.85	0.99	27.5	50.67	101
<b>BF4</b>	59.6	0	82.5	0.72	0.00	27.5	19.87	40

Table 7-4 Calculation for collector design forces in the C2 structure

<i>RF</i>	$V_L$	$V_R$	$B$	$v_L=V_L/B$	$v_R=V_R/B$	$L$	$P_{collector}$ (kips)	$\Omega_0 P_{collector}$
	(kips)	(kips)	(ft)	(kips/ft)	(kips/ft)	(ft)	$(v_L + v_R)*L$	(kips)
<b>BF1</b>	151.8	94.5	82.5	1.84	1.15	27.5	82.10	164
<b>BF2</b>	-18.6	130.0	82.5	-0.23	1.58	27.5	37.13	74
<b>BF3</b>	97.5	80	82.5	1.18	0.97	27.5	59.17	118
<b>BF4</b>	72	76	82.5	0.87	0.92	27.5	49.33	99
<i>4F</i>	$V_L$	$V_R$	$B$	$v_L=V_L/B$	$v_R=V_R/B$	$L$	$P_{collector}$ (kips)	$\Omega_0 P_{collector}$
	(kips)	(kips)	(ft)	(kips/ft)	(kips/ft)	(ft)	$(v_L + v_R)*L$	(kips)
<b>BF1</b>	134.2	83.5	82.5	1.63	1.01	27.5	72.57	145
<b>BF2</b>	-16.4	115.0	82.5	-0.20	1.39	27.5	32.87	66
<b>BF3</b>	86.1	70.7	82.5	1.04	0.86	27.5	52.27	105
<b>BF4</b>	63.5	67.1	82.5	0.77	0.81	27.5	43.53	87
<i>3F/2F</i>	$V_L$	$V_R$	$B$	$v_L=V_L/B$	$v_R=V_R/B$	$L$	$P_{collector}$ (kips)	$\Omega_0 P_{collector}$
	(kips)	(kips)	(ft)	(kips/ft)	(kips/ft)	(ft)	$(v_L + v_R)*L$	(kips)
<b>BF1</b>	117.5	73	82.5	1.42	0.88	27.5	63.50	127
<b>BF2</b>	-14.3	100.5	82.5	-0.17	1.22	27.5	28.73	57
<b>BF3</b>	75.2	61.7	82.5	0.91	0.75	27.5	45.63	91
<b>BF4</b>	55.4	58.6	82.5	0.67	0.71	27.5	38.00	76

The collector elements have to resist the amplified seismic loads in structures which belong to SDC C through SDC F. According to the requirement of ASCE 7, the overstrength factor,  $\Omega_0$  of collectors is taken as 2.0. The amplified collector design axial forces,  $\Omega_0 P_{collector}$ , are used to design the collectors shown in Table 7-3 and Table 7-4 According to Figure 7-6, the collector axial forces in BF2 and BF3 in C1 and BF1 in C2 are the highest one among the four braced frames.

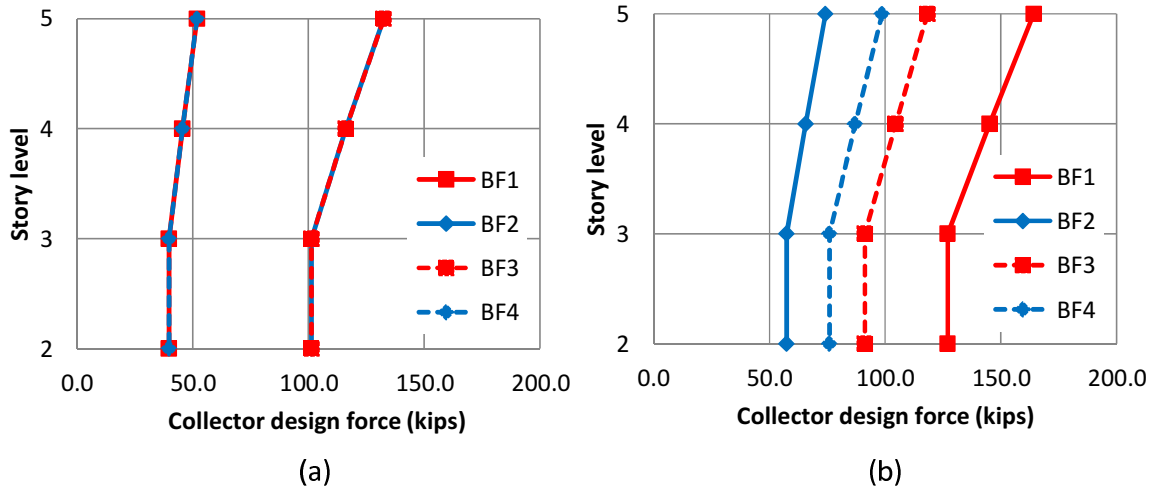


Figure 7-6 Collector design axial forces based on ASCE 7: (a) C1 and (b) C2

For the design of chords, the additional axial forces in the perimeter girders are considered as the target forces for the chord design. This approach neglects the contribution of the joists parallel to chord lines. Table 7-5 and Table 7-6 show the design chord axial forces including the redundancy factor (i.e.,  $\rho=1.00$  for C1 and 1.30 for C2 as defined in Subsection 3.4.3) for each diaphragm in the C1 and C2 structures. The results show that the chord axial forces in the RF are higher than at the other three levels. This is caused by the design seismic forces of the roof diaphragm,  $F_{PX}$  at the RF, is the highest one.

Table 7-5 Calculation for chord design forces in the C1 structure

<i>C1</i>	Moment (kips-ft)	B (ft)	$P_{chord}$ (kips)	$\rho P_{chord}$ (kips)
RF	1178	82.5	14.3	14.3
4F	1040	82.5	12.6	12.6
3F/2F	903	82.5	10.9	10.9

Table 7-6 Calculation for chord design forces in the C2 structure

<i>C2</i>	Moment (kips-ft)	B (ft)	$P_{chord}$ (kips)	$\rho P_{chord}$ (kips)
RF	4174	82.5	50.6	65.8
4F	3960	82.5	48.0	62.4
3F/2F	3221	82.5	39.0	50.8

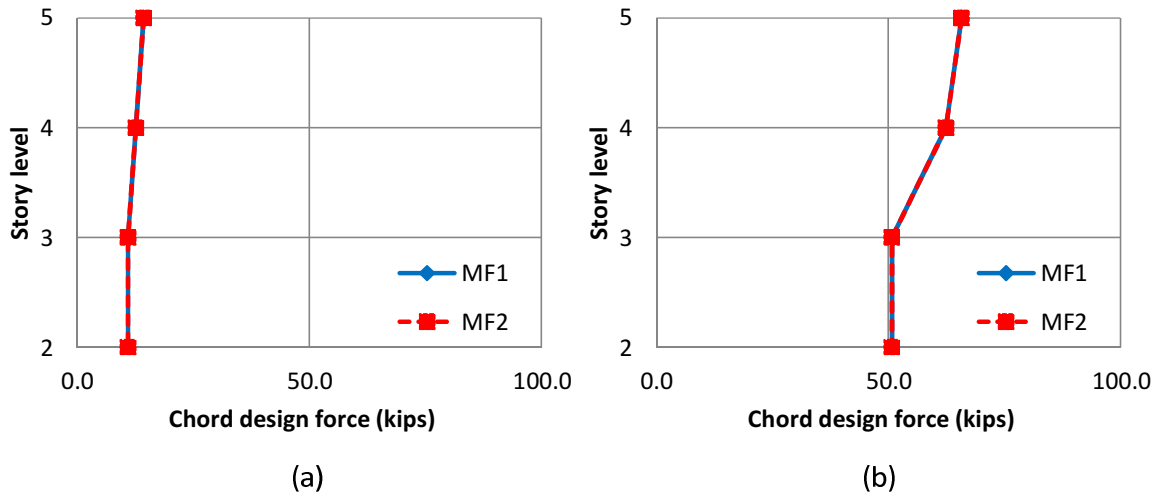


Figure 7-7 Chord design axial forces based on ASCE 7: (a) C1 and (b) C2

### 7.3 Behavior of collectors in the NSA

Figure 7-8 and Figure 7-9 display the variation of axial force for the collectors in BF1 and BF4 in the C1 structure, respectively. Positive values denote “compressive” axial forces in collectors. According to the two figures, the collector axial forces in the RF are the highest ones regardless of whether the bi-axial effects are included in the analytical models. In addition, the collector axial forces in BF1 are higher than those in BF4. This is caused by the fact that the magnitudes of lateral displacement of BF1 are significantly larger in BF4 due to the structural rotation, resulting in the different magnitudes of collector axial forces in BF1 and BF4.

For the collectors at the 4F, 3F and 2F in BF1, the axial forces do not increase as the lateral displacement progresses beyond initial buckling in the Y-direction in the NSA. The phenomenon of brace buckling and fracture illustrated in Figure 7-8 (c) leads to the loss of story lateral strength and thus limits the increment of axial forces in these collectors.

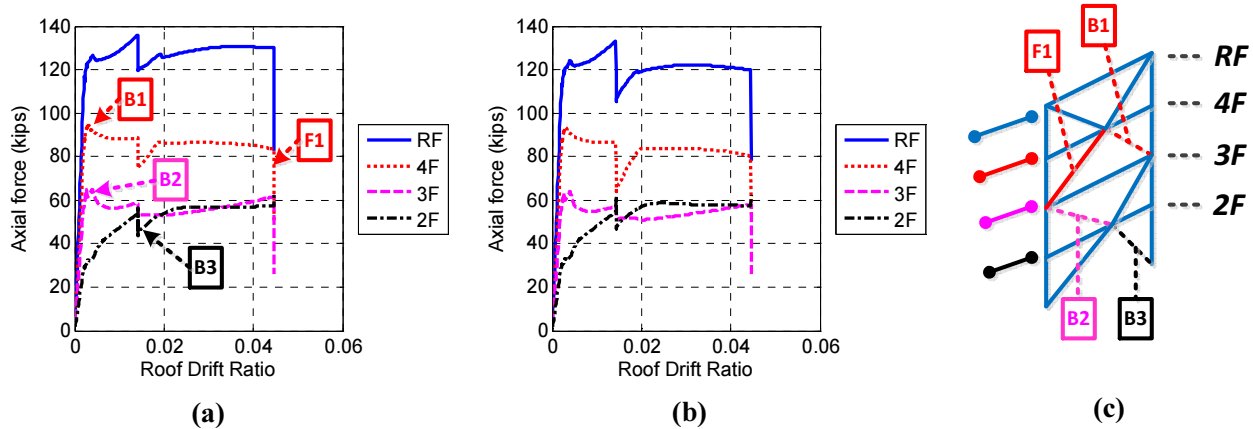


Figure 7-8 Axial forces in collectors at BF1 in C1: (a)  $M_{Ia_1}$ , (b)  $M_{Ia_2}$  and (c) sequence of brace failure

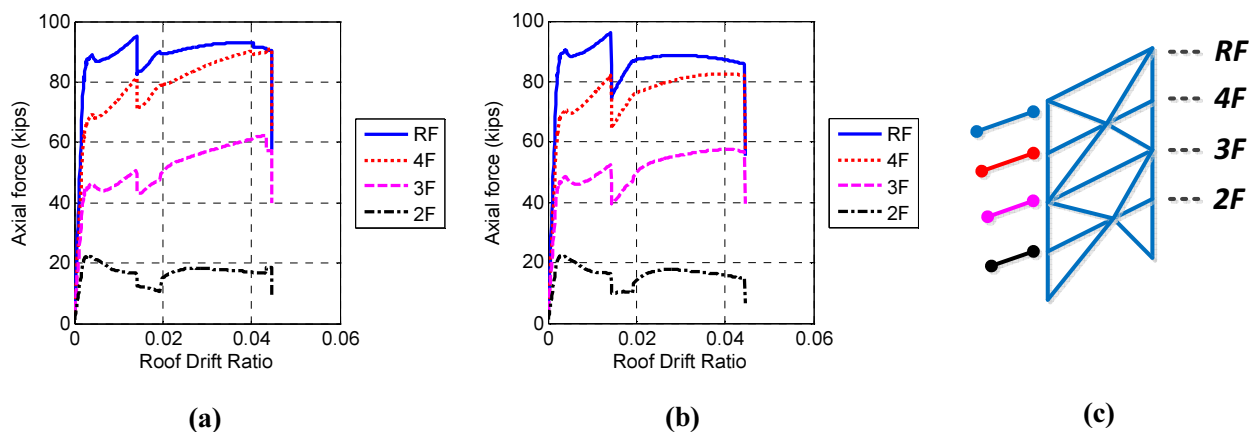


Figure 7-9 Axial forces in collectors at BF4 in C1: (a)  $M_{Ia_1}$ , (b)  $M_{Ia_2}$  and (c) sequence of brace failure

For the C2 structure, the variations of collector axial force in BF2 and BF4 are displayed in Figure 7-10 and Figure 7-11, respectively. The magnitudes of collector axial forces are higher than those in C1 because of the severe diaphragm rotation stimulated by the asymmetric structural configurations. The structure including the bi-axial effect ( $M_{Ia_2}$ ) results in slight differences in the collector axial forces when compared to those in the C2 structure with  $M_{Ia_1}$ . This means the bi-axial effect does not affect the collector behavior significantly. The collector axial forces decrease in the 2F~4F after braces buckling or fracture in the 1<sup>st</sup>~3<sup>rd</sup> story due to the loss of the lateral story stiffness.

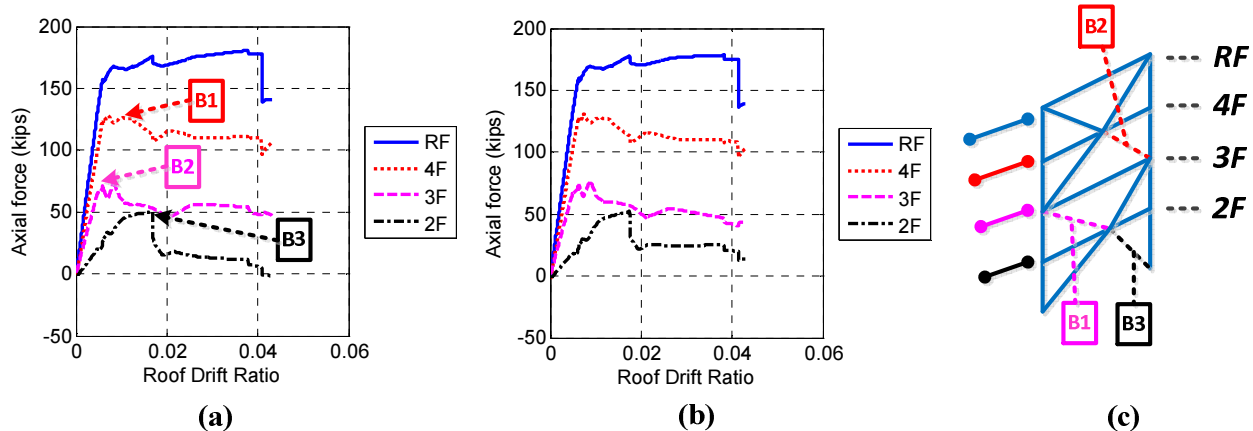


Figure 7-10 Axial forces in collectors at BF2 in C2: (a)  $M_{ta_1}$ , (b)  $M_{ta_2}$  and (c) sequence of brace failure

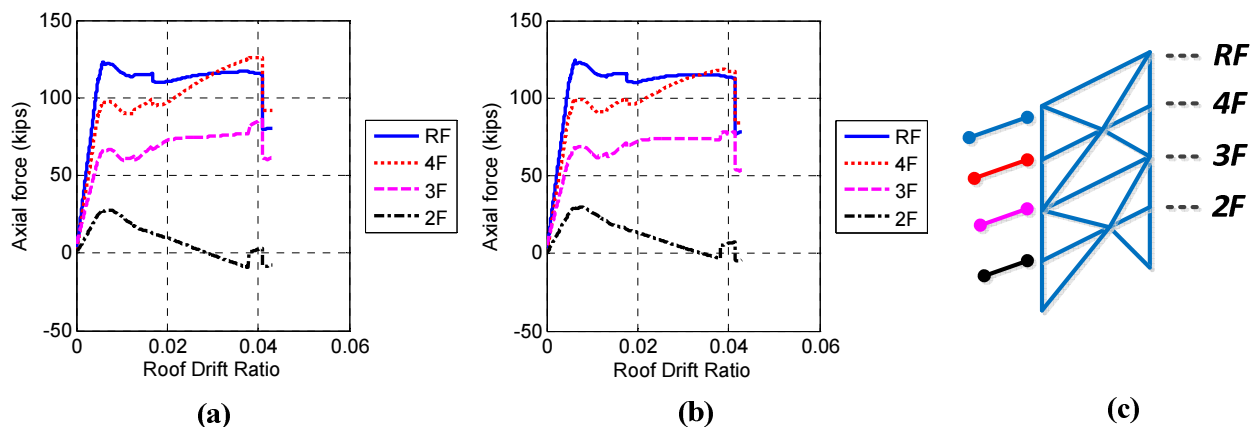


Figure 7-11 Axial forces in collectors at BF4 in C2: (a)  $M_{ta_1}$ , (b)  $M_{ta_2}$  and (c) sequence of brace failure

#### 7.4 Behavior of chords in the NSA

This section focuses on the discussion on the chord axial forces in the NSA including the effect of accidental torsion ( $M_{ta_1}$  and  $M_{ta_2}$ ). In the NSA, the axial forces in the chords may vary with the different stages illustrated in Figure 5-20. From Figure 7-12, one can observe that the axial forces in the chords in the RF are significantly higher than the others as the NSA progresses in the C2 structure. In this structure, the left part of the diaphragm in the RF behaves like a

cantilever, as shown in Figure 7-13. Therefore, higher lateral displacements are generated at the monitor point, resulting in higher axial chord forces in the RF as the NSA progresses.

However, the magnitudes of the chord forces in the 2F increase significantly in the inelastic stages, as compared to the magnitudes of chord forces in the other floors in both frames, when brace buckling begins, as shown in Figure 7-12. Points A to C correspond to the brace buckling in the 1<sup>st</sup> story in BF1 and BF3, respectively. This phenomenon indicates that the increment of in-plane deformation in the 2F diaphragm is higher than the others due to the higher diaphragm rotation. This directly results in a larger increment of axial forces in the chords. The diaphragm deformed shape corresponding to the sequence of brace buckling in the 1<sup>st</sup> story are displayed in Figure 7-13. The magnitudes of these axial forces in the all chords are small compared with the yielding strength of chord (i.e.  $P_Y=675$  kips, W18x46), but are much larger than those provided by the typical two (68.5 kips) or three (108 kips) bolt shear connection.

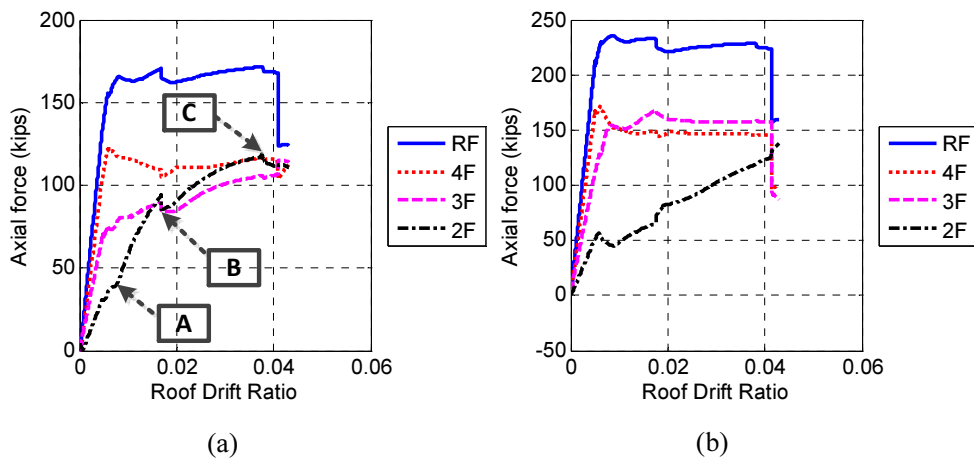


Figure 7-12 Axial forces in chords at MF1 in C2: (a)  $M_{ta\_1}$  and (b)  $M_{ta\_2}$

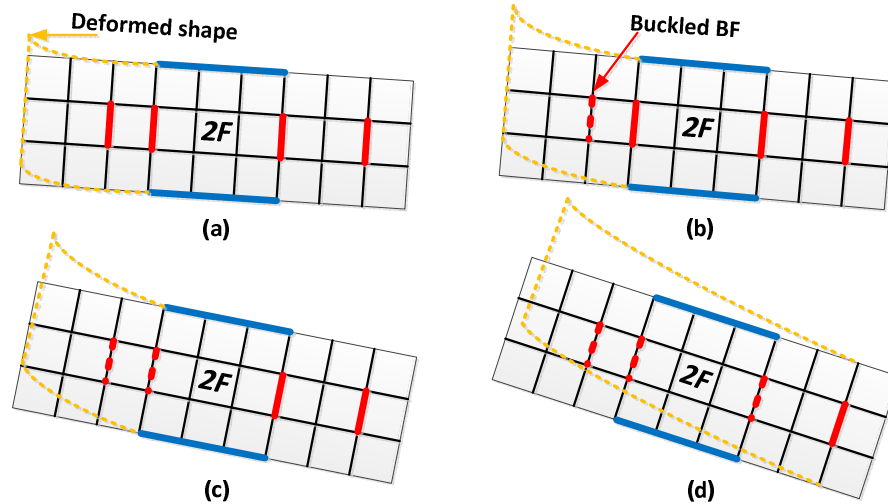


Figure 7-13 Deformed shape of 2F diaphragm in the C2 structure as the NSA progresses (a) elastic stage, (b) brace buckles in the 1<sup>st</sup> story in BF1, (c) brace buckles in the 1<sup>st</sup> story in BF2 and (d) brace buckles in the 1<sup>st</sup> story in BF3

## 7.5 Behavior of collectors in NDA

This section discusses the peak axial forces in the collectors as extracted from the NDA. By using the seven ground motions with the two different intensities (i.e. DBE and MCE-level) defined in Subsection 3.11.3, the absolute maximum axial force in the collectors can be determined.

Figure 7-14 illustrates the peak collector axial forces in each floor when considering the effect of  $M_{ta_1}$  and  $M_{ta_2}$  for the C1 structures under the DBE and MCE-level ground motions. One can observe that the axial forces in the RF and 3F are higher than those in the 2F and 4F under the DBE-level earthquakes. This is caused by the higher local lateral stiffness provided by braces. However, the difference in the collector axial forces among the diaphragms decreases under the MCE-level ground motions. For the MCE-level ground motions, the story lateral stiffnesses reduce significantly due to the buckling and fracture of braces. In this scenario, the four stories evidence similar lateral stiffness as well as magnitudes of collector axial forces. In addition, the

collector forces under the MCE-level ground motions are slightly higher than those under DBE-level ground motions.

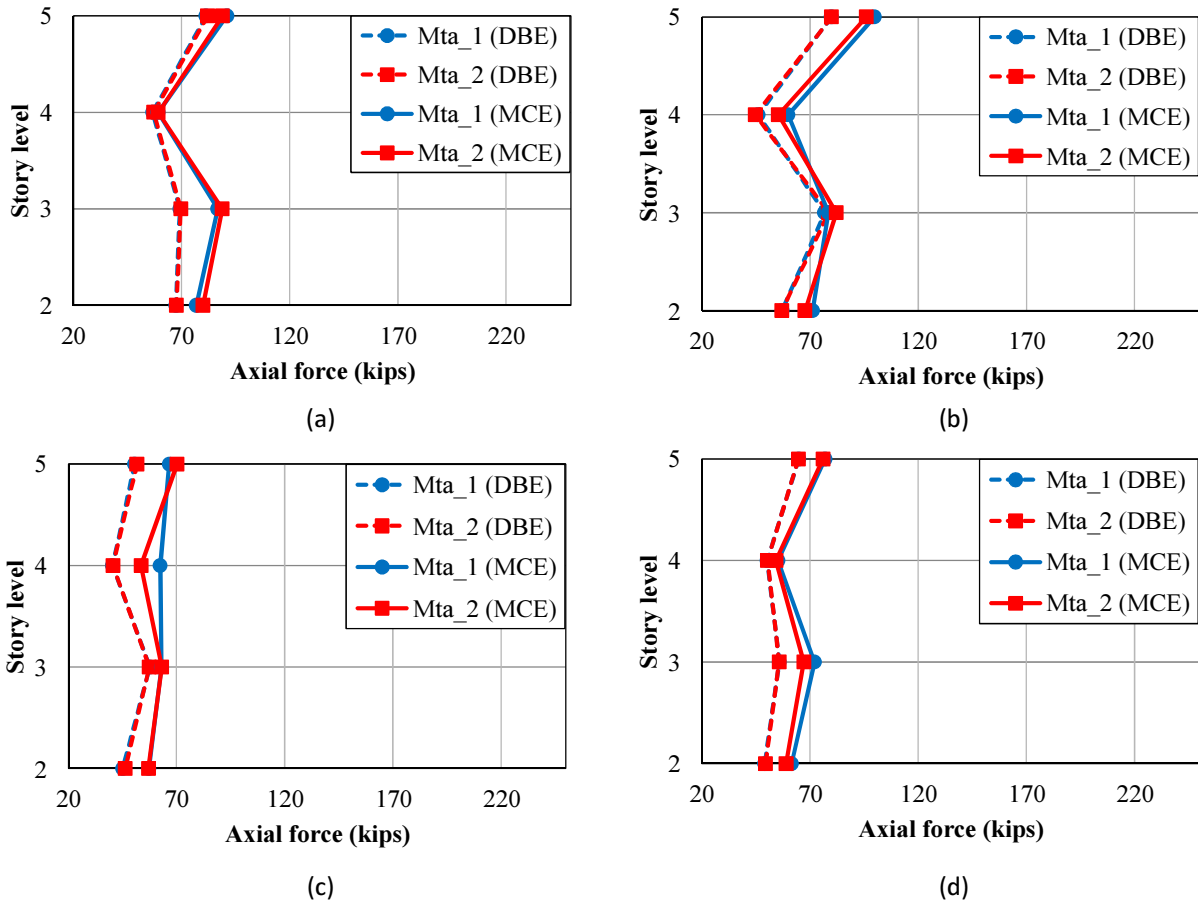


Figure 7-14 Peak axial forces in collectors in C1: (a) BF1, (b) BF2, (c) BF3 and (d) BF4

For the C2 structures, the difference in axial force in the collectors between the two ground motions intensities is more significant, as shown in Figure 7-15. This indicates the magnitudes of collector axial force can be significantly affected by the different structural configurations (i.e., symmetric or asymmetric). Apparently, the higher structural irregularities, such as those in the C2 structure, lead to larger collector axial forces. In addition, the forces in BF1 and BF4 are higher than those in BF2 and BF3. This phenomenon results in the collectors in the peripheral braced frames having higher strength demands. The increment in strength demand for the

collectors will not significantly affect the selection of collector size. However, the redesign of connections between these members and the LFRS may be necessary.

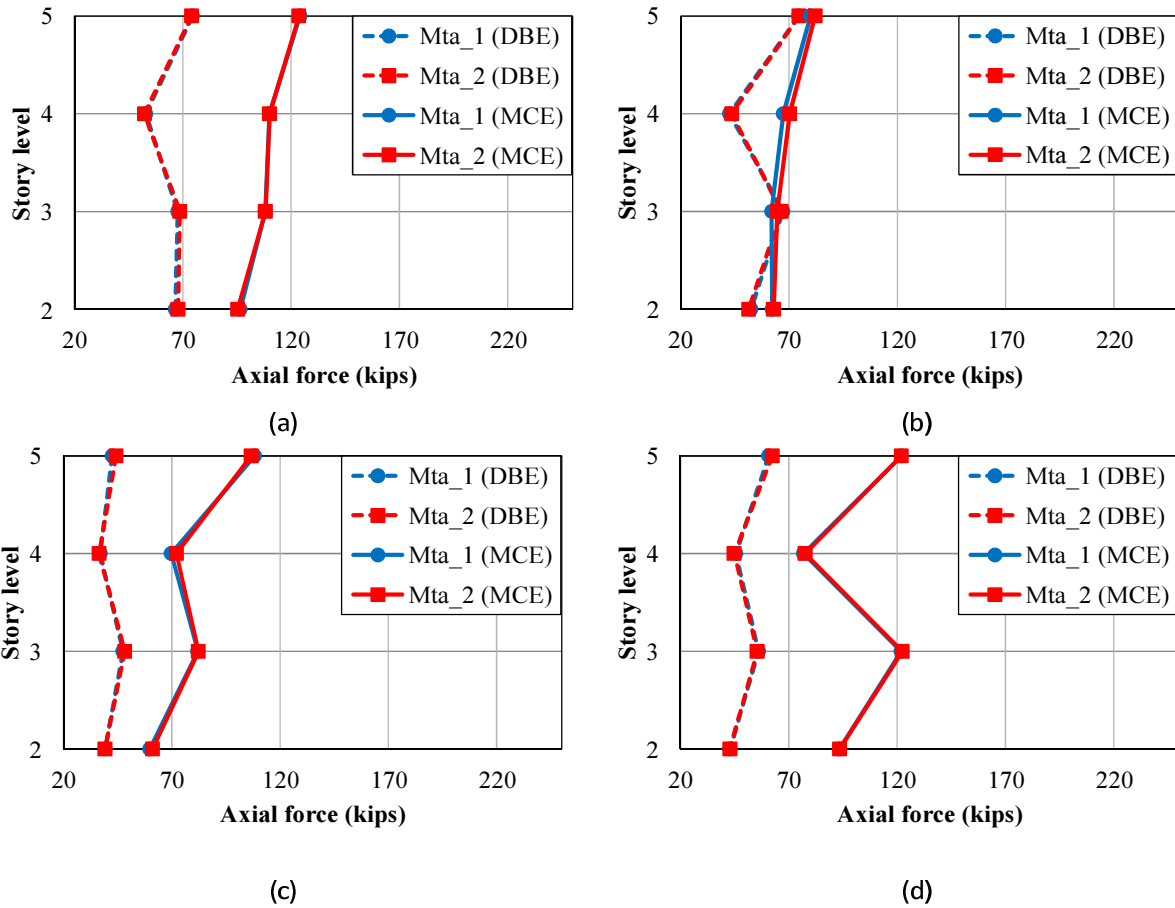


Figure 7-15 Peak axial forces in collectors in C2: (a) BF1, (b) BF2, (c) BF3 and (d) BF4

## 7.6 Behavior of chords in the NDA

Figure 7-16 and Figure 7-17 show the peak chord forces corresponding to different structures including the effect of  $M_{ta_1}$  and  $M_{ta_2}$ . For the semi-rigid diaphragm structures (*CF*), the magnitude of axial forces in chords depends totally on the in-plane deformation of the diaphragm as this is a direct reflection of the in-plane bending moments of diaphragms. In other words, the magnitude of “beam action” of diaphragms dominates the magnitude of axial forces in the chords.

Figure 7-16 shows the average peak chord axial forces in the C1 structure. The chord axial forces in the RF are the highest one under the DBE-level earthquakes. However, high axial forces in the other floor diaphragm (3F) are also generated due to the development of significant deformation of those diaphragms under the MCE-level ground motions. The inclusion of bi-axial effect increases the magnitudes of chord axial force slightly.

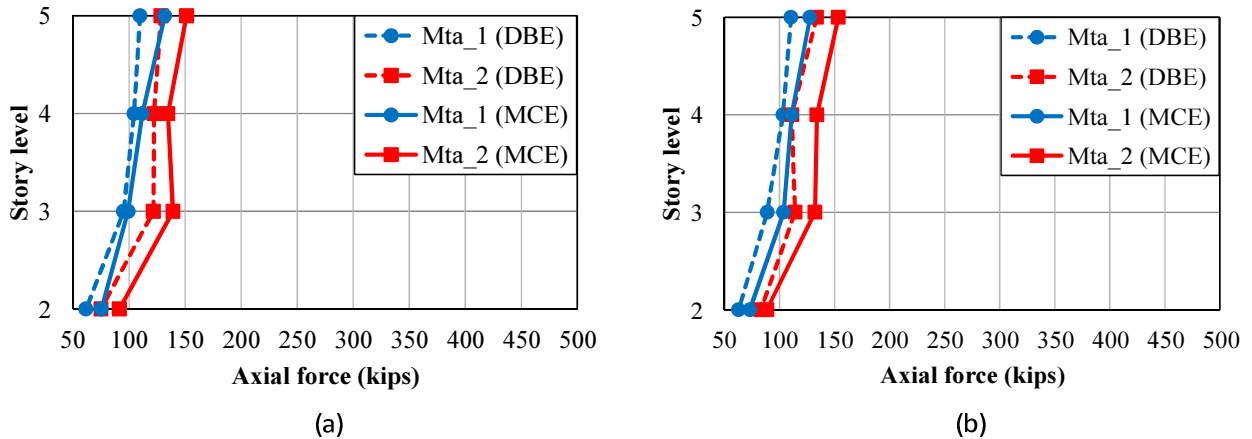


Figure 7-16 Average peak axial forces in chords in C1: (a) MF1 and (b) MF2

For the structures with asymmetric configurations (C2) shown in Figure 7-17, the chord axial forces are higher than those in symmetric configurations (C1). The peak axial forces in the asymmetric structures are developed in the 4F diaphragms under both the DBE and MCE-level ground motions. This is caused by (1) the higher torsional irregularity and (2) the inelastic behavior (buckling of braces) in the 2<sup>nd</sup> and 3<sup>rd</sup> story. In addition, one can observe that the increment of chord axial force is significant in the C2 structure when the intensities increase from DBE to MCE-level. This means the change of intensities of ground motions affects the chord behavior significantly in the asymmetric structures.

The average peak axial forces in the chords of each configuration are not large enough to significantly change the size of the selection used for the chords. However, the connections between LFRS and these chords may need to be redesigned. In addition, the bi-axial effect (i.e.,

$M_{ta_2}$ ) slightly increases the axial forces in these chords. The beam analogy may or may not appropriately reflect such behavior of collectors and chords mentioned above. Section 7.7 gives more details on the applicability of the beam analogy to these structures.

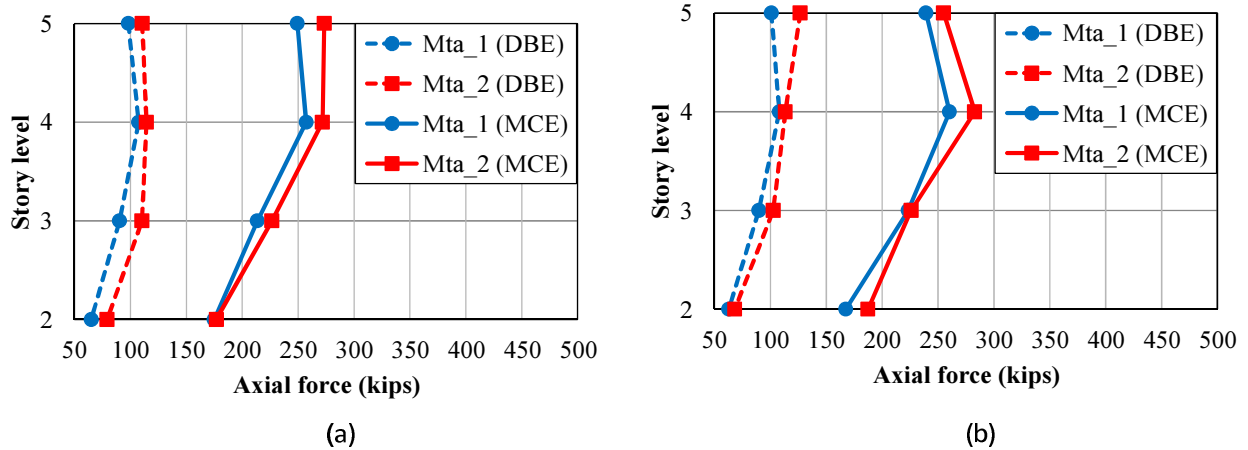


Figure 7-17 Peak axial forces in chords in C2: (a) MF1 and (b) MF2

## 7.7 Comparison between analytical results and conventional design provisions

To identify differences in the axial forces in chords and collectors between the design provision and the analytical results, this section focuses on (1) verifying the appropriateness of the beam analogy from the standpoint of diaphragm design, and (2) determining the appropriateness of the amplification factor (i.e. 1.25). The design chord and collector axial forces based on ASCE 7 in the C1 and C2 structures are defined in Figure 7-6 and Figure 7-7.

### 7.7.1 Evaluation of axial forces in chords and collectors based on AISC seismic provision

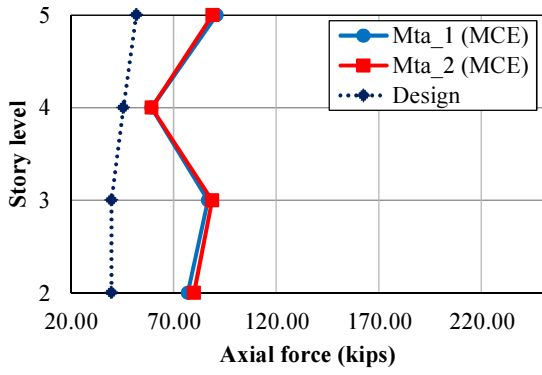
To evaluate the appropriateness of design provision for the chords and collectors, the axial forces based on AISC/ASCE 7 are compared with the analytical results from the NDA in the C1 and C2 structures, as shown in Figure 7-18 and Figure 7-19.

For the collectors in C1 illustrated in Figure 7-18 (a) to (d), the collector axial forces from NDA in BF1 and BF4 are higher than those specified by the code provision. This indicates the

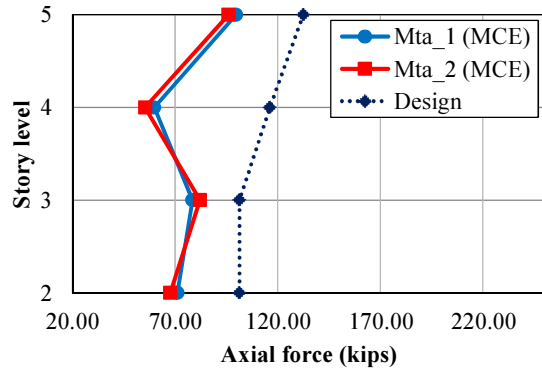
evaluation of axial forces based on the code is not conservative. For the chord axial forces in C1, as illustrated in Figure 7-18 (e) to (f), the code significantly underestimates the design forces in all diaphragm levels (i.e., 2F~RF).

For the collectors in C2 as illustrated in Figure 7-19 (a) to (d), the collector axial forces from NDA in BF4 are higher than those required by the code provision even if the amplification factor for diaphragm design (i.e., 1.25) is included in this configuration design. For the chord axial forces in C2, as illustrated in Figure 7-19 (e) to (f), the specification may significantly underestimate the requirement of design forces at the all diaphragm levels (i.e., 2F~RF).

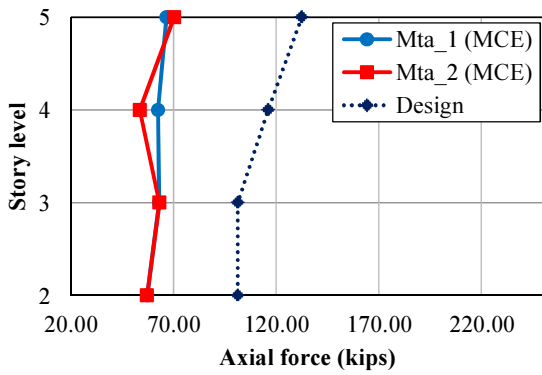
These results indicate that the consideration of finite in-plane stiffness of diaphragms will increase the magnitudes of axial force in the both chord and collector members, as well as the axial ductility demand in these members. Based on the results of these comparisons, the tension capacity of connections between edge chords and LFRS in the asymmetric structures may need to be strengthened beyond what is currently required by the code.



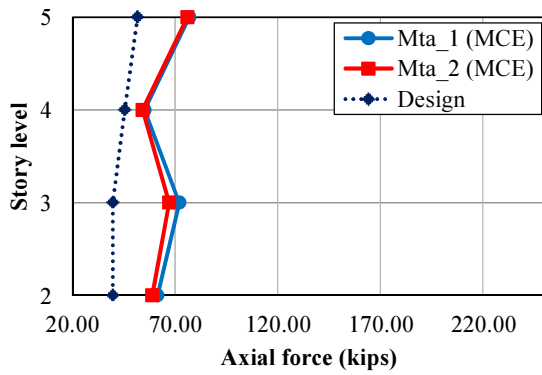
(a)



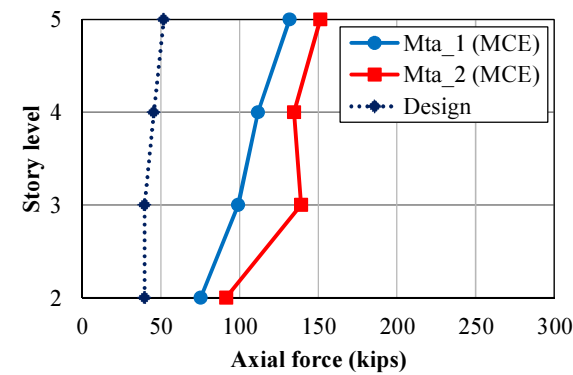
(b)



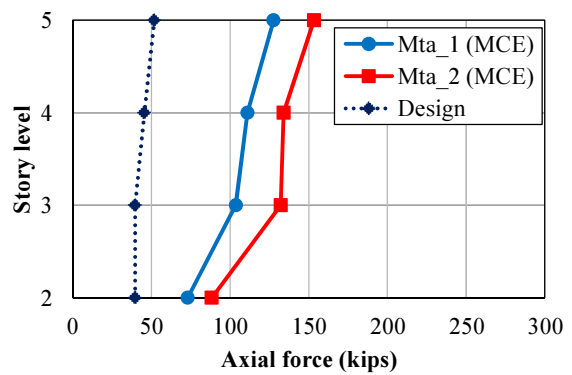
(c)



(d)



(e)



(f)

Figure 7-18 Comparisons of collector and chord axial forces between analytical results and design code in C1: (a) BF1, (b) BF2, (c) BF3, (d) BF4, (e) MF1 and (f) MF2

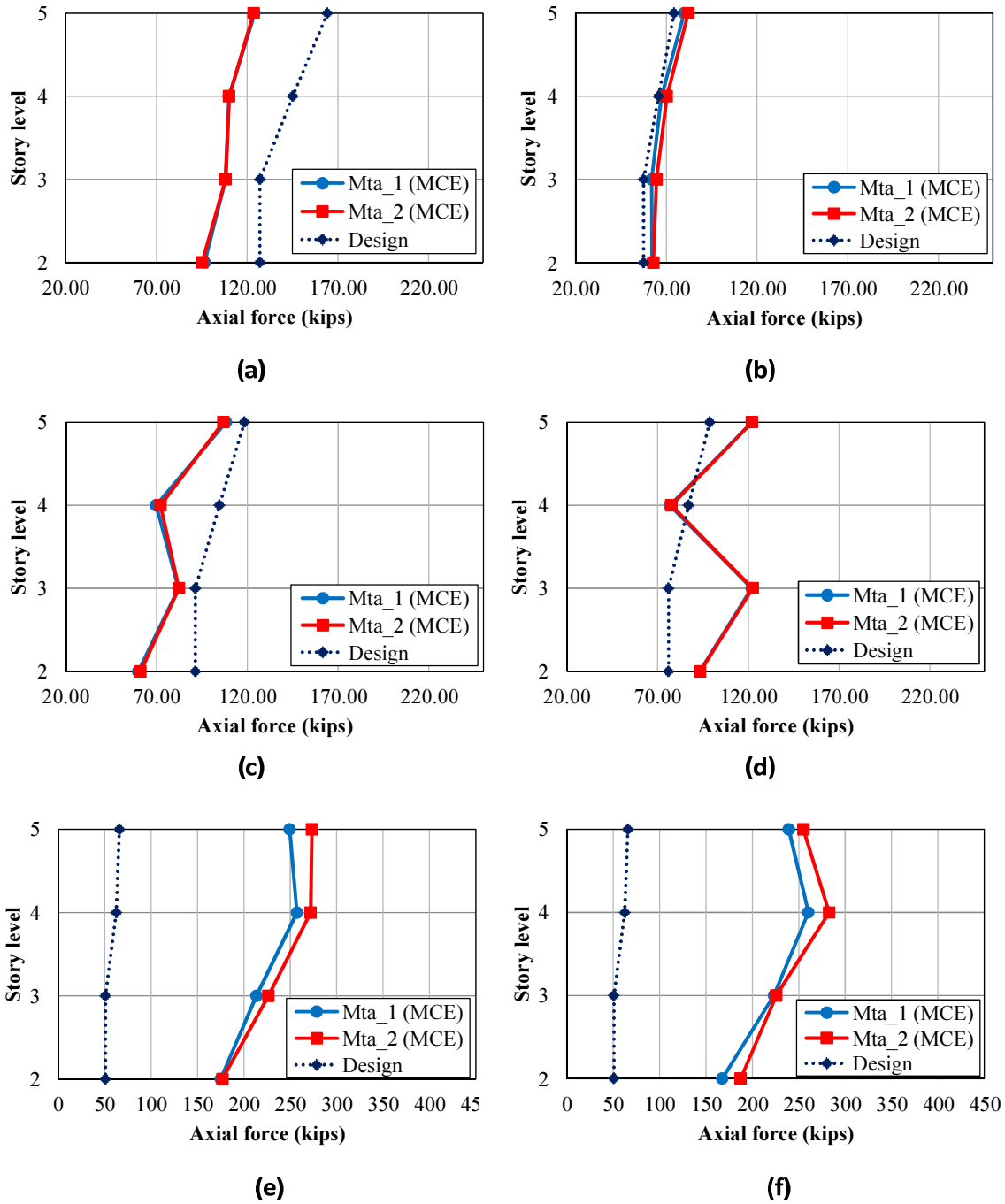


Figure 7-19 Comparisons of collector and chord axial forces between analytical results and design code in C2: (a) BF1, (b) BF2, (c) BF3, (d) BF4, (e) MF1 and (f) MF2

## 7.7.2 Verifications of the behavior of edge collectors and chords

This section verifies the appropriateness of simulation approaches for edge chords and collectors in the modeling of 3D structures. The simulation approaches of the edge beams, including edge chords and collectors, are presented in Subsection 3.5.7. The analytical models are defined in Figure 3-22. Based on the hysteretic loops shown in Figure 3-24, the amplification factors, which are used to describe the composite axial, in-plane and out-of plane bending behavior for the edge collectors and chords, can be determined.

Figure 7-20 (a) and (b) illustrates static and cyclic resistance of edge chords and collectors, respectively, modeled as composite elements (Subsection 3.5.7). In the figure, (1)  $T_{\text{capacity}}$  corresponds to the initial yielding of the tension fibers in the steel section; much of the concrete is already cracked at this level. (2)  $C_{\text{capacity}}$  corresponds to crushing of the concrete; note that because this is a composite member, tensile and compressive capacities ( $T_{\text{capacity}}$  and  $C_{\text{capacity}}$ ) are very different. (3) Buckling will be governed by the distortional mode that cannot be easily modelled as it will need to track the effect of concrete crush. (4)  $T_{\text{design}}$  represents the maximum design force for the edge collector and chord based on ASCE 7, as listed in Table 7-3 and Table 7-6. (5)  $T_{\text{analysis}}$  denotes the maximum analytical axial forces in the edge chords and collectors extracted from NDA.

In Figure 7-20 (a), which displays the maximum analytical and design force for the chords in the C2 structure, the chord demand and design forces at the RF are 283 and 65.8 kips, respectively. The yielding strength of this member is 495 kips corresponding to composite tensile and -950 kips corresponding to composite compressive forces. From Figure 7-20 (a), one can observe that the chord members are in the elastic stage because  $T_{\text{analysis}}$  (283kips) is smaller than  $T_{\text{capacity}}$

(495kips). Similarly, the comparison of edge beam members along Y-dir (edge collector) is shown in Figure 7-20 (b). The analytical axial forces in the edge collectors in C1 (91 kips) are also smaller than  $T_{capacity}$  (520 kips). The results indicate that the assumption of using elastic beam column element with composite effect for simulating the behavior of chords and collectors is appropriate.

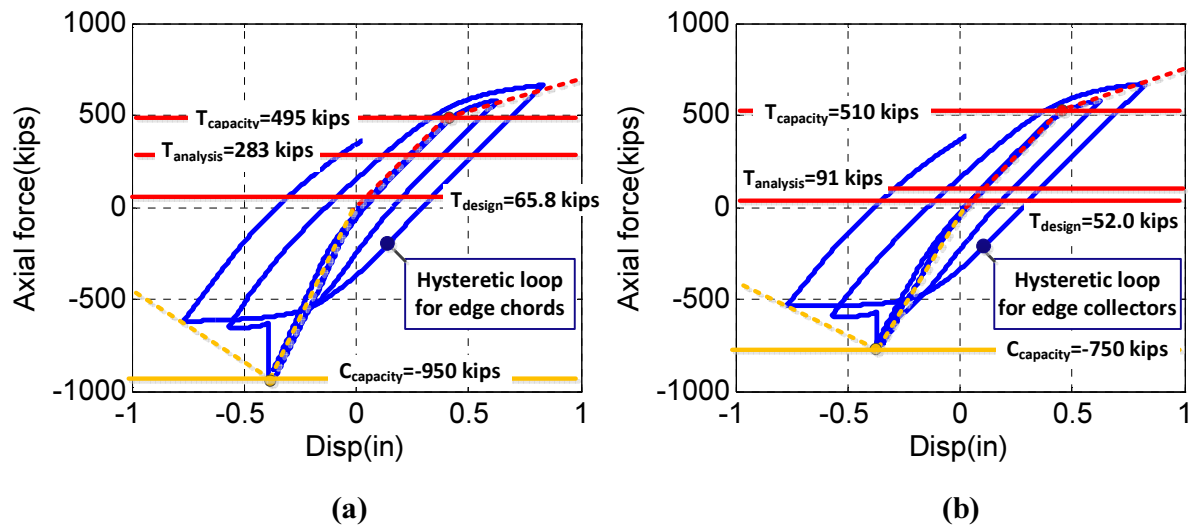


Figure 7-20 Comparisons of hysteretic loops, design forces and analytical forces for the edge beams (a) X-dir (edge chords) (b) Y-dir (edge collectors)

## 7.8 Conclusions

The chapter compared design and analysis force in collectors and chords. The analyses included both NSA and NDA with different diaphragm assumptions and horizontal irregularities (i.e. horizontal configurations of vertical LFRS). The analytical results indicate that for chords and collectors:

1. The maximum axial forces in collectors developed in the RF diaphragms: Based on the analytical results from NSA and NDA, the axial forces in the collectors in the RF diaphragms are higher than those in other diaphragms. There are three reasons for this

phenomenon: (1) the vertical layout of braced frame affects the magnitude of axial force in collectors; the collectors connected directly by braces at the roof and 3F have a stronger local restraint; (2) the highest magnitude of the pushover lateral loads act on the RF diaphragms, which imposes a larger lateral load in RF during NSA; and (3) the variation of collector axial force depends on the buckling sequence of braces. The unbalanced forces stimulated by the buckling of braces must be transferred to other structural members through collectors. Therefore, the braces directly connected to the collectors have a significant change of axial forces.

2. The maximum axial forces in the chords are generated in the diaphragms with highest in-plane deformation: In general, the braces buckling leads to the increment of in-plane deformation of the adjacent diaphragms, as well as the change of magnitude of axial force in chords. The chords in the RF and 4F diaphragms have the highest axial forces in the elastic stages as well as the early inelastic stages. However, the forces in the 2F diaphragm become the highest one once the braces buckle in the 1<sup>st</sup> story.
3. The peak axial forces of collectors in peripheral braced frames are higher than the one predicted by ASCE 7/AISC 341: The use of amplification factor (1.25) and overstrength factors ( $\Omega_0$ ) for diaphragm design forces may be appropriate for the design of collectors in symmetric structures. However, for the collectors in the structures with extreme torsional irregularities, the use of both factors (amplification factor and overstrength factor) still underestimates the strength demand. The inclusion of bi-axial effect does not affect the strength requirement of collector significantly.
4. The redundancy factors may not be appropriate to evaluate the design forces of chords: In both the symmetric and asymmetric structures, the chord design forces are significantly

smaller than maximum axial forces provided by NDA. This indicates the use of this factor results in the underestimation of the chord design forces. One possible solution is to use the overstrength factor in the chord design.

5. Comparing the yield strength of chord and collector members ( $P_y$ ), the amplitudes of axial force in chord and collectors from NDA are small: According to the analytical results, the maximum amplitudes of axial forces in chords and collectors are around 0.6 and 0.2  $P/P_y$ , respectively. The forces may not be big enough to change the size selection for chords and collectors. However, the simple connections between chords/collectors and LFRS may need to be redesigned to ensure the robustness of the axial force transfer mechanism of connections.

## Chapter 8 Conclusions and Recommendations

This thesis focuses on the seismic behavior of steel structures with rigid or semi-rigid diaphragms. For the theme structures with different (1) in-plane diaphragm stiffness, (2) configurations of vertical LFRS and (3) different combinations of diaphragm modeling, both the linear and nonlinear behavior was evaluated through nonlinear static (NSA) and non-linear dynamic history (NDA) analyses. Chapter 4 discusses the difference in behavior of 2D SMRFs, 2D SCBFs and single-story 3D structure with and without composite action and rigid diaphragm constraints. Chapter 5 concentrates on the behavior of the multi-story 3D structures considering the effect of  $M_{ta}$  with different assumptions of diaphragm. Chapter 6 discusses behavior of peripheral frames by implementing NDA and NSA. Chapter 7 focuses on the behavior of the chords, collector in NDA and NSA. The following are the conclusions of this study organized from the analytical results of Chapters 4 to 7.

### ***Structures with rigid and semi-rigid diaphragms (Chapter 4):***

1. For the 2D structures with lower LFRS stiffness, such as SMRFs, the inclusion of composite action and rigid diaphragm constraints in the analysis can increase the strength noticeably (e.g. +12.3% of ultimate strengths between **CF+R** and **BF+R** in the 2D SMRFs). However, for the structures with higher LFRS stiffness, such as SCBFs, the inclusion of composite action and rigid diaphragm constraints has only slight and local effects on the strength of the structure (e.g. +4.7% of ultimate strengths between **CF+R** and **BF+R** in the Chevron-type braced frame).
2. In general, the structures exhibited very good behavior under 2D pushover loads, with only a slight decrease in strength when the first braces buckled. The structures also showed comparatively very good ductility for a braced frame system. This superior

behavior was due to the fact that it was not the first story braces that failed first and that the two-story brace configuration used results in only moderate unbalanced forces in the beams. The structures appear to have generated large forces on chords and collectors, which was the intent in the design.

3. The single-story 3D models with elastic shell elements indicated a very different behavior with respect to both ultimate and post-buckling strength. The 3D structures with elastic shell elements showed significant hardening after initial buckling, often exceeding the pre-buckling strength.
4. The higher out-of plane stiffness of diaphragm provided by the elastic shell elements provided an interesting interaction with brace elements, counteracting the initial brace imperfections and resulting in both higher brace buckling strengths and higher lateral resistance of the entire structure.

***Effect of  $M_{ta}$  on the structures with rigid or semi-rigid diaphragms in 3D (Chapter 5):***

5. In 3D, the structures exhibited similarly superior behavior under pushover loads, such as the insignificant degradation of post buckling stiffness, but the torsion generated activated contributions from both the transverse frames and gravity frames.
6. The inelastic behavior in the LFRS significantly affects the torsional irregularity (i.e.  $TC$ ) of the structures. For the structures with asymmetric configurations (C2) an inherent torsion (i.e.  $M_t$ ) exists in the structures in both the elastic and inelastic stages as the NSA progresses. For these structures, buckling of braces develops in the 3<sup>rd</sup> story of the braced frames first, leading to the development of a soft story in the vertical LFRS. The position of the center of rigidity first moves away from the damaged frames as they buckle and

then moves back (“snaps back”) to near its original position when all braced frames in the LFRS in the story buckle.

7. The peak magnitude of the  $TC$  for each diaphragm in the inelastic stages is significantly higher than the boundary for distinguishing between a typical and an extreme torsional irregularity ( $TC=1.4$ ) defined in ASCE 7. In addition, the highest magnitude of  $TC$  typically develops in the 2F diaphragm due to the significant inelastic behavior in the 1<sup>st</sup> story. This indicates that the current provision for defining the boundary of horizontal structural irregularity may not be appropriate when the structures enter into the inelastic stage and that additional requirements for the design of the second floor (2F) diaphragms may need to be considered in future codes for structural systems that rely on yielding at the base of the structures.
8. From the results from the NDA, the average maximum roof displacement ratio ( $RDR_{max}$ ), the average interstory drift ratio ( $IDR_{max}$ ) and the diaphragm rotations in the asymmetric structures with semi-rigid diaphragms ( $CF$ ) are higher than the ones with rigid diaphragms ( $CF+R$  and  $BF+R$ ). For instance, the  $RDR_{max}$  of  $CF$  structures in C2 is higher than those of the  $CF+R$  structures by 8.3%. The phenomenon indicates that the global ductility requirements for the asymmetric structures with semi-rigid diaphragms is higher than those for structures with rigid diaphragm constraints. The most likely reason is the effect of “higher modes,” which is used in this thesis to indicate that yielding and buckling in the inelastic range considerably changes the deformed shape from the first mode one assumed in the elastic analyses used for the design.
9. The 3D models with rigid diaphragm constraints ( $CF+R$  and  $BF+R$ ) exhibit higher ultimate strengths due to the robust in-plane force transfer mechanism in the rigid

diaphragms. In this scenario, if the structural components such as braces in the LFRS buckle, the unbalanced forces can be delivered to other LFRS through those rigid links efficiently. This leads to a higher structural strength.

10. From the results of the NSA for the 3D models, the pre-buckling and ultimate strengths of the structures decrease because of the inclusion of bi-axial effect ( $M_{ta\_2}$ ). The decrement of the strengths in the asymmetric structures, such as the structures in the C2 group, is more significant than the others with symmetric configurations. The pre-buckling and ultimate strengths of individual braced frame develop separately from one another due to the effect of  $M_{ta\_2}$ . Therefore, the sequence of brace buckling influences the strengths of structures. In other words, the inclusion of bi-axial effect is a sensitive factor for affecting the strengths of asymmetric structures.
11. The contribution of base shear from peripheral frames (SMRFs) in the structure increases after the SCBFs reach their ultimate capacities. From the NSA, the reactions in SMRFs increase significantly after the ultimate strength develops in the SCBFs. Additionally, the contribution of gravity systems to the base shear is similar as that provided by SMRFs. In this scenario, the lateral resistance of the entire structure is primarily provided by these three systems instead of SCBFs only..

***Behavior of peripheral frames (Chapter 6):***

12. For the columns of the SMRFs located in the 1<sup>st</sup> story perpendicular to the direction of considered seismic loads, inelastic behavior occurs as the NSA progresses. The inelastic behavior develops at the base of the columns due to significant bi-axial bending caused by both the considered seismic loads as well as the structural torsions (i.e.  $M_t$  and  $M_{ta}$ ). For the C2 structures with  $M_{ta\_1}$ , the inelasticity of the columns is dominated by the

weak-axis bending. However, for the C2 structures with  $M_{I\alpha_2}$ , the section behavior is dominated by the strong-axis bending.

13. The in-plane rigidity of diaphragm provides a stronger in-plane constraint for the peripheral frames when the C2 structures rotate significantly, leading to a smaller magnitude of base shear in the peripheral frames. In other words, the asymmetric *CF* structure exhibits a higher magnitude of base shear ( $V_{xI}/W$ ) along the perpendicular axis.

***Behavior of chords and collectors (Chapter 7):***

14. Based on the analytical results from both NSA and NDA, the axial forces in the collectors in the roof diaphragms are higher than those of other floors. There are two reasons causing the phenomenon. The first reason is the vertical layout of the braced frame, as the collectors directly connected to vertical braces carry higher axial forces. The second reason is the shape of the pushover load patterns, as higher magnitudes of lateral load are applied at the roof level (RF). Both of these reasons cause higher magnitudes of axial forces in collectors in the nonlinear analyses.
15. The variation in collector axial forces depends on the buckling sequence of the braces. In the NSA, the magnitudes of axial force in collectors significantly change due to the buckling of braces near the collectors of interest. The development of the inelasticity in braces (buckling and fracture) changes the lateral stiffness of braced frames. The corresponding mechanism of force redistribution leads to the change of magnitude of axial force in collectors. The collectors not connecting to vertical braces directly are not significantly influenced by the buckling of braces.
16. The chords in the higher floors, such as the roof (RF) and fourth floor (4F) diaphragms, may have the highest axial forces in the elastic stages as well as the early inelastic stages

due to the in-plane deformation of diaphragm from the buckling of braces. However, the in-plane deformation of second floor (2F) diaphragms becomes significant when the braces buckle in the 1<sup>st</sup> story. The forces in the 2F diaphragm may become the highest one once the braces buckle in the 1<sup>st</sup> story.

17. Based on the results from NDA, the use of overstrength factor ( $\Omega_0$ ) and the amplification factor for diaphragm design force (1.25) for the collector design in the asymmetric structures may not be enough to satisfy the demands under inelastic action.
18. The redundancy factors ( $\rho$ ) may not be appropriate to evaluate the design forces of chords in both the symmetric and asymmetric structures. In the C1 and C2 structures, the chord design forces are significantly smaller than maximum axial forces provided by the NDA. This indicates the use of this factor results in the underestimation of the chord design forces.

### ***Future Work***

The results of this study highlighted several areas which require further work, including:

- a. Rigid diaphragm elements useful for describing infinite in-plane and finite out-of plane stiffness and strength limits including nonlinear properties are needed. Such elements are not currently available in the element library of OpenSEES. A more accurate assessment of the behavior for structures with rigid diaphragms can be obtained through using this type of element instead of using “rigid diaphragm constraints”.
- b. The appropriateness of the connection design forces for chords and collectors based specified by ASCE-7 and the AISC Seismic Provisions commentary need to be studied further. The typical connections designed for gravity loads may not satisfy the strength requirements from

the additional axial forces in collectors and chords due to the in-plane deformation of diaphragms subjected to large seismic loads.

- c. The re-distribution of in-plane force in diaphragms needs to be investigated when the inelastic behavior develops in the diaphragms. The diaphragms near the connections between braces and beams may exhibit high in-plane diaphragm forces that exceed the amplified design diaphragm forces. These elements should be simulated with nonlinear material behavior to reflect the real distribution of in-plane forces. A simpler approach, based on strut and tie models or stringer and panel method, may need to be developed for design.
- d. The computational efficiency of analyses for 3D structures with semi-rigid diaphragms should be improved, especially for NDA. The advantages and disadvantages of the simplified beam-truss model proposed in the appendices (Appendix C) of this thesis to replace the conventional shell elements needs to be ascertained. In addition, the truss-and-tie or stringer-and-panel method may also be good approaches to replace shell elements and improve the computational efficiency.

## References

- Advanced Research Computing. (2014): Virginia Tech. Retrieved from <http://www.arc.vt.edu>
- Aghayere A. and Vigil J. (2009). *Structural Steel Design*: Pearson.
- American Concrete Institute. (2008). Building Code Requirements for Structural Concrete (ACI 318-08) and Commentary (ACI 318R-08). Farmington Hills, Michigan: American Concrete Institute Committee 318 (ACI).
- American Institute of Steel Construction. (2010a). Seismic Provisions for Structural Steel Buildings, ANSI/AISC 341-10. Chicago, IL: American Institute for Steel Construction (AISC).
- American Institute of Steel Construction. (2010b). Specification for Structural Steel Buildings, ANSI/AISC 360-10. Chicago, IL: American Institute for Steel Construction (AISC).
- American Institute of Steel Construction. (2011). Steel Construction Manual (13<sup>th</sup> ed.): American Institute of Steel Construction.
- American Society of Civil Engineers. (2010). Minimum Design Loads For Buildings and Other Structures ASCE 7-10. Reston, VA: American Society of Civil Engineers.
- American Society of Civil Engineers. (2013). Seismic evaluation and retrofit of existing building (ASCE 41-13): ASCE.
- American Society of Civil Engineers. (2016). *Minimum Design Loads For Buildings and Other Structures ASCE 7-16 (Draft)*. Reston, VA.
- American Society of Testing and Materials. (1999). *Standard Specification for Steel Bars, Carbon, Cold-Finished, Standard Quality (ASTM A108-99)* (American Society of Testing and Materials. Ed. Vol. 04.07). West Conshohocken, PA: American Society of Testing and Materials (ASTM).
- Basu D. and Jian S.K. (2004). Seismic analysis of asymmetric buildings with flexible floor diaphragms. *Journal of Structural Engineering*, 130(8).
- Blaauwendraad J. and Hoogenboom P. (1996). Stringer Panel Model for Structural Concrete Design. *ACI Structural Journal*, 93(3).
- Bruneau M., Uang C. M., and Sabelli R. (2011). *Ductile Design of Steel Structures* (2<sup>nd</sup> Ed.): McGraw-Hill Companies Inc.
- Chai C.-F. and Loh C.-S. (2002). Modeling of phase spectrum to simulation design ground motions. *Journal of the Chinese Institute of Engineers*, 447-459.
- Charney F. A. (2008). Unintended Consequences of Modeling Damping in Structures. *J. Struct. Engrg.*, 134(4), 581-592.
- Charney F. A. and Down W. M. (2004). *Modeling procedures for panel zone deformations on moment resisting frames*. Paper presented at the Connections in Steel Structures V, Amsterdam.

- Charney F.A. (2008). Unintended Consequences of Modeling Damping in Structures. *Journal of Structural Engineering*, 134(4).
- Chopra A.K. (2007). *Dynamics of Structures*: Pearson.
- Computer and Structures Inc. (2009). SAP2000 14.0.0. Berkeley, CA.
- Computers and Structures Inc. (2009). *CSI Analysis Reference Manual-For SAP2000, ETABS, and SAFE*. Berkeley, CA: Computers and Structures Inc.
- Cook R. D., Malkus D. S., Plesha M. E., and Witt R. J. (2001). *Concepts and Applications of Finite Element Analysis* (4<sup>th</sup> Ed.): John Wiley & Sons Inc.
- Cowie K., Hicks S., MacRae G., Clifton G.C., and Fussell A. (2013). Seismic design of composite metal deck and concrete-filled diaphragms-A discussion paper. *Composite Constructon VII*.
- Davies J. M. and Fisher J. (1979). *The diaphragm action of composite slabs* Paper presented at the Proc. Insrn Civ. Engrs.
- De-la-colina. (1999). In-plane floor flexibility effects on torsionally unbalanced systems. *Earthquake Engineering and Structural Dynamics*, 28(1705-1715).
- De la Llera J. C. and Chopra A.K. (1994). Estimation of accidental torsion effects for seismic design of buildings. *Journal of Structural Engineering*, 121(1).
- DeBock D. J., Liel A.B., Haselton C. B., Hooper J. D., and Henige Jr. R. A. (2013). Importance of seismic design accidental torsion requirements for building collapse capacity. *Earthquake Engineering and Structural Dynamics*, 43(6), 831-850.
- Deierlein G. G., Reihorn A. M., and Willford M. R. (2010). *Nonlinear Structural Analysis for Seismic Design*: National Institute of Standards and Technology.
- Easterling W. S. (1987). *Analysis and Design of Steel Deck Reinforced Concrete Diaphragms*. (PhD Dissertation), Iowa state university, Ames, Iowa.
- Easterling W. S. and Porter M. L. (1994a). Steel-Deck-Reinforced Concrete Diaphragms. I. *Journal of Structural Engineering ASCE*, 120(2), 560-576.
- Easterling W. S. and Porter M. L. (1994b). Steel-deck-reinforced concrete diaphragms. II. *Journal of Structural Engineering ASCE*, 120(2), 577-596.
- Erduran E. (2012). Evaluation of Rayleigh damping and its influence on engineering demand parameter estimates. *Earthquake Engineering and Structural Dynamics*, 41, 1905–1919.
- Erduran E. and Ryan K. L. (2011). Effects of torsion on the behavior of peripheral steel-braced frame systems. *Earthquake Engineering and Structural Dynamics*, 40, 491-507.
- Essa H. S., Tremblay R., and Rogers C. A. (2003). Behavior of roof deck diaphragms under quasistatic cyclic loading. *Journal of Structural Engineering ASCE*, 129(12), 1658-1666.
- Ewing R. D., Johnson A. W., and Kariotis J. C. (1981). Methodology for mitigation of seismic hazards in existing unreinforced masonry buildings : Diaphragm testing. EI Segundo, CA: ABK.

- FEMA. (2000). *Prestandard and Commentary for the Seismic Rehabilitation of Buildings (FEMA 356)*: Federal Emergency Management Agency.
- Fisher J. M., West M. A., and Van De Pas J. P. (1991). *Design with Steel joints, Joist girders, Steel deck*. Milwaukee, Wisconsin: Computerized Structural Design, Inc.
- Fleischman R. B. and Farrow K. T. (2001). Dynamic behavior of perimeter lateral-system structures with flexible diaphragms. *Earthquake Engineering and Structural Dynamics*, 30, 745-763.
- Goel R.K. and Chopra A.K. (1991). Effects of plan asymmetric in inelastic seismic response of one-story systems. *Journal of Structural Engineering*, 117(5).
- Goel R.K. and Chopra A.K. (1993). Seismic code analysis of building without locating centers of rigidity. *Journal of Structural Engineering, ASCE*, 119(10).
- Hossain K. M. A. and Wright H. D. (1998). Performance of profiled concrete shear panels. *Journal of Structural Engineering*, 124(4).
- Jain Sudhir K. and Jennings Paul C. (1985). Analytical models for low-rise buildings with flexible diaphragms. *Earthquake Engineering and Structural Dynamics*, 13, 225-241.
- Jain Sudhir K. and Mandal Utpal K. (1995). Dynamics of buildings with Y-shape plan and flexible floor diaphragms. *Journal of Structural Engineering*, 121(6).
- Jarrett J.A., Zimmerman R.B., and Charney F.A. (2014). *Accidental torsion in nonlinear response history analysis*. Paper presented at the Tenth U.S. National Conference on Earthquake Engineering, Anchorage, Alaska.
- Ju S. H. and Lin M. C. (1999). Comparison of building analysis assuming rigid or flexible floors. *Journal of Structural Engineering ASCE*, 125, 25-31.
- Kent D. C. and Park R. (1971). Flexural members with confined concrete. *J. Struct. Engrg.*, 97(7), 1969-1990.
- Kim S-C. and White D. W. (2003). Linear static analysis of low-rise buildings with flexible diaphragms using the structural separation method. *Engineering Structures*, 26, 83-93.
- Kim S-C. and White D. W. (2004). Nonlinear analysis of a one-story low-rise masonry building with a flexible diaphragm subjected to seismic excitation. *Engineering Structures*, 26, 2053-2067.
- Kunnath Sashi K., Panahshahi Nadar, and Reihorn Andrei M. (1991). Seismic response of RC buildings with inelastic floor diaphragms *Journal of Structural Engineering*, 117(4).
- Leon R. T. (1998). Analysis and design problems for FR composite frames subjected to seismic loads *Engineering Structures*, 20(4-6), 364-371.
- Love E. (2001). The OpenSees plate element. CA: SEMM, Department of Civil and Environmental Engineering, University of California.
- Malone R. T. and Rice R. W. (2012). *The Analysis of Irregular Shaped Structures*: McGraw Hill.
- Mazzoni S., McKenna F., Scott M. H., and Fenves G. L. (2007). *OpenSees Command Language Manual*

- Moon S.K. and Lee D-G. (1992). Effects of inplane floor slab flexibility on the seismic behaviour of building structures. *Engineering Structures*, 16(2).
- Naeim F. (2001). *The Seismic Design Handbook* (2<sup>nd</sup> Ed.). MA, USA: Kluwer Academic Publishers Inc.
- NEHRP. (2009). NEHRP Recommended Seismic Provisions (FEMA 750).
- NEHRP. (2010). Evaluation of the FEMA P-695 Methodology for Quantification of Building Seismic Performance Factors (ATC-76): National Institute of Standards and Technology.
- NEHRP. (2011). *Selecting and Scaling Earthquake Ground Motions for Performing Response-History Analyses*.
- NIST. (2010). Evaluation of the FEMA P-695 Methodology for Quantification of Building Seismic Performance Factors: National Institute of Standards and Technology.
- OpenSeesWiki. The Open System for Earthquake Engineering Simulation. from <http://opensees.berkeley.edu/>
- Orbison James G., McGuire William, and Abel John F. (1982). Yield surface applications in nonlinear steel frame analysis. *Computer methods in applied mechanics and engineering*, 33(557-573).
- Pacific Earthquake Engineering Research Center. (2013). OpenSEES (Version 2.4.2).
- Pacific Earthquake Engineering Research Center. (2014). from <http://peer.berkeley.edu/>
- Pallares L. and Hajjar J. F. (2009a). Headed Steel Stud Anchors in Composite Structure: Part I - Shear: Newmark Structural Engineering Laboratory.
- Pallares L. and Hajjar J. F. (2009b). Headed Steel Stud Anchors in Composite Structure: Part II - Tension and Interaction: Newmark Structural Engineering Laboratory.
- Peralta D. F., Bracci J. M., and Huset M. B. (2003). Seismic Performance of Rehabilitated Wood Diaphragms. College Station, TX: Texas A&M University.
- Prestressed Concrete Institute. (2004). PCI Design Handbook: Precast and Prestressed Concrete (6 ed.). Chicago, IL: Precast /Prestressed Concrete Institute (PCI).
- Sabelli R., Roeder C.W., and Hajjar J. F. (2013). Seismic Design of Steel Special Concentrically Braced Frame Systems *NEHRP Seismic Design Technical Brief No.8*: National Institute of Standards and Technology
- Sabelli R., Sabol T. A., and Easterling W. S. (2011). Seismic Design of Composite Steel Deck and Concrete-filled Diaphragms *Seismic Design Technical Brief No. 5*. Gaithersburg, MD: National Institute of Standard and Technology.
- Sadashiva V. K., MacRae G. A., Deam B. L., and Spooner M. S. (2012). Quantifying the seismic response of structure with flexible diaphragms *Earthquake Engineering and Structural Dynamics*, 41, 1365-1389.
- Saffarini H.S. and Qudaimat M.M. (1992). In plane floor deformations in RC structures. *Journal of Structural Engineering ASCE*, 118(11), 3089-3102.

- Shrestha K., Franquet J., Rogers C. A., and Tremblay R. (2009). *OpenSees Modeling of the Inelastic Seismic Response of Steel Roof Deck Diaphragms*. Paper presented at the STESSA 2009 - Behavior of Steel Structures in Seismic Areas, London, UK.
- Spacone E. and El-Tawil S. (2004). Nonlinear analysis of steel-concrete composite structures: State-of-the-art. *Journal of Structural Engineering ASCE*, 130(2), 159-168.
- Taranath B.S. (2012). *Structural Analysis and Design of Tall Buildings*: CRC Press.
- Tena-Colunga Arturo and Abrams Daniel P. (1995). Simplified 3-D dynamic analysis of structures with flexible diaphragms. *Earthquake Engineering and Structural Dynamics*, 24, 221-232.
- Terzic V. (Producer). (2011). Force-based Element vs. Displacement-based Element.
- Tremblay R. and Stiemer S. F. (1996). Seismic behavior of single-story steel structure with a flexible diaphragm. *Canadian Journal of Civil Engineering*, 23, 49-62.
- Tso W.K. (1990). Static eccentricity concept for torsional moment estimations. *Journal of Structural Engineering, ASCE*, 116(5), 1199-1212.
- U.S. Geological Survey. (2014). from <http://www.usgs.gov/>
- Uriz P. and Mahin S. (2008). *Toward Earthquake-Resistant Design of Concentrically Braced Steel-Frame Structures*: PEER.
- Widjaja B.R. (1993). *Analytical Investigation of Composite Diaphragms Strength and Behavior*. (Master Thesis), Virginia Tech, Blacksburg, VA.
- Wright H. D. and Hossain K. M. A. (1997). In-plane shear behavior of profiled steel sheeting. *Thin Walled Structures*, 29(1), 79-100.

## Appendix A

Table A-1 Seismic load coefficients

C1/C2	CuTa	R	Cs1(Eq. 12.8-2)	Cs2(Eq. 12.8-3)	Cs3(Eq. 12.8-5)	Cs4(Eq. 12.8-6)	Cs,use	H=	52.5	ft
SCBF (Y-dir)	0.546	6	0.167	0.192	0.044	0.0525	0.167	S <sub>DS</sub> =	1	
SMRF (X-dir)	0.932	8	0.125	0.084	0.044	0.0394	0.084	S <sub>D1</sub> =	0.63	

Table A-2 Vertical distribution of seismic forces (SCBFs)

C1	w <sub>x</sub> =w <sub>px</sub>	∑w <sub>i</sub>	h	∑h	w <sub>x</sub> h <sub>k</sub>	∑w <sub>x</sub> h <sub>k</sub>	C <sub>v</sub> <sub>x</sub>	F <sub>x</sub>	k=	1.023	
5F	2112.50	2112.50	12.50	52.50	121484.2	121484.2	0.392	553.2	T=	0.546	(CuTa)
4F	2112.50	4225.00	12.50	40.00	91982.3	213466.4	0.297	418.9	C <sub>s</sub> =	0.167	
3F	2112.50	6337.50	12.50	27.50	62695.2	276161.6	0.202	285.5	T=	0.580	(Analytical)
2F	2112.50	8450.00	15.00	15.00	33723.9	309885.5	0.109	153.6	W=	8450	kips
∑							1.000	1411.2	V=	1411	kips
C2	w <sub>x</sub> =w <sub>px</sub>	∑w <sub>i</sub>	h	∑h	w <sub>x</sub> h <sub>k</sub>	∑w <sub>x</sub> h <sub>k</sub>	C <sub>v</sub> <sub>x</sub>	F <sub>x</sub>	k=	0.99	
5F	2112.50	2112.50	12.50	52.50	106599.3	106599.3	0.388	546.9	T=	0.546	(CuTa)
4F	2112.50	4225.00	12.50	40.00	81439.7	188039.0	0.296	417.8	C <sub>s</sub> =	0.167	
3F	2112.50	6337.50	12.50	27.50	56200.0	244239.0	0.204	288.3	T=	0.480	(Analytical)
2F	2112.50	8450.00	15.00	15.00	30840.9	275079.9	0.112	158.2	W=	8450	kips
∑							1.000	1411.2	V=	1411	kips

Table A-3 Vertical distribution of seismic forces (SMRFs)

C1/C2	w <sub>x</sub> =w <sub>px</sub>	∑w <sub>i</sub>	h	∑h	w <sub>x</sub> h <sub>k</sub>	∑w <sub>x</sub> h <sub>k</sub>	C <sub>v</sub> <sub>x</sub>	F <sub>x</sub>	k=	1.216	
5F	2112.50	2112.50	12.50	52.50	260921.8	260921.8	0.418	296.7	T=	0.932	(CuTa)
4F	2112.50	4225.00	12.50	40.00	187457.0	448378.8	0.300	213.2	C <sub>s</sub> =	0.084	
3F	2112.50	6337.50	12.50	27.50	118857.1	567236.0	0.190	135.2	T=	1.720	(Analytical)
2F	2112.50	8450.00	15.00	15.00	56875.3	624111.3	0.091	64.7	W=	8450	kips
∑							1.000	709.8	V=	709.8	kips

Table A-4 Drift and stability check (C1 and C2)

C1	ft	Drift check							Level height	Stability check				
		L	R	A <sub>x</sub>	F <sub>x</sub>	ΔM <sub>ta</sub>	C <sub>d</sub> *δ <sub>x</sub>	Δ <sub>allow</sub>		W <sub>x</sub>	P <sub>x</sub>	0	0/1+0	0 <sub>max</sub>
SCBF	RF	0.1039	0.0730	0.9582	553.3	0	0.51	1.05	630.00	2206.0	2206.0	0.003	0.003	0.10
	4F	0.0770	0.0541	0.9582	419.0	0	0.38	0.80	480.00	2206.0	4412.0	0.005	0.005	0.10
	3F	0.0500	0.0350	0.9612	285.6	0	0.25	0.55	330.00	2206.0	6618.0	0.008	0.008	0.10
	2F	0.0200	0.0150	0.9070	153.6	0	0.10	0.30	180.00	2206.0	8824.0	0.006	0.006	0.10

C2	ft	Drift check							Level height	Stability check					
		Left	Right	A <sub>x</sub>	F <sub>x</sub>	ΔM <sub>ta</sub>	δ <sub>x</sub> (w/ A <sub>x</sub> )	C <sub>d</sub> *δ <sub>x</sub>		Δ <sub>allow</sub>	W <sub>x</sub>	P <sub>x</sub>	0	0/1+0	0 <sub>max</sub>
SCBF	RF	0.0940	0.0340	1.4981	553.3	3411	0.106	0.52	1.05	630.00	2112.0	2112.0	0.003	0.003	0.10
	4F	0.0730	0.0260	1.5103	419.0	2646	0.082	0.41	0.80	480.00	2112.0	4224.0	0.005	0.005	0.10
	3F	0.0480	0.0170	1.5148	285.6	1819	0.053	0.26	0.55	330.00	2112.0	6336.0	0.008	0.008	0.10
	2F	0.0220	0.0071	1.5877	153.6	1117	0.024	0.12	0.30	180.00	2112.0	8448.0	0.007	0.007	0.10

C1/C2	Drift check										Level height	Stability check				
	ft	L	R	Ax	Fx	ΔMta	Cd*δx	Cd*δx.RBS	Δallow	Wx		Px	θ	θ/1+θ	θmax	
SMRF	RF	0.1479	0.1478	0.6949	296.8	0	0.79	0.86	1.05	630.00	2206.0	2206.0	0.007	0.007	0.09	
	4F	0.1352	0.1329	0.7064	213.2	0	0.73	0.79	0.80	480.00	2206.0	4412.0	0.017	0.017	0.09	
	3F	0.0990	0.0955	0.7197	135.2	0	0.54	0.58	0.55	330.00	2206.0	6618.0	0.031	0.030	0.09	
	2F	0.0511	0.0509	0.6972	64.7	0	0.28	0.30	0.30	180.00	2206.0	8824.0	0.043	0.041	0.09	

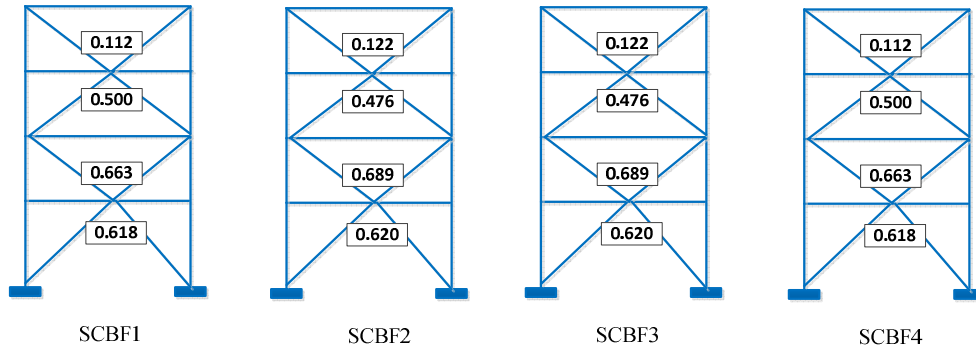


Figure A-1 D/C ratios for braces in SCBFs (C1)

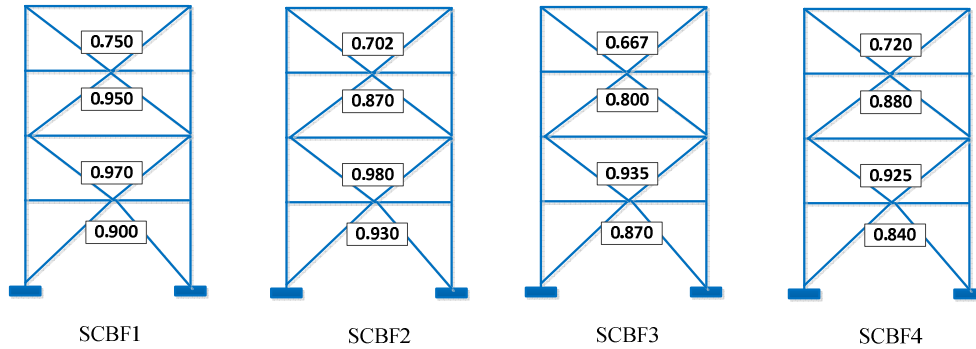


Figure A-2 D/C ratios for braces in SCBFs (C2)

Table A-5 D/C ratios for columns in SCBFs (C1)

	Column (Left)					Column (Right)			
	Size	DEAD	LIVE	EQ	Shear	DEAD	LIVE	EQ	Shear
4F	W12X106	36.6	6.6	-2	1.1	36.6	6.6	2	1.1
3F	W12X106	75.1	25.2	-2	1.4	75.1	25.2	2	1.4
2F	W14X132	106.7	41.1	-107	1.4	106.7	41.1	107	1.4
1F	W14X132	145.9	60.1	-107	4.72	145.9	60.1	107	4.72

Mechanism Analysis				Code Provision		Design for Mechanism analysis				Design for Code Provision					
Pemh	Temh	PuP	PuT	PuP	PuT	Section	Capacity(T)	Capacity(C)	Ratio	Ratio	Section	Capacity(T)	Capacity(C)	Ratio	Ratio
375.4	-195.3	429.9	-143.5	60.1	22.4	W12X106	1400	1210	0.103	0.355	W12X106	1400	1210	0.016	0.050
376.8	-195.3	494.5	-89.5	123.7	49.6	W12X106	1400	1210	0.064	0.409	W12X106	1400	1210	0.035	0.102
1044.5	-832.7	1214.4	-682.6	385.9	-138.3	W14X132	1750	1300	0.390	0.934	W14X132	1750	1300	0.079	0.297
1045.9	-832.7	1280.2	-626.1	454.9	-108.6	W14X132	1750	1300	0.358	0.985	W14X132	1750	1300	0.062	0.350

Table A-6 D/C ratios for columns in SCBF1 and SCBF4 (C2)

	Column (Left)					Column (Right)			
	Size	DEAD	LIVE	EQ	Shear	DEAD	LIVE	EQ	Shear
4F	W12X106	67	12	-148	0	67	12	148	0
3F	W12X106	144	50	-226	0	144	50	226	0
2F	W14X176	205	79	-650	0	205	79	650	0
1F	W14X176	282	116	-724.3	0	282	116	724.3	0

Mechanism Analysis				Code Provision		Design for Mechanism analysis				Design for Code Provision					
Pemh	Temh	PuP	PuT	PuP	PuT	Section	Capacity(T)	Capacity(C)	Ratio	Ratio	Section	Capacity(T)	Capacity(C)	Ratio	Ratio
462.6	-365.8	562.4	-272.0	395.8	-249.1	W12X106	1400	1210	0.194	0.465	W12X106	1400	1210	0.178	0.327
462.6	-365.8	689.2	-164.2	678.6	-351.2	W12X106	1400	1210	0.117	0.570	W12X106	1400	1210	0.251	0.561
1670.9	-1578.3	1997.4	-1291.3	1626.5	-1156.5	W14X176	2330	2130	0.554	0.938	W14X176	2330	2130	0.496	0.764
1670.9	-1578.3	2123.7	-1183.5	1901.4	-1251.2	W14X176	2330	2130	0.508	0.997	W14X176	2330	2130	0.537	0.893

Table A-7 D/C ratios for columns in SCBF2 and SCBF3 (C2)

	Column (Left)					Column (Right)			
	Size	DEAD	LIVE	EQ	Shear	DEAD	LIVE	EQ	Shear
4F	W12X106	67	12	-148	0	67	12	148	0
3F	W12X106	144	50	-226	0	144	50	226	0
2F	W14X176	205	79	-650	0	205	79	650	0
1F	W14X176	282	116	-724.3	0	282	116	724.3	0

Mechanism Analysis				Code Provision		Design for Mechanism analysis				Design for Code Provision					
Pemh	Temh	PuP	PuT	PuP	PuT	Section	Capacity(T)	Capacity(C)	Ratio	Ratio	Section	Capacity(T)	Capacity(C)	Ratio	Ratio
462.6	-365.8	562.4	-272.0	371.8	-225.1	W12X106	1400	1210	0.194	0.465	W12X106	1400	1210	0.161	0.307
462.6	-365.8	689.2	-164.2	652.6	-325.2	W12X106	1400	1210	0.117	0.570	W12X106	1400	1210	0.232	0.539
1556.9	-1427.3	1876.8	-1145.9	1429.9	-969.3	W14X176	2330	2130	0.492	0.881	W14X176	2330	2130	0.416	0.671
1556.9	-1427.3	2004.5	-1036.7	1713.6	-1070.7	W14X176	2330	2130	0.445	0.941	W14X176	2330	2130	0.460	0.805

Table A-8 D/C ratios for beams (C1)

2nd floor beam				4nd floor beam			
Method 1 (Strength)		Method 2 (Post Buckling)		Method 1 (Strength)		Method 2 (Post Buckling)	
Py	-19.7	Py	-97.1	Py	36.2	Py	14.1
Px	-51.6	Px	-31.8	Px	42.5	Px	40.8
Veh	9.8	Veh	48.5	Veh	18.1	Veh	7.1
Meh	135.3	Meh	667.4	Meh	249.2	Meh	97.1
Pu	-51.6	Pu	97.1	Pu	42.5	Pu	14.1
Vu	83.2	Vu	121.9	Vu	91.5	Vu	80.4
Mu	515.0	Mu	1047.1	Mu	628.9	Mu	476.8
W27X114				W24X76			
Ry	1.1	Fy	50	Ry	1.1	Fy	50
φMp	1290.0			φMp	825.0		
Check	OK			Check	OK		
3rd floor beam				5rd floor beam			
Method 1 (Strength)		Method 2 (Post Buckling)		Method 1 (Strength)		Method 2 (Post Buckling)	
Px	259.1	Py	137.0	Px	612.5	Py	354.3
Pu	148.5	Pu	321.2	Pu	306.2	Pu	177.1
Mu	439.2			Mu	439.2		
Vu	63.9			Vu	63.9		
W21X57				W21X57			
A	16.7	Ix	1170	A	16.7	Ix	1170
Lx	27.5	Iy	30.6	Lx	27.5	Iy	30.6
Lz	9.17	Cw	3190	Lz	9.17	Cw	3190
rx	8.36	J	1.77	rx	8.36	J	1.77
d	21.1			d	21.1		
Fy/Fe1	0.272	Fcr1	44.6	Fy/Fe1	0.272	Fcr1	44.6
Fy/Fe2	0.872	Fcr2	34.7	Fy/Fe2	0.872	Fcr2	34.7
Q(assume)	0.9	Pn	522	Q(assume)	0.9	Pn	522
φPn	469.6			φPn	469.6		
Check	OK			Check	OK		

Table A-9 D/C ratios for beams in SCBF1 and SCBF4 (C2)

2nd floor beam				4nd floor beam			
Method 1 (Strength)		Method 2 (Post Buckling)		Method 1 (Strength)		Method 2 (Post Buckling)	
Py	-12.6	Py	-131.7	Py	-33.1	Py	-101.1
Px	-44.5	Px	-27.2	Px	-38.7	Px	-28.0
Veh	6.3	Veh	65.9	Veh	16.6	Veh	50.6
Meh	86.8	Meh	905.6	Meh	227.7	Meh	695.1
Pu	<b>-44.5</b>	Pu	<b>131.7</b>	Pu	<b>-38.7</b>	Pu	<b>101.1</b>
Vu	<b>79.7</b>	Vu	<b>139.2</b>	Vu	<b>89.9</b>	Vu	<b>123.9</b>
Mu	<b>466.5</b>	Mu	<b>1285.3</b>	Mu	<b>607.4</b>	Mu	<b>1074.8</b>
W27X129				W27X114			
Ry	1.1	Fy	50	Ry	1.1	Fy	50
φMp	1480.0			φMp	1290.0		
Check	OK			Check	OK		
3rd floor beam				5rd floor beam			
Method 1 (Strength)		Method 2 (Post Buckling)		Method 1 (Strength)		Method 2 (Post Buckling)	
Px	497.0	Py	244.0	Px	894.7	Py	469.2
Pu	<b>129.1</b>	Pu	<b>502.7</b>	Pu	<b>447.3</b>	Pu	<b>234.6</b>
Mu	<b>439.2</b>			Mu	<b>439.2</b>		
Vu	<b>63.9</b>			Vu	<b>63.9</b>		
W21X73				W21X57			
A	21.5	Ix	1600	A	16.7	Ix	1170
Lx	27.5	Iy	70.6	Lx	27.5	Iy	30.6
Lz	9.17	Cw	7410	Lz	9.17	Cw	3190
rx	8.54	J	3.02	rx	8.36	J	1.77
d	21.2			d	21.1		
Fy/Fe1	0.261	Fcr1	44.8	Fy/Fe1	0.272	Fcr1	44.6
Fy/Fe2	0.516	Fcr2	40.3	Fy/Fe2	0.872	Fcr2	34.7
Q(assume)	0.9	Pn	780	Q(assume)	0.9	Pn	522
φPn	701.6			φPn	469.6		
Check	OK			Check	OK		

Table A-10 D/C ratios for beams in SCBF2 and SCBF3 (C2)

2nd floor beam				4nd floor beam			
Method 1 (Strength)		Method 2 (Post Buckling)		Method 1 (Strength)		Method 2 (Post Buckling)	
Py	-16.9	Py	-127.7	Py	-33.1	Py	-101.1
Px	-60.7	Px	-37.2	Px	-38.7	Px	-28.0
Veh	8.5	Veh	63.9	Veh	16.6	Veh	50.6
Meh	116.3	Meh	878.0	Meh	227.7	Meh	695.1
Pu	<b>-60.7</b>	Pu	<b>127.7</b>	Pu	<b>-38.7</b>	Pu	<b>101.1</b>
Vu	<b>81.8</b>	Vu	<b>137.2</b>	Vu	<b>89.9</b>	Vu	<b>123.9</b>
Mu	<b>496.0</b>	Mu	<b>1257.7</b>	Mu	<b>607.4</b>	Mu	<b>1074.8</b>
W27X114				W24X103			
Ry	1.1	Fy	50	Ry	1.1	Fy	50
φMp	1290.0			φMp	1050.0		
Check	OK			Check	NG		
3rd floor beam				5rd floor beam			
Method 1 (Strength)		Method 2 (Post Buckling)		Method 1 (Strength)		Method 2 (Post Buckling)	
Px	210.8	Py	113.4	Px	894.7	Py	469.2
Pu	<b>149.1</b>	Pu	<b>486.3</b>	Pu	<b>447.3</b>	Pu	<b>234.6</b>
Mu	<b>439.2</b>			Mu	<b>439.2</b>		
Vu	<b>63.9</b>			Vu	<b>63.9</b>		
W21X73				W21X57			
A	21.5	Ix	1600	A	16.7	Ix	1170
Lx	27.5	Iy	70.6	Lx	27.5	Iy	30.6
Lz	9.17	Cw	7410	Lz	9.17	Cw	3190
rx	8.54	J	3.02	rx	8.36	J	1.77
d	21.2			d	21.1		
Fy/Fe1	0.261	Fcr1	44.8	Fy/Fe1	0.272	Fcr1	44.6
Fy/Fe2	0.516	Fcr2	40.3	Fy/Fe2	0.872	Fcr2	34.7
Q(assume)	0.9	Pn	780	Q(assume)	0.9	Pn	522
φPn	701.6			φPn	469.6		
Check	OK			Check	OK		

Table A-11 Strong column – weak beam check (2F)

<b>Interior joint (2F)</b>	<b>Beam dimension</b>							
	W27X114	Zx=	343.00	in <sup>4</sup>	RBS design parameters	Cpr=	1.15	
		tbf=	0.94	in		Ry=	1.10	
		d=	27.50	in		Fy=	50.00	ksi
		bf=	10.50	in		a=	6.56	in
		L'=	302.3	in		b=	20.63	in
		wu=	1.49	k/ft		c=	1.05	in
	<b>RBS properites</b>							
		Ze=	290.6	in <sup>4</sup>		Ve=	121.6	kips
		Sh=	16.9	in		Vg=	18.8	kips
		Mpr=	18378.6	kips-in		Vp=	140.4	kips
	<b>Strong column weak beam check</b>							
		Mpb,R=	21849	kips-in		Mpb,L=	20920.91	kips-in
		∑Mpb*=	42769.9	kips-in		∑MBF=	43178.73	kips-in
		Vc*=	380.177	kips				
		∑Mpc*=	48406.2	kips-in		∑Mpc*/∑Mpb*=		<b>1.13</b>

Table A-12 Strong column – weak beam check (3F)

<b>Interior joint (3F)</b>	<b>Beam dimension</b>							
	W24X84	Zx=	224.00	in <sup>4</sup>	RBS design parameters	Cpr=	1.15	
		tbf=	0.77	in		Ry=	1.10	
		d=	24.10	in		Fy=	50.00	ksi
		bf=	9.00	in		a=	5.63	in
		L'=	302.3	in		b=	18.08	in
		wu=	1.49	k/ft		c=	0.90	in
	<b>RBS properites</b>							
		Ze=	191.7	in <sup>4</sup>		Ve=	80.2	kips
		Sh=	14.7	in		Vg=	18.8	kips
		Mpr=	12122.8	kips-in		Vp=	99.0	kips
	<b>Strong column weak beam check</b>							
		Mpb,R=	14301.4	kips-in		Mpb,L=	13475.14	kips-in
		∑Mpb*=	27776.5	kips-in		∑MBF=	29318.5	kips-in
		Vc*=	246.903	kips				
		∑Mpc*=	32293.7	kips-in		∑Mpc*/∑Mpb*=		<b>1.16</b>

Table A-13 Strong column – weak beam check (4F)

<b>Interior joint (4F)</b>	<b>Beam dimension</b>							
	W24X76	Zx=	200.00	in <sup>4</sup>	RBS design parameters	Cpr=	1.15	
		tbf=	0.68	in		Ry=	1.10	
		d=	23.90	in		Fy=	50.00	ksi
		bf=	8.99	in		a=	5.62	in
		L'=	302.3	in		b=	17.93	in
		wu=	1.49	k/ft		c=	0.90	in
	<b>RBS properites</b>							
		Ze=	171.6	in <sup>4</sup>		Ve=	71.8	kips
		Sh=	14.6	in		Vg=	18.8	kips
		Mpr=	10854.4	kips-in		Vp=	90.6	kips
	<b>Strong column weak beam check</b>							
		Mpb,R=	12840.9	kips-in		Mpb,L=	12017.67	kips-in
		∑Mpb*=	24858.5	kips-in		∑MBF=	21940.52	kips-in
		Vc*=	220.965	kips				
		∑Mpc*=	24581	kips-in		∑Mpc*/∑Mpb*=		<b>0.99</b>

Table A-14 Strong column – weak beam check (RF)

<b>Interior joint (RF)</b>	<b>Beam dimension</b>							
	W21X44	Zx=	95.40	in <sup>4</sup>	RBS design parameters	Cpr=	1.15	
		tbf=	0.45	0.77		Ry=	1.10	
		d=	20.70	in		Fy=	50.00	ksi
		bf=	6.50	in		a=	4.06	in
		L'=	302.3	in		b=	15.53	in
		wu=	1.45	k/ft		c=	0.65	in
	<b>RBS properites</b>							
		Ze=	83.6	in <sup>4</sup>		Ve=	35.0	kips
		Sh=	11.8	in		Vg=	18.3	kips
		Mpr=	5284.8	kips-in		Vp=	53.2	kips
	<b>Strong column weak beam check</b>							
		Mpb,R=	5914.46	kips-in		Mpb,L=	5482.334	kips-in
		∑Mpb*=	11396.8	kips-in		∑MBF=	10970.25	kips-in
		Vc*=	101.305	kips				
		∑Mpc*=	12018.8	kips-in		∑Mpc*/∑Mpb*=		<b>1.05</b>

Table A-15 D/C ratios of panel zones

<b>Panel zone check (2F)</b>	Ru=	1040.46	kips	<b>Panel zone check (3F)</b>	Ru=	784.482	kips
	0.75Pc=	2325	kips		0.75Pc=	2325	kips
	Rn=	588.34	kips		Rn=	605.17	kips
	tdoub=	1.5	in		tdoub=	1.5	in
	$\phi vRn=$	1765.84	kips		$\phi vRn=$	1782.67	kips

<b>Panel zone check (4F)</b>	Ru=	709.051	kips	<b>Panel zone check (RF)</b>	Ru=	396.07	kips
	0.75Pc=	1455	kips		0.75Pc=	1455.00	kips
	Rn=	343.17	kips		Rn=	352.25	kips
	tdoub=	1.25	in		tdoub=	0.75	in
	$\phi vRn=$	1261.92	kips		$\phi vRn=$	903.50	kips

Table A-16 Spring stiffness of panel zones

2F	<b>Panel zone spring calculation</b>			3F	<b>Panel zone spring calculation</b>		
	Vp=	793.687	in <sup>3</sup>		Vp=	703.836	in <sup>3</sup>
	Sp=	8852788	kips-in		Sp=	7850586	ksi
	Myp=	25318.6	kips-in		Myp=	22452.4	kips-in
	$\theta_{yp}=$	0.00286	kips-in/rad		$\theta_{yp}=$	0.00286	kips-in/rad
	<b>Flange spring calculation</b>				<b>Flange spring calculation</b>		
	Sf=	321661	ksi		Sf=	321661	ksi
	Myf=	3806.64	kips-in		Myf=	3806.64	kips-in
	$\theta_{yf}=$	0.01183	kips-in/rad		$\theta_{yf}=$	0.01183	kips-in/rad

4F	<b>Panel zone spring calculation</b>			RF	<b>Panel zone spring calculation</b>		
	Vp=	539.896	in <sup>3</sup>		Vp=	349.129	in <sup>3</sup>
	Sp=	6022001	ksi		Sp=	3894190	ksi
	Myp=	17222.7	kips-in		Myp=	11137.2	kips-in
	$\theta_{yp}=$	0.00286	kips-in/rad		$\theta_{yp}=$	0.00286	kips-in/rad
	<b>Flange spring calculation</b>				<b>Flange spring calculation</b>		
	Sf=	130462	ksi		Sf=	130462	ksi
	Myf=	1543.93	kips-in		Myf=	1543.93	kips-in
	$\theta_{yf}=$	0.01183	kips-in/rad		$\theta_{yf}=$	0.01183	kips-in/rad

Table A-17 Amplification factors of *CF1* and *CF2*

Interior gravity beam	W18X46 (Y-dir)	IXX=	712	in <sup>4</sup>	A=	13.5	in <sup>2</sup>	t=	3	in
		d=	18	in	be=	82.5	in	gap=	3	in
		y=	5.95	in	Icomp,1=	2382.88	in <sup>4</sup>	Icomp,2=	124804	
		Iavg=	1547.44	in <sup>4</sup>	CF1=	2.17		CF2=	5546.8	
	W24X76 (X-dir)	IXX=	2100	in <sup>4</sup>	A=	22.4	in <sup>2</sup>	t=	4.5	in
		d=	24	in	be=	82.5	in	gap=	1.5	in
		y=	7.79	in	Icomp,1=	5770.71	in <sup>4</sup>	Icomp,2=	187254	
		Iavg=	3935.35	in <sup>4</sup>	CF1=	1.87		CF2=	2269.8	
External gravity beam	W18X46 (X-dir)	IXX=	712	in <sup>4</sup>	A=	13.5	in <sup>2</sup>	t=	4.5	in
		d=	18	in	be=	41.25	in	gap=	1.5	in
		y=	7.29	in	Icomp,1=	2073.21	in <sup>4</sup>	Icomp,2=	23419	
		Iavg=	1392.60	in <sup>4</sup>	CF1=	1.96		CF2=	1040.8	
	W18X46 (Y-dir)	IXX=	712	in <sup>4</sup>	A=	13.5	in <sup>2</sup>	t=	3	in
		d=	18	in	be=	41.25	in	gap=	3	in
		y=	8.19	in	Icomp,1=	1963.79	in <sup>4</sup>	Icomp,2=	15620	
		Iavg=	1337.89	in <sup>4</sup>	CF1=	1.88		CF2=	694.2	

Table A-18 Amplification factors of *AF1* (ACI approach)

	bE		t		I <sub>slab</sub>		0.25xI <sub>slab</sub>		t <sub>eq2</sub>		AF1
W24x76 (X-dir)	82.50	in	4.50	in	626.00	in <sup>4</sup>	156.60	in <sup>4</sup>	2.16	in	<b>2.16</b>
W18x46 (Y-dir)	82.50	in	3.00	in	185.60	in <sup>4</sup>	46.40	in <sup>4</sup>	1.89	in	<b>2.28</b>

Table A-19 Amplification factors of *AF1* (Equivalent thickness approach)

	bE		t		Y (Neutral axis)		t <sub>eq3</sub>		AF1
W24x76 (X-dir)	82.50	in	4.50	in	14.21	in	2.21	in	<b>1.90</b>
W18x46 (Y-dir)	82.50	in	3.00	in	11.21	in	2.16	in	<b>2.47</b>

Table A-20 Amplification factor of *AFI* for edge beams

<b>W18x46 (Y-dir)</b>	<i>Keq,T</i>	1170	k-in/in	<i>teq,T</i>	0.15	in	<i>AFI,T</i>	1.05	<i>AFI,avg</i>	<b>1.375</b>
	<i>Keq,C</i>	2017	k-in/in	<i>teq,C</i>	1.38	in	<i>AFI,C</i>	1.70		
<b>W18x46 (X-dir)</b>	<i>Keq,T</i>	1215	k-in/in	<i>teq,T</i>	1.06	in	<i>AFI,T</i>	1.06	<i>AFI,avg</i>	<b>1.580</b>
	<i>Keq,C</i>	2500	k-in/in	<i>teq,C</i>	2.11	in	<i>AFI,C</i>	2.11		

Table A-21 Selected ground motions from PEER Data base

Ground Motions	PEER NGA ID	Year	Site Class	Magnitude	Fault type	Epicentral distance (km)	Direction 1	Direction 2
<b>Northridge - 01</b>	<b>1078</b>	<b>1994</b>	<b>D</b>	<b>6.7</b>	<b>Reverse</b>	<b>14.66</b>	<b>090</b>	<b>000</b>
<b>Imperial Valley - 02</b>	<b>6</b>	<b>1940</b>	<b>D</b>	<b>7</b>	<b>Strike slip</b>	<b>12.98</b>	<b>270</b>	<b>180</b>
<b>San Fernando</b>	<b>68</b>	<b>1971</b>	<b>D</b>	<b>6.6</b>	<b>Reverse</b>	<b>39.49</b>	<b>090</b>	<b>180</b>
<b>Loma Prieta</b>	<b>758</b>	<b>1989</b>	<b>D</b>	<b>6.9</b>	<b>Reverse Oblique</b>	<b>96.5</b>	<b>260</b>	<b>350</b>
<b>Northern Calif - 03</b>	<b>20</b>	<b>1954</b>	<b>D</b>	<b>6.5</b>	<b>Strike slip</b>	<b>30.79</b>	<b>044</b>	<b>314</b>
<b>Superposition</b>	<b>723</b>	<b>1987</b>	<b>D</b>	<b>6.5</b>	<b>Strike slip</b>	<b>15.99</b>	<b>225</b>	<b>315</b>
<b>Hollister</b>	<b>23</b>	<b>1961</b>	<b>D</b>	<b>5.6</b>	<b>Strike slip</b>	<b>20.6</b>	<b>271</b>	<b>181</b>

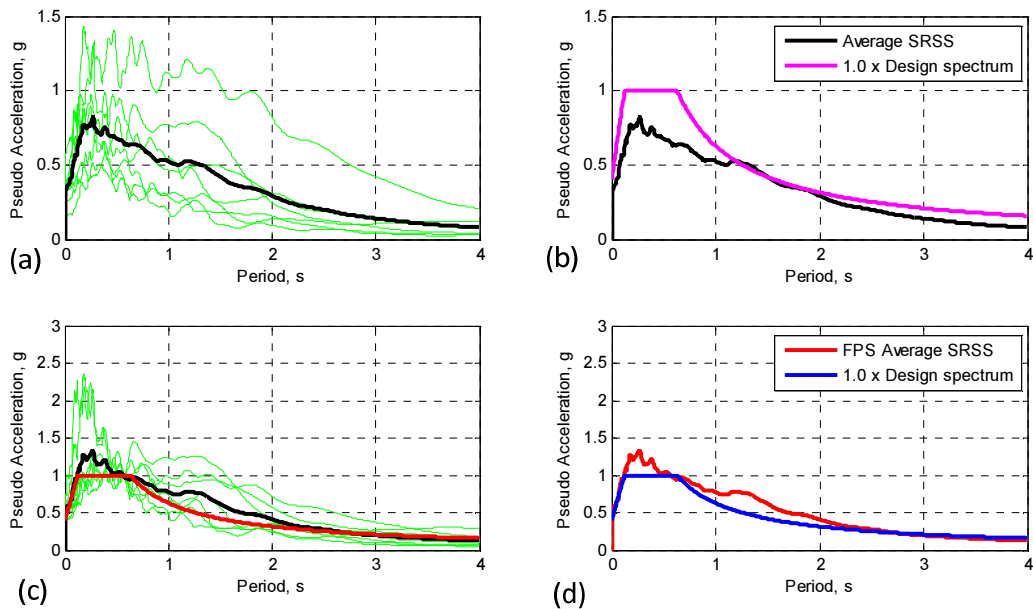


Figure A-3 Various spectra from the 3D ground motions scaling process for C1: (a) Unscaled SRSS, (b) Unscaled SRSS and 1.0x design, (c) FP SRSS and 1.0x design and (d) FP average SRSS and 1.0x design

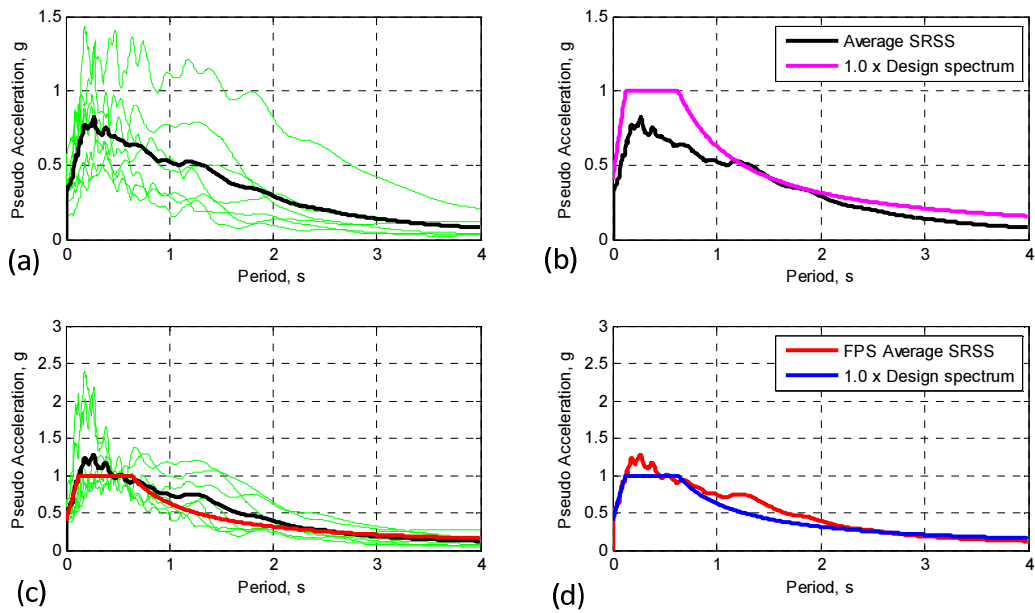


Figure A-4 Various spectra from the 3D ground motions scaling process for C2: (a) Unscaled SRSS, (b) Unscaled SRSS and 1.0xdesign, (c) FP SRSS and 1.0xdesign and (d) FP average SRSS and 1.0xdesign

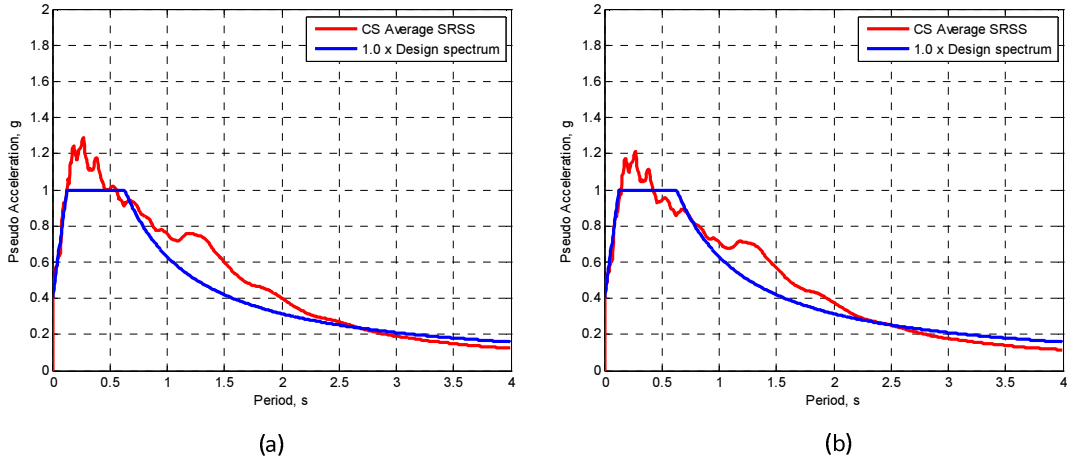


Figure A-5 Combined SRSS and 1.0xdesign: (a) C1 and (b) C2

Table A-22 Scaling factor for ground motions for C1 and C2

Ground Motions	Configuration 1		Configuration 2	
	FP factor	S factor	FP factor	S factor
Northridge – 01	1.65	0.97	1.68	0.95
Imperial Valley - 02	1.19		1.05	
San Fernando	2.50		2.30	
Loma Prieta	1.60		1.52	
Northern Calif - 03	1.88		2.12	
Superposition	0.88		0.76	
Hollister	2.56		2.52	

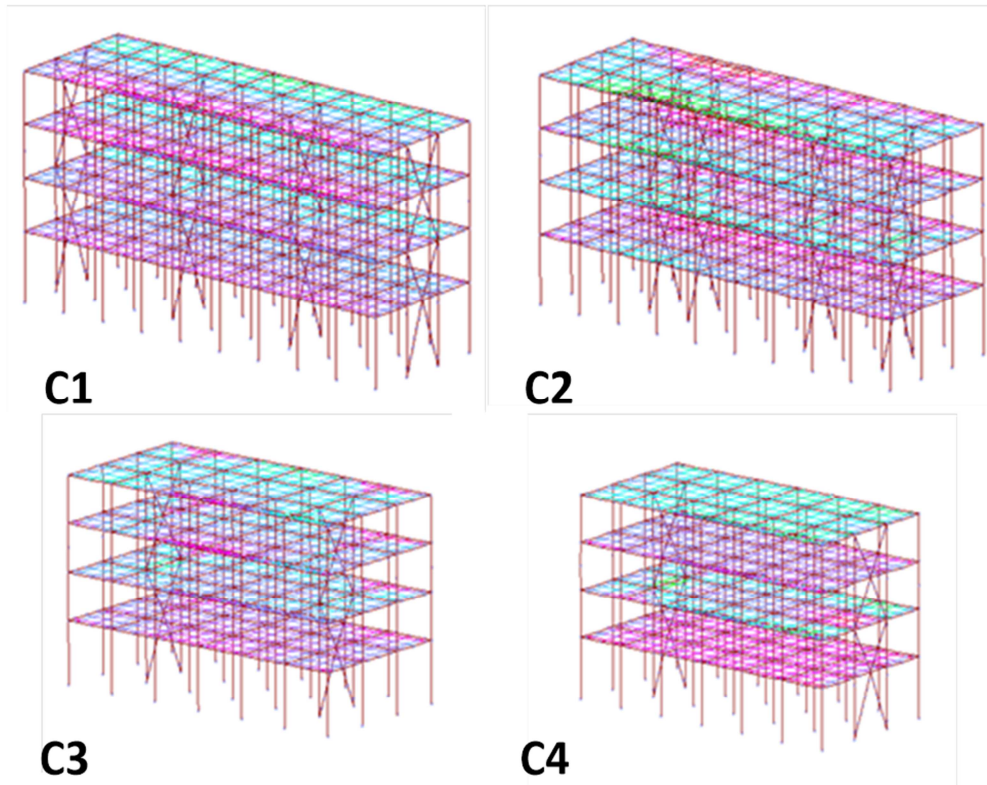


Figure A-6 Un-deformed theme structures in OpenSEES in the initial design

## Appendix B

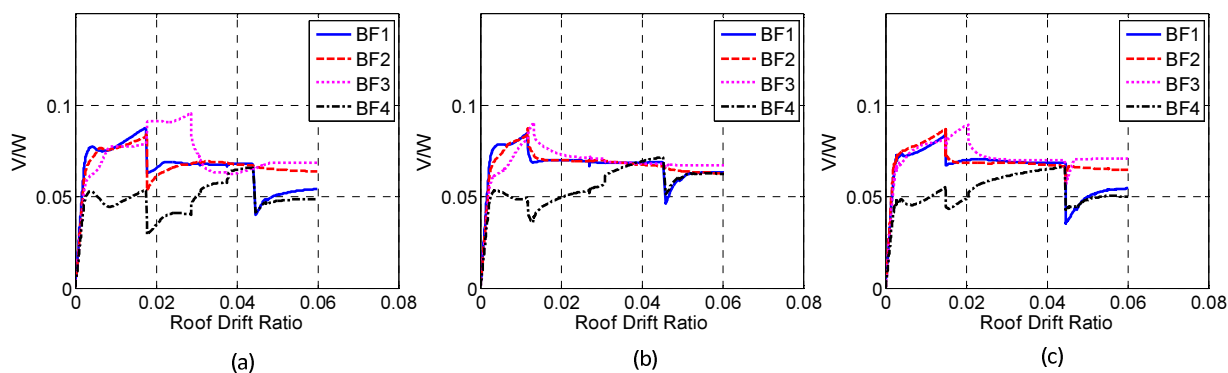


Figure B-1 Capacity curves of braced frames of C1 with  $M_{1a_1}$ : (a) **BF+R**, (b) **CF+R** and (c) **CF**

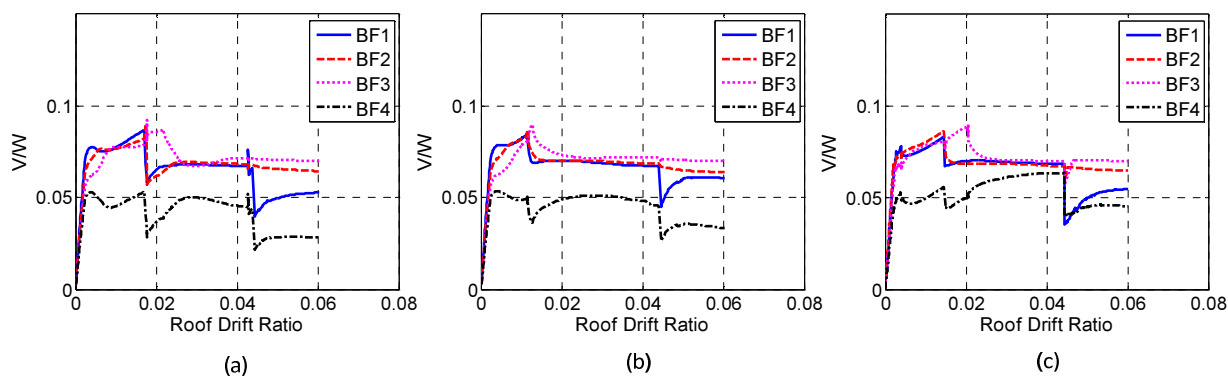


Figure B-2 Capacity curves of braced frames of C1 with  $M_{1a_2}$ : (a) **BF+R**, (b) **CF+R** and (c) **CF**

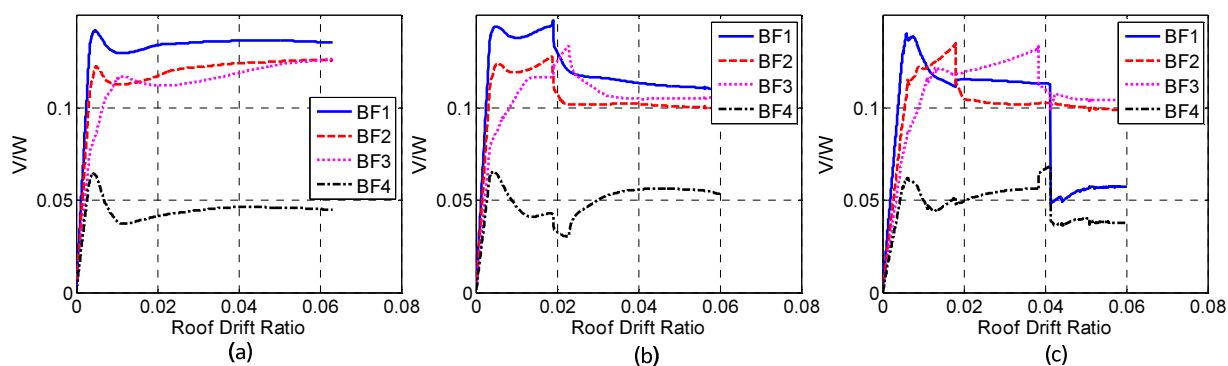


Figure B-3 Capacity curves of braced frames of C2 with  $M_{1a_1}$ : (a) **BF+R**, (b) **CF+R** and (c) **CF**

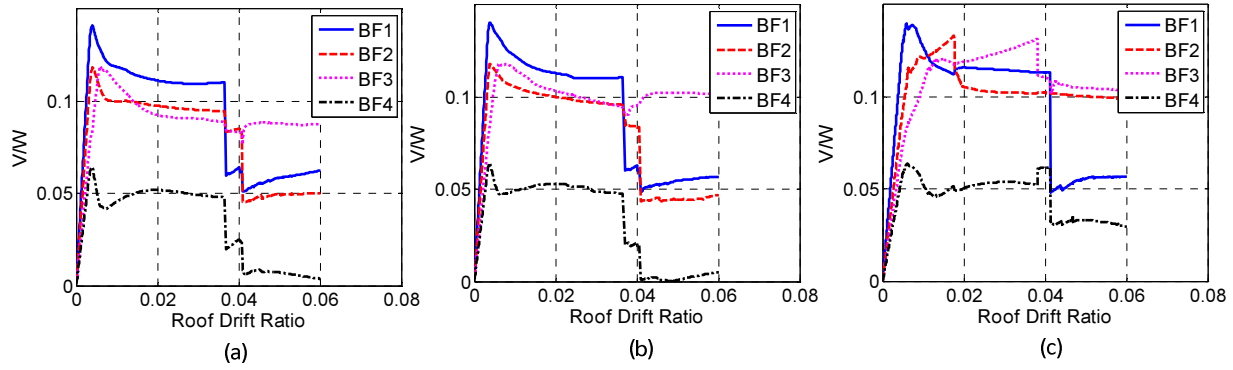


Figure B-4 Capacity curves of braced frames of C2 with  $M_{1a_2}$ : (a) **BF+R**, (b) **CF+R** and (c) **CF**

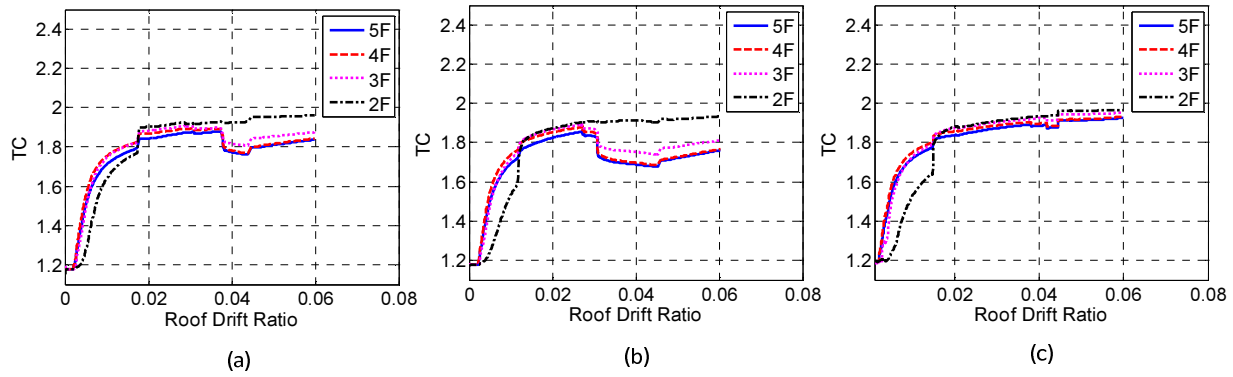


Figure B-5 TC of C1 with  $M_{1a_1}$ : (a) **BF+R**, (b) **CF+R** and (c) **CF**

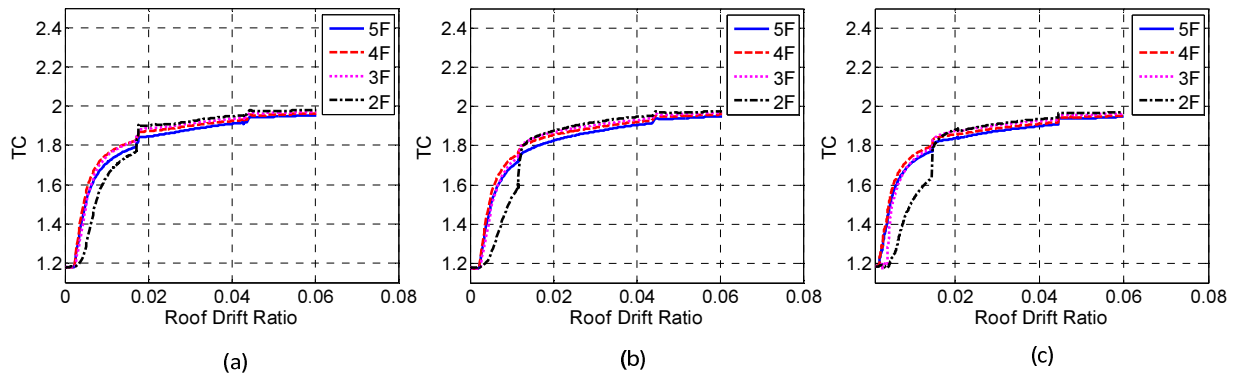


Figure B-6 TC of C1 with  $M_{1a_2}$ : (a) **BF+R**, (b) **CF+R** and (c) **CF**

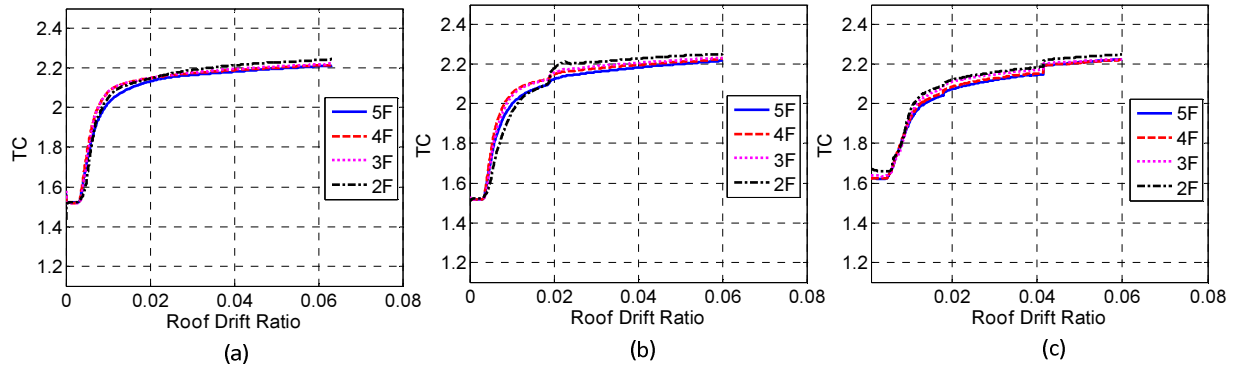


Figure B-7 TC of C2 with  $M_{ta\_1}$ : (a) **BF+R**, (b) **CF+R** and (c) **CF**

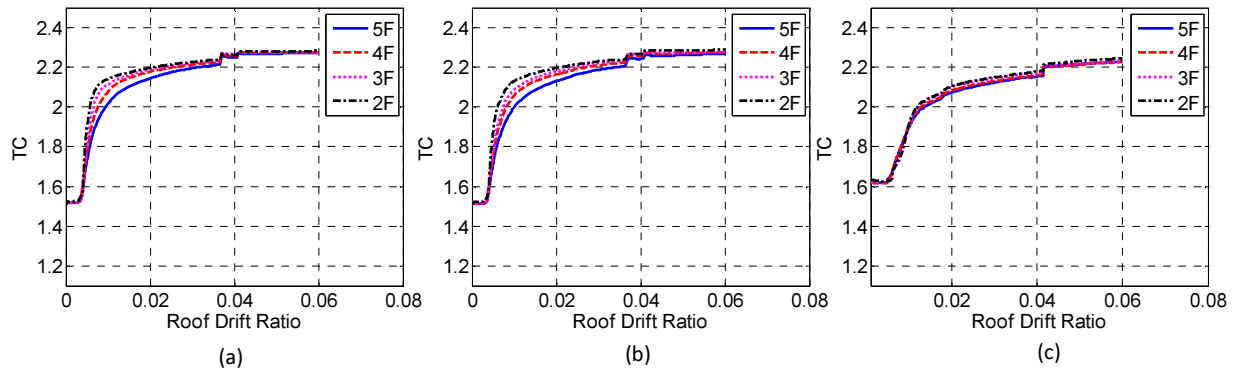


Figure B-8 TC of C2 with  $M_{ta\_2}$ : (a) **BF+R**, (b) **CF+R** and (c) **CF**

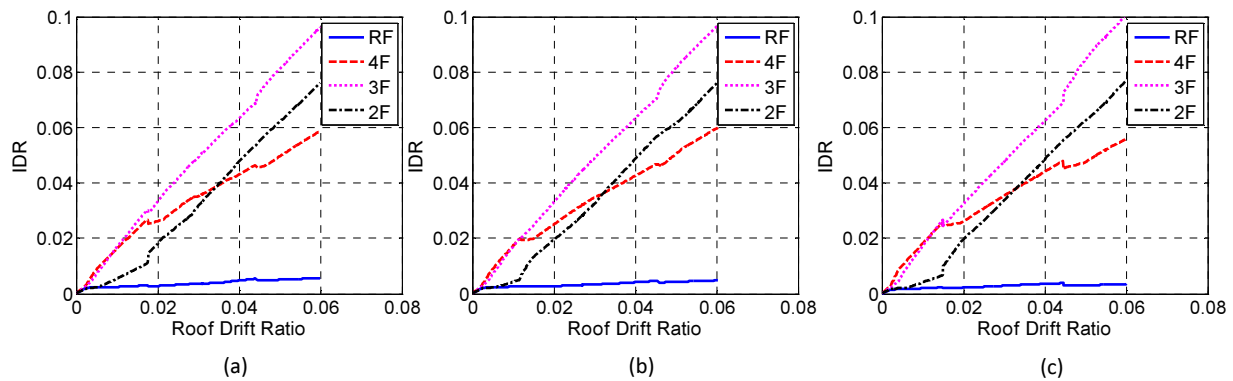


Figure B-9 IDR of C1 at left corner with  $M_{ta\_1}$ : (a) **BF+R**, (b) **CF+R** and (c) **CF**

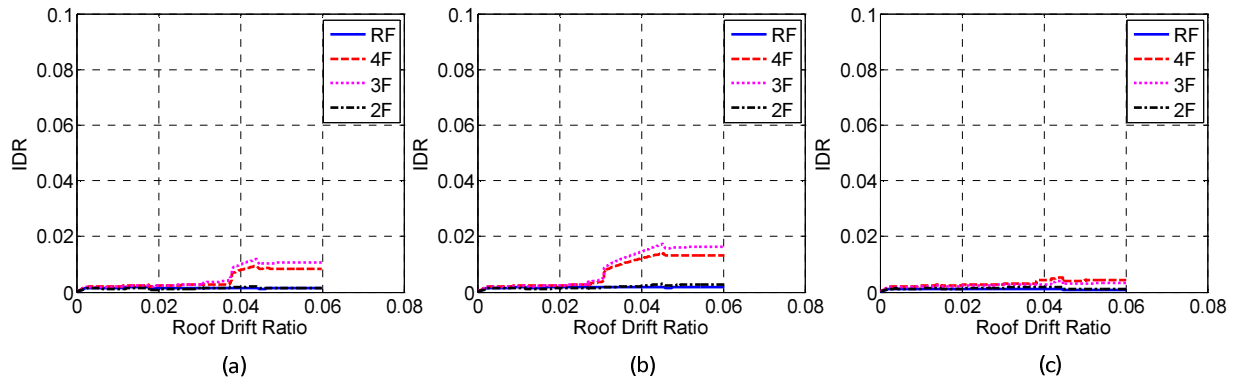


Figure B-10 IDR of C1 at right corner with  $M_{ta_1}$ : (a) **BF+R**, (b) **CF+R** and (c) **CF**

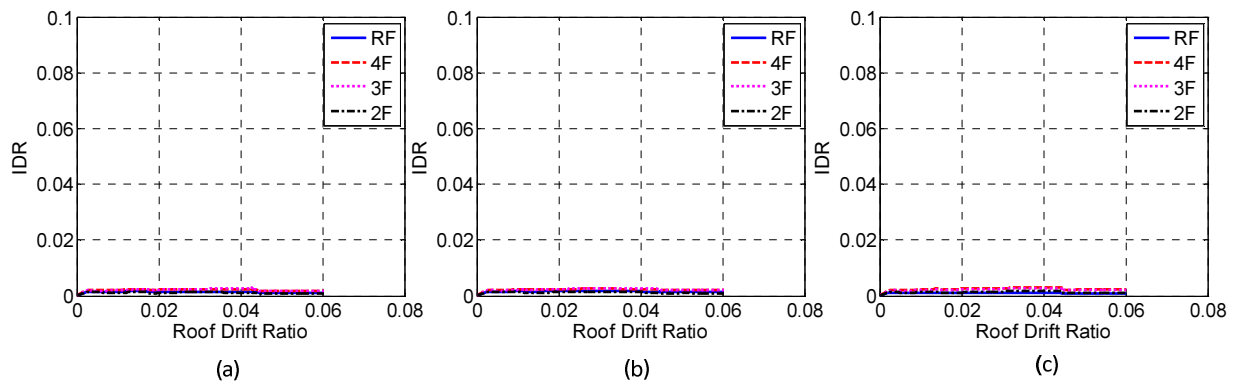


Figure B-11 IDR of C1 at right corner with  $M_{ta_2}$ : (a) **BF+R**, (b) **CF+R** and (c) **CF**

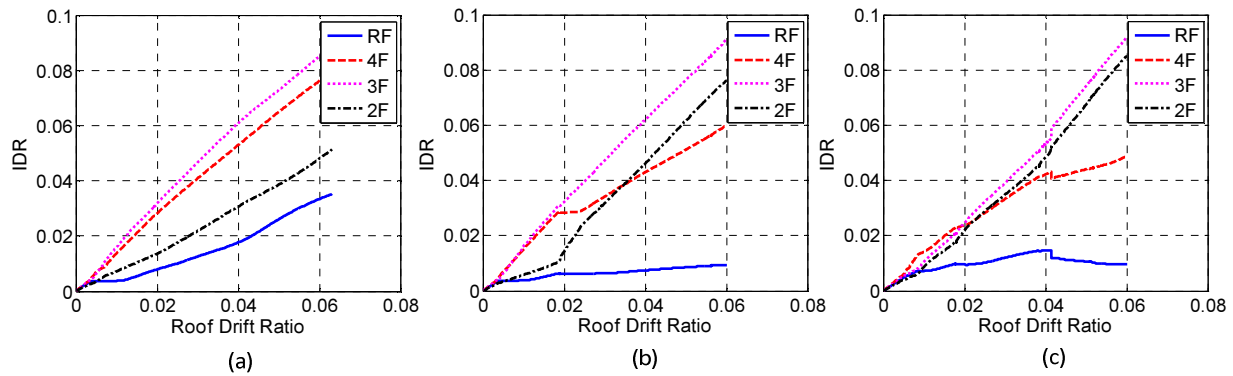


Figure B-12 IDR of C2 at left corner with  $M_{ta_1}$ : (a) **BF+R**, (b) **CF+R** and (c) **CF**

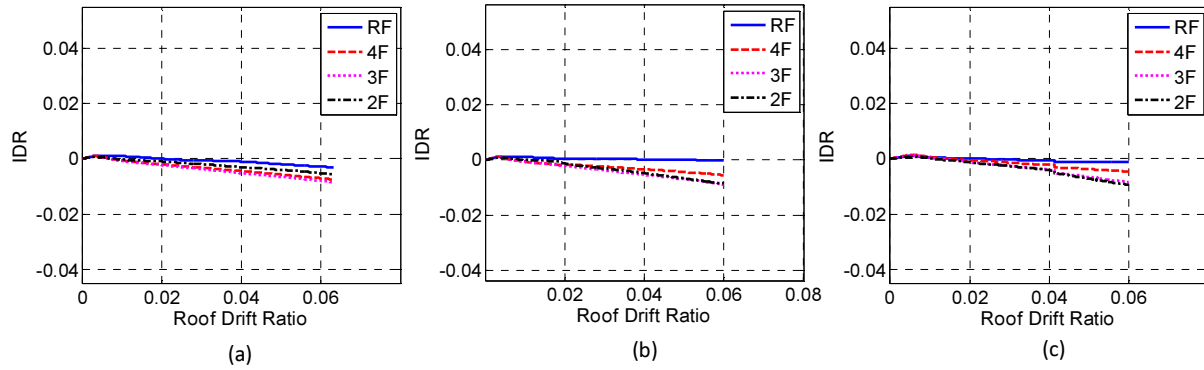


Figure B-13 IDR of C2 at right corner with  $M_{1a_1}$ : (a) **BF+R**, (b) **CF+R** and (c) **CF**

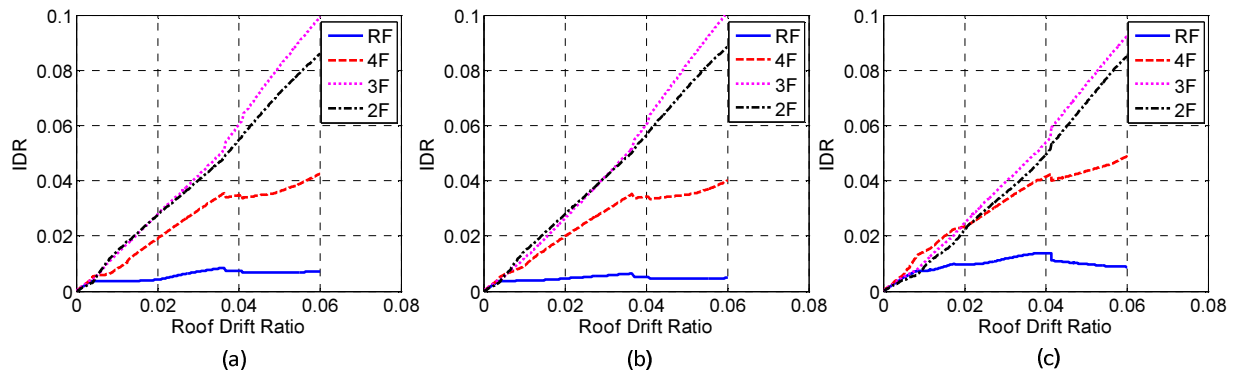


Figure B-14 IDR of C2 at left corner with  $M_{1a_2}$ : (a) **BF+R**, (b) **CF+R** and (c) **CF**

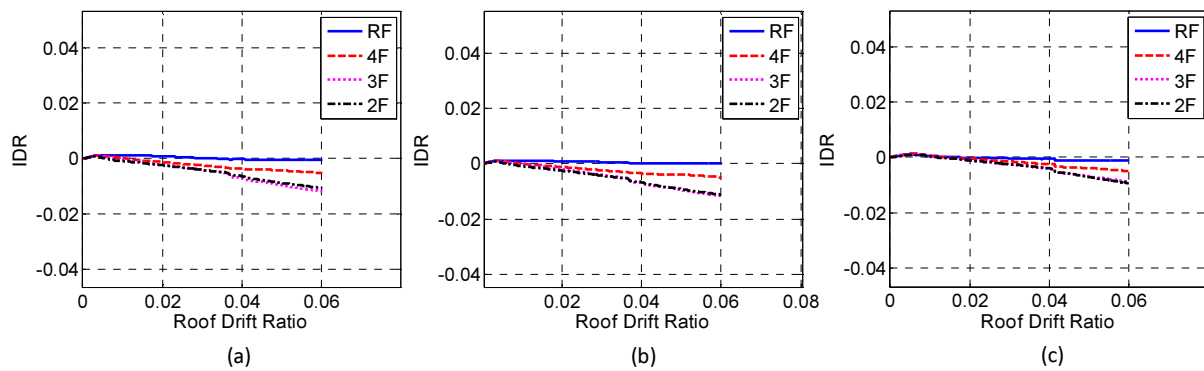


Figure B-15 IDR of C2 at right corner with  $M_{1a_2}$ : (a) **BF+R**, (b) **CF+R** and (c) **CF**

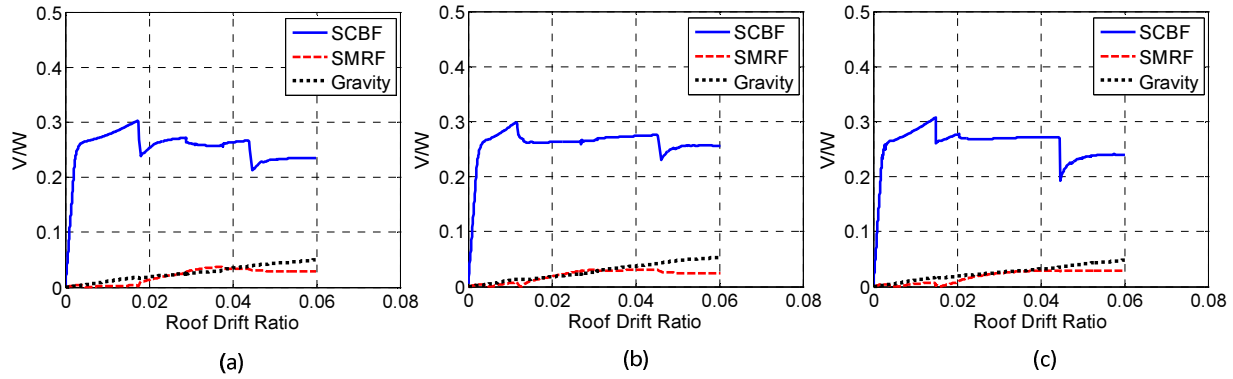


Figure B-16 Capacity curves of each system of C1 with  $M_{ta\_1}$ : (a) **BF+R**, (b) **CF+R** and (c) **CF**

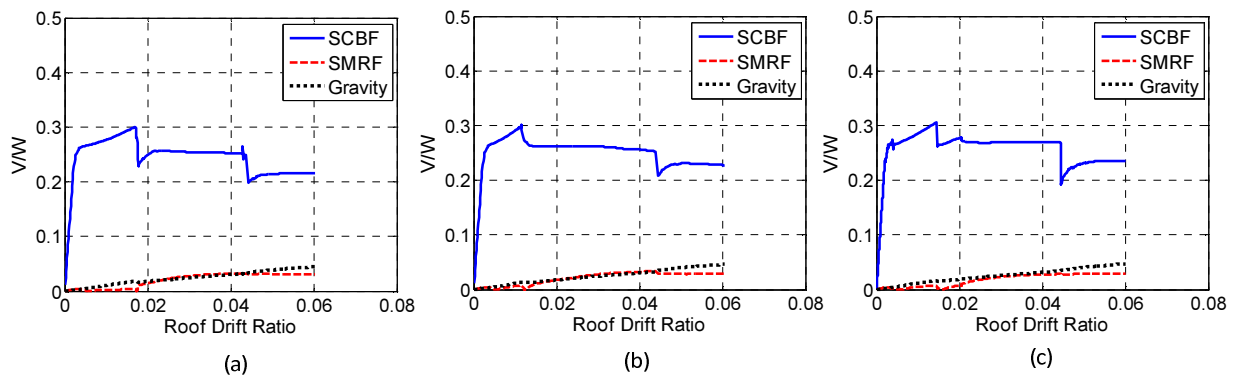


Figure B-17 Capacity curves of each system of C1 with  $M_{ta\_2}$ : (a) **BF+R**, (b) **CF+R** and (c) **CF**

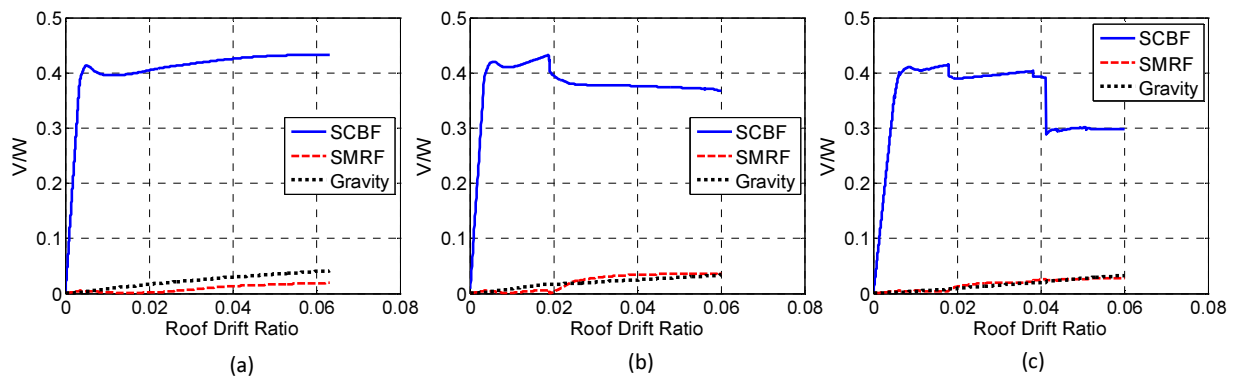


Figure B-18 Capacity curves of each system of C2 with  $M_{ta\_1}$ : (a) **BF+R**, (b) **CF+R** and (c) **CF**

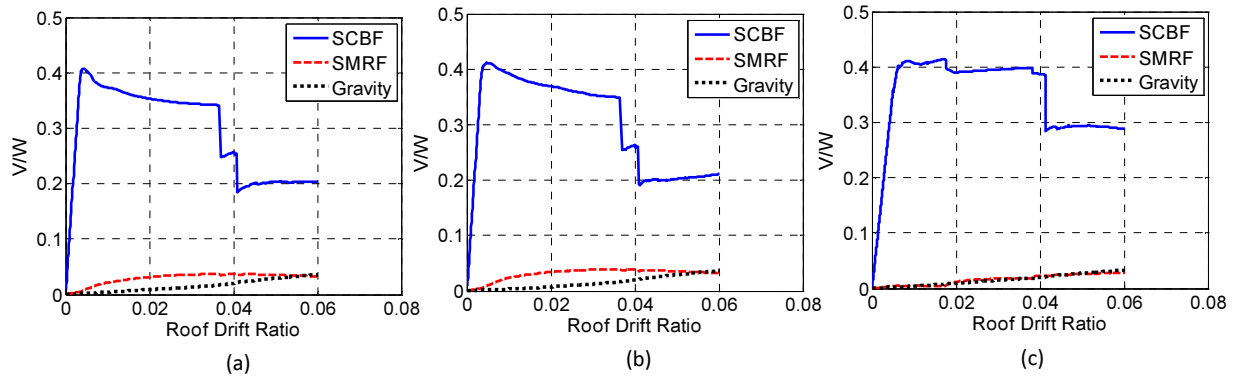


Figure B-19 Capacity curves of each system of C2 with  $M_{ta_2}$ : (a) **BF+R**, (b) **CF+R** and (c) **CF**

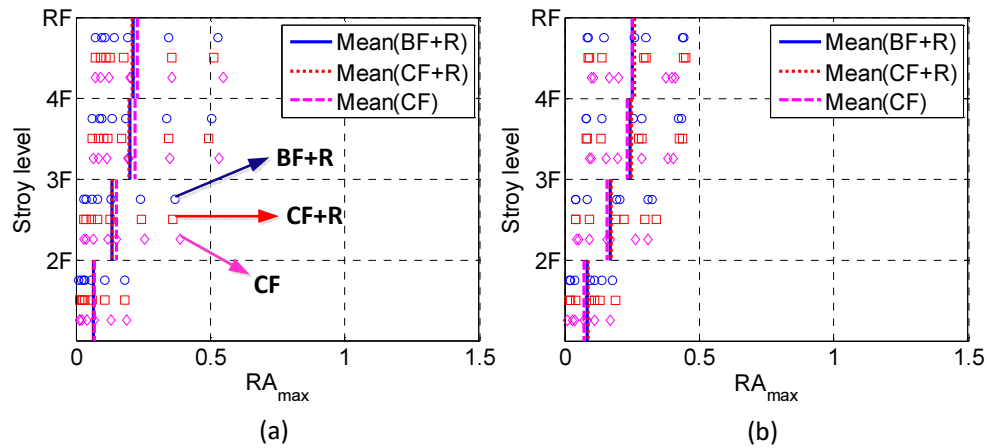


Figure B-20 Variation of RA in C1 with  $M_{ta_1}$ : (a) DBE and (b) MCE

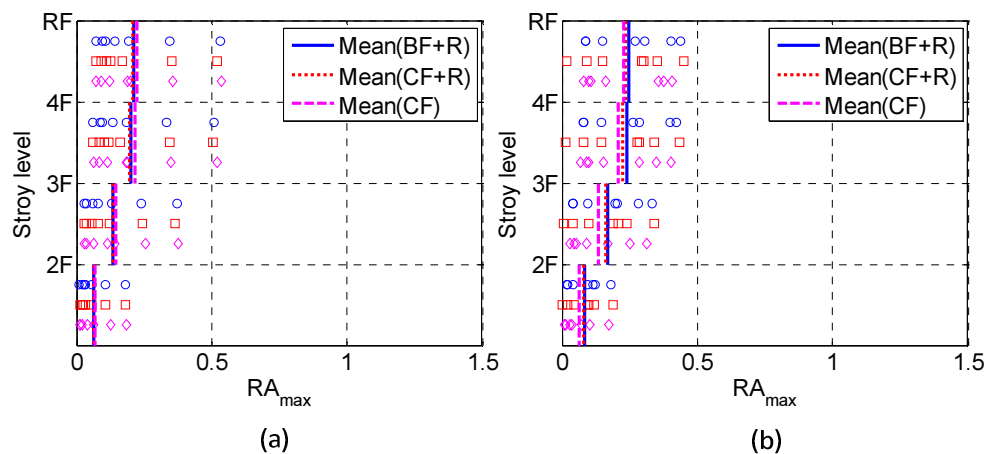


Figure B-21 Variation of RA in C1 with  $M_{ta_2}$ : (a) DBE and (b) MCE

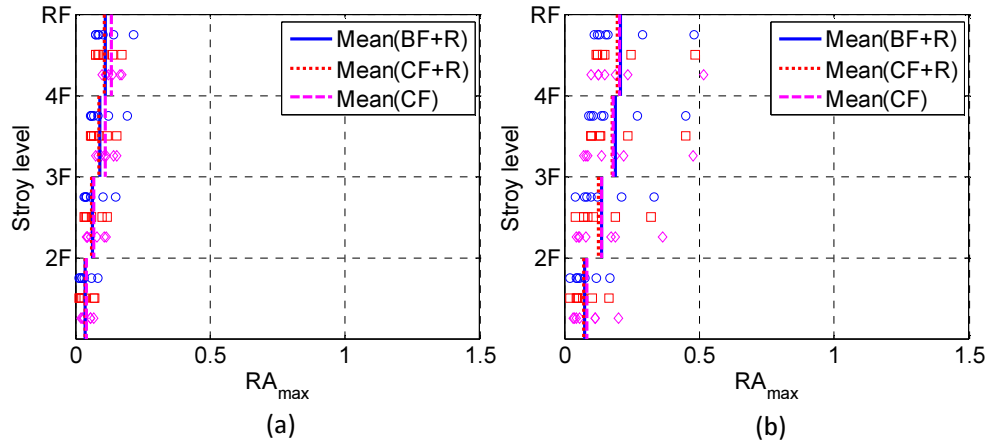


Figure B-22 Variation of RA in C2 with  $M_{ta\_1}$ : (a) DBE and (b) MCE

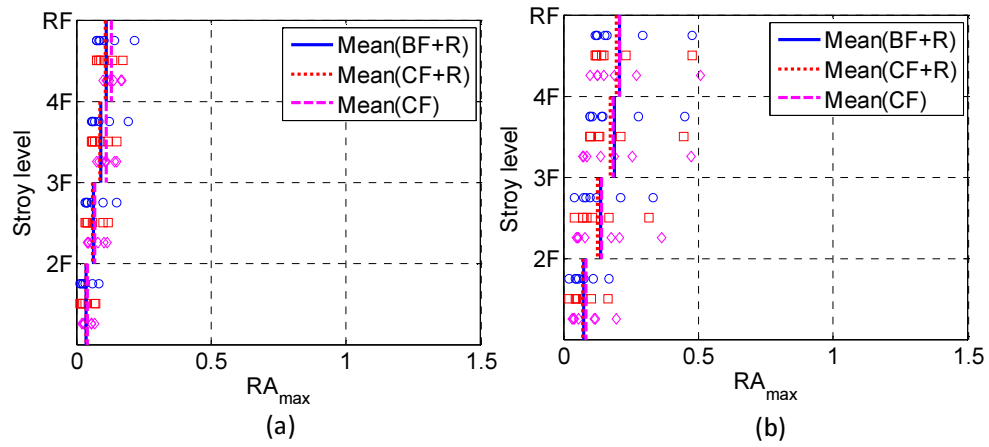


Figure B-23 Variation of RA in C1 with  $M_{ta\_2}$ : (a) DBE and (b) MCE

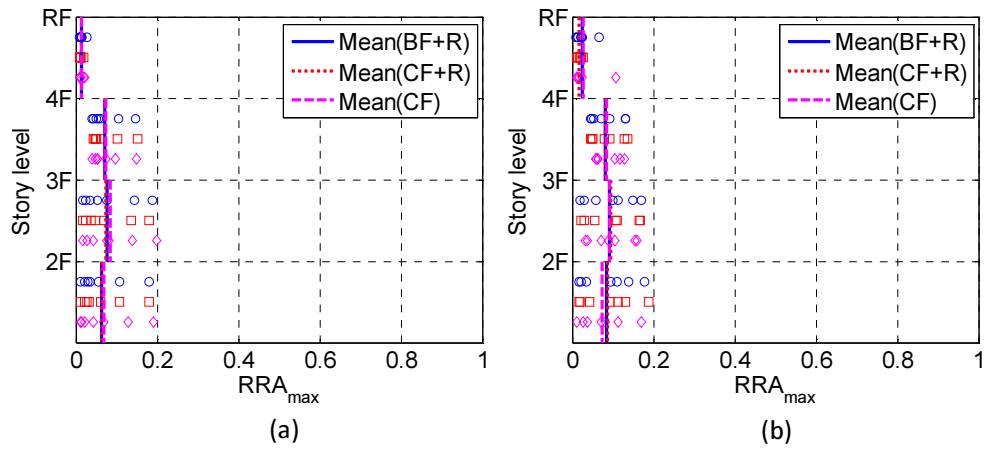


Figure B-24 Variation of RRA in C1 with  $M_{ta\_1}$ : (a) DBE and (b) MCE

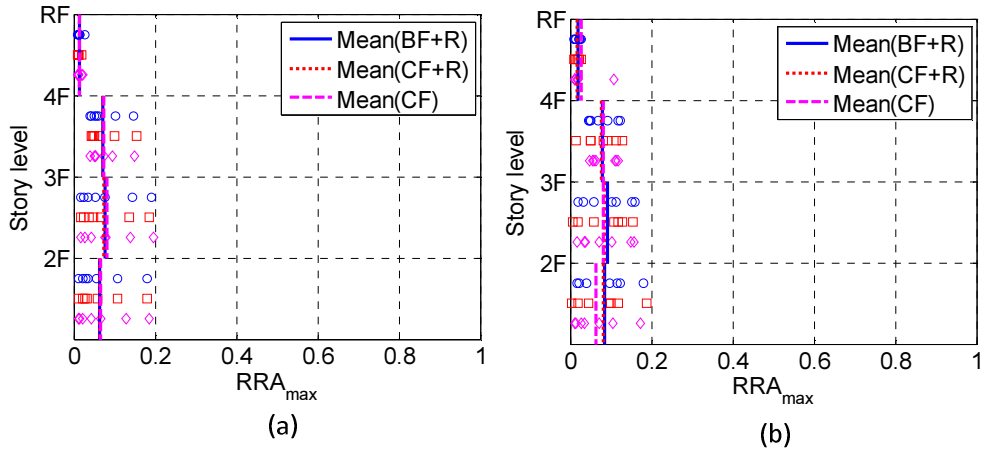


Figure B-25 Variation of RRA in C1 with  $M_{ta\_2}$ : (a) DBE and (b) MCE

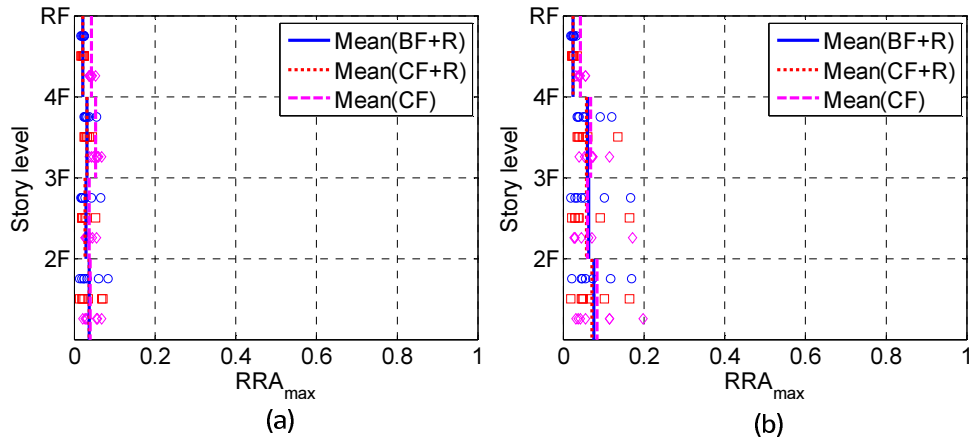


Figure B-26 Variation of RRA in C2 with  $M_{ta\_1}$ : (a) DBE and (b) MCE

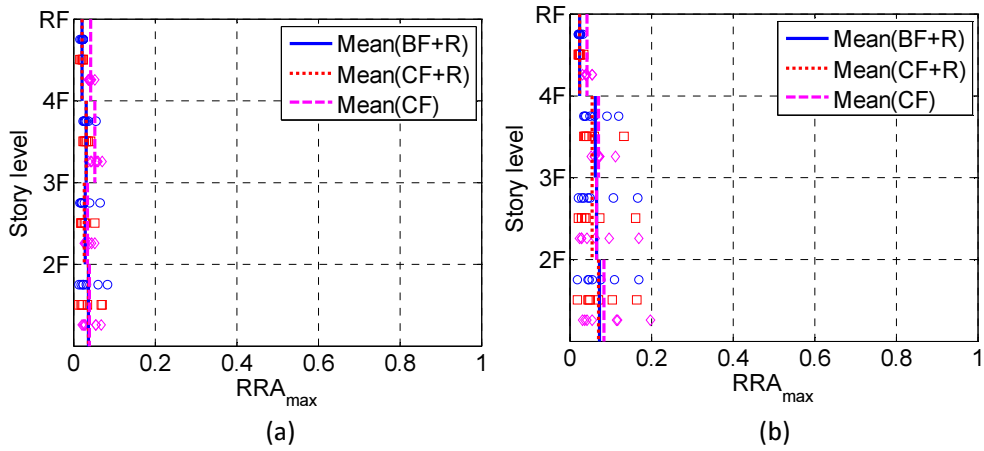


Figure B-27 Variation of RRA in C2 with  $M_{ta\_2}$ : (a) DBE and (b) MCE

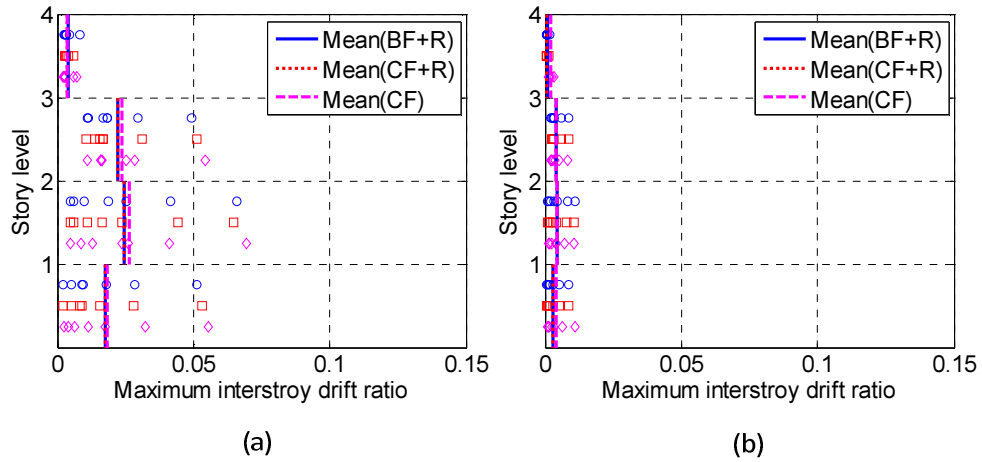


Figure B-28 IDR in C1 with  $M_{1a_1}$  with DBE ground motions: (a) Y-dir and (b) X-dir

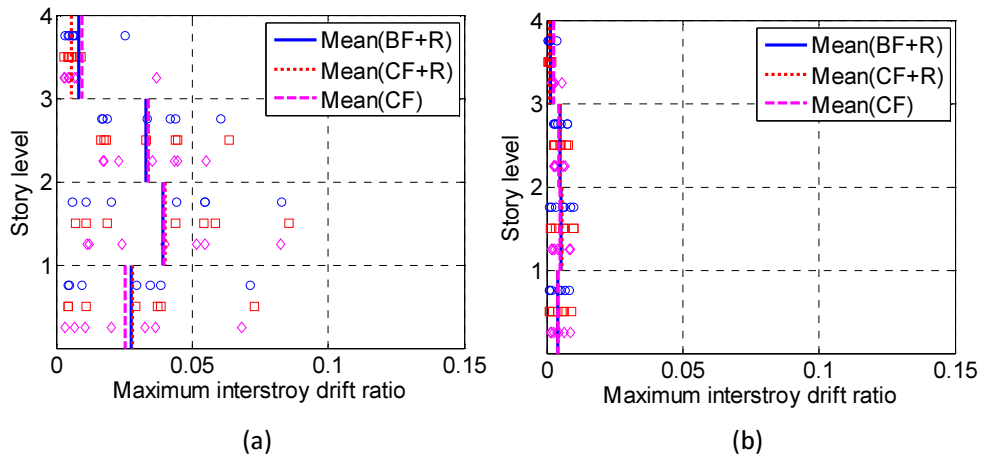


Figure B-29 IDR in C1 with  $M_{1a_1}$  with MCE ground motions: (a) Y-dir and (b) X-dir

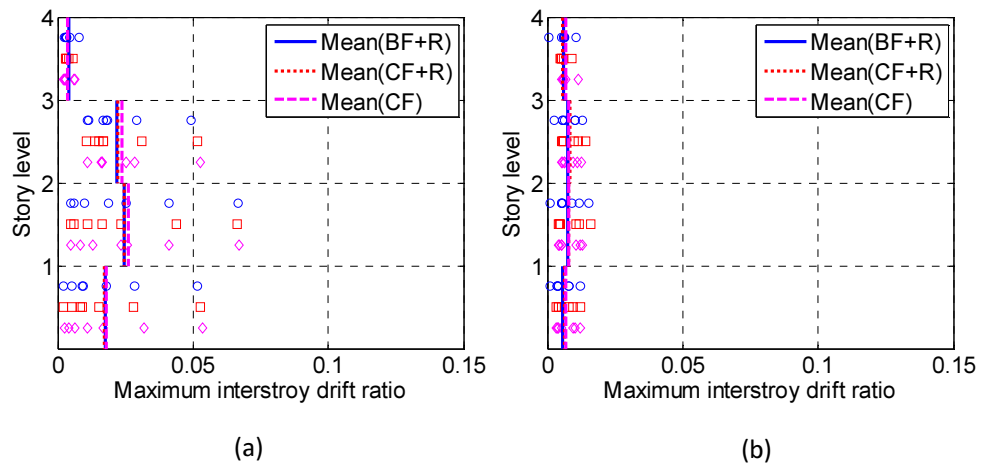


Figure B-30 IDR in C1 with  $M_{1a_2}$  with DBE ground motions: (a) Y-dir and (b) X-dir

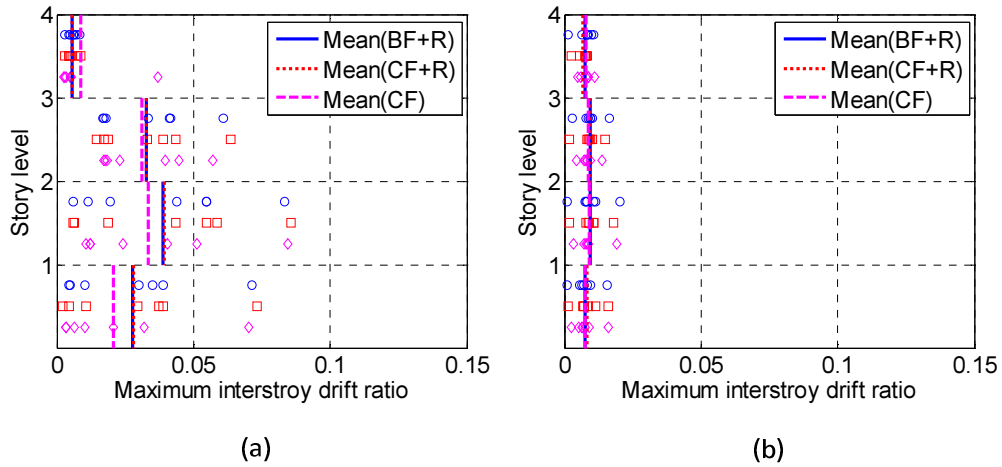


Figure B-31 IDR in C1 with  $M_{ta\_2}$  with MCE ground motions: (a) Y-dir and (b) X-dir

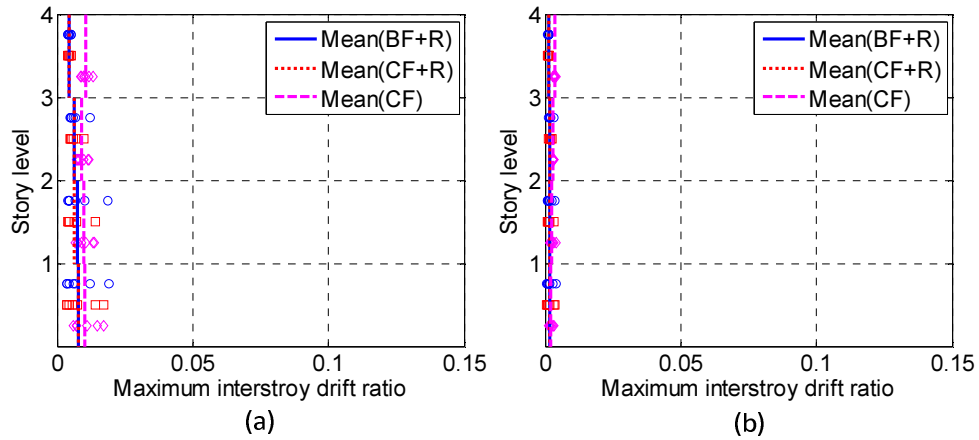


Figure B-32 IDR in C2 with  $M_{ta\_1}$  with DBE ground motions: (a) Y-dir and (b) X-dir

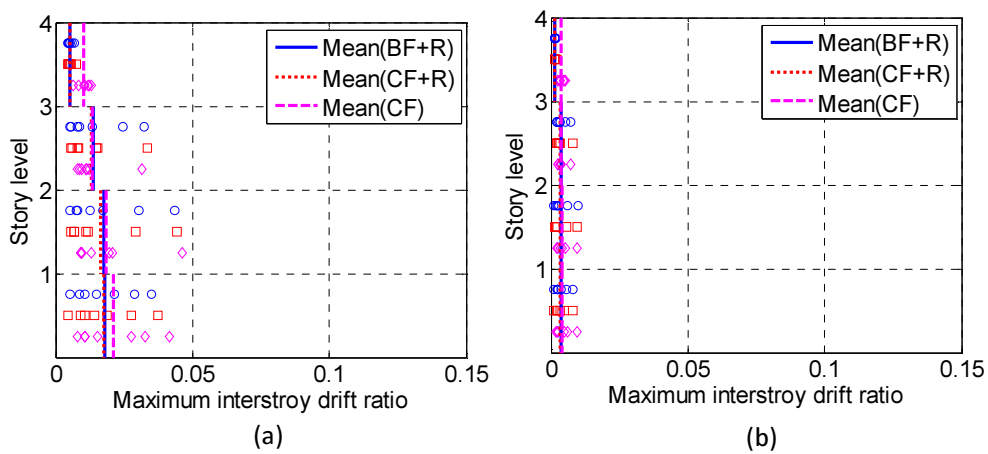


Figure B-33 IDR in C2 with  $M_{ta\_1}$  with MCE ground motions: (a) Y-dir and (b) X-dir

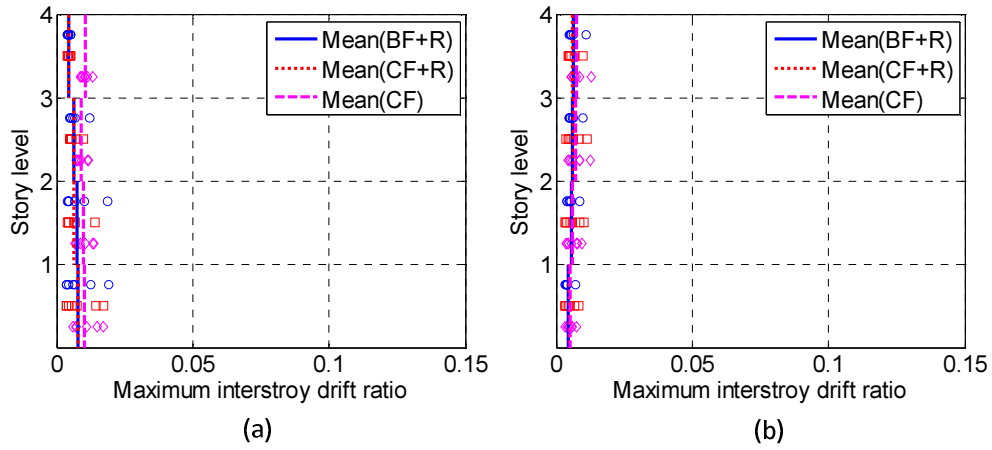


Figure B-34 IDR in C2 with  $M_{Ia\_2}$  with DBE ground motions: (a) Y-dir and (b) X-dir

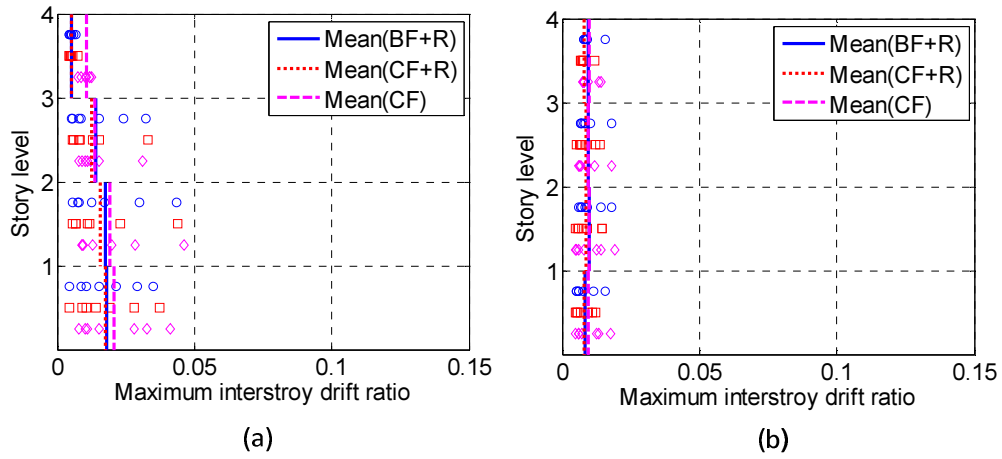
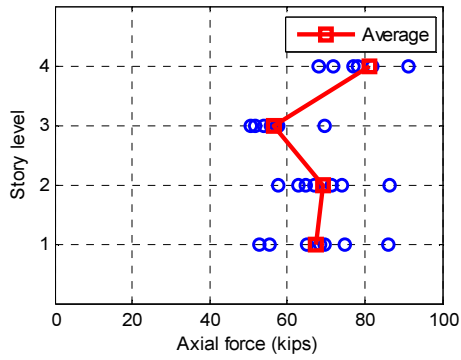
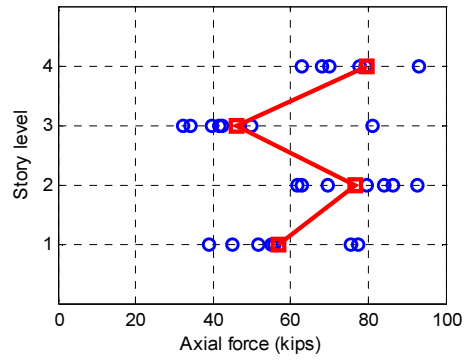


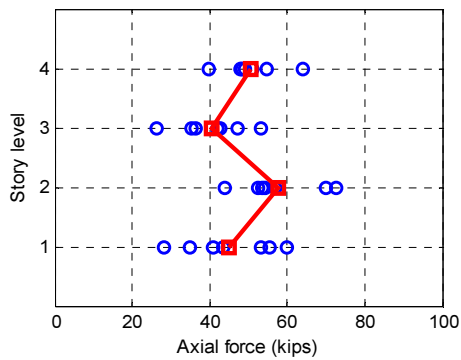
Figure B-35 IDR in C2 with  $M_{Ia\_2}$  with MCE ground motions: (a) Y-dir and (b) X-dir



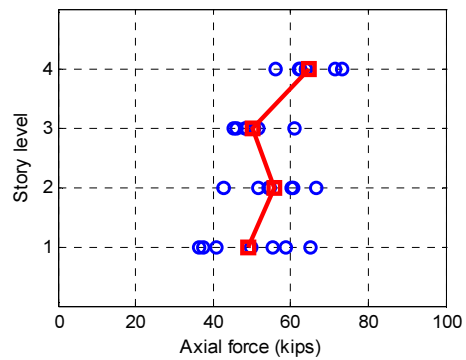
(a)



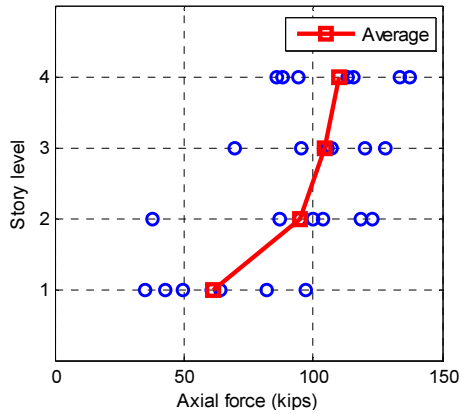
(b)



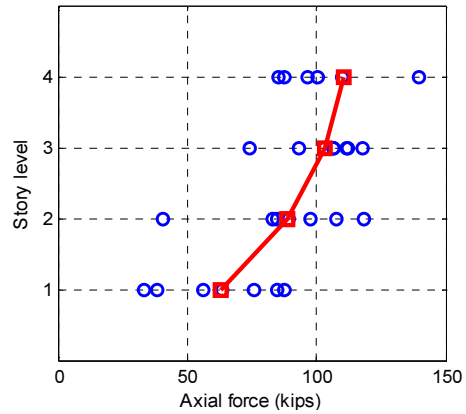
(c)



(d)

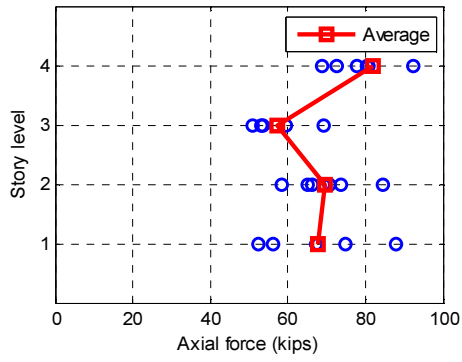


(e)

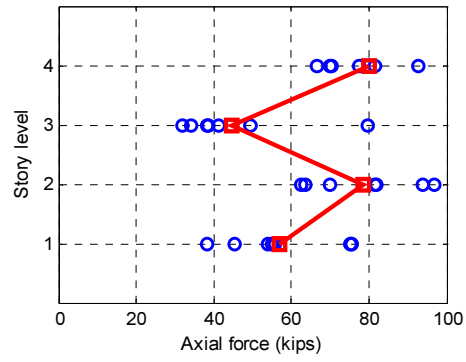


(f)

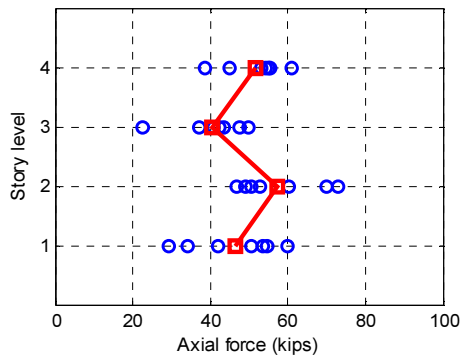
Figure B-36 Axial forces in collectors and chords in C1 under DBE-level ground motions with  $M_{ta_I}$ : (a) BF1, (b) BF2, (c) BF3, (d) BF4, (e) MF1, and (f) MF2



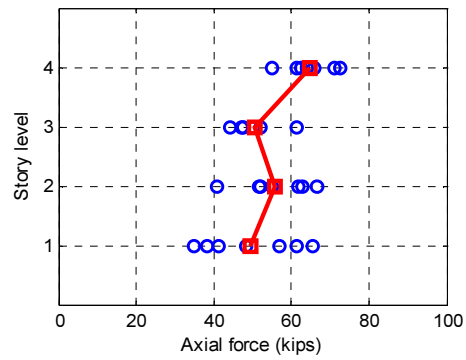
(a)



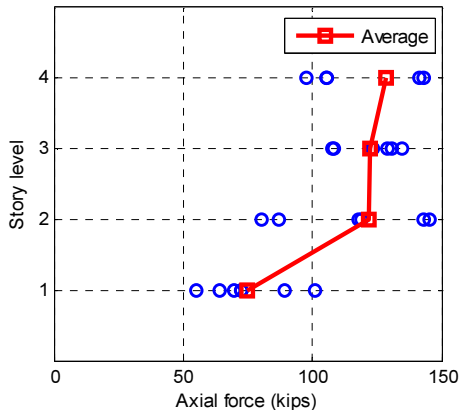
(b)



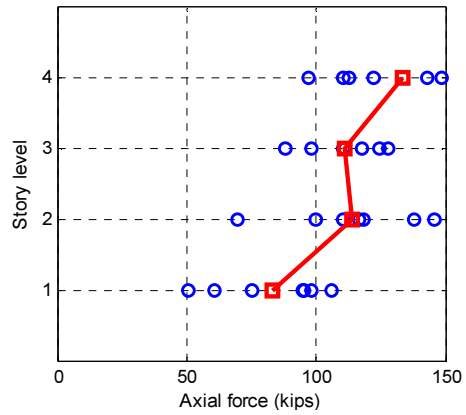
(c)



(d)

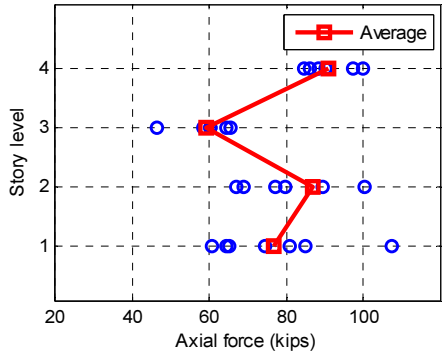


(e)

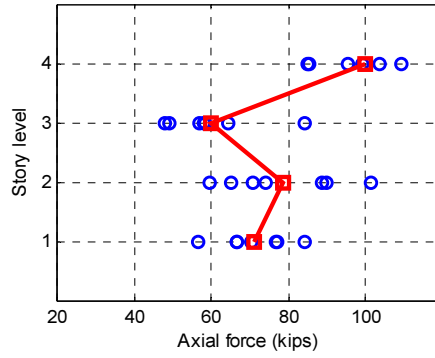


(f)

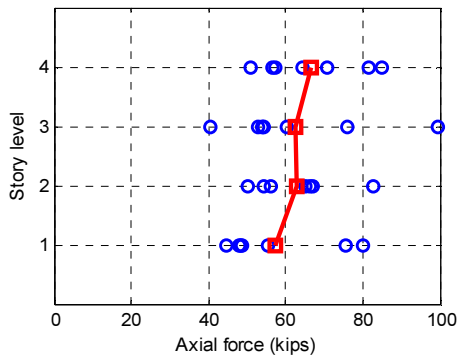
Figure B-37 Axial forces in collectors and chords in C1 under DBE-level ground motions with  $M_{ta\_2}$ : (a) BF1, (b) BF2, (c) BF3, (d) BF4, (e) MF1, and (f) MF2



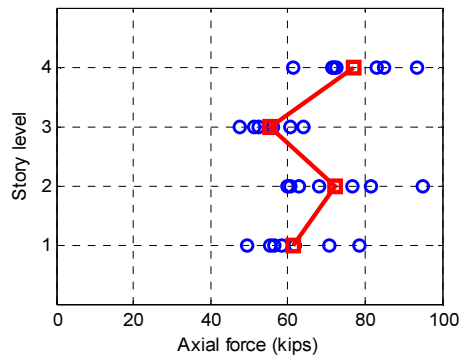
(a)



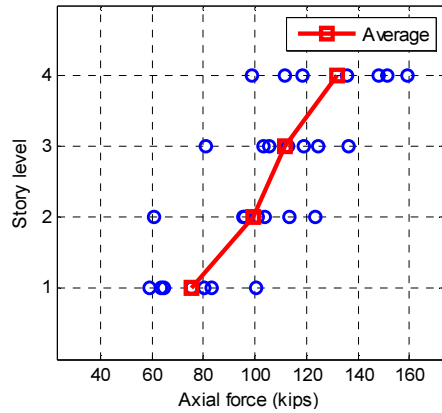
(b)



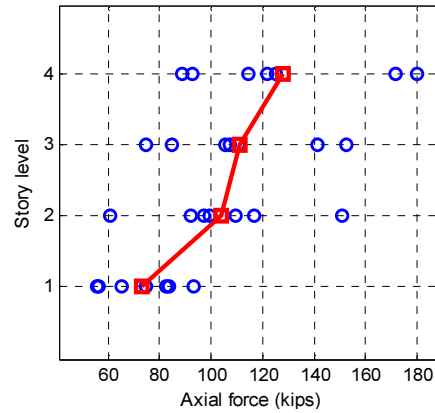
(c)



(d)



(e)



(f)

Figure B-38 Axial forces in collectors and chords in C1 under MCE-level ground motions with  $M_{Ia\_I}$ : (a) BF1, (b) BF2, (c) BF3, (d) BF4, (e) MF1, and (f) MF2

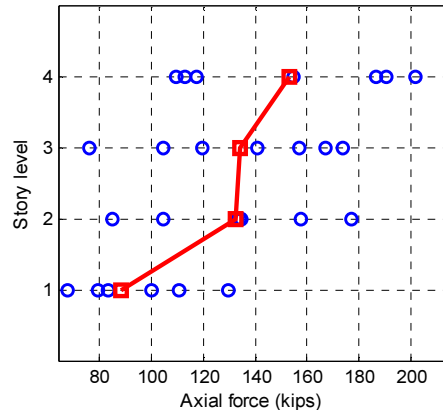
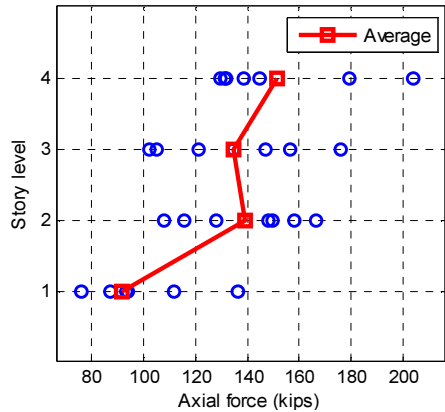
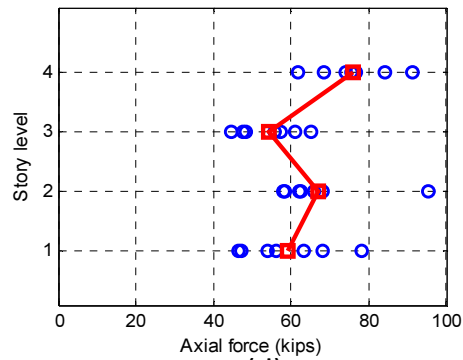
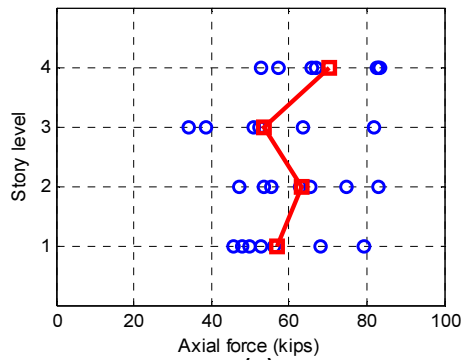
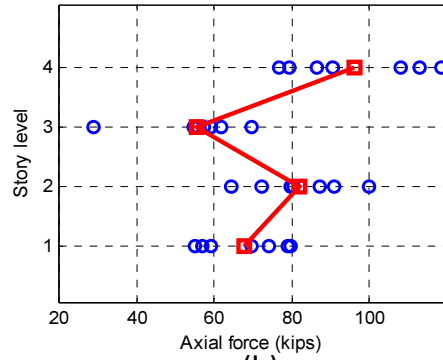
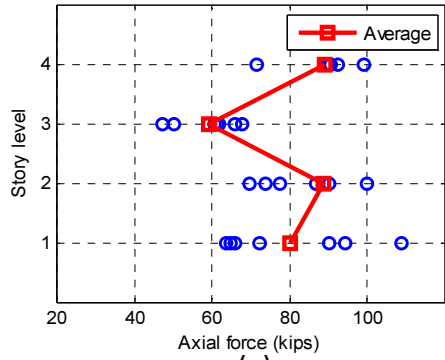
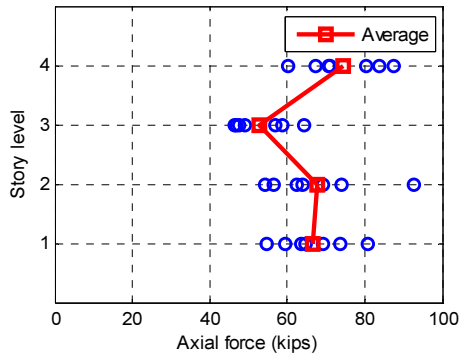
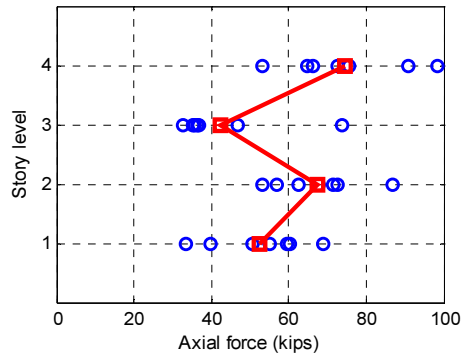


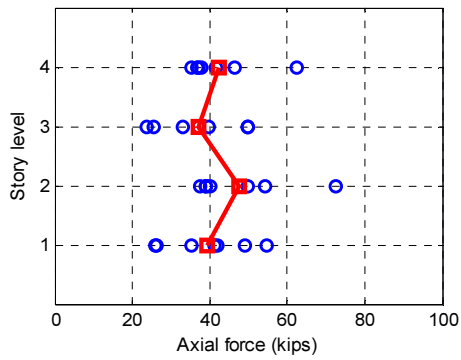
Figure B-39 Axial forces in collectors and chords in C1 under MCE-level ground motions with  $M_{Ia\_2}$ : (a) BF1, (b) BF2, (c) BF3, (d) BF4, (e) MF1, and (f) MF2



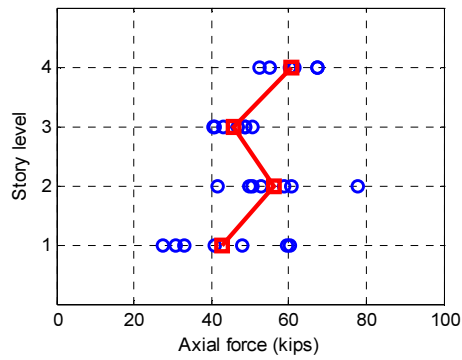
(a)



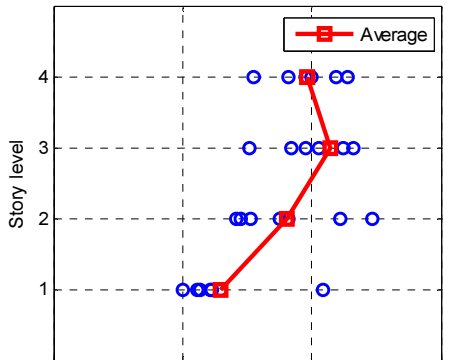
(b)



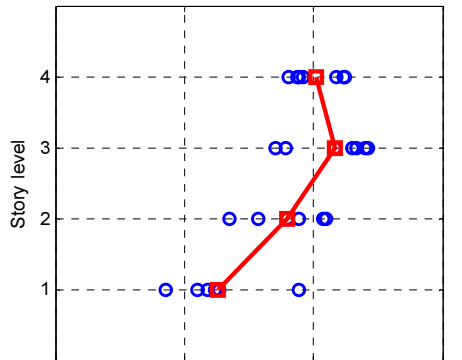
(c)



(d)

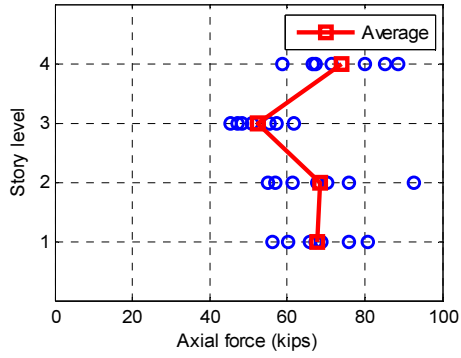


(e)

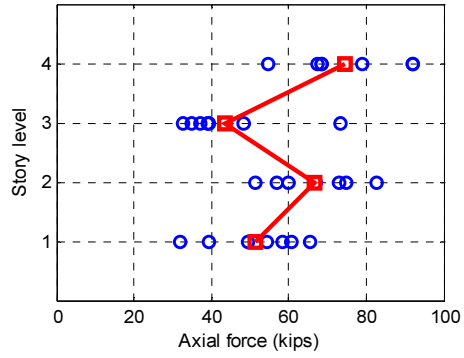


(f)

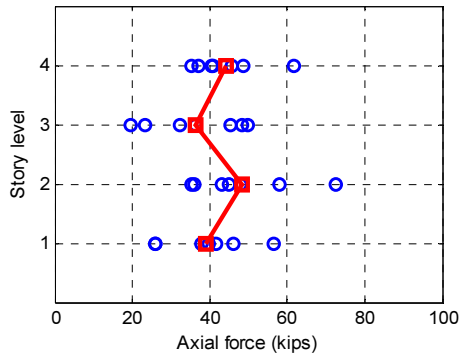
Figure B-40 Axial forces in collectors and chords in C2 under DBE-level ground motions with  $M_{ta_1}$ : (a) BF1, (b) BF2, (c) BF3, (d) BF4, (e) MF1, and (f) MF2



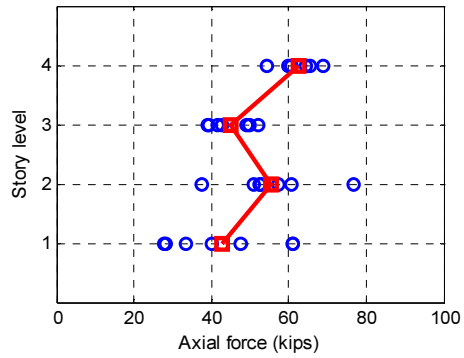
(a)



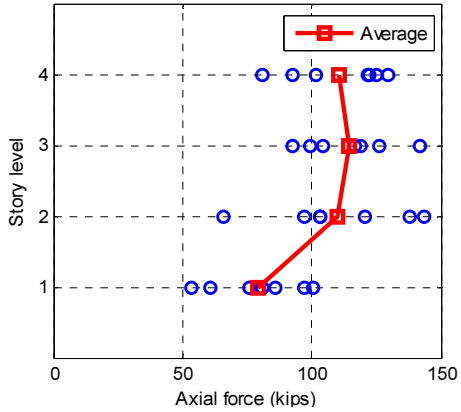
(b)



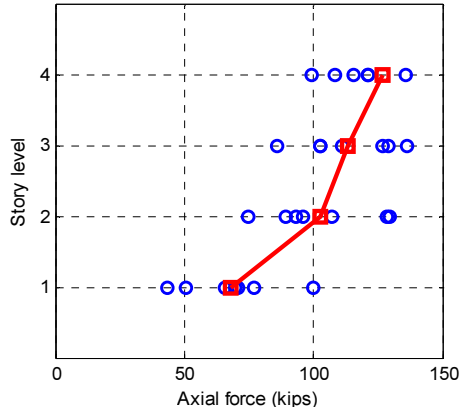
(c)



(d)

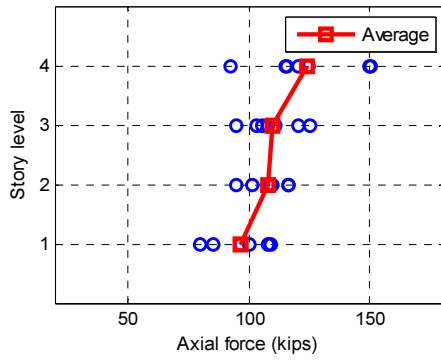


(e)

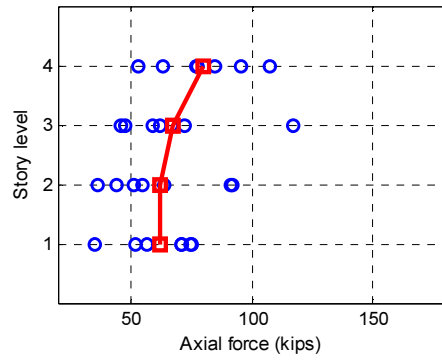


(f)

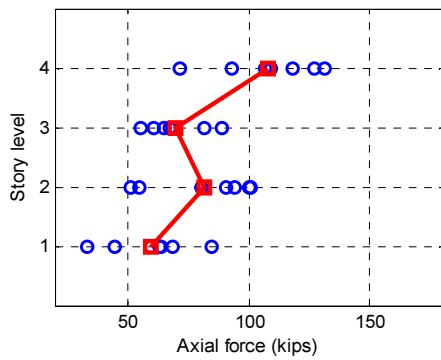
Figure B-41 Axial forces in collectors and chords in C2 under DBE-level ground motions with  $M_{Ia\_2}$ : (a) BF1, (b) BF2, (c) BF3, (d) BF4, (e) MF1, and (f) MF2



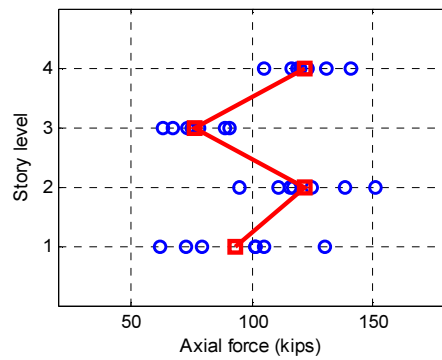
(a)



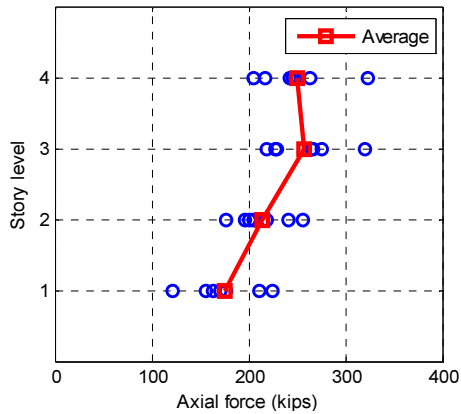
(b)



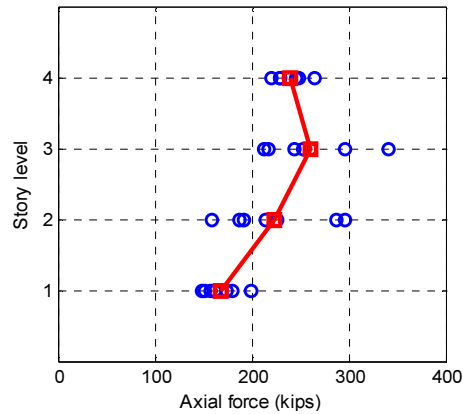
(c)



(d)

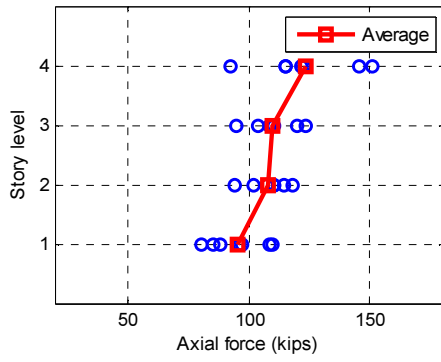


(e)

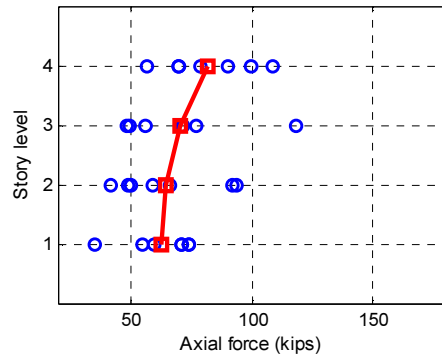


(f)

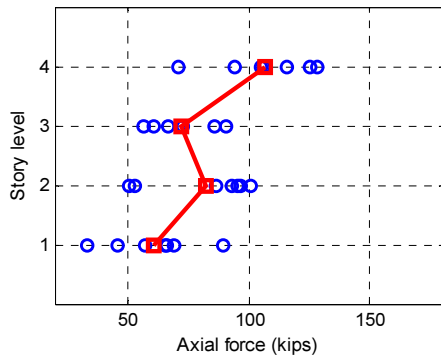
Figure B-42 Axial forces in collectors and chords in C2 under MCE-level ground motions with  $M_{Ia\_1}$ : (a) BF1, (b) BF2, (c) BF3, (d) BF4, (e) MF1, and (f) MF2



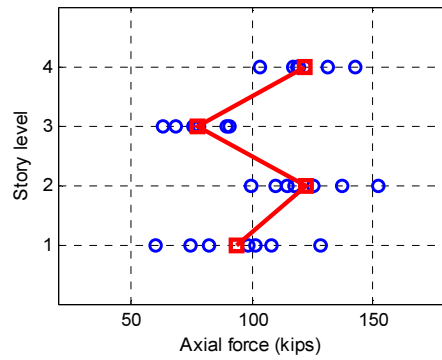
(a)



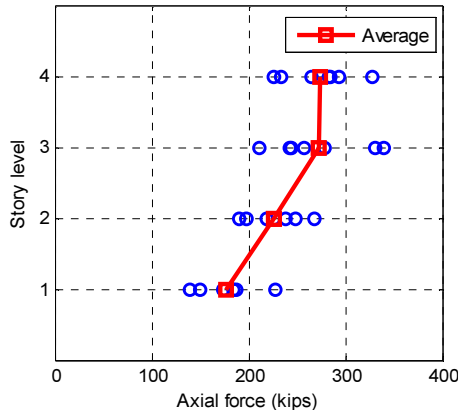
(b)



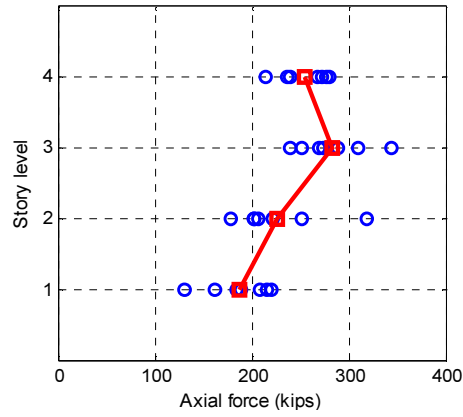
(c)



(d)



(e)



(f)

Figure B-43 Axial forces in collectors and chords in C2 under MCE-level ground motions with  $M_{ta\_2}$ : (a) BF1, (b) BF2, (c) BF3, (d) BF4, (e) MF1, and (f) MF2

## **Appendix C**

### **The Simulation and Behavior of Single-Story Steel Structures with Flexible Diaphragm**

#### **Abstract**

For the 3D design of steel structures, shell elements are the typical one used for simulating the in-plane and out-of plane behavior of the composite floor. Nevertheless, these models may not be computational efficient due to a large number of degrees of freedom (DOFs) needed to model the floor. This appendix provides an approach to simulate the orthotropic behavior of semi-rigid diaphragm using simplified beam-truss models. The orthotropic elastic behavior of corrugated composite slabs can be considered in the material properties of shell elements through specifying property modification factors. By applying specified stiffness combinations of beam and truss elements, the in-plane deformation of shell elements with orthotropic behavior can be mimicked through changing the dimensions of truss and beam elements. Using this technique, the shell elements can be replaced by simplified beam-truss models. The number of DOFs of the single-story baseline steel structure with shell elements can be reduced by at least one order of magnitude. Therefore, the simplified beam-truss model is capable of improving the computational efficiency for 3D structural analysis. By conducting linear static and eigenvalue analyses, the results show the maximum difference in lateral displacement and periods between the simplified and baseline structure is 2.0% and 2.6%, respectively.

## C.1 Introduction

In conventional structural analytical models, composite slabs are usually simulated as rigid diaphragms. Nodes connect to the master nodes by using the links with infinite in-plane rigidity. The in-plane membrane deformation of the diaphragm is prohibited under this assumption. In this scenario, the girders connected with diaphragms are not capable of developing the additional internal axial forces.

For the irregular diaphragms, however, the in-plane deformation may be significant. A series of research discusses the behavior of structure considering the in-plane flexibility of floor systems. Esterling and Porter (1994a), (1994b) investigated the in-plane shear capacity by conducting a series of experiments with different thickness and deck types. Three limit states are purposed for evaluating the in-plane shear capacity of composite slab. Ju and Lin (1999) implemented a series of analytical simulation for the concrete structure with flexible and rigid diaphragm under seismic loading. Shell elements were selected to simulate the behavior of in-plane diaphragms. The results indicate that the column moments have a large difference under the different assumptions of diaphragm. Fleischman and Farrow (2001) discussed the principal parameters used for governing the dynamic behavior of concrete structures with flexible diaphragms. The authors provided an index of global diaphragm flexibility to distinguish the difference of deformation pattern between rigid and flexible diaphragm structures.

As noted before, there is a few research focuses on the dynamics behavior of steel structures with composite slab under the assumption of flexible diaphragms. For the steel structures with irregular diaphragms or the diaphragms with high aspect ratios, the in-plane deformation is significant. The application of shell elements is necessary in the simulation procedures for reflecting the behavior of in-plane and out-of plane of diaphragms. However, for the large

structures or multi-stories structures, the calculation efficiency and requirement of computational resource highly depends on the number of DOFs. High meshing density for simulating the diaphragms using shell elements needs more computational resource due to the increment of DOFs.

To improve the problem of computational efficiency mentioned above, a beam-truss model consists of beam and diagonal truss elements are proposed for replacing the shell elements. In this study, the comparison of lateral displacement and periods of the structures with shell elements and beam-truss models, will be presented and discussed. Rectangular, U, and L-shape single-story steel structures are the four theme structures in this study. In addition, the orthotropic mechanics behavior of the corrugated composite slab is considered in the analytical models. The four-node shell elements (Mindlin Shell elements) with orthotropic elastic material properties are used to describe the in-plane and out-of plane behavior of flexible diaphragms.

## **C.2 Orthotropic stiffness modification for composite slab**

Corrugated composite slab is commonly used in the floor systems. To simulate the orthotropic behavior of corrugated composite slab, the material properties of longitudinal and transverse direction,  $E_x$  and  $E_y$ , should be modified corresponding to the size and direction of rib. In this study, the subscription “y” presents the direction of axis parallel to the rib, and “x” is the direction perpendicular to the rib. Saffaini H.S. (1992) provided the formulas to estimate the material properties ( $E_{x,c}$ ,  $E_{y,c}$ ,  $G_c$ ) of the concrete slab within rib as shown from Equations C-1 to C-3. For considering the stiffness of metal deck in these properties, Equations C-1 to C-3 can be modified as shown in Equations C-4 to C-6. The second term in Equations C-4 and C-5 is presented as the axial stiffness contribution providing by the metal deck. In this study, there is no slip generated between metal deck and concrete slab. The definition of geometry shape and basic

material properties of the composite slab are illustrated in Figure C-1 and Figure C-2, respectively.

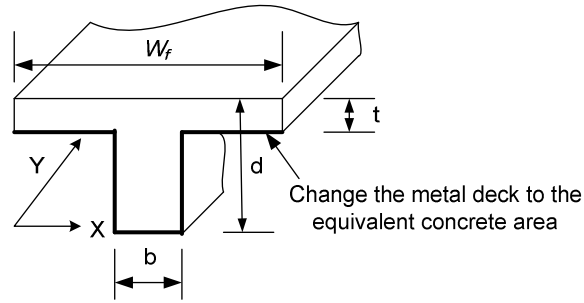


Figure C-1 Geometry definition of corrugated slab

$$E_{x,c} = 1.02 \cdot E_{ci} \quad \text{Equation C-1}$$

$$E_{y,c} = \left[ 1 + \frac{b(d-t)}{w_f \cdot t} \right] \cdot E_{ci} \quad \text{Equation C-2}$$

$$G_c = \left[ \frac{E_{x,c} \cdot E_{y,c}}{E_{x,c} \cdot (1 + \mu_{y,c}) + E_{y,c} \cdot (1 + \mu_{x,c})} \right] \quad \text{Equation C-3}$$

$$E_{x,d} = 1.02 \cdot E_{ci} + \frac{w_f \cdot t_s \cdot n_s}{w_f \cdot t} \cdot E_{ci} \quad \text{Equation C-4}$$

$$E_{y,d} = \left[ \frac{w_f \cdot t + b(d-t) + (w_f + (d-t) \cdot 2) \cdot t_s \cdot n_s}{w_f \cdot t} \right] \cdot E_{ci} \quad \text{Equation C-5}$$

$$G_d = \left[ \frac{E_{x,d} \cdot E_{y,d}}{E_{x,d} \cdot (1 + \mu_{y,d}) + E_{y,d} \cdot (1 + \mu_{x,d})} \right] \quad \text{Equation C-}$$

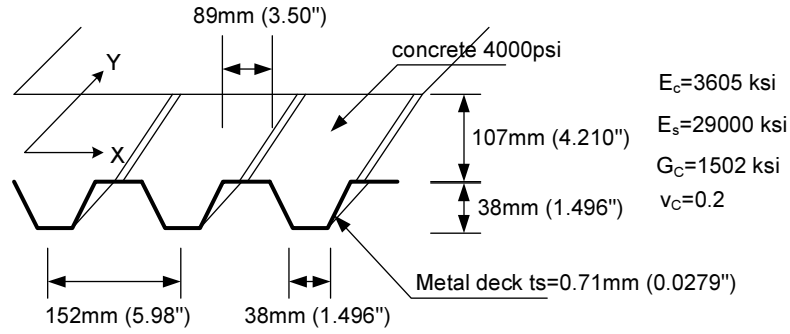


Figure C-2 Geometry and material properties for composite slab

Table C-1 shows the orthotropic material properties of corrugated slab with and without considering the effect of metal decks as illustrated in Figure C-2. The orthotropic properties,  $E_{x,d}$  and  $E_{y,d}$ , increase due to the consideration of corrugated metal deck. In addition, the orthotropic material properties along the both two directions are higher than the one with isotropic properties because of the effect of corrugated rib. These orthotropic material properties are used for simulating the in-plane and out-of plane behavior of flexible diaphragm in this study.

Table C-1 Comparison of material properties of different material assumption

Material properties comparison					
Isotropic – without metal deck		Orthotropic – with metal deck		Orthotropic – without metal deck	
$E_{ci}$	3605	$E_{x,d}$	3869	$E_{x,c}$	3671
		$E_{y,d}$	4420	$E_{y,c}$	4114
$G_{ci}$	1502	$G_d$	1739	$G_c$	1633

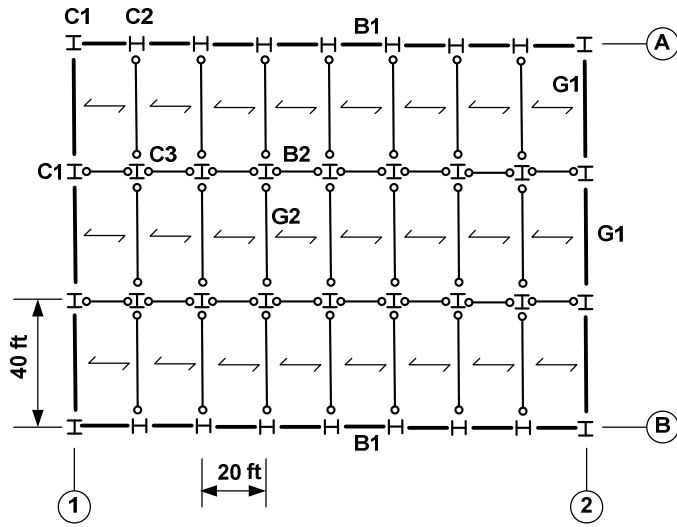
Unit: kips/ in<sup>2</sup>

### C.3 The simulation of flexible diaphragm-base line structures

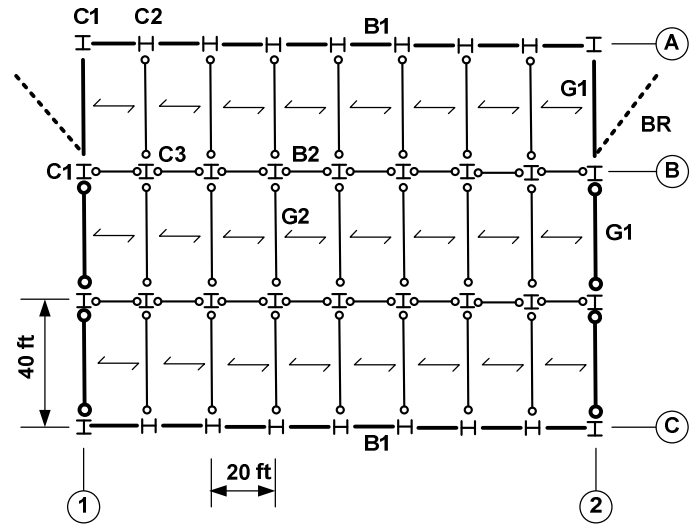
From Section C.3, the orthotropic properties of composite slab are determined. The baseline structures with flexible diaphragms including the slabs with orthotropic behavior are simulated in

SAP2000. A 24 DOFs, four-nodes, 2.5ft by 2.5ft, square shell element within these orthotropic material properties considering both in-plane and out-of plane behavior is chosen as the fundamental element for the simulation of flexible diaphragms in the baseline structures. The 3D beam-column element is chosen for simulating the columns and beams. The average thickness of slab based on Figure C-2 is 4.96 in.

In this study, four structures with different irregularities are utilized as the baseline theme models. In these structures, the typical span at X-direction and Y-direction are 20ft and 40ft, respectively. TYPEA is a single-story steel structure with four peripheral moment resistant frames (MRF), which are frames A B, 1 and 2, as shown in Figure C-3(a). The inner columns and beams are designed as the gravity system. For TYPEA1, the beam and column dimensions are the same as that of TYPEA. Two diagonal braces are added in peripheral frames at the Y-direction (Frame 1 and 2). Pin connections are imposed at the end of beams used to connect the peripheral concentrically braced frames (CBF, Frame 1 and 2). TYPE B1 and C1 are L-shaped and U-shaped braced structures. The peripheral CBFs are located at the Y-direction, and the MRFs at the X-direction. The structure configurations as well as member dimensions are shown in Figure C-3. The schematic diagrams for these four configurations are illustrated in Figure C-4.



**TYPE A**

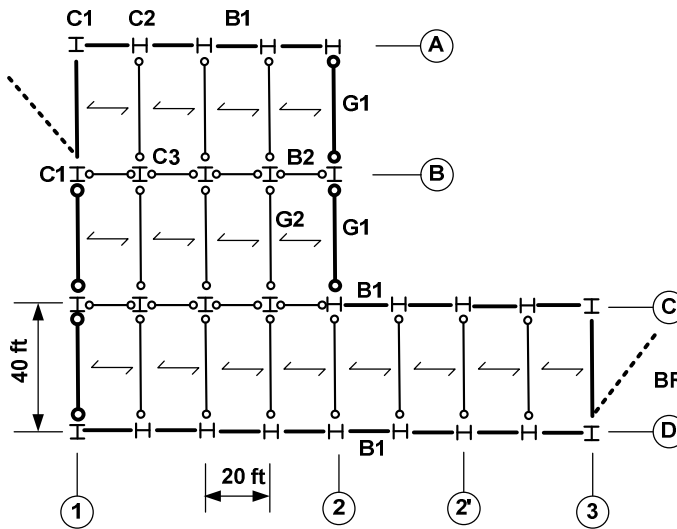


**TYPE A1**

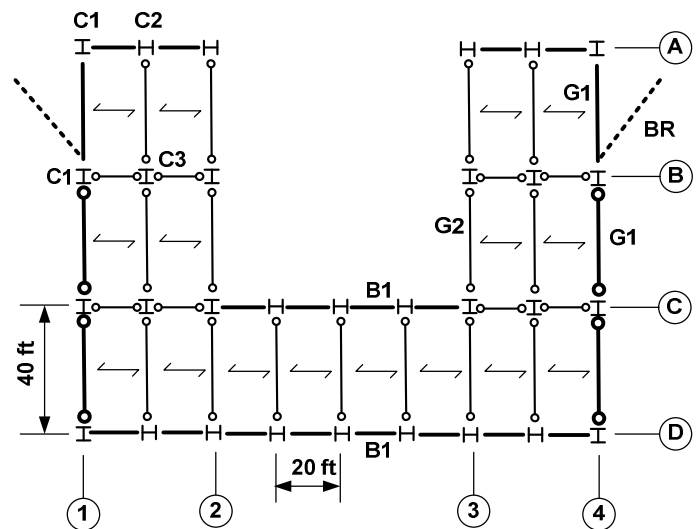
**NOTE:**

1. TYPEA: Frame 1,2,A and B - Moment Resistant Frames
2. TYPEA1: Frame A, C - Moment Resistant Frames
3. TYPEA1: Frame 1, BAY A~B - Centrically Braced Frames  
Frame 2, BAY A~B - Centrically Braced Frames

**Member size:**  
 B1- W30X116 G1- W36X135  
 B2- W27X102 G2- W33X118  
 C1- W14X233 C2- W14X159  
 C3- W14X132 BR-HP14X102



**TYPE B1**



**TYPE C1**

**NOTE:**

1. TYPEB1: Frame C, BAY 2~3 - Moment Resistant Frames ; Frame A, D - Moment Resistant Frames
2. TYPEB1: Frame 1, BAY A~B - Centrically Braced Frames ;  
Frame 3, BAY C~D - Centrically Braced Frames
3. TYPEC1: Frame A, D - Moment Resistant Frames ; Frame C, BAY2~3 - Moment Resistant Frames
4. TYPEC1: Frame 1, BAY A~B - Centrically Braced Frames ;  
Frame 4, BAY A~B - Centrically Braced Frames

**Member size:**  
 B1- W30X116 G1- W36X135  
 B2- W27X102 G2- W33X118  
 C1- W14X233 C2- W14X159  
 C3- W14X132 BR-HP14X102

Figure C-3 Configurations of single-story steel structures

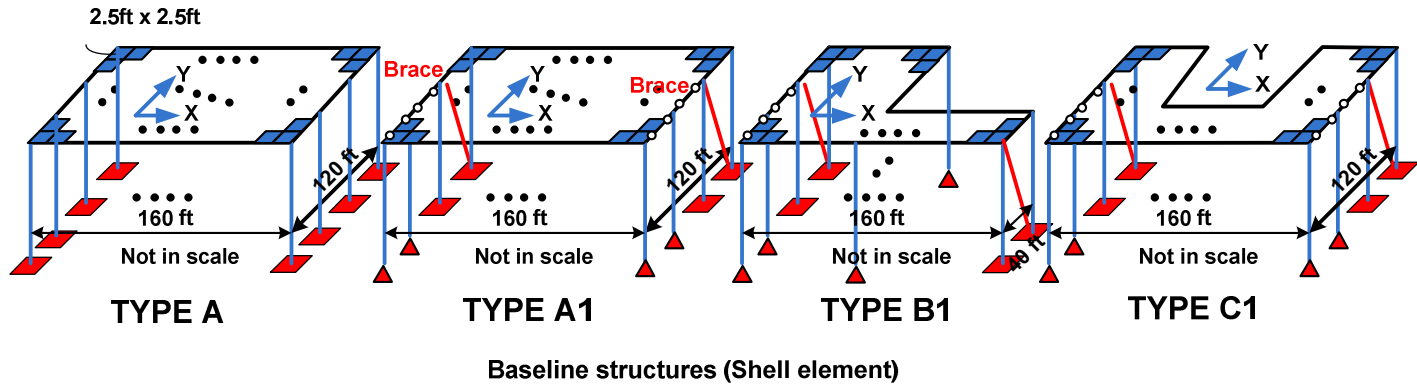


Figure C-4 Configuration of the structure simulation by using shell elements

## C.4 The simulation of flexible diaphragm-simplified structure

### C.4.1 Concepts of beam-truss model

The conventional shell elements are used for simulating the behavior of flexible diaphragm as mentioned in Section C.3. To simplify the model simulation and improve the calculation efficiency for the baseline structures, a beam-truss model is used to describe the in-plane behavior of diaphragms to replace the shell elements. In this appendix, an individual beam-truss model is proposed for mimicking the in-plane behavior that a 10ft by 10ft shell elements model provides.

The in-plane deformation of diaphragm is caused by the in-plane shear,  $V$ . To determine the dimensions of beam and truss, the beam-truss model should perform the same lateral displacement as that the shell element model provides (i.e.  $\Delta_H$ ). Both of the models subject the same pure shear force, as shown in Figure C-5. The lateral stiffness at X-direction of these two different models shown in Equation C-7 shall be the same as each other when the both models exhibit the same lateral displacement,  $\Delta_H$ . From Figure C-5, one can observe that the number of DOFs of beam truss model is 9, and 24 for the shell element model.

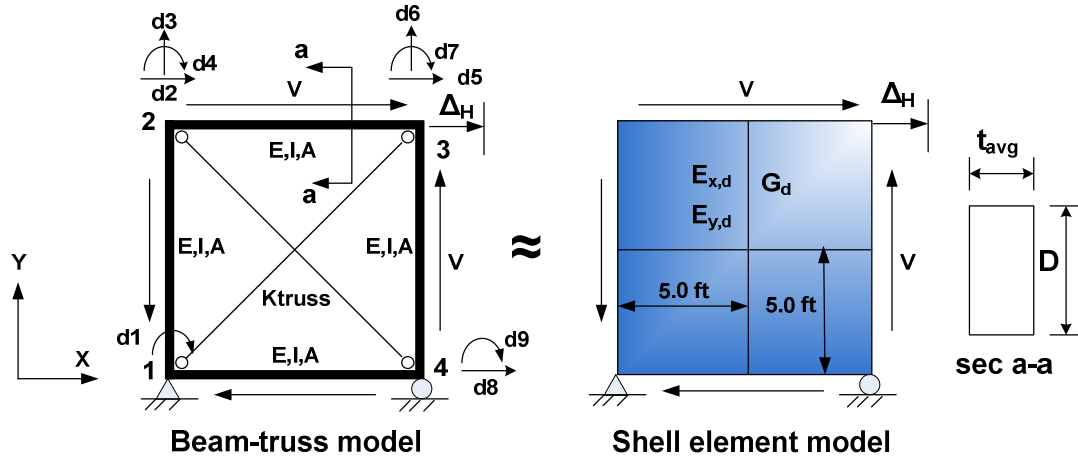


Figure C-5 Beam-truss and shell element model

$$K_{BT} = K_P = \frac{V}{\Delta_H} \quad \text{Equation C-7}$$

The lateral stiffness of beam-truss model,  $K_{BT}$ , can be divided into two parts,  $K_B$  and  $K_T$ .  $K_B$  and  $K_T$  are the lateral stiffness provided by beam and truss systems, respectively. The forces that act on beam and truss systems,  $V_1$  and  $V_2$ , can be determine under any specified ratio of  $K_B/K_T$ . Fig. 6 illustrates the relationships between truss and beam system.  $V_1$  and  $V_2$  are determined based on Equation C-9 and Equation C-10.

$$K_{BT} = K_B + K_T \quad \text{Equation C-8}$$

$$V_1 = V \times \frac{K_B}{K_{BT}} \quad \text{Equation C-9}$$

$$V_2 = V \times \frac{K_T}{K_{BT}} \quad \text{Equation C-10}$$

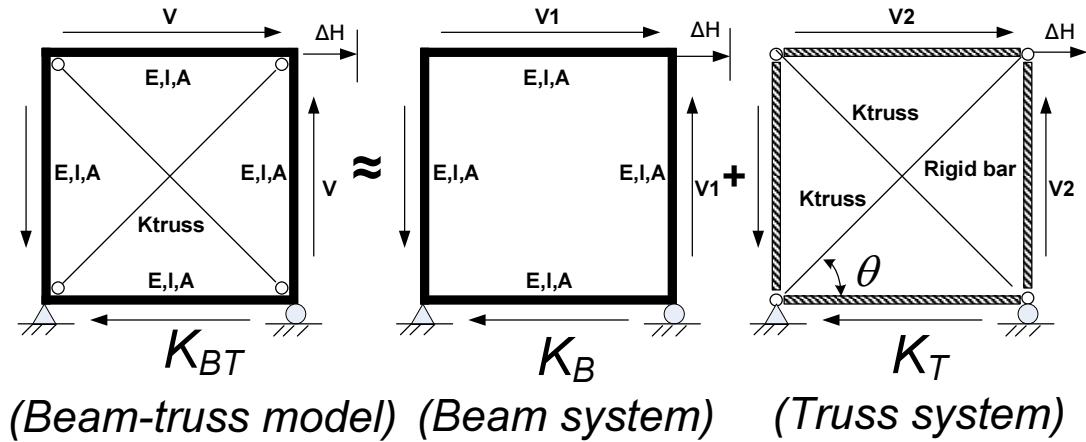


Figure C-6 Decomposition of beam-truss model

According to Equation C-9, the truss dimensions can be determined using Equation C-11. The two diagonal trusses provide the lateral stiffness of the truss system. In addition, the dimensions of beams in the beam system can be determined by iterating the depth of the beam (i.e. “D” in Figure C-5) to match the target lateral displacement (i.e.  $\Delta_H$ ). The stiffness matrix of beam system,  $\mathbf{K}_B$ , should be built first. The 9 by 9 stiffness matrix is shown in Figure C-7, which corresponds to the 9 DOFs in the beam system. The order of DOFs in the displacement vector is defined in Figure C-5. The lateral displacement,  $d_5$ , is the same as  $\Delta_H$ .

$$K_T = K_{truss} = \frac{V_2}{2 \times \cos^2 \theta \times \Delta_H} \quad \text{Equation C-11}$$

$$\mathbf{K}_B = \begin{bmatrix}
\frac{8EI}{L} & \frac{-6EI}{L} & 0 & \frac{2EI}{L} & 0 & 0 & 0 & 0 & \frac{2EI}{L} \\
& \frac{EA}{L} + \frac{12EI}{L^3} & 0 & \frac{-6EI}{L^2} & \frac{-EA}{L} & 0 & 0 & 0 & 0 \\
& & \frac{EA}{L} + \frac{12EI}{L^3} & \frac{-6EI}{L^2} & 0 & \frac{-12EI}{L^3} & \frac{-6EI}{L^2} & 0 & 0 \\
& & & \frac{8EI}{L} & 0 & \frac{6EI}{L^2} & \frac{2EI}{L} & 0 & 0 \\
& & & & \frac{EA}{L} + \frac{12EI}{L^3} & 0 & \frac{-6EI}{L^2} & \frac{-12EI}{L^3} & \frac{-6EI}{L^2} \\
& & & & & \frac{EA}{L} + \frac{12EI}{L^3} & \frac{6EI}{L^2} & 0 & 0 \\
& & \text{symm.} & & & & \frac{8EI}{L} & \frac{6EI}{L^2} & \frac{2EI}{L} \\
& & & & & & & \frac{EA}{L} + \frac{12EI}{L^3} & \frac{6EI}{L^2} \\
& & & & & & & & \frac{8EI}{L}
\end{bmatrix}$$

Figure C-7 Stiffness matrix of beam system

#### C.4.2 Parameters study of the beam-truss model

For the beam-truss model, the depth of beam (D) can be iterated by tracking  $\Delta_H$  ( $d_5$ ) in the beam system through applying the external force vector  $\mathbf{P}$  and the stiffness matrix of beam system ( $\mathbf{K}_B$ ) with specified width of beam (b), elastic modulus (E) and stiffness ratio ( $K_B/K_T$ ). The procedures shown in Figure C-8 includes the tracking steps to obtain the “D” corresponding to  $\Delta_H$  subjecting external force vector  $\mathbf{P}$  in the beam system. In this system, the average thickness  $t_{avg}$  of composite slab, 4.96in, is assumed as the beam width. The known displacement vector  $\mathbf{D}_P$ , including  $d_5$ , is extracted from the shell element model in SAP2000. The tracking procedures are terminated until the displacement difference in  $\Delta_H$  between the one from beam system and the other from shell element system is smaller than 1%. The analytical results are shown in Figure

C-9. This figure shows the  $D$  and  $A_{\text{truss}}$  under the different stiffness ratio  $K_T/K_B$  (i.e. 1 to 100) and  $E$  (i.e. 3605 to 29000ksi). For the case with low  $K_T/K_B$ , “ $D$ ” is larger than those with higher stiffness ratios. In other words, this means the beam system would take more in-plane shear. Besides, the “ $A_{\text{truss}}$ ” does not have a significant variation corresponding to the increment of elastic modulus. Table C-2 lists the dimension combinations of beam and truss under different stiffness ratio within two different elastic modules, 3605 and 29000ksi, respectively. The performance of these beam-truss models in the single-story structures are discussed in Section C.4.3.

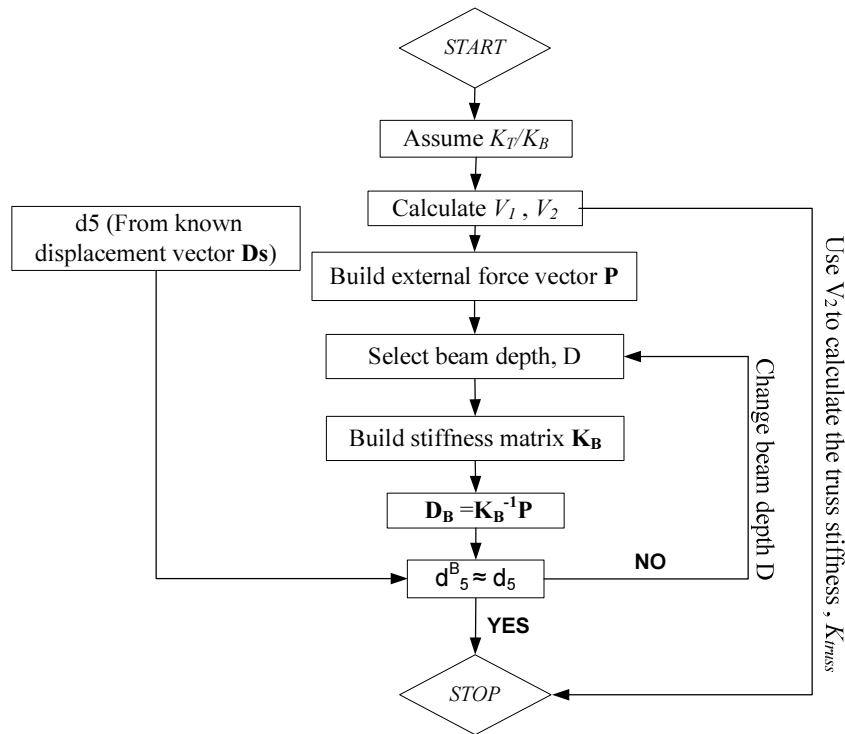


Figure C-8 Procedures for determining the beam depth,  $D$

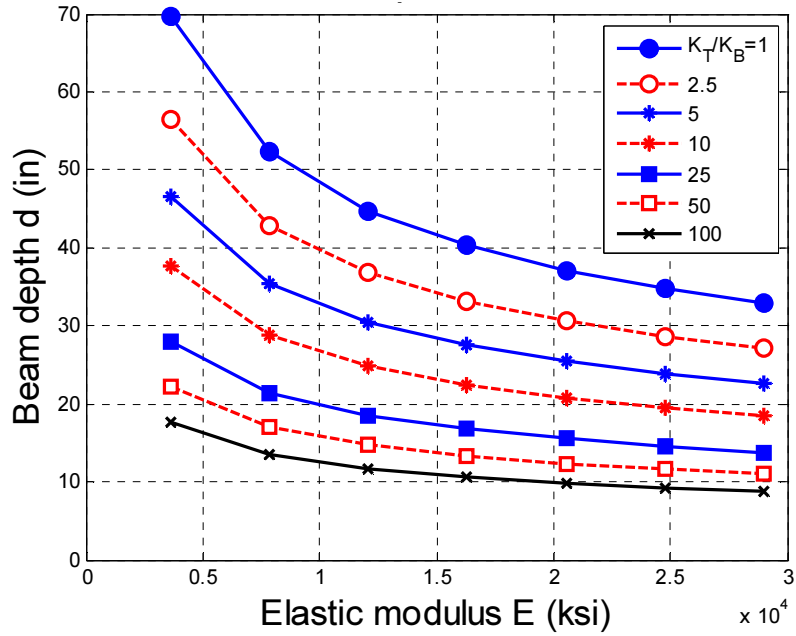


Figure C-9 The variation of  $d$  with different  $K_T/K_B$  and  $E$

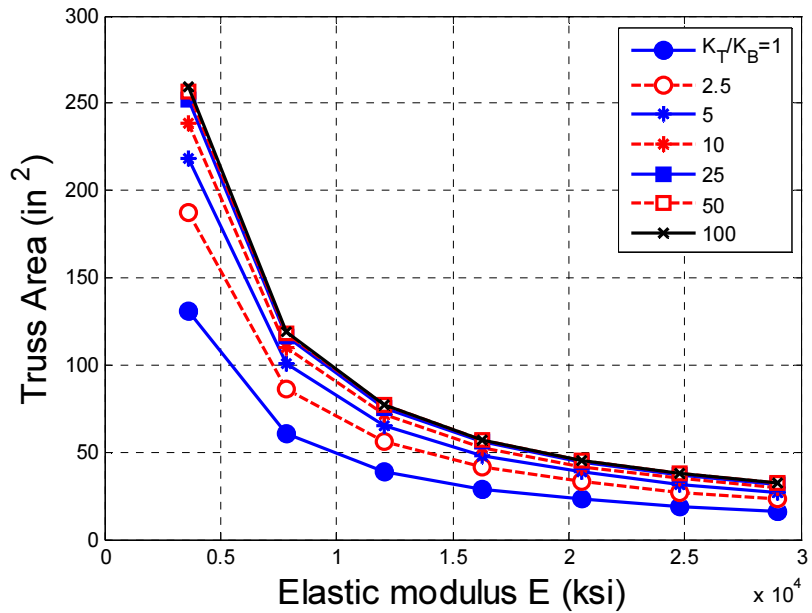


Figure C-10 The variation of  $A_{truss}$  with different  $K_T/K_B$  and  $E$

Table C-2 Combination of truss and beam with different stiffness ratio and elasticity of modulus

$K_T/K_B$	E=29000 ksi		E=3605 ksi	
	D(in)	A(in <sup>2</sup> )	D(in)	A(in <sup>2</sup> )
1	33	20	20	15
2.5	27	32	35	25
5	23	40	45	30
10	19	45	50	35
25	14	55	60	40
50	11	65	70	45
100	9	75	80	50

(stiffness ratio)				
100	8.76	32.53	17.63	259.46
50	11.02	31.93	22.21	256.91
25	13.79	32.32	27.94	251.97
10	18.36	29.60	37.61	238.23
5	22.61	27.15	46.56	218.38
2.5	27.16	23.27	56.57	187.18
1	32.90	16.29	69.68	131.03

### C.4.3 Simplified structures simulation

The flexible diaphragm could be simulated by beam-truss models in SAP2000 once the dimension of beam and truss are determined. The baseline structures with flexible diaphragms mentioned in Section C.3 are simulated as simplified structures consisted of beam and truss elements. Figure C-11 shows the configuration of simplified structure (TYPE A). In such structures, the dimension of each beam-truss model is 10ft by 10ft as shown in Figure C-9. The beam dimensions are extracted from the iteration procedures mentioned above ( $E=29000\text{ksi}$ ).

These simplified structures are used to verify the performance of beam truss model. The comparison of number of DOF for the baseline and simplified structure is shown in Table C-3. The result shows that the DOFs of the baseline structure (TYPEA) with shell elements (flexible diaphragm) have fourteen times more than those in the simplified structure with beam-truss models. A large number of DOF of a structure indicates a high computational requirement as well as low computational efficiency. By applying beam-truss model to simulate the flexible diaphragms, the disadvantage above can be improved due to the reduction of the number of DOF.

The other three baseline structures, TYPE A1, B1 and C1, use the same beam-truss model to simulate the flexible diaphragm, as shown in Figure C-12.

In this study, the static lateral load is 20 percent of total weight of structure applied on structures at the Y-direction. For baseline structures with shell elements, the load is uniformly distributed on the shell elements; however, for the simplified structures with beam-truss models, the equivalent point loads are applied on the intersection points of girders or beams. Figure C-12 shows the schematic diagrams of baseline and simplified structures. The red solid circles indicate the positions where the lateral displacements are extracted for comparison.

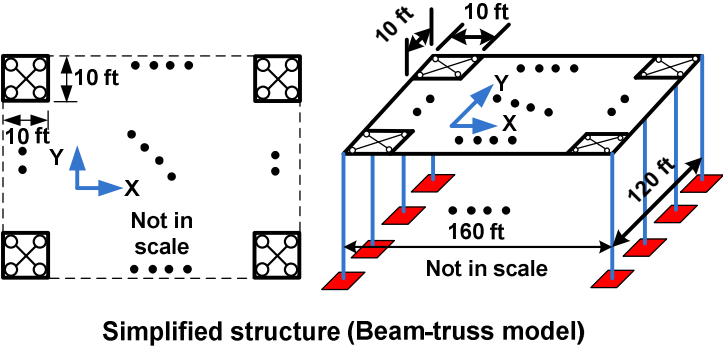


Figure C-11 Configuration of the structure simulation by using beam-truss model (simplified structure, TYPE A)

Table C-3 Comparison the number of DOF between baseline and simplified structures (TYPE A)

		Structure Type A	
		Baseline	Simplified
Number of	DOF	19152	1368

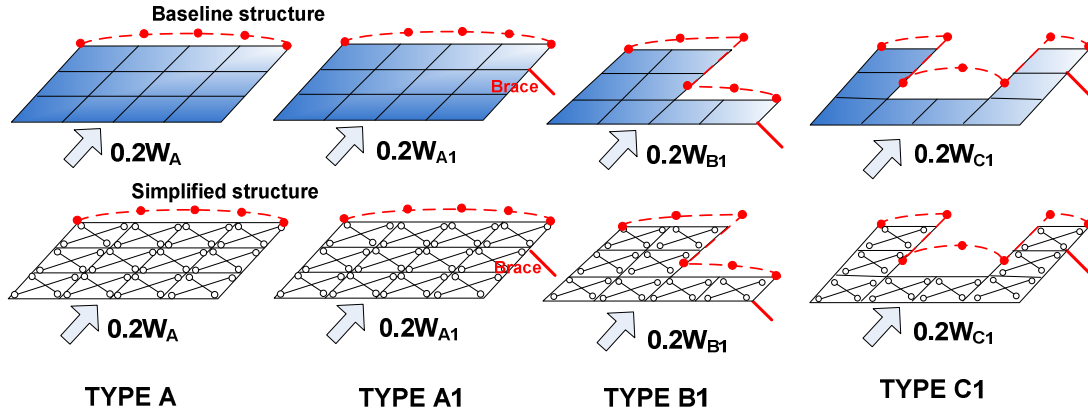


Figure C-12 Configurations of baseline and simplified structures

## C.5 Analysis results and comparison

### C.5.1 Comparison of flexible and rigid diaphragm structures

For the baseline structures, the structure elastic response might have a significant difference between the structures with rigid and flexible diaphragms by implementing the modal and linear elastic analysis. Table C-5 shows the comparison of the first three periods of each structure. The difference in period of each type is determined based on the definition of Equation C-12. In addition, the lateral normalized displacement distribution of each structure with lateral static load is extracted by using Equation C-13.

$$\Delta T_{avg} (\%) = \frac{\sum_{i=1}^n |T_{sim}^i - T_{base}^i| / T_{base}^i}{n} \times 100 \quad \text{Equation C-12}$$

$$NormalizedDisp_k^j = \frac{Disp_k^j}{max(Disp_k^{j,base})} \quad \text{Equation C-13}$$

According to Table C-4, the average period difference is not significant between the structure TYPE A with rigid and flexible diaphragms. However, the difference is significant in the

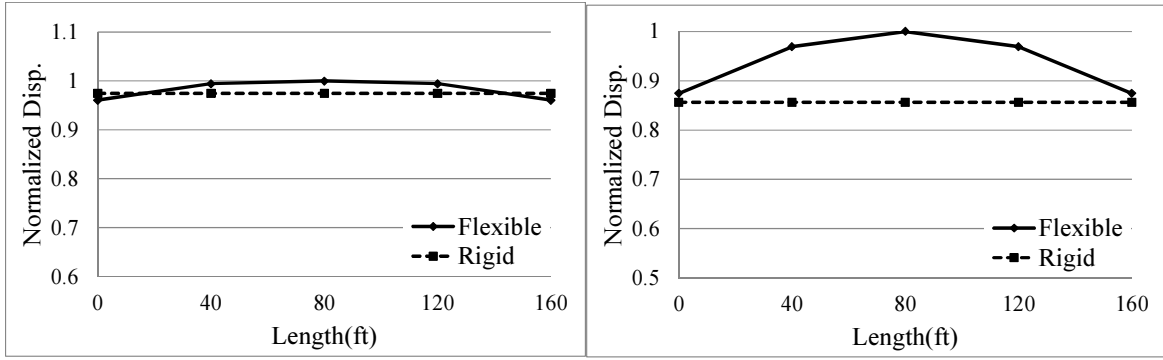
structures TYPE A1, B1 and C1. The majority of difference in the period is contributed by the 2<sup>nd</sup> modes (i.e. Y-direction). This phenomenon indicates that the diaphragm in-plane behavior is obvious in the structures with braced frames.

For the lateral displacement as shown in Figure C-13, the results indicate that a similar phenomenon can be detected as the difference in the comparison of the period. The maximum displacement difference between the structures with rigid and flexible diaphragms is 3% in TYPE A; however, the difference increases obviously over 10% in TYPE A1, B1 and C1. The results demonstrate the influence from in-plane stiffness of diaphragm is significant in the structures with braced frames and irregular diaphragms.

Table C-4 Structure periods of flexible and rigid diaphragm structures

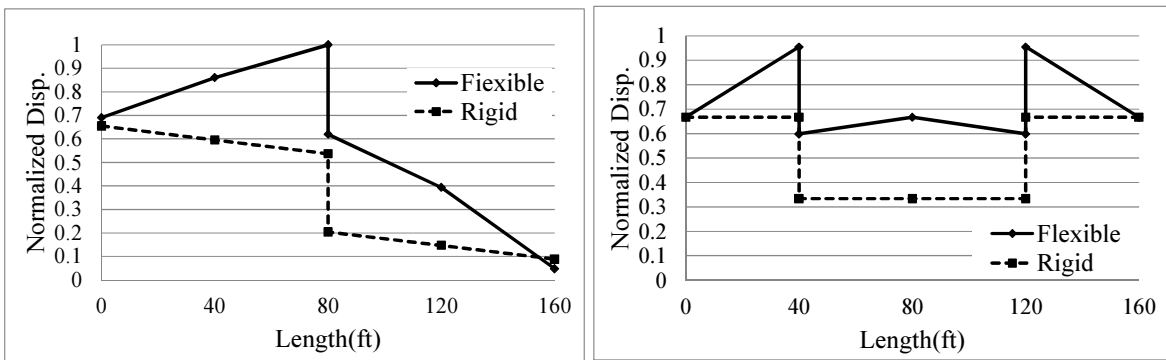
Dir.		TYPE A		TYPE A1		TYPE B1		TYPE C1	
		F <sup>(1)</sup>	R <sup>(2)</sup>	F	R	F	R	F	R
1 <sup>st</sup>	X	0.327	0.324	0.301	0.300	0.251	0.249	0.248	0.246
2 <sup>nd</sup>	Y	<b>0.288</b>	<b>0.287</b>	<b>0.212</b>	<b>0.200</b>	<b>0.209</b>	<b>0.173</b>	<b>0.204</b>	<b>0.166</b>
3 <sup>rd</sup>	R <sub>Z</sub>	0.206	0.204	0.145	0.140	0.133	0.137	0.139	0.136
$\Delta T_{avg}(\%)$		---	1.07	---	3.15	---	7.01	---	7.20

Note: <sup>(1)</sup> F represents the structure w/ flexible diaphragm. <sup>(2)</sup> R represents the structures w/ rigid diaphragm. Unit: sec/cycle



(a)TYPE A

(b) TYPE A1



(c)TYPE B1

(d) TYPE C1

Figure C-13 Comparison of normalized displacement between flexible and rigid diaphragm structures

### C.5.2 Comparison between baseline and simplified structures -TYPE A

To verify the global behavior of the beam-truss model, structure TYPE A is simulated by the model with different stiffness ratios with keeping the elastic modulus at 29000ksi. Table C-5 shows the first third periods between the baseline and simplified structures. The results show that the difference in periods is less than 3% within different stiffness ratios. In addition, the normalized displacement distribution of the structures is shown in Figure C-14. The comparison of deformation shapes in each configuration indicates that the shapes are similar between the baseline and simplified structure when the stiffness ratio  $K_T/K_B$  is 25. In this scenario, the maximum difference in the displacement between baseline and simplified structure is less than

2%. This means the beam-truss models are capable for providing a similar lateral stiffness as those from shell elements in the entire structures.

Table C-5 Structure periods of baseline and simplified structures (TYPE A)

	Dir.	Stiffness ratio $K_T/K_B$							Baseline
		100	50	25	10	5	2.5	1	
1 <sup>st</sup>	X	0.335	0.330	0.326	0.322	0.318	0.315	0.313	0.327
2 <sup>nd</sup>	Y	0.295	0.292	0.290	0.286	0.284	0.282	0.280	0.288
3 <sup>rd</sup>	R <sub>Z</sub>	0.213	0.212	0.211	0.210	0.209	0.208	0.208	0.206
$\Delta T_{avg}(\%)$		2.626	1.783	0.985	0.145	0.865	1.539	2.203	---

Unit: sec/cycle

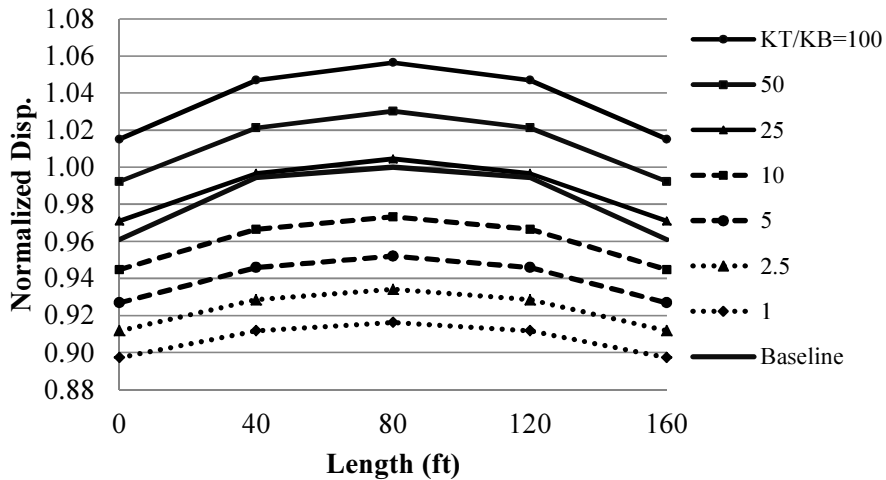


Figure C-14 Comparison of normalized displacement between baseline and simplified structures (TYPE A)

### C.5.3 Comparison of baseline and simplified structures -TYPE A1, B1 and C1

In order to understand the behavior of beam-truss model for the structures with irregular diaphragms with braces, the three baseline structures, TYPE A1, B1 and C1, are simulated as simplified structures using beam-truss models.

According to the analytical results in Section C.5.2, stiffness ratio  $K_T/K_B=25$  performs the minimum displacement difference between baseline and simplified structures. For the other three types of simplified structures in this section, this specified stiffness ratio is used in the simulation of flexible diaphragms. Table C-6 shows the difference in period between both simulation methods with this specified stiffness ratio. The results show the average difference in period between the baseline and simplified braced structures is from 0.96 to 3.10%. In addition, Figure C-15 shows the deformation shapes of diaphragms of each configuration. The maximum difference in the lateral deformation between two simulation approaches of TYPE A1, B1 and C1 is 0.4%, 9.5% and 3.5%, respectively. The results show the beam-truss models perform a favorable match for periods and deformation.

In order to reduce the displacement difference in TYPE B1, the diaphragms enclosed by grid line 2, 2', C and D as shown in Figure C-3 could be simulated as a different combination of beam-truss model. From above sections, the dimension combinations of beam-truss model are based on the application of pure shear on the both beam-truss and shell elements model (Figure C-4). However, for the in-plane diaphragm behavior is not dominated by the in-plane shear. Table 2 does not appropriate to be used for the simulation of beam-truss model. One can apply a horizontal concentrated load at Point 2 (Figure C-5), and utilize the same iteration procedures mentioned in Section C.4 to generate a new combinations of beam and truss with the same specified stiffness ratio,  $K_T/K_B$ , 25 and elastic modulus, 29000ksi. Therefore, the new dimension combination of beam and truss are  $D=16.7$  in and  $A_{\text{truss}}=7.03$  in<sup>2</sup>, respectively.

Through using the new dimensions of beam and truss, the average difference of first three periods is reduced from 0.96% to 0.66%, as shown in Table C-6. The subscript “**mod**” in the table presents the application of modified beam-truss model. In Figure C-15, the maximum

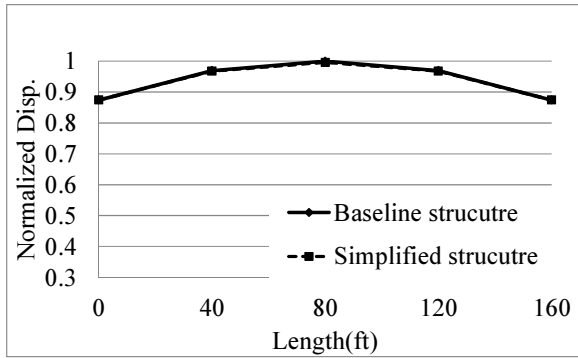
displacement difference between the baseline and simplified structures with modified beam-truss model (TYPE B1\_Mod) is 3.9%. This means the displacement difference reduced by 60% comparing with the case without modifying the stiffness.

Table C-6 Structure period of baseline and simplified structures (TYPE A1, B1 and C1)

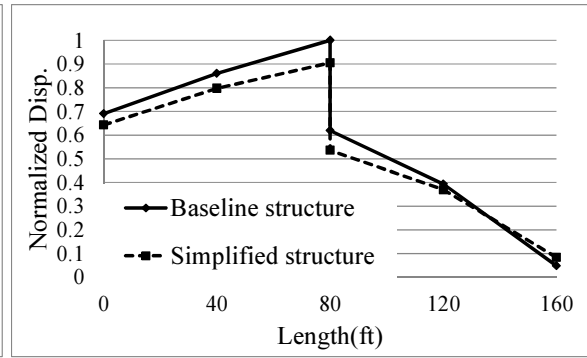
	Dir.	TYPE A1		TYPE B1			TYPE C1	
		B	S	B	S	S <sub>mod</sub>	B	S
1 <sup>st</sup>	X	0.301	0.303	0.251	0.251	0.251	0.248	0.265
2 <sup>nd</sup>	Y	0.212	0.211	0.209	0.203	0.208	0.204	0.199
3 <sup>rd</sup>	R <sub>Z</sub>	0.145	0.148	0.133	0.133	0.135	0.139	0.139
$\Delta T_{avg}(\%)$		---	1.07	---	0.96	0.66	---	3.10

*B: Baseline structures ; S: Simplified structures*

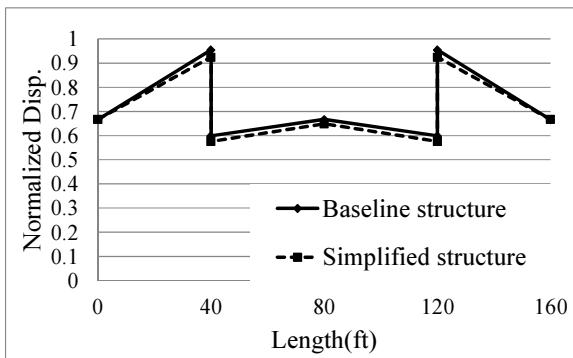
*Unit: sec/cycle*



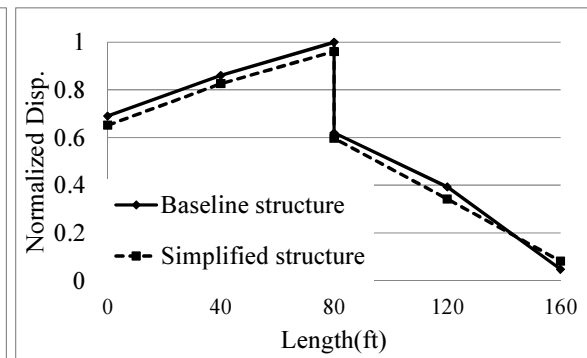
(a) TYPEA



(b) TYPEB1



(c) TYPEA



(d) TYPEB1\_Mod

Figure C-15 Comparison of normalized displacement between baseline and simplified model (TYPE A1, B1 and C1)

## C.6 Conclusion

The difference in periods and lateral displacement between steel structures with flexible and rigid diaphragm is significant in this study. For the structures with irregular diaphragm shapes and braces, the period and displacement might have significant difference between two different diaphragm assumptions. This is caused by the development of significant in-plane behavior in such structures. Comparing with shell elements, the research provides a relative simple way to evaluate the behavior in the analysis of single-story steel structure. A beam-truss model is proposed to replace shell elements. Orthotropic material behavior of composite ribbed slab has been considered in the beam-truss model to improve the simulation accuracy. The

results indicate that the periods and displacement of simplified structures can provide a similar behavior of those baseline structures provides. The difference in displacement and periods between the two simulation approaches is smaller than 3 percent when the stiffness ratio  $K_T/K_B$  is 25. In addition, the calculation efficiency is improved because of the significant decrement of degree of freedom using simplified beam truss models.

## Notations

$\mu_c$  Poisson's ratio of concrete

$E_{ci}, E_s$  Modulus of elasticity for concrete and steel, respectively

$E_{x,c}, E_{y,c}$  Modulus of elasticity for corrugated concrete slab at x and y direction, respectively

$E_{x,d}, E_{y,d}$  Modulus of elasticity for corrugated concrete slab with metal deck at x and y direction, respectively

$G_c, G_d$  Shear modulus of corrugated concrete slab without and with metal deck, respectively

$G_{ci}$  Elastic shear modulus of concrete

$t$  Thickness of metal deck

$t_s$  Thickness of concrete slab without rib

$d$  Total depth of corrugated slab

$w_f$  The flange width

$\mu_{x,c} = \mu_y \times (E_{x,c} / E_{y,c})$  Poisson's ratio at x direction

$\mu_{x,d} = \mu_y \times (E_{x,d} / E_{y,d})$  Poisson's ratio at x direction with the effect of metal deck

$n_s = E_s / E_{ci}$  The ratio of steel to concrete elastic modulus

$\mu_{y,c} = \mu_{y,d} = \mu_c$  Poisson's ratio at y direction (same as those of concrete)

$K_{BT}$  and  $K_P$  Lateral stiffness of beam-truss and shell element model, respectively.

$V$  Shear acts on the models

$K_{truss}$  Truss axial stiffness in beam-truss model

$K_B$  and  $K_T$  Lateral stiffness of beam and truss system, respectively.

$t_{avg}$  Average thickness of ribbed concrete

$D$  Depth of beam in beam system.

$\mathbf{D}_S$  Displacement vector of shell element model

$\mathbf{D}_B$  Displacement vector of beam system

$\mathbf{K}_B$  Stiffness matrix of beam system

$\mathbf{P}$  External force vector of beam system

$\Delta_H = d_5$  Lateral displacement due to pure shear in beam-truss model

$\Delta_{H=d_5}^B$  Lateral displacement in beam system

$\Delta T_{avg}$  Average difference of periods between baseline and simplified structures (%)

$n$  number of period

$T_{base}^i$  Baseline structural period of  $i^{th}$  mode

$T_{sim}^i$  Simplified structural period of  $i^{th}$  mode

**Normalized  $\text{Disp}_k^j$**  Lateral normalized displacement distribution vector with diaphragm type  $j$  in structure type  $k$

**$\text{Disp}_k^j$**  Lateral displacement distribution vector with diaphragm type  $j$  in structure type  $k$

**$\text{Disp}_k^{j,base}$**  Lateral displacement distribution vector with diaphragm type  $j$  in baseline structure type

## Appendix D

### **Evaluation of the effect of accidental torsion on the structures with semi-rigid diaphragms**

[A manuscript accepted by *The Eighth International Conference on Advance in Steel Structures (ICASS2015)*]

**Chia-Hung Fang and Roberto T. Leon**

#### **Abstract**

This paper discusses the nonlinear seismic behavior of steel structures with semi-rigid diaphragms, with emphasis on the effect of torsion. A simple approach to include the effect of torsion in nonlinear frame analyses is to modify the mass distribution on the diaphragms. This approach is used to design eight theme structures, corresponding to (1) different aspect ratios of the diaphragm (2) different configurations of the lateral force resisting system, (3) different in-plane diaphragm stiffness (rigid and semi-rigid), and (4) different thickness of diaphragms. Both nonlinear static (pushover) and dynamic time history analyses are carried out in OpenSEES. The results show that the strengths and ductility of the structures decrease, sometimes significantly, when the effect of accidental torsion is included. In addition, the structures with rigid diaphragms show a higher ductility than those with semi-rigid diaphragms.

#### **D.1 Introduction**

In conventional USA seismic design, the assumption of a rigid diaphragm is commonly used to simulate the in-plane behavior of the floor systems. In this approach, the effect of accidental torsion ( $M_{ta}$ ) is included in the analyses by shifting the position of the center of mass (C.M.) by 5% of the dimension of the structure perpendicular to the considered earthquake force (American

Society of Civil Engineers, 2010). By specifying a C.M. (i.e., a master joint) on a rigid diaphragm, constraint equations allow the condensations of the three in-plane degree of freedoms (DOFs) at each slave joint, considerably speeding up the analysis. To include the effect of  $M_{ta}$  in the static or dynamic analyses, one can simply shift the position of the master joint of each rigid diaphragm. Current design or research software, such as SAP2000 (Computer and Structures Inc., 2009) or OpenSEES (Pacific Earthquake Engineering Research Center, 2013), provides simple input options to accomplish this.

There is a comparatively large volume of literature on the seismic and collapse behavior of structures with  $M_{ta}$ . DeBock et al. (2013) discussed the importance of the  $M_{ta}$  requirement for evaluating building collapse capacity. For 3D structures with high torsional irregularity, the design  $M_{ta}$  leads to a significant change in collapse capacity for structures in Seismic Design Categories D, E and F. Erduran and Ryan (2011) evaluated the seismic behavior of 3D steel braced structures with rigid diaphragms including the effect of  $M_{ta}$ . Through nonlinear static (NSA) and dynamic analyses (NDA), they showed that the structural torsion amplification factor increases when members yield in the lateral force resisting systems (LFRS). De la Llera and Chopra (1994), and Goel and Chopra (1993) conducted extensive analytical work comparing the dynamic behavior of asymmetric-plan systems with symmetric-plan systems. Their results indicate that the effect of asymmetric configurations is more significant in the elastic systems than in the inelastic ones. Jarrett et al. (Jarrett J.A. et al., 2014) carried out the nonlinear dynamic analyses for the torsionally-regular structures with  $M_{ta}$ . This research indicates that the inelastic behavior of structures is significantly affected by  $M_{ta}$ , and the inclusion of  $M_{ta}$  should be considered in the dynamic procedures appropriately.

The scope of the previous research is limited to the evaluation of the seismic behavior for the structures subjected to the  $M_{ta}$  with rigid diaphragms. However, for some structures with highly torsional irregularity including (a) irregular diaphragms (b) irregular distributions of vertical systems across the floor systems, and (c) irregular mass distribution on diaphragms, the in-plane behavior of the diaphragm may be significant. In these cases, the assumption of a semi-rigid diaphragm may be necessary to reflect the actual behavior.

To investigate the nonlinear behavior of steel structures with semi-rigid diaphragms, including the effect of  $M_{ta}$ , both NDA and NSA are carried out for a set of theme structures with rigid and semi-rigid diaphragms using OpenSEES (Mazzoni S. et al., 2007). By modifying the distribution of mass on the diaphragms (as stated in C12.8.4.2, ASCE7 (American Society of Civil Engineers, 2010)), the effect of  $M_{ta}$  was included for structures with semi-rigid diaphragms. The structural response of the theme structures, based primarily on capacity curves and torsional coefficients, are evaluated in this study.

## **D.2 Description of theme structures**

Eight 4-story 3D theme steel structures with different diaphragm types, diaphragm aspect ratios and horizontal layouts of LFRS, were designed. All the structures have the same story heights; the 1st story is 20 ft. (6.01m) and other stories are 15 ft. (4.57m). The typical span is 27.5 ft. (8.38m). Figure D-1 illustrates the typical plan layouts, with special concentric braced frames (SCBF) in the Y direction and perimeter special moment resisting frames in the X-direction (SMFR). Configurations 1 (C1) and 2 (C2) are structures with borderline compliant diaphragms (i.e. aspect ratio 3.0 as limited by ASCE 7 for equivalent lateral load analyses), while configurations C3 and C4 are structures with stiffer diaphragms (i.e. aspect ratio 2.0). Configurations C2 and C4 are asymmetric and therefore have an inherent torsion ( $M_t$ ).

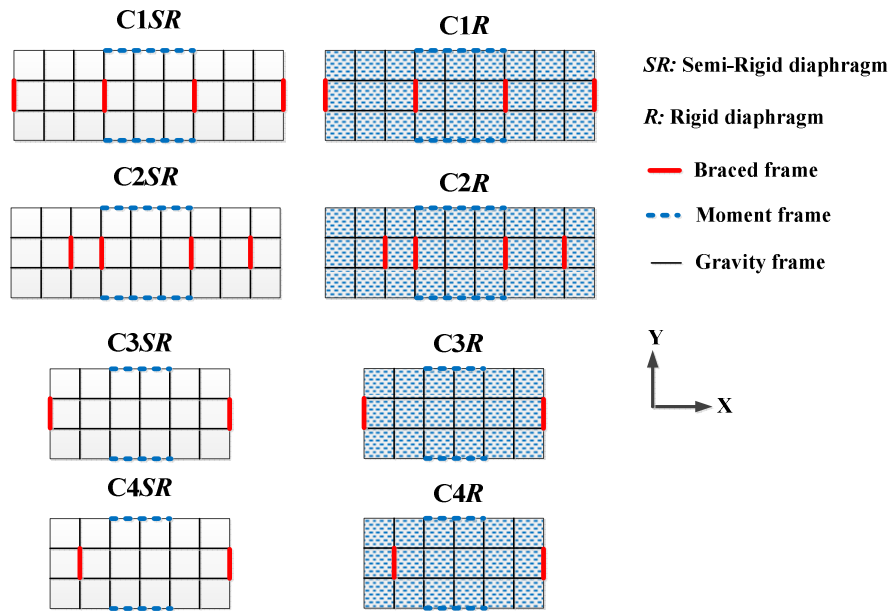


Figure D-1 Plan layout of theme structures

In Figure D-1, the symbol “**R**” means the assumption of rigid diaphragm is used for simulating the floor systems, and “**SR**” is used for presenting the assumption of semi-rigid diaphragms. In this study, the typical thickness of slab is 4.5in. (0.115m), which is presented by the subscript “**A**”. In addition, to consider the effect of cracking in diaphragms, the thickness of slabs near columns is reduced by 75% for structures with the subscript “**B**”. The elastic modulus of the diaphragms for all cases is 3122ksi (2152.5KN/m<sup>2</sup>). For both the SMRFs and SCBFs, the columns are fixed at their bases and resist lateral forces through bending about their two principal axes. The columns in the gravity system are pinned at the base and a pin connection is added at the mid-height of columns in the 3<sup>rd</sup> story to simulate the behavior of splices. The orientation of columns in these frames is shown in Figure D-2 and the elevations are illustrated in Figure D-3. The structural components are determined by the preliminary design procedures in ASCE 7 (American Society of Civil Engineers, 2010) and the design requirements of AISC 341

(American Institute of Steel Construction, 2010a) and 360 (American Institute of Steel Construction, 2010b), as shown in Table D-1 and Table D-2.

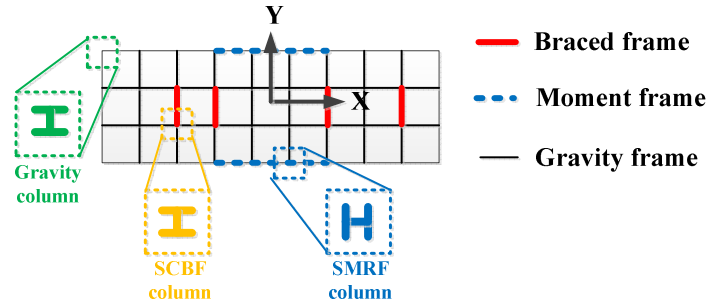


Figure D-2 Orientations of columns in the structures.

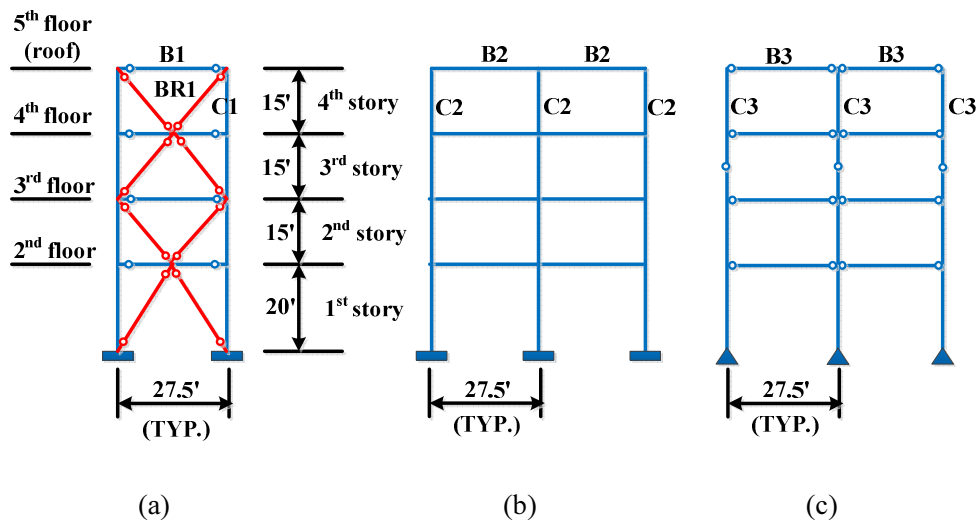


Figure D-3 Elevation layout of vertical frames: (a) Braced frames, (b) Moment frames and (c) gravity frames.

Table D-1 Dimension of structural components of the structures (C1 and C2)

Story	Story Height(ft)	C1	C2	C3	BR1	B1	B2	B3
4 <sup>th</sup>	15	W14x61	W24x176	W12x53	HSS6x6x1/2	W21x57	W18x46	W18x46
3 <sup>rd</sup>	15	↓	↓	W12x65	HSS7x7x1/2	W24x76	W21x57	↓
2 <sup>nd</sup>	15	W14x109	W27x307	W14x90	HSS7x7x5/8	W24x84	W24x84	↓
1 <sup>st</sup>	20	↓	↓	↓	HSS9x9x1/2	W27x114	W27x94	↓

Table D-2 Dimension of structural components of theme structures (C3 and C4)

Story	Story Height(ft)	C1	C2	C3	BR1	B1	B2	B3
4 <sup>th</sup>	15	W14x109	W24x176	W12x53	HSS6x6x1/2	W21x57	W18x46	W18x46
3 <sup>rd</sup>	15	↓	↓	W12x65	HSS7x7x1/2	W24x84	W21x57	↓
2 <sup>nd</sup>	15	W14x132	W27x307	W14x90	HSS8x8x1/2	W24x84	W24x84	↓
1 <sup>st</sup>	20	↓	↓	↓	HSS9x9x5/8	W27x178	W27x94	↓

### D.3 Modification of diaphragm mass distribution

To consider the effect of  $M_{ta}$  in the structures with semi-rigid diaphragms, the distribution of mass on a diaphragm shall be modified based on ASCE 7 (C12.8.4.2). This approach assumes that the  $M_{ta}$  in semi-rigid and rigid diaphragms are the same. The following steps show the modification of the mass distribution for a diaphragm with an arbitrary shape:

**Step1: Define the position of C.M. and the magnitude of  $M_{ta}$  for each rigid diaphragm.** The position of the old (original) C.M. is the same as the centroid of the rigid diaphragm. The position of new C.M. for generating  $M_{ta}$  can be determined by shifting the old C.M. by a specified distance,  $\beta L$ . The distributed seismic loads are lumped at the new C.M. as a concentrated load ( $F$ ) as defined in Equation D-1. The  $M_{ta}$  on a rigid diaphragm can be determined by using the concentrated seismic load times the eccentricity between new C.M. and old C.M. (i.e.  $\beta L$ ), as defined in Equation D-2. The relationships between  $F$ ,  $\beta L$  and C.Ms are illustrated in Figure D-4 (a).

$$F = F_A \times A + F_B \times B \quad \text{Equation D-1}$$

$$M_{ta} = F\beta L \quad \text{Equation D-2}$$

Where  $M_{ta}$  is the accidental torsion on the specified diaphragm.  $\beta$  is 0.05 based on the requirement of ASCE 7.  $L$  is the dimension of the diaphragm perpendicular of the direction of seismic loads.  $F$  is the seismic load applied on the diaphragm, and  $F_A$  and  $F_B$  are the distributed seismic loads based on the proportional mass distribution of a diaphragm.

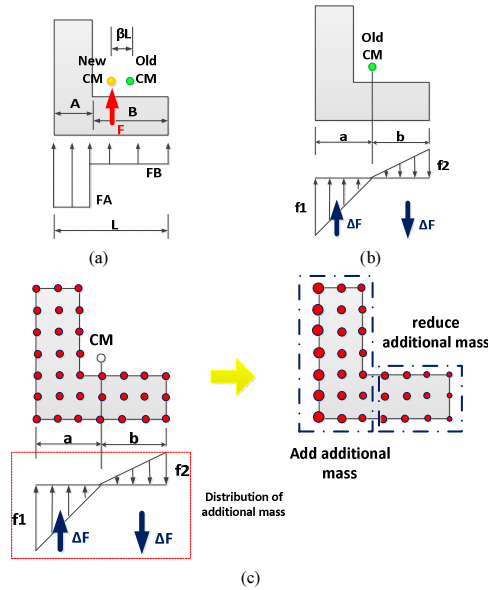


Figure D-4 Diaphragm force on a rigid diaphragm.

**Step2: Define  $M_{ta}$  of each semi-rigid diaphragm.** By assuming the same magnitude of  $M_{ta}$  between the structures with rigid and semi-rigid diaphragms,  $M_{ta}$  in the semi-rigid diaphragm structures can be generated by a couple of triangular forces applied to the semi-rigid diaphragms. The force couple generates  $M_{ta}$ , rotating about the old C.M. of the semi-rigid diaphragm (Figure D-4 (b)). Therefore,  $M_{ta}$  on a semi-rigid diaphragm can be re-expressed as Equation D-3:

$$M_{ta} = \frac{1}{2} f_1 \left( \frac{2}{3} L \right) a = \frac{1}{2} f_2 \left( \frac{2}{3} L \right) b \tag{Equation D-3}$$

Where  $a$  and  $b$  are the perpendicular distances to the applied loads used to define the location of the virtual C.M. on a semi-rigid diaphragm and  $f_1$  and  $f_2$  are the peak magnitudes of the linear triangular couple distributed forces.

**Step3: Establish relationships between the structures with rigid and semi-rigid diaphragms.**

By combining Equations D-1 and D-3, one can establish a relationship between  $M_{ta}$  and the distributed force as shown in Equation D-4:

$$F\beta L = f_1\left(\frac{L}{3}\right)a = f_2\left(\frac{L}{3}\right)b \quad \text{Equation D-4}$$

Therefore, based on Equation D-4,  $f_1$  and  $f_2$  can be re-expressed as follows (Figure D-4(c)):

$$f_1 = 3F\beta / a \quad \text{Equation D-5}$$

$$f_2 = 3F\beta / b \quad \text{Equation D-6}$$

Both Equations D-5 and D-6 indicate that the magnitude of  $M_{ta}$  is affected by the seismic loads, the eccentricity ratios of C.Ms and the shapes of diaphragms.

**Step4: Modify the mass distribution on a diaphragm.** For including the effect of  $M_{ta}$  in the analytical procedures automatically, the relationship between total diaphragm mass,  $M$ , and the linear triangular coupled distributed forces,  $f_1$  and  $f_2$ , have to be built. One can use Equation D-7 to bridge the two items.

$$F = MA \quad \text{Equation D-7}$$

where  $M$  is the total mass of the specified diaphragm and  $A$  is the horizontal acceleration of the diaphragm generated by the ground motions. By combining Equations D-5 to D-7, the relationship between the coupled distributed forces and diaphragm mass is re-defined as follows:

$$f_1 = (3M\beta / a)A \quad \text{Equation D-8}$$

$$f_2 = (3M\beta / b)A \quad \text{Equation D-9}$$

From Equations D-8 and D-9, the force distribution can be expressed by the combinations of the mass distribution as well as the horizontal acceleration on diaphragms. The magnitudes of  $f_1$  and  $f_2$  are proportional to  $\beta$ . In addition, based on the portions of Equation D-8 and D-9 in parenthesis, the additional mass acting on the diaphragm can be determined. Therefore, the effect of  $M_{ia}$  can be considered automatically in the structure during NDA through adding these additional masses to the original discrete mass distribution systems. Figure D-4 (c) illustrates the distribution of diaphragm mass before and after considering the effect of  $M_{ia}$ . Table D-3 includes the parameters for mass redistribution in each configuration.

Table D-3 Mass modification parameters of each configuration

Types of Configuration	W (kips)	M=W/g (k-s <sup>2</sup> /in)	$\beta$	a (ft)	b (ft)	$\frac{3M\beta}{a}$
C1	1430.5	3.71	0.05	123.8	123.8	0.0045
C2	1430.5	3.71	0.05	123.8	123.9	0.0045
C3	933.8	2.42	0.05	82.5	82.5	0.0044
C4	933.8	2.42	0.05	82.5	82.5	0.0044

## **D.4 Nonlinear static analyses (NSA)**

### **D.4.1 Lateral load distributions in NSA for the structures with $M_{ta}$**

In this study, for the structures with rigid diaphragms,  $M_{ta}$  is included by shifting the positions of the master joints (i.e. C.Ms) by 5% on each diaphragm and applying a set of concentrated loads along the Y-direction at the master joints. For the structures with semi-rigid diaphragms, however, the above approach is not appropriate; instead, the load patterns must be modified as discussed in Section D.3.

### **D.4.2 Capacity curves**

The capacity curves are used to evaluate the global inelastic static behavior of the theme structures (i.e. C1 and C2) with and without  $M_{ta}$  as shown in Figure D-5 and Figure D-6. The notation “M”, “B” and “G” present the summation of reaction from moment frames, braced frames and gravity frames, respectively. One can observe the following phenomena:

The yield strengths of the structures with  $M_{ta}$  are lower than those without  $M_{ta}$ . For instance, the base shears corresponding to the yield strengths in C1SRA and C2SRA are 0.53V/W and 0.50V/W, respectively. However, for C1SRA<sub>A</sub> and C2SRA<sub>A</sub> including the effect of  $M_{ta}$ , the base shears are 0.50V/W and 0.40V/W. The yield strengths decrease by 6% and 25% in the C1 and C2 structures, respectively. This indicates that the strengths of these structures with asymmetric configurations (e.g. C2) are affected by the  $M_{ta}$  significantly. The main reason is that the inclusion of  $M_{ta}$  leads to an earlier brace buckle in BF1. Therefore, the structures with  $M_{ta}$  enter into the inelastic stage earlier.

The ultimate strengths of the structures are affected by the  $M_{ta}$ . The ultimate strengths of C1SRA<sub>A</sub> and C2SRA<sub>A</sub> are 0.62V/W and 0.58V/W, which are both lower than those in C1SRA

and C2SRA (0.75V/W and 0.70V/W).  $M_{ta}$  stimulates the buckling of the 2nd brace of the 3rd story in BF1, which results in the development of the ultimate strength of the entire structures. For C1SRA<sub>A</sub> and C2SRA<sub>A</sub>, the post yield stiffness between these structures (with and without the  $M_{ta}$ ) are similar to each other because the global lateral stiffness is primarily provided by the SMRFs in this stage.

The inclusion of  $M_{ta}$  affects the roof drift ratios corresponding to the development of ultimate strengths. In Figure D-5 and Figure D-6, it is clear that the roof drift ratios corresponding to the development of ultimate strengths in the structures with the  $M_{ta}$  are lower than those without considering the  $M_{ta}$ . This indicates that the application of  $M_{ta}$  generates a lower structural global ductility of entire structures.

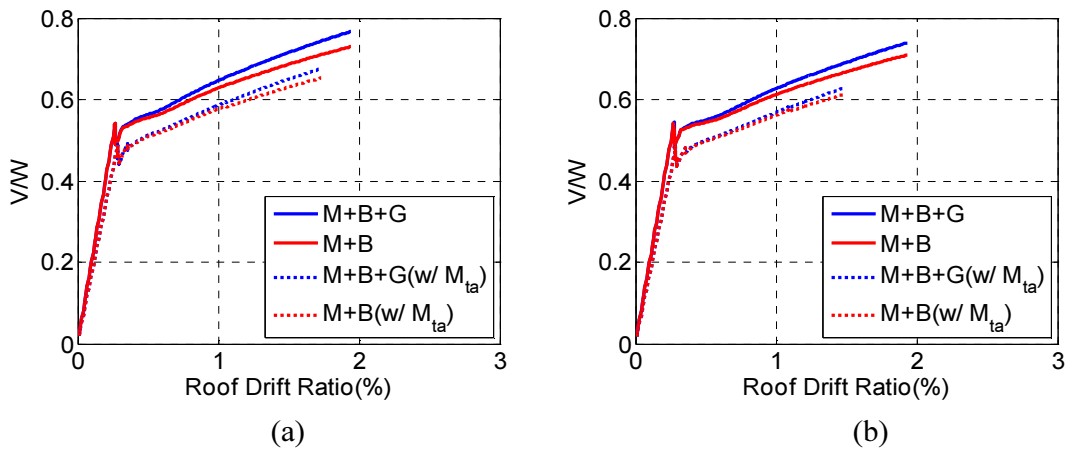


Figure D-5 Capacity curves: (a) C1SRA<sub>A</sub> and (b) C1SRA<sub>B</sub>

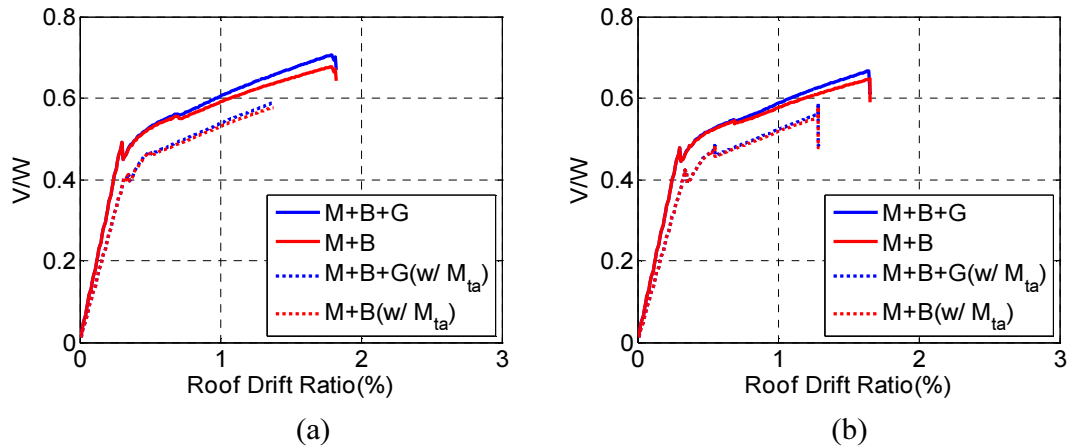


Figure D-6 Capacity curves: (a) C2SRA<sub>A</sub> and (b) C2SRA<sub>B</sub>

#### D.4.3 Rotation behavior of the diaphragms

The rotation of the diaphragms is caused by the existence of inherent torsion ( $M_t$ ) and  $M_{ta}$  as the NSA progresses. By using the torsion coefficient ( $TC$ ) defined in ASCE 7 (Table 12.3-1), the effect of  $M_{ta}$  in these theme structures is evaluated in the elastic and inelastic stages. Equation D-10 shows the definition of  $TC$ .

$$TC_j = \frac{D_{\max}^j}{D_{\text{avg}}^j} \quad \text{Equation D-10}$$

Where  $TC_j$  is the torsional coefficient at j-level,  $D_{\max}^j$  is the maximum story drift at j-level,  $D_{\text{avg}}^j$  is the average story drift at j-level.

The structural rotation is more significant when the structures enter into the inelastic stage (i.e. buckling of braces) as shown in Figure D-7 and Figure D-8. This is caused by the buckling of braces in the vertical frames stimulating the increment of horizontal irregularity. For the asymmetric structures with  $M_{ta}$  such as C2SRA<sub>A</sub> and C4SRA<sub>A</sub>, the maximum  $TC$  in the 2F-level diaphragm of the two structures are 2.00 and 1.81, respectively (Table D-4). These  $TC$ s are higher than those in C2SR<sub>A</sub> and C4SR<sub>A</sub> by 10.5% and 3.4%. This demonstrates the  $M_{ta}$  amplifies

the magnitude of  $TC$  as the NSA progresses. All of the  $TC$ s in Table D-4 are higher than the extreme horizontal irregularity limits defined in ASCE 7 (i.e. 1.40). This indicates that the effect of  $M_{ta}$  increases the rotational irregularity when the structures enter into the inelastic stage.

In addition, the reduction of thickness affects the variation of  $TC$  slightly. In Figure D-7 (b) and Figure D-8 (b), the magnitudes of  $TC$ s in the structures with reduced thickness (C2SRA<sub>B</sub> and C4SRA<sub>B</sub>) are slightly higher than those with uncracked diaphragms (C2SRA<sub>A</sub> and C4SRA<sub>B</sub>). This phenomenon indicates that the reduction of diaphragm thickness may not be an important factor for influencing the torsional resistance of structure. From this table, the  $TC$ s in the structures with rigid diaphragms (i.e. C2RA and C4RA) are higher than those with semi-rigid diaphragms (C2SRA<sub>A</sub> and C4SRA<sub>A</sub>). This indicates that the rigid diaphragm structures evidence a lower resistance for both  $M_t$  and  $M_{ta}$ . The phenomenon is caused by the existence of efficient force transfer mechanism in the rigid diaphragms. The  $TC$ s in C1SRA and C3SRA should be zero because of their symmetric configurations.

Table D-4 Maximum  $TC$ : C2SRA<sub>A</sub>, C2SRA<sub>B</sub>, C4SRA<sub>A</sub> and C4SRA<sub>B</sub>

Floor	C2SRA <sub>B</sub>	C2SRA <sub>A</sub>	C2RA	C4SRA <sub>B</sub>	C4SRA <sub>A</sub>	C4RA
5F	1.55	1.92	1.75	1.60	1.72	1.84
4F	1.60	1.98	2.00	1.63	1.75	1.85
3F	1.70	2.00	2.05	1.68	1.79	1.86
2F	1.81	2.00	2.08	1.75	1.81	1.86

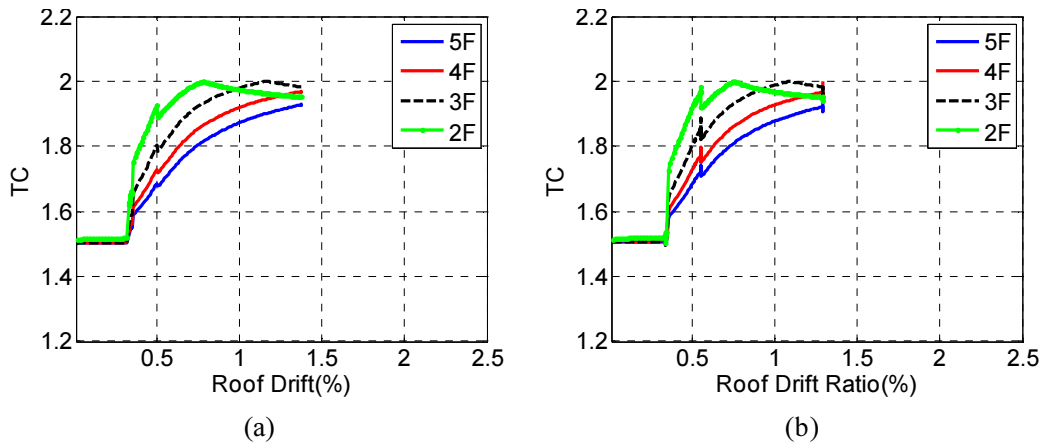


Figure D-7 *TC* of each diaphragm: (a) C2SRA<sub>A</sub> and (b) C2SRA<sub>B</sub>

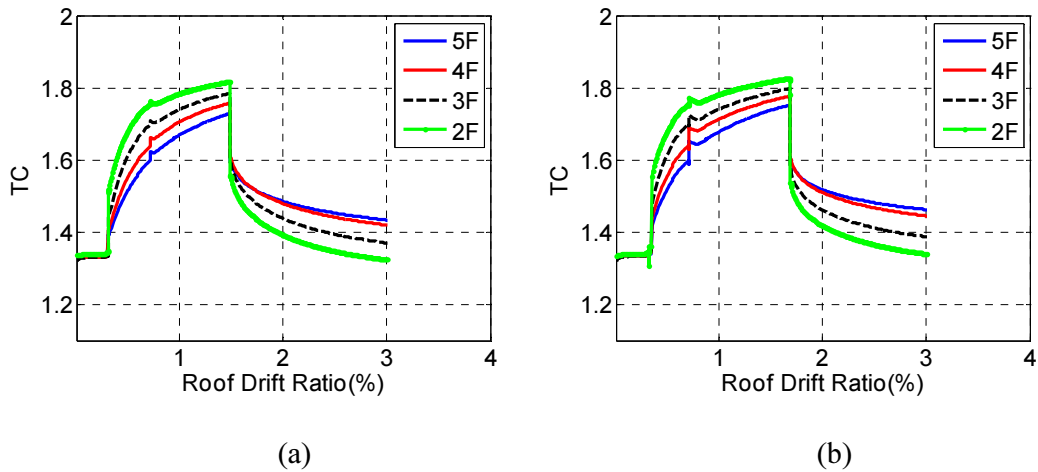


Figure D-8 *TC* of each diaphragm: (a) C4SRA<sub>A</sub> and (b) C4SRA<sub>B</sub>

#### D.4.4 Bi-axial NSA for the structures with $M_{ta}$

This section discusses the analytical results of NSA considering the bi-axial effect of  $M_{ta}$ . Based on the design requirement of ASCE 7 (ELF approach), the design load combinations of structural components shall include the bi-axial effect of seismic loads. The bi-axial effect in the NSA is generated by applying the two seismic load patterns about the two principal axes of the structures. The magnitudes of seismic loads about the minor axis (X-direction) are 30% of the considered earthquake forces about the major axis (Y-direction). The ELF does not require that the 5%

eccentricities be applied in both directions (12.8.4.2) at the same time, but shall be applied in the direction that produces the greater effect. In this study, however, the eccentricities of the two patterns are both considered in the NSA to investigate the inelastic behavior under the different combinations of eccentricity.

For the structures with low lateral redundancy as well as asymmetric configurations, the different combinations of the bi-axial eccentricities at the two principal directions may significantly affect the inelastic behavior of the structure. In this study, the asymmetric structures in the C4 group are selected as the target structures to evaluate the influence of bi-axial effect from  $M_{ta}$ .

Figure D-9 illustrates the load patterns for the C4 structures. On the basis of the discussion in Section D.4.1, the load patterns for the rigid diaphragm structures consist of a set of concentrated loads. Several cases are considered:

**CASE1:** The NSA does not include the effect of  $M_{ta}$ .

**CASE2:** The NSA includes the effect of  $M_{ta}$  due to the eccentricity along the Y-axis.

**CASE3:** The NSA includes the effect of  $M_{ta}$  due to biaxial eccentricity (i.e., Case 2 plus 30% eccentricity about the X-axis).

**CASE4:** The NSA includes the effect of  $M_{ta}$  due to the biaxial eccentricity (Case 3), but the position of the C.M. on the rigid diaphragms is shifted towards the C.R. by an additional  $0.05 \times L$ . Therefore, the magnitude of  $M_t$  and  $M_{ta}$  are both increased.

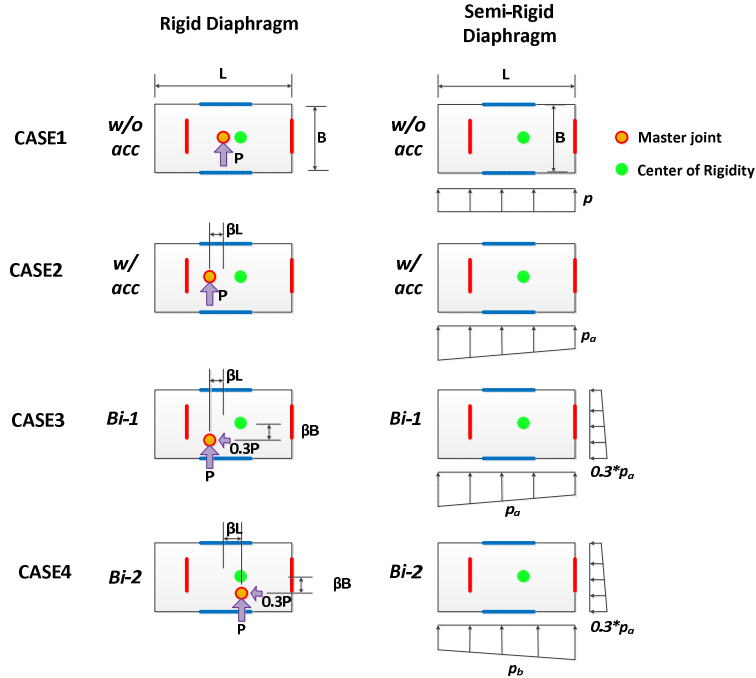


Figure D-9 Bi-axial NSA in the structures with rigid and semi-rigid diaphragms

Figure D-10 shows the capacity curves of the C4 structures corresponding to different combinations of load patterns (i.e. CASE1 to CASE4). In these curves, the yield and ultimate strengths in C4SRA<sub>A</sub> (Figure D-10 (b)) are higher than those in C4RA (Figure D-10 (a)) because of the inclusion of the out-of plane stiffness of diaphragm. In addition, the yield and ultimate strengths in CASE4 for both rigid and semi-rigid diaphragm structures are higher than other cases. In CASE4, the positions of the load patterns are closer to the C.R. This indicates that the irregularity due to the mass eccentricities is smaller than the other three cases, and thus the strengths of structure are improved. However, CASE3 exhibits the lowest yield and ultimate strengths. This is caused by the magnitude of eccentricity between C.M. and C.R. is the highest among the four cases.

The individual capacity curves of braced frames from CASE1 to CASE4 are shown in Figure D-11. BF1 in C4SRA<sub>A</sub> develops their yield strengths in each case. In other words, obvious peaks in

these curves appear as shown in Figure D-11 (a). For the BF2 in C4SRA<sub>A</sub> (Figure D-11 (b)), however, the development of the peak in CASE4 is sooner than the other three cases as the NSA progresses. This reduces the magnitudes of global yield and ultimate strengths. This phenomenon indicates that the shift or modification of the distribution of diaphragm mass significantly changes the structural behavior in the inelastic stage.

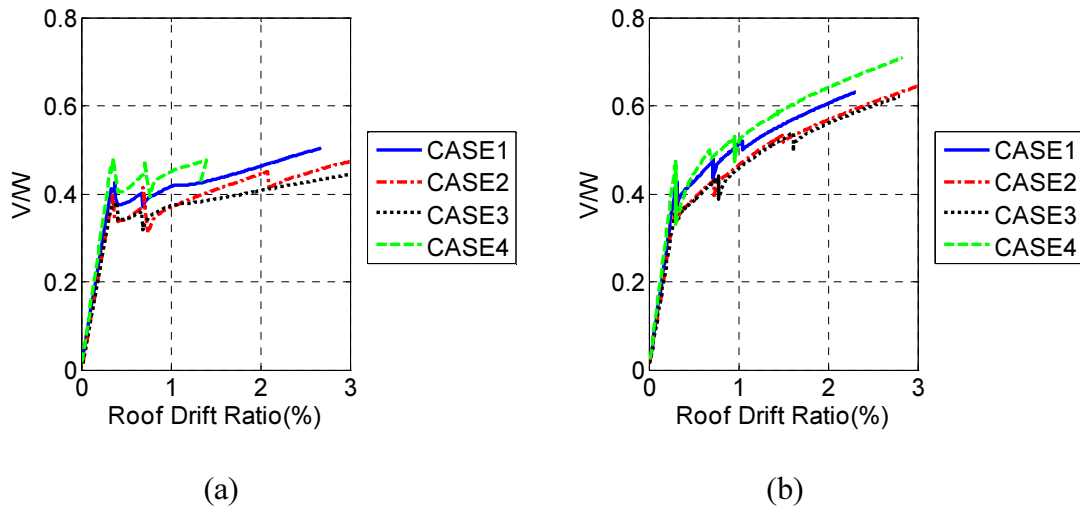


Figure D-10 Capacity curves of each case in C4 structures: (a) C4RA and (b) C4SRA<sub>A</sub>

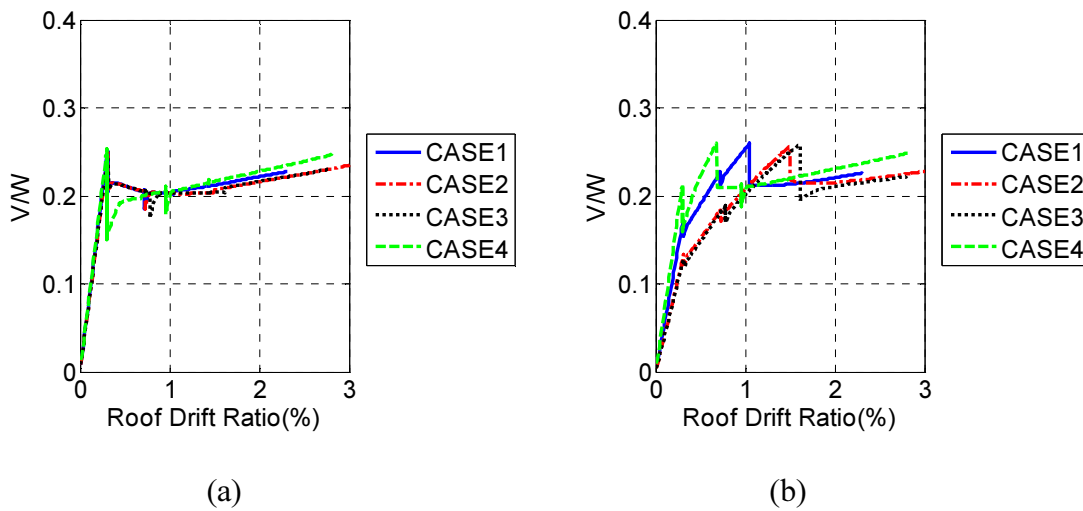


Figure D-11 Capacity curves of each braced frame in C4SRA<sub>A</sub>: (a) BF1 and (b) BF2

## D.5 Nonlinear Dynamic Analyses (NDA) for the C2 structures with $M_{ta}$

### D.5.1 The selection of G.Ms

In this study, NDA is the other approach used to evaluate the effect of  $M_{ta}$  on the structures with different in-plane diaphragm stiffness. Three spectrum compatible ground motions (G.Ms) (Chai C.-F. and Loh C.-S., 2002) based on the original earthquake records provided by PEER (Pacific Earthquake Engineering Research Center, 2014) with different hazard levels (DBE and  $MCE_R$ ), are utilized: (1) Northridge (NGA ID: 127), (2) San Fernando (NGA ID: 30) and (3) Loma Prieta (NGA ID: 118), respectively. The mapped acceleration parameters  $S_S$  and  $S_1$  are 1.50g and 0.63g, respectively (U.S. Geological Survey, 2014). The effect of  $M_{ta}$  on the structural behavior under the two diaphragm assumptions will be characterized by the rotation angles of the diaphragms as well as the inter-story drift ratios. The C2 structures are the target models in this study. This is because their asymmetric configurations may lead to an obvious inelastic behavior due to  $M_{ta}$ .

### D.5.2 Rotation angles of diaphragms

The absolute maximum rotation angles in the C2 structures with  $M_{ta}$  are evaluated in this subsection, as shown in Figure D-12. The definition of rotation angle of diaphragm ( $RA$ ) is given in Equations D-11. From this Figure, one can observe that the absolute maximum  $RA$  the roof diaphragm (Figure D-3 (a)) is the largest one among the four levels. In addition, the magnitudes of the angle in the structures with rigid diaphragms are slightly higher than those with semi-rigid diaphragms under the MCE-level G.Ms.

$$RA_j = \frac{|\Delta_j^R - \Delta_j^L|_{\max}}{L_j}$$

Equation D-11

Where,  $RA_j$  is the rotation angle (in degree) at  $j$ -th level,  $L_j$  is the dimension of diaphragm at  $j$ -th level perpendicular to the direction of seismic loads,  $\Delta_j^R$  is the lateral displacement at the right corner of diaphragm at  $j$ -th level, and  $\Delta_j^L$  is the lateral displacement at the left corner of diaphragm at  $j$ -th level.

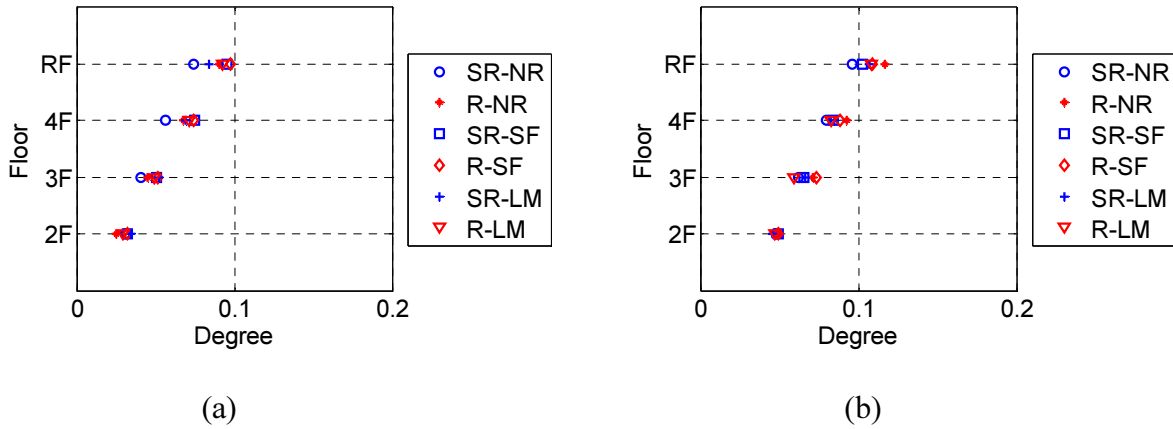


Figure D-12 Maximum  $RA$  of each diaphragm in  $C2SRA_A$ : (a) DBE and (b) MCE

However, the  $RA$  as described so far is related to the global displacements of the floors. By measuring the relative rotation angles ( $RRD$ ) between two contiguous diaphragms, a measure akin to the interstory drift can be developed. Therefore, the  $RRD$  is probably a better measure of the instantaneous horizontal irregularity between floors and thus of the torsional forces on individual diaphragms. The definition of  $RRD$  is:

$$RRD_{\max}^j = |RA_{j+1} - RA_j|_{\max} \quad \text{Equation D-12}$$

Where  $RRD_{\max}^j$  is the maximum relative rotation angle in the  $j^{th}$  story,  $RA_{j+1}$  is the maximum relative rotation angle in the  $j+1^{th}$  diaphragm, and  $RA_j$  is the maximum relative rotation angle in the  $j^{th}$  diaphragm.

The  $RRD_{max}$  of each diaphragm in C2SRA<sub>A</sub> are shown in Figure D-13. It is clear that the  $RRD_{max}$  at the 2F diaphragm is higher than those at other diaphragms. The phenomenon means a higher torsional irregularity develops in the lower stories. Such phenomenon is the same as the one illustrated in Subsection D.4.3.

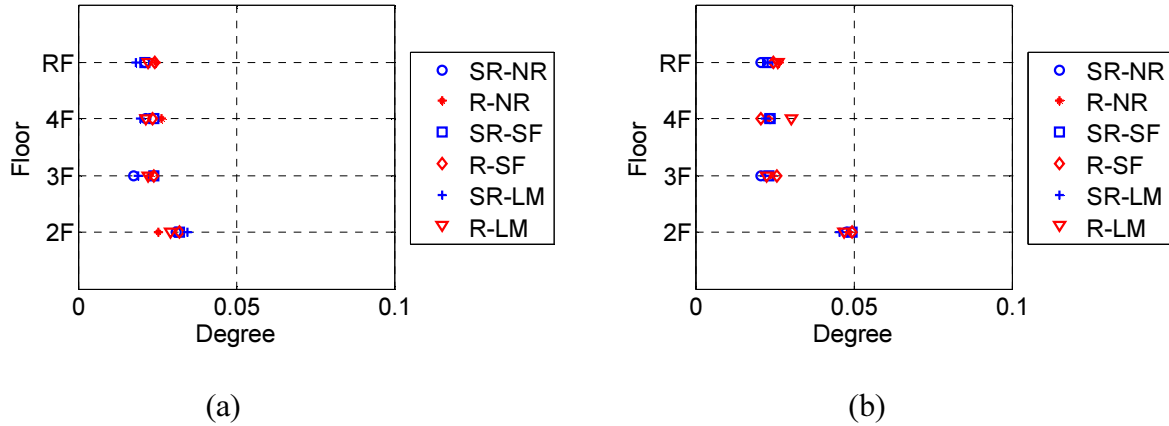


Figure D-13  $RRD_{max}$  of each diaphragm in C2SRA<sub>A</sub>: (a) DBE and (b) MCE

In addition, the results show that the magnitude of  $RRD_{max}$  is significantly affected by the  $M_{Ia}$ . By comparing the magnitude of  $RRD_{max}$  of each diaphragm between C2SRA and C2SRA<sub>A</sub>, as shown in Table D-5, the  $RRD_{max}$  in C2SRA<sub>A</sub> are higher than those in C2SRA by 90~120%.

Table D-5 Comparison of diaphragm  $RRD_{max}$  for the structures with and without  $M_{Ia}$  (C2SRA and C2SRA<sub>A</sub>)

Floor	DBE		MCE	
	w/o $M_{Ia}$	w/ $M_{Ia}$	w/o $M_{Ia}$	w/ $M_{Ia}$
RF	0.011	0.025	0.014	0.026
4F	0.012	0.026	0.012	0.030
3F	0.012	0.024	0.012	0.026
2F	0.022	0.034	0.023	0.049

Units: Degrees (°)

### D.5.3 Maximum inter-story drift ratio

Maximum inter-story drift ratio (*IDR*) is one of the most important indices used to evaluate the non-linear time history seismic performance of structures. In this study, *IDR* and *RRD* are the two independent indices used to evaluate the elastic and inelastic behavior of the theme structures. The *RRD* is used to measure the horizontal irregularity of the target stories, and the *IDR* is used to investigate the vertical irregularity of the structures. Both of the two parameters are primarily generated by the development of inelastic behavior in the vertical frames. The *IDR* in each story are shown in Figure D-14 and Figure D-15. One can observe the following phenomena:

For the C2 structures with or without  $M_{ta}$ , the maximum *IDR* in the 1<sup>st</sup> story in the rigid diaphragm structures is higher than those with semi-rigid diaphragms under the MCE-level G.Ms. This is caused by the development of a significant rotation in the structures with rigid diaphragms. A robust transfer mechanism for the in-plane forces in rigid diaphragms is maintained as the NDA progresses.

The effect of  $M_{ta}$  is not significant on the structures under the DBE-level G.Ms. From Figure D-14 (a) and Figure D-15 (a), the magnitudes of  $IDR_{max}$  between the stories do not exhibit a significant difference. This indicates that the  $M_{ta}$  may not significantly influence the structural response under the design level earthquakes.

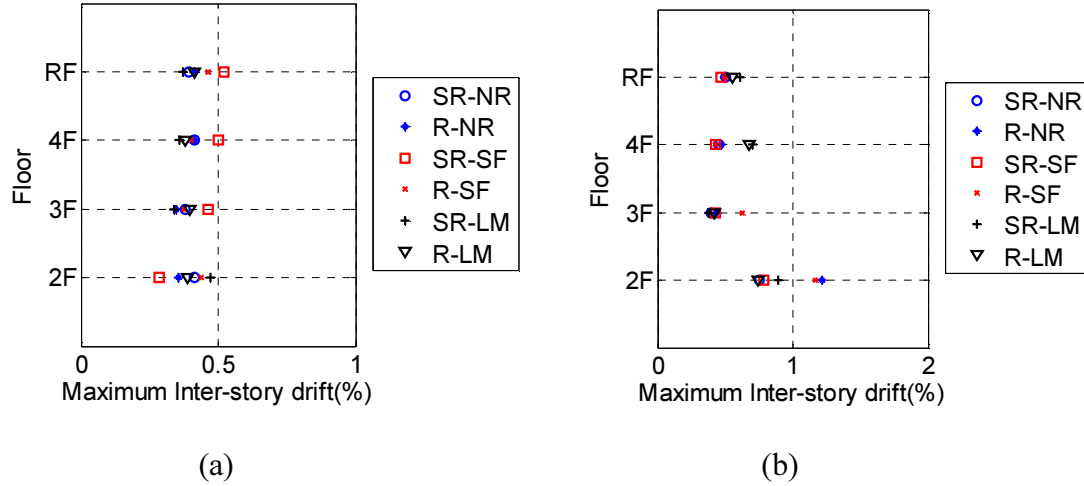


Figure D-14 Maximum  $IDR$  of the C2 structures with  $M_{ta}$  (a) DBE-level (b) MCE-level

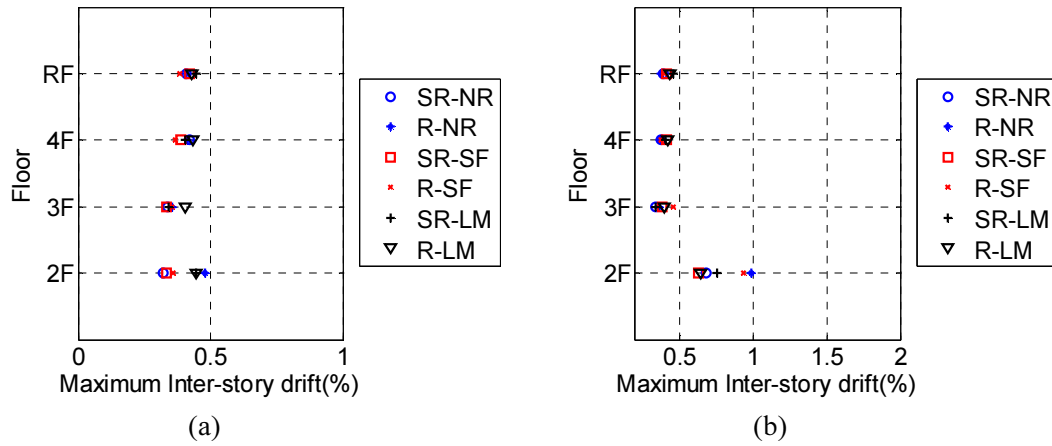


Figure D-15 Maximum  $IDR$  of the C2 structures without  $M_{ta}$  (a) DBE-level (b) MCE-level

## D.6 Conclusions

1. From the results of the NSA, the yield and ultimate strengths of the theme structures decrease due to the effect of  $M_{ta}$ . This phenomenon is more significant in the asymmetric structures.
2. The magnitudes of  $TC$ s in the asymmetric structures (i.e. C2 and C4 structures) increase significantly due to the  $M_{ta}$ . The analytical results show that the inclusion of  $M_{ta}$  in these asymmetric structures in NSA leads to the increment of  $TC$  ranging from 11%~25%.

3. The structures with rigid diaphragms exhibit higher magnitudes of  $TCs$ . This is caused by the existence of efficient force transfer mechanism in the rigid diaphragms.
4. For the structures considering the effect of bi-axial eccentricity in NSA, the positions of C.Ms significantly affect the yield and ultimate strengths of the structures. When the position of C.M. is close to the C.R. (i.e. CASE4), the behavior of the asymmetric structure is similar as the one provided by the symmetric structures. However, when the C.M. moves away from C.R. (i.e. CASE3), the asymmetric behavior of the structure is severe, and thus the strengths reduces significantly.
5. Based on the results extracted from the NDA, the structures with higher aspect ratios of diaphragm (i.e. C2 and C4) perform a higher magnitude of the maximum  $RA$  of diaphragm. Such phenomenon is obvious when the intensities of G.Ms increase. In addition, the magnitudes of rotation angles ( $RRD$ ) in the structures with rigid diaphragms are higher than those with semi-rigid diaphragms. This indicates that the rotational resisting ability for the rigid diaphragm structures is lower than the structures with semi-rigid diaphragms.